

Final Design Review

Enoch Lee

Simon He

Fangzhou Liu

Contents

List of Figures	4
List of Tables	6
Introduction	7
Progress Report.....	9
Aircraft Specifications.....	10
Force and Load Evaluation.....	11
Reynolds Number Calculation.....	11
Airfoil Lift Profile	13
V-n Diagram	15
Load Determination	21
Load Distribution: finding $l(z)$ and $d(z)$ functions.....	22
Load Distribution: finding W_x and W_y load intensity functions	24
Centroid and Moments of Inertia	31
The Airfoil Section.....	32
Shear, Moment, and Deflections	35
Failure Analysis	40
Shear Flow.....	40
Two-Cell Shear Flow Calculations	44
Shear Flow Validation	50
Column Buckling	52
Skin Buckling	54
Von Mises Failure Criteria.....	57
Fatigue and Crack Analysis.....	59
Optimization and Failure Correction	61
Finite Element Analysis	64
Computer-Aided Design.....	65
Finite Element Analysis – Stress and Deflection.....	68
Modal Analysis	72
Wing Divergence and Aileron Reversal Checks.....	77
Conclusion.....	80
Appendix A: Centroid and moments determination of a Simple Box beam	83

Appendix B: Shear forces, Moments, and Deflections	90
Appendix C: Direct Stresses	109
Appendix D: Shear Flows and Shear Stresses	122
Section D.1: Shear Flow	122
Section D.2: Shear Stress	129
Appendix E: Additional Failure Plots.....	142
Section E.1: Von Mises	142
Section E.2: Direct Stress Skin Buckling	148
Appendix F: Maneuvering	155
Appendix G: COMSOL Multiphysics Results.....	159
Reference	174

List of Figures

Figure 1: Linear Cl vs. angle of attack at sea level	13
Figure 2: Linear Cl vs. angle of attack at 14600 ft.....	14
Figure 3: Flight envelope at sea level without gust loads.....	17
Figure 4: Flight envelope at 14600 ft. altitude without gust loads	17
Figure 5: V-n Diagram at Sea Level	19
Figure 6: V-n Diagram at 14600 ft.....	20
Figure 7: Drag distribution at PHAA at service ceiling	23
Figure 8: Lift distribution at PHAA at service ceiling.....	24
Figure 9: Sign convention and frame of reference as shown in [4]	25
Figure 10: Load intensity at PHAA and PLAA at sea level	26
Figure 11: Load intensity at PHAA and PLAA at service ceiling.....	27
Figure 12: Load intensity at NHAA and NLAA at sea level	28
Figure 13: Negative Gust Loads at sea level	29
Figure 14: Negative Gust Loads at service ceiling.....	30
Figure 15: Stringer and spar cap idealization.....	33
Figure 16: Moment distribution of the wing at sea level (PHAA)	38
Figure 17: Shear distribution of the wing at sea level (PHAA)	38
Figure 18: Wing deflection from root to tip (sea level, PHAA)	39
Figure 19: Direct stresses at root of wing, PHAA conditions with original dimensions.....	41
Figure 20: Example boom distribution across an open cross-section	43
Figure 21: Constant shear flows for a multi-cell cross-section	45
Figure 22: Example constant shear flows for a closed section	46
Figure 23: Total shear flow magnitude about airfoil surface at sea level PHAA.....	48
Figure 24: Shear stress distribution about skin panels on wing root airfoil surface at sea level PHAA	49
Figure 25: Shear stress distribution about skin panels on half-wing airfoil surface at sea level PHAA	49
Figure 26: Example of Eulerian beam buckling.....	52
Figure 27: Visualization of thin plate buckling loads	55
Figure 28: Skin buckling from direct stress at sea level PHAA. Red lines indicate failure	56
Figure 29: Percentage of equivalent/yield stress at sea level PHAA	58
Figure 30: Direct stresses after failure corrections.....	63
Figure 31: Direct stress skin buckling after failure corrections.....	63
Figure 32: Wing skin CAD model.....	65
Figure 33: Wing internal structure CAD model, showing the stringers, ribs, and spars of the wing.....	66
Figure 34: Cross-sectional view of the wing, showing spars, z-stringers, and skin.....	67
Figure 35: Wing CAD model, showing the stringers, ribs, and spars of the wing.....	67
Figure 36: COMSOL Multiphysics finite element analysis for stress and deflection at PHAA	69
Figure 37: Wing Deflection at PHAA	70
Figure 38: COMSOL Multiphysics finite element analysis for internal structures stress and deflection at PHAA	71
Figure 39: First mode at an Eigenfrequency of 8.08 Hz (wing)	73
Figure 40: First mode at an Eigenfrequency of 8.08 Hz (internal)	73

Figure 41: Second mode at an Eigenfrequency of 32.58 Hz (wing)	74
Figure 42: Second mode at an Eigenfrequency of 32.58 Hz (internal)	74
Figure 43: Third mode at an Eigenfrequency of 44.00 Hz (wing)	75
Figure 44: Third mode at an Eigenfrequency of 44.00 Hz (internal).....	75
Figure 45: Fourth mode at an Eigenfrequency of 54.76 Hz (wing)	76
Figure 46: Fourth mode at an Eigenfrequency of 54.67 Hz (internal)	76

List of Tables

Table 1: Project progress	9
Table 2: Pertinent aircraft and wing parameters.....	10
Table 3: FAR 23 aircraft loading requirements	11
Table 4: Three dimensional lift coefficient data	15
Table 5: Velocity and Load Factor values at Critical Design Points at Sea Level.	19
Table 6: Velocity and Load Factor values at Critical Design Points at 14600 ft.....	20
Table 7: Area Moments of Inertia of the wing.....	35
Table 8: Maximum Direct Stresses on Wing	42
Table 9: Cycles to Failure at Different Critical Points.....	60
Table 10: New moments of inertia of the wing	62
Table 11: Parameters used in the CAD model.	65
Table 12: Dimensions of the simplified cantilever beam model	85
Table 13: Centroid calculations for the simplified cantilever beam model. X and y coordinates of the beam model are highlighted.	86
Table 14: Moment of inertia calculations for spars.....	87
Table 15: Moment of Inertia calculations for brackets.....	88
Table 16: Moment of inertia calculations for skins. Total moments of inertia of the cantilever beam model are highlighted.....	89

Introduction

This project focused on the structural analysis and optimization of a small commercial aircraft similar to a Cessna 177. The initial design process required wing loading estimates. These load estimates were made through the use of analytical equations as well as aerodynamic codes like Xfoil. These results were then used along with FAR 23 regulations to generate flight envelopes that identified points of critical operational loading.

These flight envelopes gave performance data at these critical points, which allowed for the estimation of total three dimensional lift and drag forces at the different critical points. These loads were then applied to the simple box beam geometry example given in lecture to determine deflections and shear forces. With the given dimensions, total wing tip deflections were found to be small and on the order of magnitude of a millimeter.

A similar loading analysis was then applied to the cross-section of an actual NACA 2415 airfoil, with the final 20% cut off for control surfaces. With the given starting dimensions, maximum deflections increased to the order of approximately 10 cm along the z axis. In most cases, x axis deflections remained constrained to under 1 cm.

These loads were also useful in determining the stresses acting on the wing. This required shear flow calculations, which made use of several geometric idealizations. Particularly, boom area idealizations were used to greatly simplify these shear flow calculations. The closed, two-cell nature of the cross-section also required the use of an angle of twist compatibility equation to solve for final shear flows. The resulting shear flows were approximately 10^4 N/m in magnitude, while the resulting shear forces ranged from 10-35 MPa in magnitude.

The resulting loads were then applied to several failure checks. These included buckling, Von Mises yield, and fatigue analysis. While the equivalent Von Mises stress was found to be under yield at all conditions, the skin buckling and fatigue behaviors of the wing were much worse. It was found that the wing skin would buckle under both direct and shear stresses at the wing roots at PHAA. Furthermore, it was shown that these stress concentrations occurred near the front of the wing. Fatigue analysis showed that the given stress amplitudes would result in fatigue crack propagation at less than 10000 cycles.

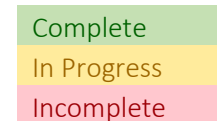
However, these failure criteria as well as fatigue cycles were remedied by increasing stringer and cap areas. Skin thickness, though increased the overall mass of the wing, was increased in an attempt to satisfy the predefined specifications. The final parameters were used to generate a CAD model via SolidWorks and was then imported to COMSOL Multiphysics for additional finite element analysis as well as modal analysis. The results were then compared with findings from the calculations from Matlab.

Finally, a wing divergence and aileron reversal analysis was conducted to find velocities at which these phenomena would occur. The results indicated that the maximum speeds at which the wing is expected to be operating in fall under the calculated divergence and aileron reversal speeds, indicating wing divergence and aileron reversal are not expected to occur under normal circumstances.

Progress Report

Table 1: Project progress

Week	1	2	3	4	5	6	7	8	9	10
Xfoil Lift Coefficient Analysis	✓									
Construct V-n diagrams	✓									
Load Distribution Analysis (finding $l(z)$ and $d(z)$)		✓								
Load intensity (W_x and W_y)		✓								
Centroid and moment of inertia of airfoil		✓								
Shear, moment, and displacement calculations			✓							
Multiaxial bending			✓							
Choose materials for skin and supports				✓						
Shear flow calculations				✓						
Failure estimates (Von Mises and buckling)					✓					
Fatigue analysis						✓				
CAD model of wing							✓			
Optimization of wing sizing and supports							✓	✓	✓	
Finite Element modelling							✓	✓	✓	



Aircraft Specifications

The basic dimensions of the aircraft wing and the required weights used for analysis were:

Table 2: Pertinent aircraft and wing parameters

Airfoil	NACA 2415
Maximum Gross Weight (mass)	1100 kg
Maximum Gross Weight	10791 N
Standard Empty Weight (mass)	680 kg
Standard Empty Weight	6670.8 N
Cruise Speed	230 km/h (63.89 m/s)
Maneuvering Speed	250 km/h (69.44 m/s)
Total Wing Span	10.82 m
Chord	1.5m
Oswald Efficiency Factor	0.79
Wing Planform Area	16.23 m ²

Several additional assumptions were made to further simplify this project. First, the wings were assumed to have no taper. Similarly, the wings were assumed to have rectangular planforms to maintain a constant cross section. This greatly simplified the process of finding the wing centroid and moments of inertia for later use in bending analysis. The load factor requirements for this project were taken from FAR 23 aircraft regulations. Table 3 lists the critical load factors used for this report.

Table 3: FAR 23 aircraft loading requirements

Positive Limit Maneuvering Load	Negative Limit Maneuvering Load	Negative Limit at Dive Speed	Load at PHAA	Load at NHAA
$n_1 = 4.4$	$n_1 = -0.4 * 4.4 = -1.76$	$n_3 = -1$	4.4	-1.76

Force and Load Evaluation

The loads on the aircraft were evaluated for later use in failure predictions. Along with the performance requirements discussed previously, several idealizations were used to estimate the forces and moments affecting the aircraft wings at different flight conditions. The primary source of these force idealizations was Xfoil, which was used to calculate the two-dimensional lift, drag, and pitching moment of the NACA 2415 airfoil used for the wings. This Xfoil analysis, however, also required Reynolds and Mach number terms to account for more realistic conditions.

Reynolds Number Calculation

The aerodynamic loads were determined through specifically using the viscous regime of Xfoil. This regime required Reynolds and Mach numbers at sea level and ceiling operating conditions in order to provide accurate predictions. With these inputs, lift, drag, and moment coefficients at varying angles of attack were found. The Reynolds numbers for sea level and ceiling conditions were calculated using the standard Reynolds number Eq. (1). This equation relates inertial qualities of a flowing fluid and its viscosity.

$$Re = \frac{\rho V c}{\mu} \quad (1)$$

Here ρ coincided with air density, V represented relative air velocity, c was the chord length of the wing section, and μ was the dynamic viscosity of air. The chord length and velocity used in Eq. (1) were given in

the project constraints as 1.5 m and 250 km/h respectively. The density and viscosity of air were calculated for both sea level conditions and service ceiling conditions at 14600 ft. to account for potential differences flow behavior. Densities for sea level and service ceiling were determined to be 1.225 kg/m³ and 0.782 kg/m³ respectively. Dynamic viscosities for sea level and service ceiling flight were also determined to be 1.789E-5 N.s/m² and 1.646E-5 N.s/m² respectively. Using Eq. (1), the sea level Reynolds was found to be approximately 7.1E6 while the service ceiling operational Reynolds number was found to be approximately 4.9E6.

The Mach number inputs were derived with the following relations i.e. Eq. (2) and (3). Eq. (2) solves for the speed of sound a while Eq. (3) generates the non-dimensional Mach number M .

$$a = \sqrt{kRT} \quad (2)$$

$$M = \frac{v}{a} \quad (3)$$

The variable k was the ratio of the constant pressure and constant volume specific heat of air, which was assumed to be 1.4. R was the ideal gas constant of air, which is 287 J/kg/K. Finally, the variable T represented the atmospheric temperature. Using the U.S. standard atmosphere tables from [1] the temperature at sea level was found to be 288°K while the temperature at the service ceiling was found to be 259.1°K. Once again using the maneuvering velocity of 250 km/h as the input velocity in Eq. (3), the flight Mach numbers were determined to be 0.215 at sea level and 0.204 at the service ceiling. With operating Reynolds numbers and Mach numbers determined, the viscous Xfoil analysis was then run to generate data for load calculations.

Airfoil Lift Profile

The lift coefficient data from Xfoil was used extensively for load estimates and failure checks. However, this data needed to be processed in order to provide the necessary inputs for load and failure functions. Thus, the lift coefficient data points were first fit using excel in order to find the two dimensional lift slope of a NACA 2415 airfoil. The 2D fit curves are shown in Figs. (1) and (2) below. These figures also show the corrected three dimensional lift-curves as well.

The lift curve slope determined for flight at sea level and 14600 ft. are 6.5968/rad and 6.5344/rad respectively. These slopes were generated by applying Excel's linear fit function to the -7 degree and 10 degree data range, which was assumed to be the linear portion of the data. The data curve fits were plotted in Figs. (1) and (2) below. Furthermore, the minimum and maximum lift coefficient values were determined by running Xfoil in a total range of -20 degrees to 20 degrees. The maximum and minimum values were found to be near these two angles of attack. For sea level Cl_{max} was 1.8528 while Cl_{min} was -1.6626. Similarly, for the ceiling altitude of 14600 ft. Cl_{max} was 1.7858 while Cl_{min} was -1.5675.

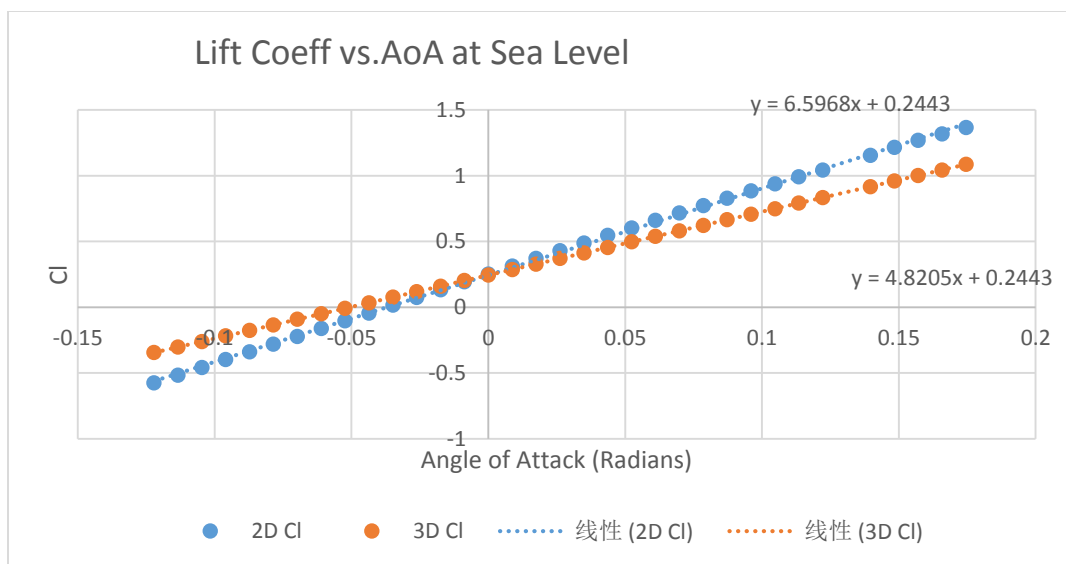


Figure 1: Linear Cl vs. angle of attack at sea level

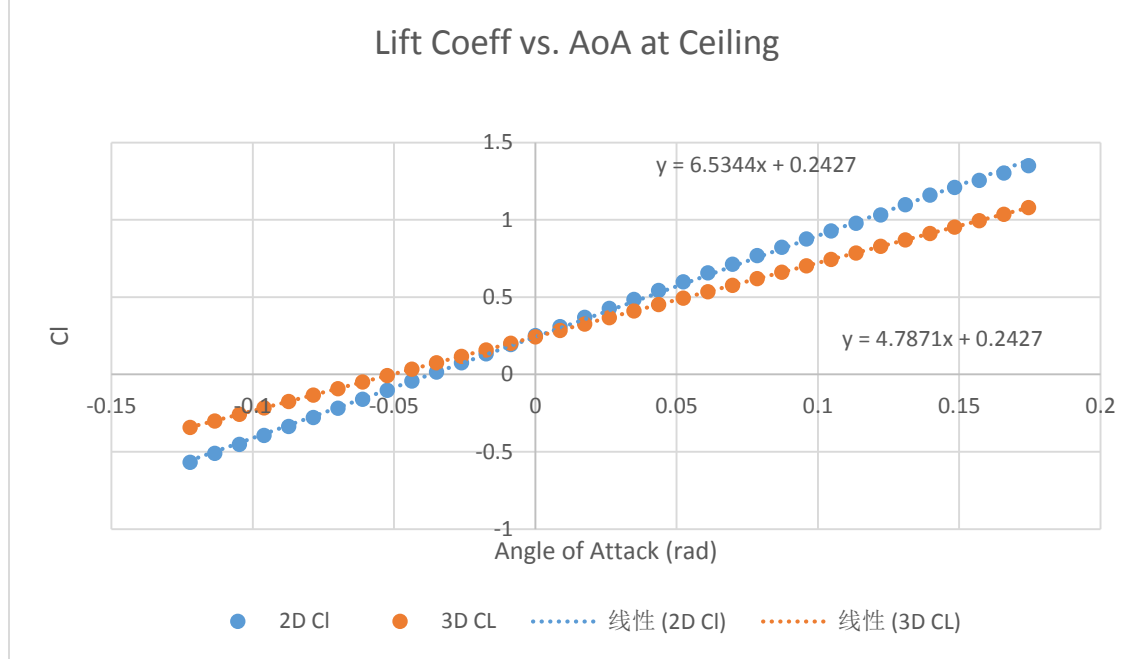


Figure 2: Linear Cl vs. angle of attack at 14600 ft.

The primary 3D corrections used for Figs. (1) and (2) are Eqs. (4) and (5). Eq. (4) uses the two 2D lift curve slope and transforms it using the wing's aspect ratio and Oswald efficiency factor into an estimate for the 3D lift curve slope. Eq. (5) relates the three dimensional and two dimensional lift curve slopes in order to directly convert between 2D and 3D lift coefficient values.

$$C_{L\alpha} = \frac{C_{l\alpha}}{1 + \frac{C_{l\alpha}}{\pi A e}} \quad (4)$$

$$C_L = \frac{C_{L\alpha}}{C_{l\alpha}} C_l \quad (5)$$

where $C_{L\alpha}$ and $C_{l\alpha}$ were representative of the 3D and 2D lift curve slopes, per radian in this case. On the same note, C_L and C_l were the 3D and 2D lift values. The variable A in Eq. (4) denoted the aspect ratio of the wing. Finally, the variable e was the Oswald efficiency factor, which was fixed at 0.79. These correction equations were applied to the Xfoil data using Matlab. The resulting three dimensional lift and drag coefficients are shown in Table 4.

Table 4: Three dimensional lift coefficient data

	Sea Level	14600 ft.
$C_{L,max}$	1.3539	1.3083
$C_{L,min}$	-1.2149	-1.1484
$C_{L,a}$	4.8205/rad	4.7871/rad

These three dimensional lift values were then used to construct the V-n diagrams with which the points of critical loading were identified.

V-n Diagram

The V-n diagram flight envelopes for the aircraft were constructed using the loading requirements given in Table 2 and the lift parameters given in Table 3. These flight envelopes were used to identify critical loading points during flight which were used for load analysis. The loading and lift parameters were used in Eq. (6) and Eq. (7) below to generate the flight envelope curves. Eq. (6) produced the positive stall curve while Eq. (7) produced the negative stall curve. In the figures further below, these stall curves are the lines that begin from the origin and end at PHAA and NHAA respectively. FAR 23 requirements dictate the rest of the envelope.

$$n_{pos} = \frac{0.5\rho C_{L,max}V^2 S}{W} \quad (6)$$

$$n_{neg} = \frac{0.5\rho C_{L,min}V^2 S}{W} \quad (7)$$

Here, $C_{L,max}$ and $C_{L,min}$ again denoted the maximum and minimum three dimensional lift coefficients. Additionally, ρ represented air density, V aircraft velocity, W aircraft weight, and S the wing planform area

of 16.23 m^2 . The density and lift coefficient values differ based on the altitude of the aircraft, and were the same as the values used in the Reynolds number calculations. With these equations, the initial stall curves were plotted.

The critical points identified in FAR 23 requirements allowed for further refinement of the diagrams. These critical points were: the Positive High Angle of Attack point (**PHAA**) where the aircraft first reached the positive maneuvering load factor limit of 4.4 while flying at a $C_{L,max}$ condition, the Positive Low Angle of Attack (**PLAA**) where the aircraft reached dive velocity while maintaining a load factor of 4.4, the Negative High Angle of Attack (**NHAA**) where the aircraft flew at a $C_{L,min}$ condition at the negative load factor limit of -1.76, and the Negative Low Angle of Attack (**NLAA**) where the aircraft reached dive velocity while maintaining the load factor limit of -1. The limiting dive velocity used to define the PLAA and NLAA points can be calculated using Eq. (8). This estimate relates dive velocity directly to cruise velocity for simplicity.

$$V_{Dive} = 1.5V_{Cruise} \quad (8)$$

Additionally, these critical points corresponded to several extreme maneuvers. These include climbing, diving, and pull-out, while banking maneuvers seemed to fall into the standard flight envelope bounded by the critical points. PHAA and NHAA referred to climbing and steady flight while PLAA and NLAA referred to diving and pull-out. Additional explanations for these maneuvers were discussed in Appendix F. The flight envelopes at both sea level and the service ceiling are shown below.

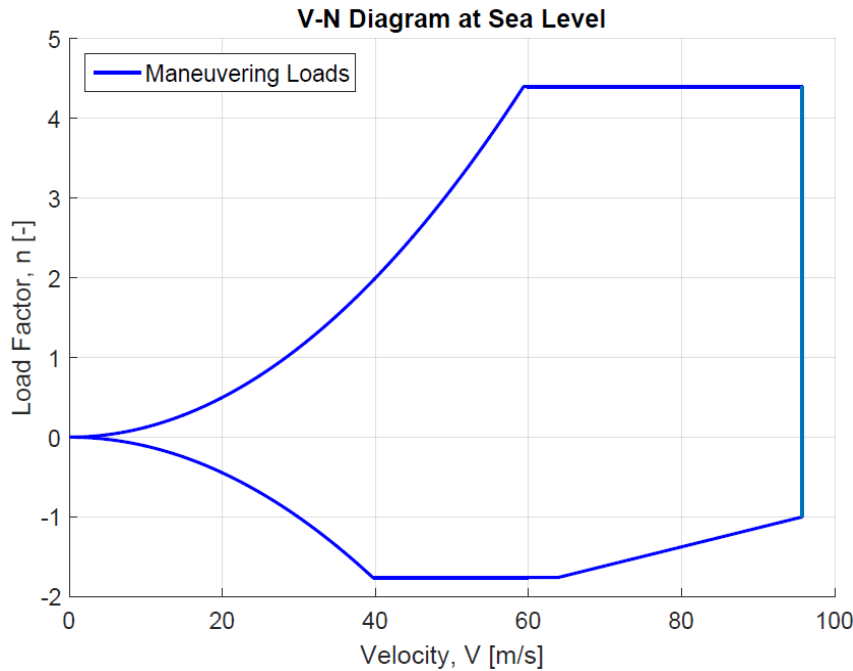


Figure 3: Flight envelope at sea level without gust loads

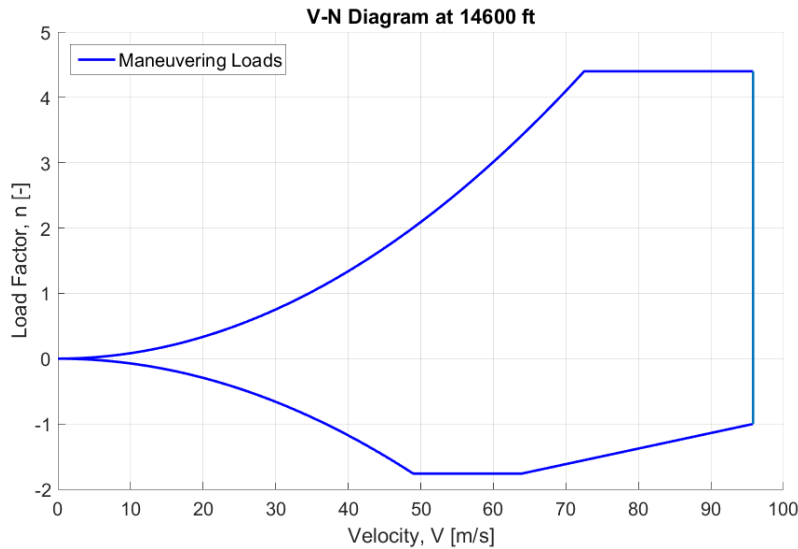


Figure 4: Flight envelope at 14600 ft. altitude without gust loads

Since air properties differed greatly between sea level and ceiling conditions, the loading conditions were also expected to be drastically different. This behavior was most notable between the stall curve slopes in Fig. (3) and Fig. (4). The reduced atmospheric density at the service ceiling greatly reduced the

slope of the stall curve calculated from Eq. (6) and Eq. (7), resulting in the relatively high velocity NHAA point found in Fig. (4) compared to Fig. (3).

Normal maneuvers are not the only source of loading for aircraft. Unpredictable inputs such as wind gusts can cause instantaneous loads that exceed the load factors from normal maneuvers. Thus, these additional gust loads were taken into account as well. These gust loads were estimated using Eq. (9) below. This relation estimates the maximum load factor a wind gust can cause at a given velocity, like cruise or dive.

$$n = \frac{K_g C_{L\alpha} U_e V}{498(\frac{W}{S})} \quad (9)$$

where K_g and factor μ are defined as

$$K_g = \frac{0.88\mu}{5.3 + \mu} \quad (10)$$

$$\mu = \frac{2(\frac{W}{S})}{\rho C \alpha g} \quad (11)$$

In Eq. (9) The $C_{L\alpha}$ term denoted the three dimensional lift curve slope of the wings in radians⁻¹, the variable V denoted the velocity in knots at either cruise or dive, U_e was the gust velocity in ft/s, and (W/S) described the ratio of the aircraft weight and its wing surface area in lb/ft². The gust velocities used in U_e correspond to both cruise and dive, and are 50 ft/s and 25 ft/s respectively from FAR 23 requirements.

For the factor μ defined in Eq. (11), C was the chord length in ft, ρ was the density of air at current flying conditions in slugs/ft², the α term denoted the current angle of attack of the plane, (W/S) once again described the ratio of the aircraft weight and its wing surface area in lb/ft², and g was the gravitational constant of 32.174 ft/s². The rest of the variables used in these equations are given in the aircraft parameters from the beginning of the report.

The positive gust load envelope was plotted by inputting cruise and velocity conditions into Eqs. (10) and (11). Lines connecting the cruise, dive, and origin points were then drawn to form the final shape of the gust envelope. Furthermore, since vertical gusts were assumed to be symmetric, this positive

envelope could be reflected about the $n = 1$ axis to produce the estimated negative gust envelope. These gust load components were plotted with the original maneuvering envelopes to develop total flight envelopes for both sea level and service ceiling flying conditions. These diagrams are Fig. (5) and Fig. (6).

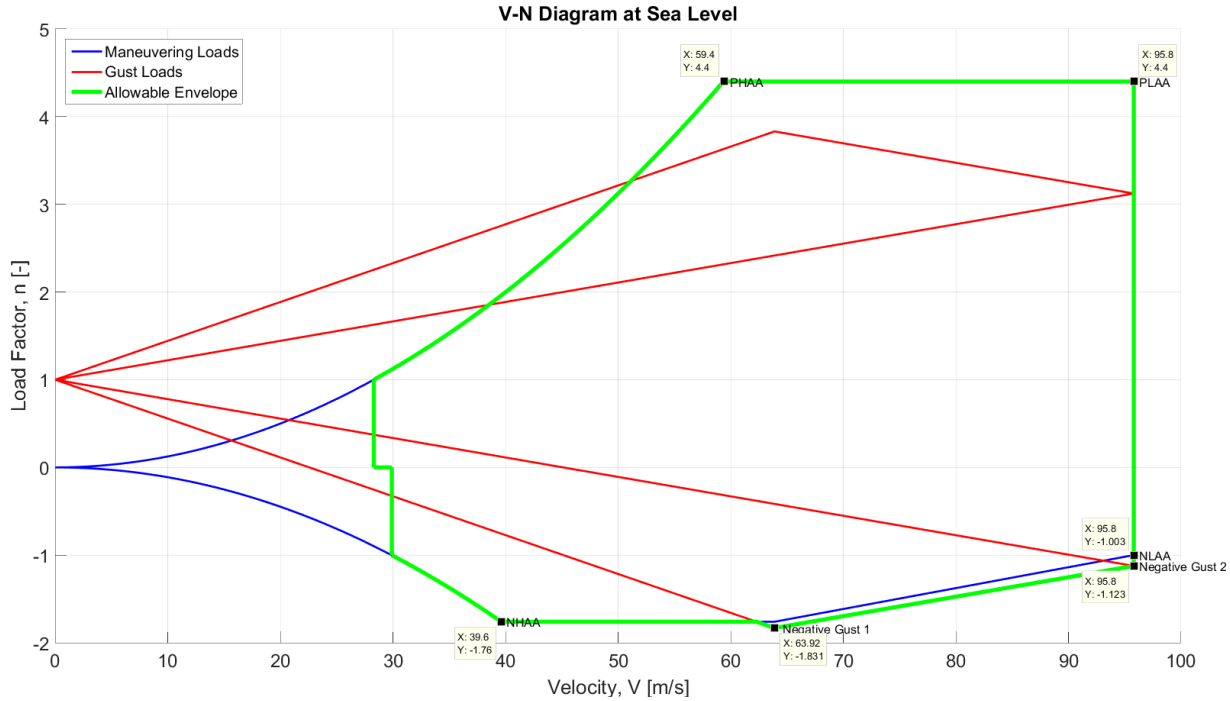


Figure 5: V-n Diagram at Sea Level

The sea level V-n diagram in Fig. (5) depicts a negligible positive gust load that remains within the standard flight envelope. Thus, at sea level the positive gust load was ignored. The negative gust slightly exceeds the negative flight envelope. In this case, the negative gust points had to be considered. The values of all critical points as determined in Fig. (5) are listed in Table 5.

Table 5: Velocity and Load Factor values at Critical Design Points at Sea Level.

	PHAA	PLAA	NHAA	NLAA	Negative Gust 1	Negative Gust 2
V (m/s)	59.4	95.8	39.6	95.8	63.9	95.8
n	4.4	4.4	-1.76	-1	-1.831	-1.123

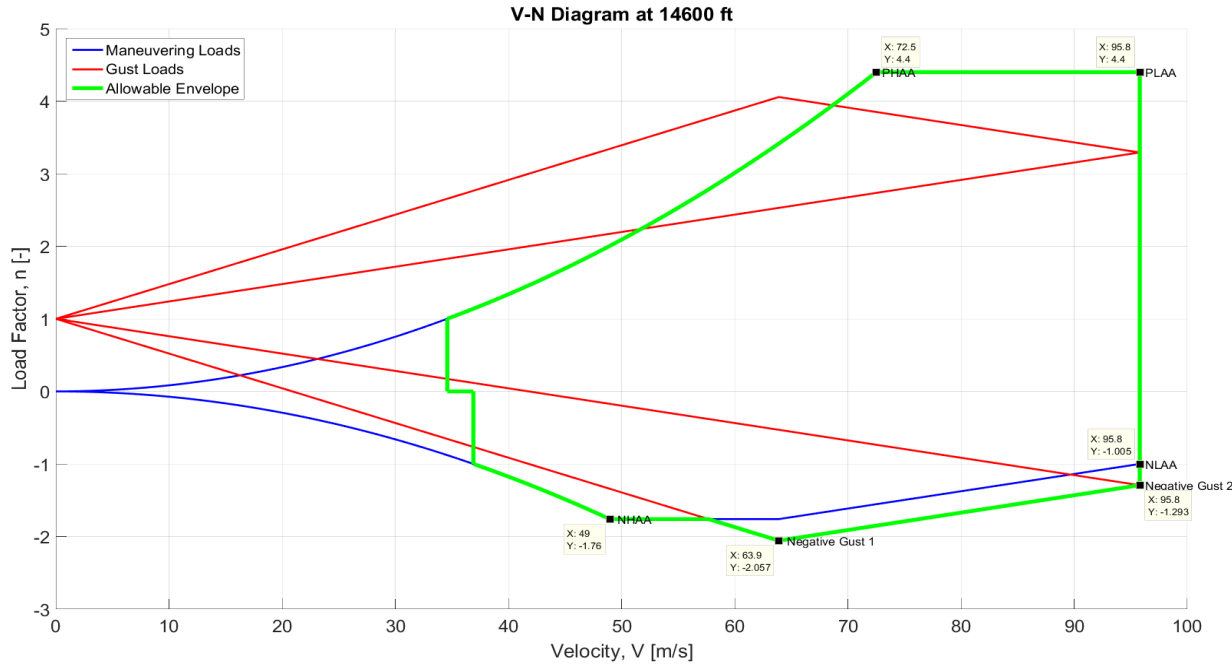


Figure 6: V-n Diagram at 14600 ft.

The V-n diagram for the aircraft service ceiling of 14600 ft. plotted in Fig. (6) also followed a similar pattern.

Here, the maximum positive gust point exceeded the gust envelope, but only before the PHAA point. This gust loading would cause stall behavior, invalidating the additional lift loads from flight at that level. Therefore, the positive gust loading in this case were also ignored. The velocity and load factor conditions at all applicable critical points are listed in Table 6.

Table 6: Velocity and Load Factor values at Critical Design Points at 14600 ft.

	PHAA	PLAA	NHAA	NLAA	Negative Gust 1	Negative Gust 2
V (m/s)	72.5	95.8	49.1	95.8	63.9	95.8
n	4.4	4.4	-1.76	-1	-2.057	-1.293

The critical point loading data above was then directly used to determine the forces acting on the wings of the Cessna 177 aircraft for later failure analysis.

Load Determination

The force loads of the aforementioned critical points were calculated through several simple relations. These loads were then transformed into distributions, which were further refined into stresses along various points of the wing. It was these stresses that were then used in various failure analyses.

First, the total lift and drag forces on the wing could be determined through a combination of data taken from the V-n diagram and basic relations for lift and drag. One relation, Eq. (12), defined the load factor as a ratio of lift and weight forces. Eqs. (12) and (13) were the standard equations that related lift and drag forces to their non-dimensional coefficients.

$$n = \frac{L}{W} \quad (12)$$

$$L = 0.5\rho S^2 C_L \quad (13)$$

$$D = 0.5\rho S^2 (C_{D0} + \frac{C_L^2}{\pi A e}) \quad (14)$$

Here, L was the 3D lift force in Newtons, D was the 3D drag force in Newtons, W was the weight of the aircraft, n was the nondimensional load factor, ρ represented the atmospheric density, S was the wing planform area, C_L was the 3D lift coefficient of the wing, C_{D0} was the drag coefficient at zero lift, V was the velocity of the aircraft and e was the Oswald efficiency factor of the wing. These values were all given previously in the report.

Since the load factor n was one of the variables plotted against in the flight envelope, it was easily determined for any flight condition. Furthermore, since the weight of the aircraft was also assumed to be known, the total aircraft lift could be calculated using Eq. (12) for each critical point. This lift force was then

used in Eq. (13) to find the three dimensional lift coefficient at the given critical points. The lift coefficient was then input into Eq. (14) to determine the total drag force of the aircraft at the various critical points. The C_{D0} drag at zero lift term was estimated directly from Xfoil data as the two dimensional drag at zero lift to simplify the process. The distributions of the lift and drag forces along the wing were also derived for use in shear force and moment calculations.

Load Distribution: finding $l(z)$ and $d(z)$ functions

First, the drag distributions along the wing for each critical point were approximated as a simple rectangular distribution. Additional drag from wing tip vortices were accounted for in each case by increasing the drag by 10% for the final 20% of span on the wing tips. The resulting drag distribution equations for this configuration are:

$$d(z) = \frac{D}{b} \quad \text{for } -0.4b \leq z \leq 0.4b \quad (15a)$$

$$d(z) = 1.1 \frac{D}{b} \quad \text{for } z > 0.4b \text{ or } z < -0.4b \quad (15b)$$

Here, D and b were representative of the total drag force and total wing span respectively. The $d(z)$ term indicated the drag force distribution per unit length, or the drag load distribution along the wings.

The lift distribution model on the wings was slightly more complex. Here, the results of a rectangular lift distribution were averaged with that of an elliptical lift distribution to generate the final model used in load calculations. This assumption was made to make the lift profile more realistic. The relations for doing are shown below:

$$l(z) = \frac{L}{b} \quad (16a)$$

$$l(z) = \frac{4L}{\pi b} \sqrt{1 - (\frac{2z}{b})^2} \quad (16b)$$

Eq. (16a) denoted the rectangular lift distribution (in N/m) in the same fashion as the rectangular drag distribution. Here, the load distribution $l(z)$ represented the lift force per unit length in both Eq. (16a) and Eq. (16b). L and b represented total lift force and the total wing span once again, while the z term in Eq. (16b) denoted the location along the wing span at which we wish to define the $l(z)$ term. The results from these two models were averaged together to generate the final lift distribution about the aircraft wings. Fig. (7) and Fig. (8) show the lift and drag distributions for the PHAA critical point.

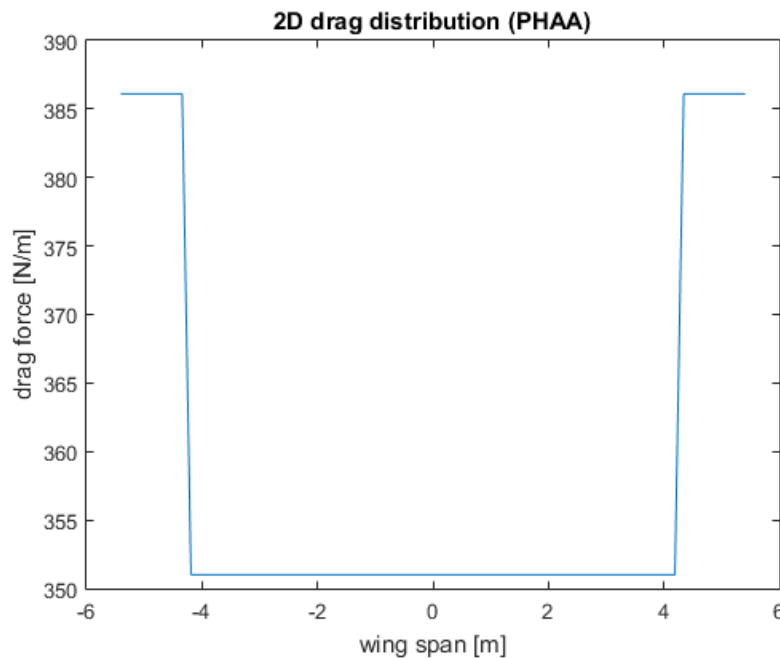


Figure 7: Drag distribution at PHAA at service ceiling

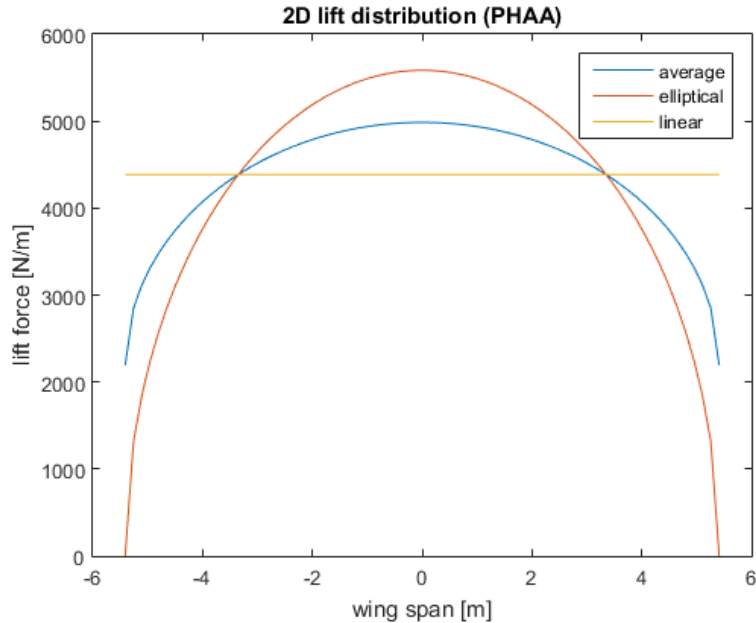


Figure 8: Lift distribution at PHAA at service ceiling

The lift and drag distributions plotted above showed the total aerodynamic forces acting on the wings. However, as the wings are tilted at varying angles of attack for each critical condition, additional corrections needed to be made to convert the loads into forms fitting the frame of reference of the wing.

Load Distribution: finding W_x and W_y load intensity functions

The lift and drag distributions needed to be transformed to the wing reference frame due to the nature of the relations since the failure relations used this frame. The coordinate frame used to define the system is shown in Fig. (9).

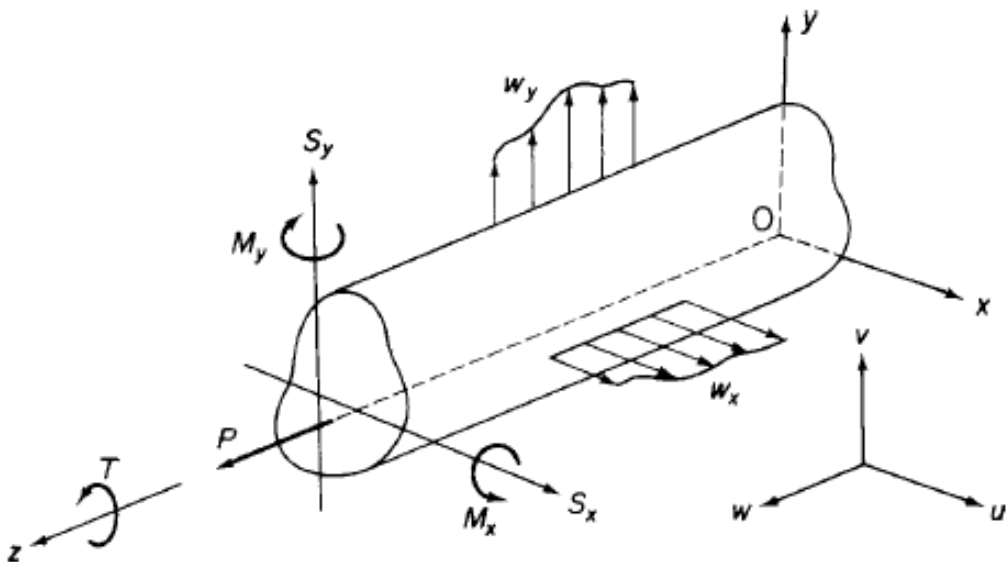


Figure 9: Sign convention and frame of reference as shown in [4]

In the above convention, the semi-span of the wing is represented by the beam above. The x-y plane corresponds to the airfoil cross-section of the wing, while the z axis runs along the span of the wing. Here, the x axis runs positively from the leading edge to the trailing edge of the airfoil. Also, the positive x and y shear forces are defined in the positive x and y directions. Additionally, the x and z moments are defined as positive in the standard right hand direction. However, the positive y moment is defined by [4] as being in the negative right hand direction. This convention was used in all the relations used in this report.

The rationale behind this was as follows. It was first assumed that the lift and drag forces would always act upward against gravity and against the direction of motion respectively. However, changing angles of attack for the aircraft also changed the relative directions of the lift and drag forces to the body frame of the aircraft. This body frame was used to define many of the equations used for shear flow, buckling, failure, and so on. Eq.(17a) and (17b) convert both the lift and the drag distributions in x and y load components in the wing frame.

$$w_x = l(z) \cos(\alpha) + d(z) \sin(\alpha) \quad (17a)$$

$$w_y = d(z) \cos(\alpha) - l(z) \sin(\alpha) \quad (17b)$$

The variables $l(z)$ and $d(z)$ used here were the lift and drag distributions discussed in the previous section.

Here, w_x and w_y are the transformed load distributions in the x and y directions of the aircraft frame. The figures below graphed the x and y load intensities against the total span of the wing.

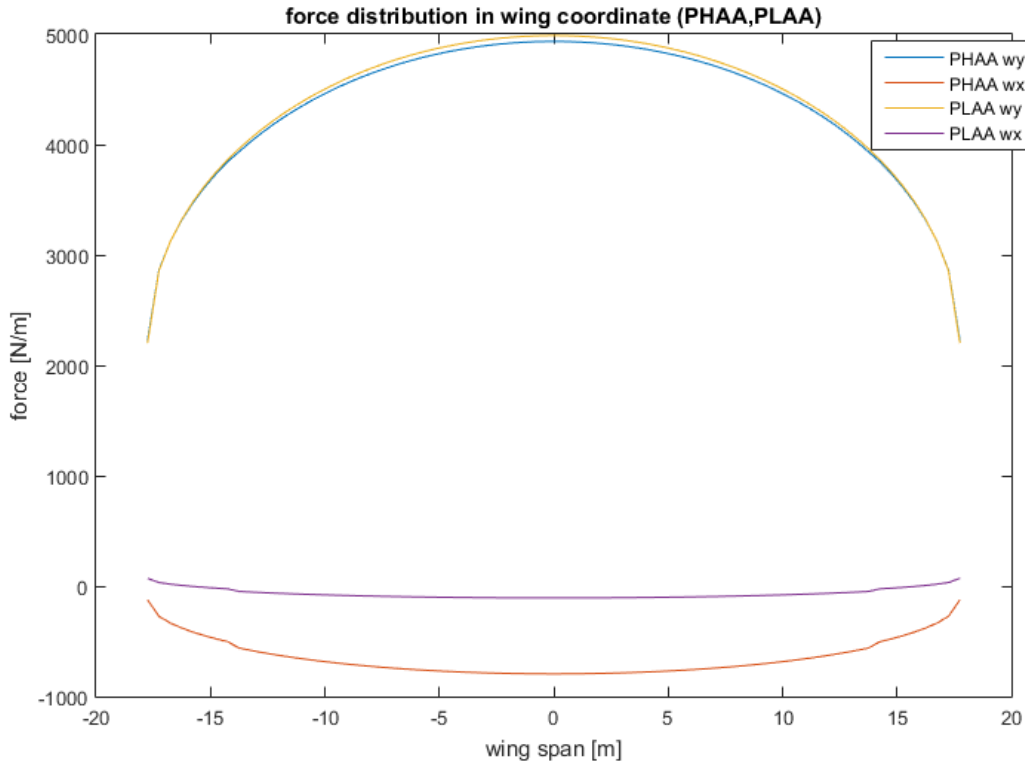


Figure 10: Load intensity at PHAA and PLAA at sea level

At PHAA w_x remained negative due to the orientation of the lift vector. Because of the high angle of attack, the lift vector contributed significantly to the negative x direction forces. This overcame the drag contribution, which resulted in a negative x load intensity. This indicated that the wing would bend forward at PHAA operating conditions. Additionally, the angles of attack at PHAA and PLAA were found to be approximately 16 degrees and 6 degrees respectively.

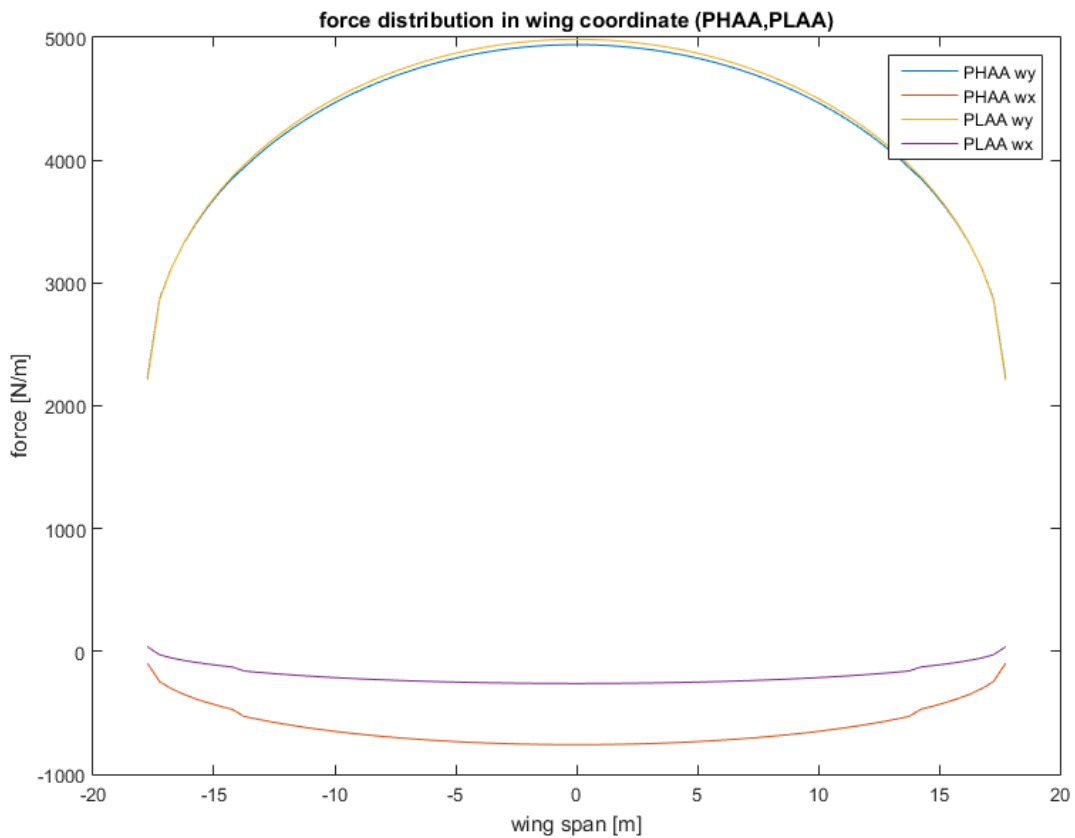


Figure 11: Load intensity at PHAA and PLAA at service ceiling

The service ceiling PHAA/PLAA plot in Fig. (11) followed the same pattern. In this case, the angle of attack at PHAA and PLAA were approximately 17 degrees and 9.7 degrees.

The NHAA/NLAA graphs from Figs. (12) and (13) also showed similar patterns. However, since lift was assumed to be negative at these maneuvering points y load intensity curves became negative. At sea

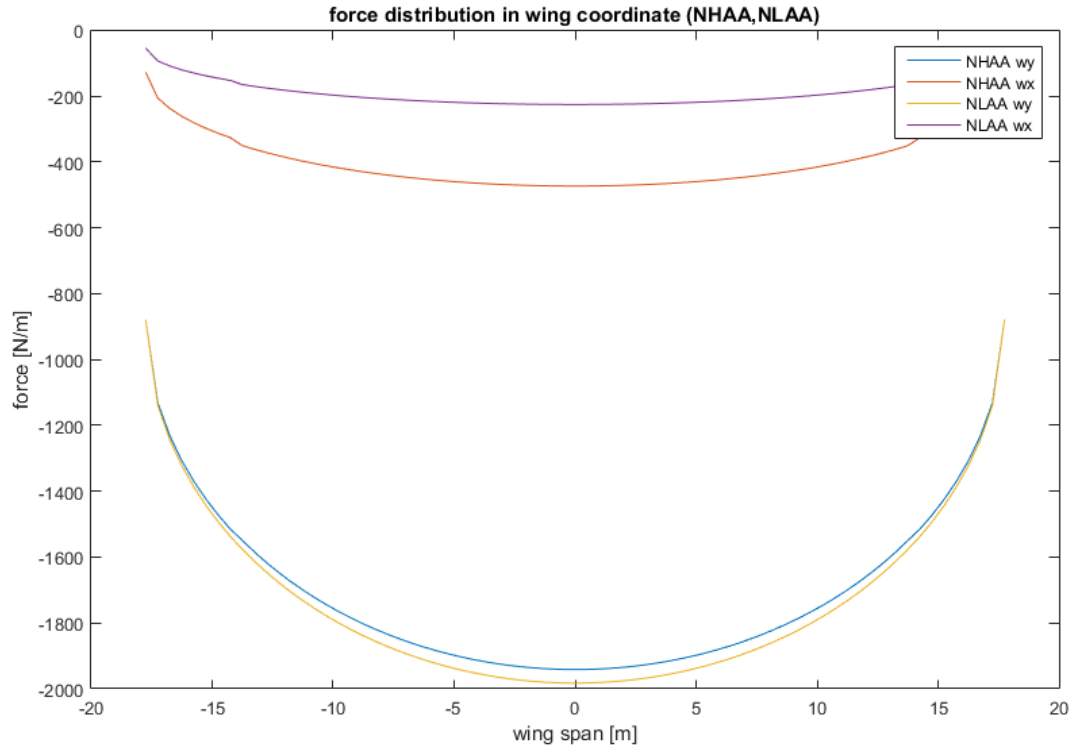


Figure 12: Load intensity at NHAA and NLAA at sea level

level, the NHAA angle of attack was -14 degrees while the NLAA angle of attack was -1.4 degrees.

Again, the service ceiling NHAA and NLAA load intensities were more or less be equal to those at sea level. The angles of attack in this case were found to be -14.9 degrees for NHAA and -2.2 degrees for NLAA. Intensity graphs were also created for the negative gust points.

The sea level gust loads were plotted in Fig. (13). Since only negative gust loads were shown to have exceeded the maneuver envelope in the V-n diagram, they were the only gust loads that were analyzed. For the sea level conditions shown in Fig. (13) the gust angles of attack were found to be approximately -4.1 degrees at the cruise gust point and approximately -1.6 degrees at the dive gust point.

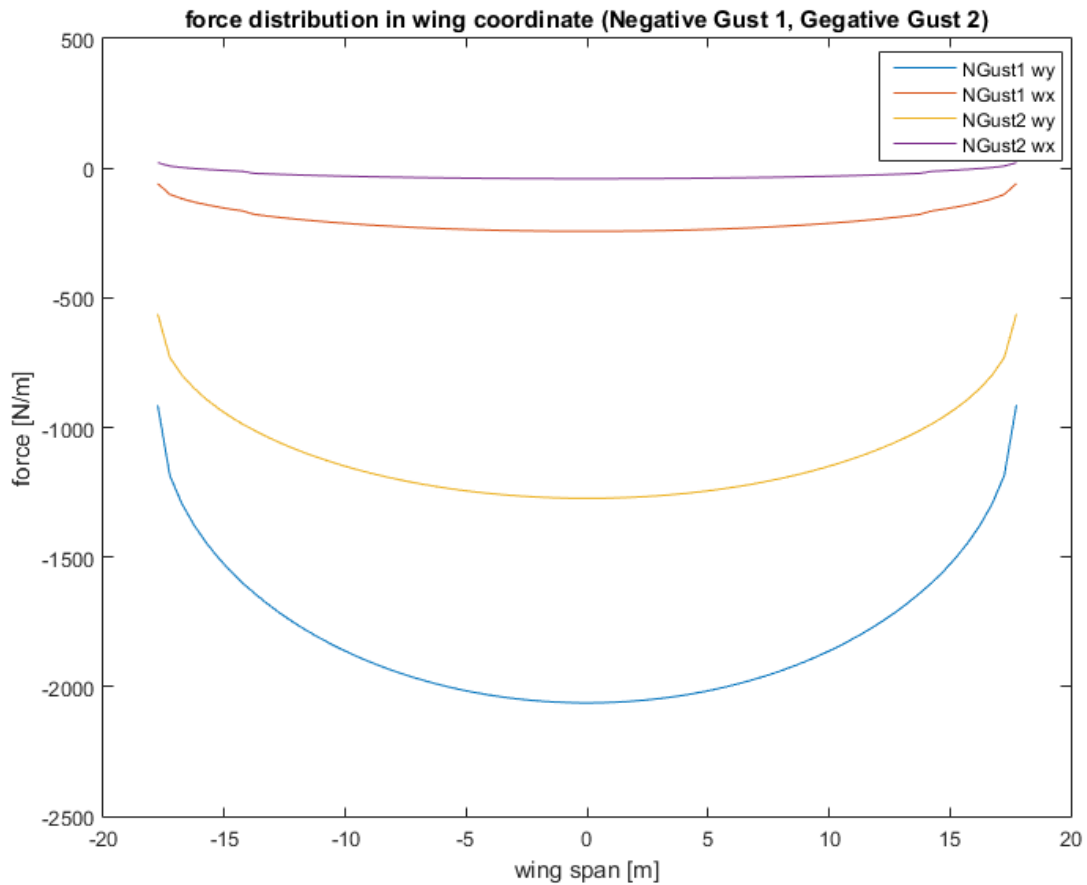


Figure 13: Negative Gust Loads at sea level

Presented in Fig. (14) were the gust load intensities for flight at the service ceiling of the aircraft. The resulting curves were very similar to those of the sea level graph except that the magnitudes of the x load intensities are somewhat higher. This can be explained in part by the fact that higher altitudes require higher angles of attack to generate the same amount of lift. This higher angle of attack directly affects the rotation of force distributions in load intensity calculations. Additionally, the load factors between the gust points at the two altitudes also differed from each other. This would also contribute to any differences found in Fig. (13) and Fig. (14). In this service ceiling case, the angles of attack for the cruise and dive gust points were found to be -7.2 degrees and -2 degrees respectively.

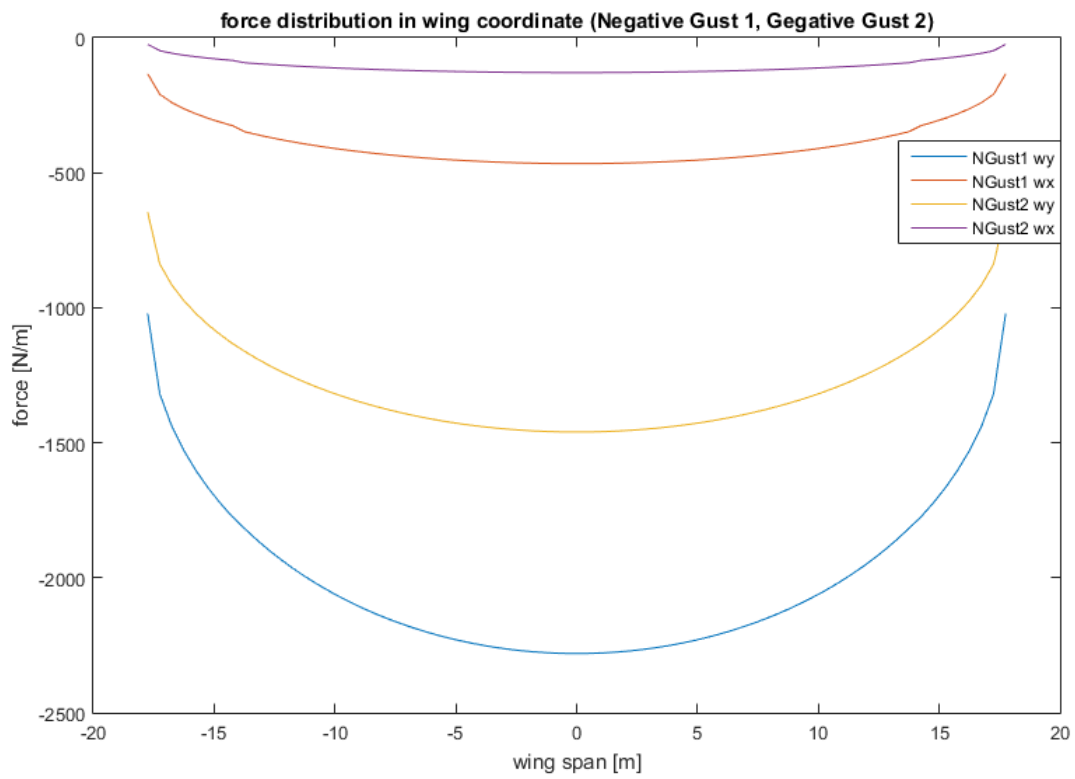


Figure 14: Negative Gust Loads at service ceiling

Centroid and Moments of Inertia

The centroid and moments of inertia of any particular shape are perhaps the most important parameters in the calculation of distributed forces on a line, area or volume. Centroid is only dependant on the shape of a given line, area or volume. If the given object is uniform in density, the centroid is at the same location as the center of gravity, where the resultant forces of gravity acts on. In this section, only two dimensional centroid and moments of inertia are considered.

Centroid is defined as the arithmetic mean position of all points in the body and can be calculated by evaluating the following equations

$$C_x = \frac{\sum_i A_i \bar{x}}{\sum_i A_i} \quad (18a)$$

$$C_y = \frac{\sum_i A_i \bar{y}}{\sum_i A_i} \quad (18b)$$

For complex structures, like a box beam that approximates a wing, the overall centroid calculation can be broken down into calculation of centroids of smaller components and finding the centroid of the overall structure using the Eq. (18a) and Eq. (18b).

Moments of inertia are important because they are needed in solving mechanics problems such as beam bending and torsions. The moment of inertia, or the second moment of area, is defined as

$$I_{xx} = \int y^2 dA \quad (19a)$$

$$I_{yy} = \int x^2 dA \quad (19b)$$

$$I_{xy} = \int xy^2 dA \quad (19c)$$

In addition, the Parallel Axis Theorem is often used to compute the moment of inertia about any arbitrary axis when one knows the moment of inertia about the centroid. This allows for the computation of moments of inertia of multi-component structures. The Parallel Axis Theorem states that

$$I = I_{cm} + Ad^2 \quad (20)$$

where A is the area and d is the distance between the axis of interest and the axis where the moment of inertia about the centroid is located. Combining Eq. (19) and Eq. (20), the moment of inertia about the centroid can be obtained. These general equations were applied to the cross-section of a NACA 2415 airfoil for later use in this project.

The Airfoil Section

Since the geometry of a cross-section directly affects the stresses it bears, it was necessary to find the geometric properties of the given NACA 2415 profile. First, the total dimensions of the cross-section were defined. The airfoil section was set with a chord length of 1.5 meters. Additionally, it was assumed that the last 20% of the airfoil section was to be cut off for control surfaces. This occurred at a chord position of 1.2 meters. The ailerons were also assumed to have no effect on the load analysis, for simplicity. A back spar was then placed at this aileron/wing intersection to provide structural support. Furthermore, an additional spar was placed at the quarter chord to provide further structural support. These spars were secured to the rest of the wing using L brackets, with cross-sectional areas of 40 mm^2 . Initial skin and spar thicknesses were set as 2 mm and 5 mm respectively. Finally, 5 mm^2 z-stringers were also dispersed evenly across the cross-section to also support loads.

In order to perform bending and shear analyses, the centroid and moments of inertia of the airfoil cross-section had to be computed using the principles discussed in the previous section. A linear panel approximation was made to simplify these calculations for the skin in the cross-section. This approximation allowed the wing skin to be modelled as a series of straight connected panels of finite thickness. In addition to this, the spars, spar caps, and stringers were treated as point loads to further

simplify calculations. The spar caps were assumed to have the same coordinates as the ends of the spars. On the same note, the stringers were idealized as being directly on the skin. This idealization is shown in Fig. (15).

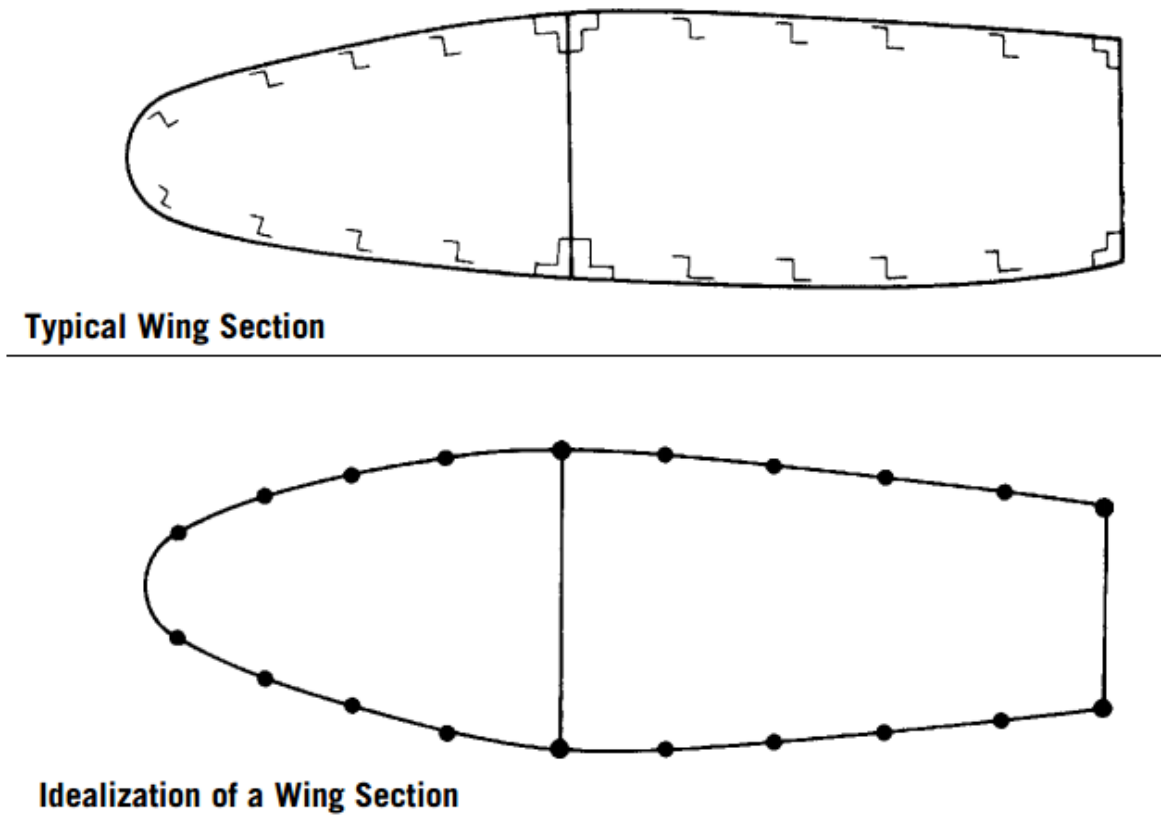


Figure 15: Stringer and spar cap idealization

This assumption allowed for the re-use of Eqs. (18a) and (18b) calculate the location of the cross-sectional centroid. The origin of the x-y coordinate system was then shifted to the centroid of the airfoil to simplify future calculations.

The skin panel approximations were the most critical portion of this calculation. The points defining the surface of the airfoil were taken from a standard NACA plotter. Evenly distributed points were then chosen along the surface of this airfoil to separate the skin into the linear panels necessary for the

approximations. These points all corresponded with spar locations defined in the code. These demarcation points along the skin were labeled as “nodes.” The spar ends were assumed to be nodes as well to further simplify the logic. Additional nodes were manually placed at the nose of the airfoil, and at the center points between the spar nodes. This would create a finer linear approximation which increased the accuracy of the calculations. Additional simplifying assumptions were made for the geometries of the stringers and the spar caps. While it was determined that z-stringers and L brackets would be used in the actual wing, calculating the exact moments of inertia and centroids for these geometries was too complex. Several approximations, which were discussed earlier, were made instead. Since the initial cross-sectional areas of the stringers were extremely small in comparison to the total cross-section, it was determined that the stringers could be assumed to be directly on the skin. A similar simplification was also made for the spar caps, which were placed exactly at the spar end nodes for calculation purposes. In this case, the spar caps were assumed to be centered on the end points of the spars themselves. The results of these simplifications was a centroid location of (0.5876,0.0228) meters from the leading edge.

For the moments of inertia, a simple parallel axis theorem assumption was applied. Since the skin panels were assumed to be small and thin, and the spar caps and stringers were assumed to be point loads, the formulas for the moments of inertia could also be simplified immensely. As the thickness and length dimensions for the skins, spar caps, and stringers were extremely small, the $1/12 bh^3$ terms in the moments of inertia were disregarded. The only remaining contributions for these moments of inertia were from the parallel axis Ad^2 terms. The final equations used to estimate the moments of inertia were:

$$I_{xx} = \sum_{i=1}^n A_i(y_i - C_y)^2 \quad (21)$$

$$I_{yy} = \sum_{i=1}^n A_i(x_i - C_x)^2 \quad (22)$$

$$I_{xy} = \sum_{i=1}^n A_i(x_i - C_x)(y_i - C_y) \quad (23)$$

In Eqs. (21) through (23) above, I_{xx} , I_{yy} , and I_{xy} represent the x, y, and xy moments of inertia of the total cross section. The A_i terms are the individual areas of the components of the cross section. This consists of the skin panels, spars, spar caps, and stringers. The x_i and y_i terms used above are the local centroid coordinates of these components, and the C_x and C_y terms are the x and y coordinates of the entire cross-section's centroid. Eqs. (21) through (23) simply sum up the parallel axis contributions of each of the smaller component parts to generate an estimate for the entire airfoil geometry. The moments of inertia for the initial configuration are in Table 7.

Table 7: Area Moments of Inertia of the wing

I_{xx} (m^4)	5.5602e-05
I_{yy} (m^4)	9.4691e-04
I_{xy} (m^4)	6.5257e-06

Shear, Moment, and Deflections

The moments of inertia and load intensities found previously were then used in conjunction with several equations listed below. These equations were used to determine shear loads, moment loads, and deflections of the box beam example. Since integrations were necessary, simple numerical methods were used for the calculations.

Eqs. (24) and (25) below were used to process the load data.

$$S_y = - \int w_y dz \quad (24a)$$

$$S_x = - \int w_x dz \quad (24b)$$

$$M_x = \int S_x dz \quad (25a)$$

$$M_y = \int S_y dz \quad (25b)$$

In these equations, the w_x and w_y variables represented the load intensities in the x and y directions of the wing frame. Eq. (24a) and Eq. (24b) related the x and y shear forces S_x and S_y to these through integration. Finally, Eq. (25a) and Eq. (25b) showed that the x and y moments M_x and M_y could also be calculated through direct integration of the shear force.

The moments and shears from Eq. (24) and Eq. (25) were then used to calculate other loading parameters. The M_x and M_y moments, for instance, were used to calculate both bending stresses along the wing cross section (Eq. (26)) and wing deflections (Eqs. (27) and (28)). The equations used to calculate these values were:

$$\sigma_z = \frac{M_x(I_{xx}y - I_{xy}x)}{I_{xx}I_{yy} - I_{xy}^2} + \frac{M_y(I_{xx}x - I_{xy}y)}{I_{xx}I_{yy} - I_{xy}^2} \quad (26)$$

$$\frac{d^2u}{dz^2} = -K(-M_xI_{xy} + M_yI_{xx}) \quad (27)$$

$$\frac{d^2v}{dz^2} = -K(-M_xI_{xy} + M_yI_{yy}) \quad (28)$$

$$K = \frac{1}{E(I_{xx}I_{yy} - I_{xy}^2)} \quad (29)$$

where E is the Young's modulus, M is the applied moment, I is the moment of inertia, and σ_z is the bending stress. Eq. (26) allowed for the calculation of the bending stress σ_z at different points in the wing cross section by inputting different x and y coordinates. It also required substituting in the previously discussed moments and area moments of inertia for the cross section. On the same note, Eq. (27), Eq. (28), and Eq. (29) define the displacements experienced by the wing due to loading. Once again u and v, or the x and y displacement terms, depend only on the resulting moment loads and cross section area moments of inertia.

In order to find deflection in the x and y direction, that is u and v , Eq. (27) and Eq. (28) were integrated using the Trapezoidal rule:

$$\int_a^b f(x)dx \approx (b - a)\left(\frac{f(a)+f(b)}{2}\right) \quad (30)$$

which states that area between $f(a)$ and $f(b)$ can be approximated by a trapezoid. For the purpose of the initial calculations, 50 points along the positive z-axis of the wing are used to carry out the numerical integration. The summation of these integration yields the distribution of wing deflection along the positive z direction of the wing.

Using the aforementioned equations, the shear forces, moment distributions, and wing deflection for PHAA at sea level was calculated. Because of a positive w_y distribution and a negative w_x distribution, as shown in Fig. (9), the shear forces and moments in the y direction are expected to start from the positive and decrease to zero as one goes from root to the tip of the wing. Likewise, shear forces and moments in the x direction start from a negative value and gradually increase across the wing from root to tip. These trends are shown in Fig. (16) and Fig. (17). For the airfoil section of interest at PHAA and sea level, M_y starts from a value of 9675.7N and decreases to 0 towards the tip while M_x begins at -5880.9N and increases to 0 towards the tip of the wing. S_y at the root of the wing is about 2306.7N and decreases to 0 towards the tip while S_x begins at about -418.8N and increases to 0 towards the tip.

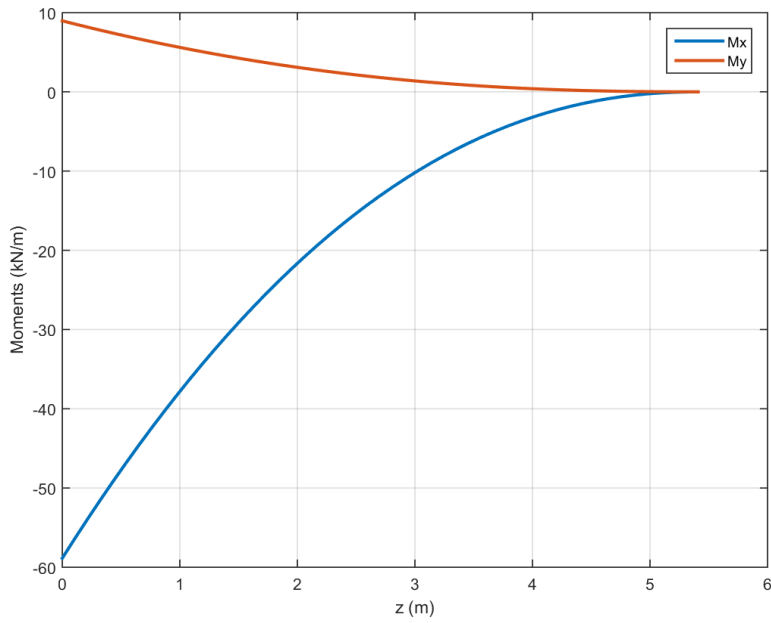


Figure 16: Moment distribution of the wing at sea level (PHAA)

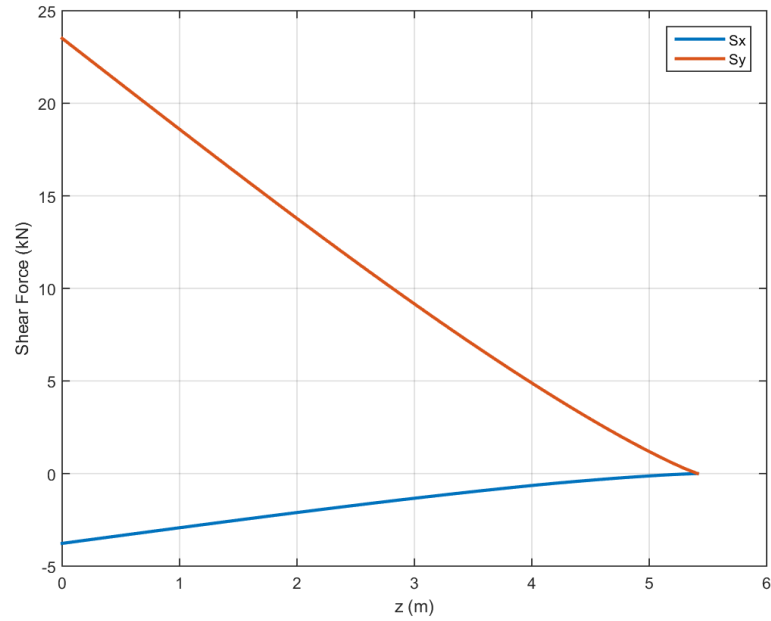


Figure 17: Shear distribution of the wing at sea level (PHAA)

From the moment distribution, deflection of the wing can be calculated through the use of Eq. (27) through Eq. (29). Given the moments of inertia of the wing approximation of Table 7, the wingtip deflects

by 0.11 m in the y direction and -0.0010 m in the x direction at the PHAA of sea level flight, as illustrated in Fig. (18). Structural deflection becomes increasing small towards the root of the wing and reaches zero at the root. The moment distribution, shear distribution, and wing deflection of other critical points can be found in Appendix B.

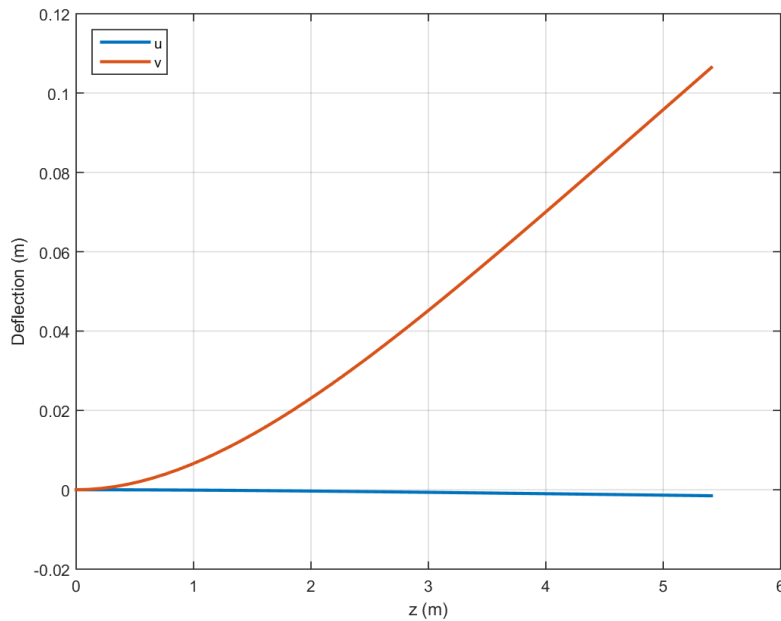


Figure 18: Wing deflection from root to tip (sea level, PHAA)

Failure Analysis

After the loads along the wing and the cross-sectional properties of the wing were determined, failure analyses could be done. These failure analyses predict the behavior of the wing structures during operation. Specifically, the points of critical loading identified previously are points of interest. The failure criteria that were analyzed here were, column buckling, plate buckling, yield, and fatigue. Each of these failure phenomena depend largely on the stresses being experienced at varying points along the wing. In the case of direct stresses, these were calculated from the load data and Eq. (26). However, determining the shear stress along a cross-section provided additional difficulty. The shear flow method was used to estimate the shear stresses in the cross-section.

Shear Flow

Shear flows are simple representations of shear stress distributions along a cross-section. These representations are useful for determining the local loading caused by shear forces. By utilizing the centroid, moments of inertia, and wing loading determined previously for the NACA 2415 wing geometry, shear flows and stresses in the airfoil cross-section were also calculated.

Complex shapes like the NACA 2415 airfoil require several structural idealizations to simplify the shear flow calculations. These idealizations stated that skin only carried shear stresses, and that the stringers only carried direct stresses (ie. σ_{zz}). To facilitate this, the skin, stringers, and spar caps were consolidated into a series of boom areas containing the total area of the cross-section. The booms would carry the direct loads like the stringers, while the infinitely thin skin panels between booms would carry only constant shear stresses. Approximately 200 booms were generated for the cross-section during this phase of analysis. This number was chosen to provide better accuracy at a reasonable computational cost. Finally, with these boom locations known, the direct stress values at each boom location could be

calculated and used for additional failure analysis. Using Eq. (26), the total distribution of these direct stresses at the wing root were plotted in Fig. (19).

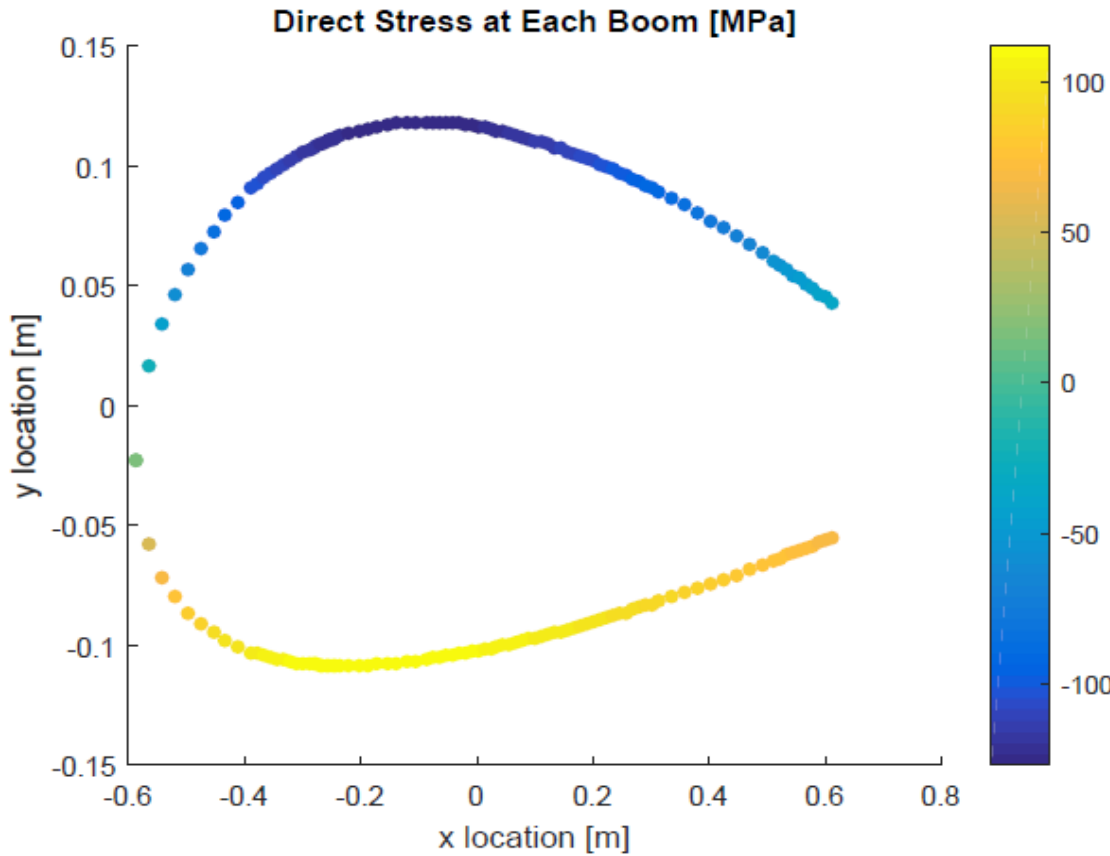


Figure 19: Direct stresses at root of wing, PHAA conditions with original dimensions

Fig. (19) shows that the maximum compressive stress was located near the top and frontal sections of the wing. This coincided with expectations from load behavior. Additionally, at the PHAA conditions shown above, the maximum compressive direct stress value was -127.15 MPa at the root. The maximum direct stress at root and center-wing critical points are shown in Table 8. Similar plots for other critical points can be found in Appendix C.

Table 8: Maximum Direct Stresses on Wing

Condition	Max Compressive Root Direct Stress (MPa)	Max Compressive Mid-Wing Direct Stress (MPa)
PHAA	127.1	28.2
PLAA	126.9	28.1
NHAA	49.2	10.9
NLAA	28.9	6.4
Gust Point 1	52.3	11.6
Gust Point 2	32.4	7.2

Table 8 shows that maximum direct stresses occur at PHAA and PLAA conditions. Additionally, the highest stresses also occur at the root of the. Thus, the failure analysis discussed later will focus on PHAA loading at the wing root.

The booms were generated using ratios of skin areas combined with local spar cap and stringer areas. By using a simple moment balance about these idealized booms, the relation detailing this combination was derived. This boom area equation depended on both direct stresses applied near the boom location, and the structural dimensions about the boom itself. Eq. (31) defined this relation as seen in the code.

$$B_i = \sum \frac{t_{Di} b_i}{6} \left(2 + \frac{\sigma_{i+1}}{\sigma_i} \right) + A_i \quad (31)$$

In Eq. (31), B_i represents the idealized boom area. Additionally, t_{Di} represents the thickness of the skin section connected to the boom location while b_i represents the length of the skin section. The σ_{i+1} and σ_i terms are the direct stresses being experienced at the location of the neighboring boom and the

current boom respectively. The A_i term represents any additional local areas, such as spar caps, which need to be included in the boom area as well. The summation indicates that the boom area at a single point is dependent on the contributions of neighboring boom points. Specifically, on the direct stresses acting at these neighboring boom locations. This couples the load bearing capabilities of the cross-section, and allows for the simplified calculation of shear flow. The boom idealization was based on the cross-section shown in Fig. (20).

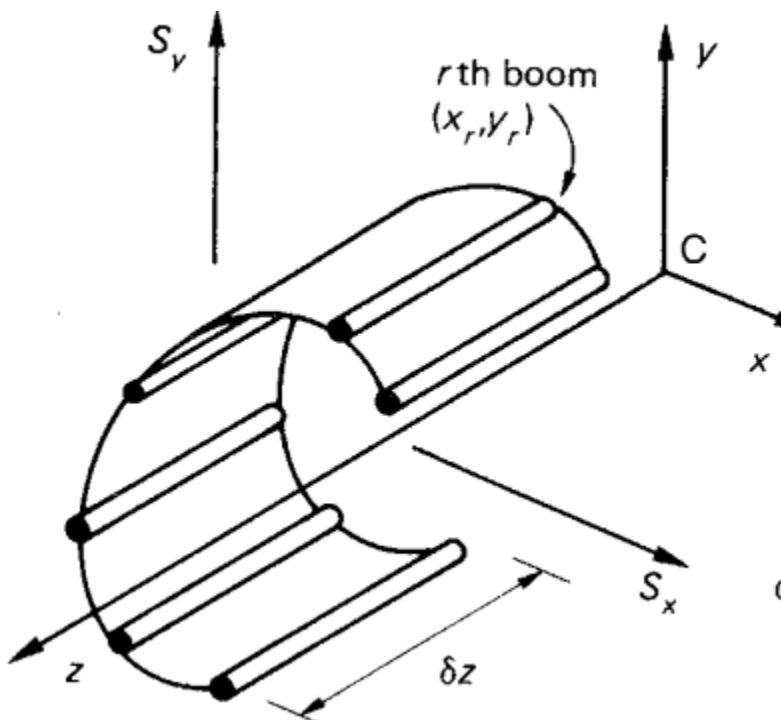


Figure 20: Example boom distribution across an open cross-section

A new equation for shear flow was also derived by performing a force balance on the idealized boom configuration. Calculations were further simplified by assuming that the shear flows were constant in the skin sections between booms. Going across the booms would cause sudden increases or decreases in shear flow, after which the shear flow would remain constant until another boom was crossed. The resulting Eq. (32) depended only on the boom areas determined from Eq. (31), the moments of inertia

determined previously for the cross-section, and the wing loading determined in the load evaluation section of the report.

$$q_2 - q_1 = -\left(\frac{S_x I_{xx} - S_y I_{xy}}{I_{xx} I_{yy} - I_{xy}^2}\right) B_r x_r - \left(\frac{S_y I_{yy} - S_x I_{xy}}{I_{xx} I_{yy} - I_{xy}^2}\right) B_r y_r \quad (32)$$

The $q_2 - q_1$ term in the equation above represented the jump in shear flow across the boom. Once again, the I_{xx} , I_{yy} , and I_{xy} terms were the area moments of inertia for the total cross section. The B_r term represented the area of the boom that the jump occurred over, while x_r and y_r were the x and y coordinates of the boom with respect to the centroid. Since the centroid was set as the origin, these calculations were slightly simplified. Finally, the S_x and S_y terms represented the x and y shear forces acting on the wing respectively. These forces were taken from the wing loading results discussed previously. Specifically, with the w_x and w_y loadings obtained for the point of operation, Eqs. (24a) and (24b) were used to determine the shear forces for the wing.

With these simplifications, the standard open cell shear flow calculations became much easier. A marching method could be used to simply calculate the jumps in shear flow across each boom along the outer skin. However, the actual geometry of the cross-section would require several additional relations to properly analyze.

Two-Cell Shear Flow Calculations

The geometric complications for the cross-section involved supporting spars. The forward and rear spars effectively separated the cross-section into a two-cell closed structure, which necessitated additional assumptions. The boom idealization discussed above dealt with an open, single-celled cross section. On the other hand, the wing cross-section was divided into two closed-cells by the spars. The full

shear flow of the wing cross-section was determined by combining the open cell shear flow calculations mentioned previously with additional closed and multi-cell corrections.

For the open-cell shear flow analysis, two cuts were made at the spars, resulting in zero shear flow along the spars. The standard shear flow calculations used the boom marching method mentioned above to simplify the contributions of the skin, stringers, and spar caps. With this, a distribution of open-section shear flows was derived for the airfoil.

The second step for this closed-cell shear flow calculation involved determining the constant shear flows in each cell. It was assumed that each cell in the original cross-section would have an additional constant shear flow, which by convention would be positive in the counter clockwise direction. Fig. (21) was used to provide this convention.

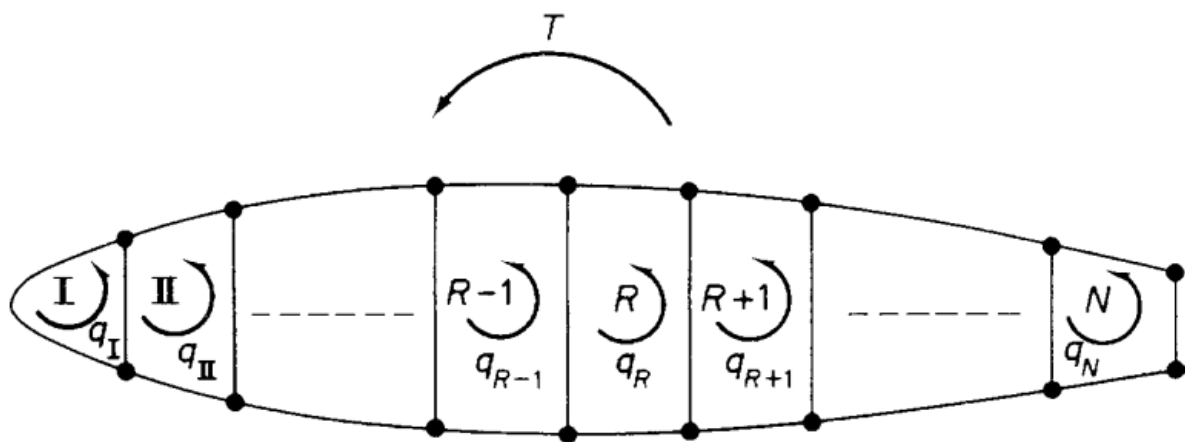


Figure 21: Constant shear flows for a multi-cell cross-section

In this case, the outer skins along each cell would have constant shear flows equivalent to their cell's. However, these constant shear flows intersect and are oriented in opposite directions at dividing spars. To account for this, the constant shear flows at these spar intersections were assumed to be the differences between the constant shear flows of the two intersecting cells. The positive shear flow in this

case would be assumed to be the cell that was being evaluated at that time. This process was defined by Eq. (33) and illustrated in Fig. (22).

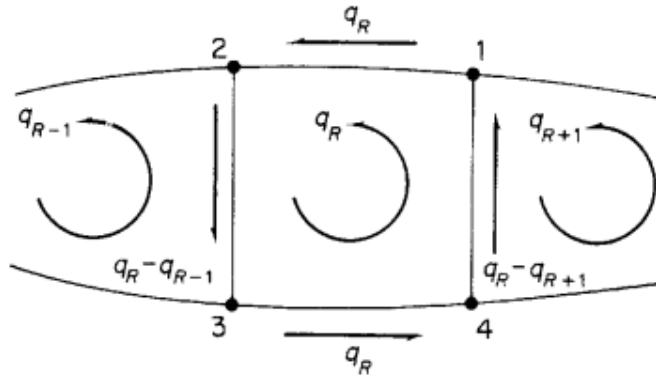


Figure 22: Example constant shear flows for a closed section

$$q_{Ri} = q_R \quad \text{for } 1-2 \text{ and } 3-4 \quad (33a)$$

$$q_{Ri} = q_R - q_{R-1} \quad \text{for } 2-3 \quad (33b)$$

$$q_{Ri} = q_R - q_{R+1} \quad \text{for } 4-1 \quad (33c)$$

For these equations, q_{Ri} represents the constant shear flow for a specific section of the cell. Similarly, q_R represents the total constant shear flow of the current cell and q_{R-1} and q_{R+1} represent the constant shear flows of the cells bordering the current cell. These constant shear flow terms were necessary to solve for the compatibility condition that was used to relate the open cell shear flow and the constant shear flow.

The system of equations used to solve for the total shear flows consisted of two relations. These were a moment balance and the angle of twist equation. The moment balance related the natural pitching moment of the wing, the aerodynamic loads, and the resulting shear flows about the centroid of the cross-section. Eq. (34) defines this moment balance.

$$M_0 + S_y x_0 - S_x y_0 = 2A_I q_{0,1} + 2A_{II} q_{0,II} + \sum_{i=1}^n 2q_{b,i} \Delta A_i \quad (34)$$

M_0 defines the pitching moment of the wing. The S_yx_0 and S_xy_0 terms are the shear force moments from aerodynamic loads on the wing. The right hand side of the equation deals with the moments that result from the constant and open cell shear flows. The first two terms, $2A_I q_{0,1}$ and $2A_{II} q_{0,II}$ are the torsion terms associated with the constant shear flow specific to each cell. The q terms in these represent that shear flow, while the A_I and A_{II} terms are the cell areas which were calculated using cross product rules. Finally, the summation term represents the torsion contribution from the open cell shear flow. This term sums up the contribution of each individual skin panel from the boom approximation. Following these steps, it was seen that Eq. (34) could not be solved explicitly. An additional equation was necessary to solve for both $q_{0,1}$ and $q_{0,II}$.

This compatibility was the angle of twist equation. The wing was assumed to move with rigid body motion. Thus, the angle of twist of the two cells would remain constant. This angle of twist, Eq. (35), was calculated simply as a function of cross-sectional areas and shear flows. It was these shear flow terms that allowed for the coupling of the angle of the twist and the moment balance equations.

$$\frac{d\theta}{dz} = \frac{1}{2A_R G} \oint_R \frac{q}{t} ds \quad (35)$$

The $\frac{d\theta}{dz}$ term refers to the angle of twist. The dz in this term indicates that the angle of twist changes along with the loading in the z-direction of the wing. On the right hand side of the equation is a selection of several constants. The A_R term represents the area of the analyzed cell. This area is the same as either A_I or A_{II} used in Eq. (34) above, and depends only on which cell is being analyzed with the equation. Furthermore, G is simply the shear modulus of the material. This constant was assumed to be 28 GPa for the given Aluminum 2024 T3 material. The surface integral sums the contributions to the angle of twist from the shear flows in the walls of the cell. For this project, this was done by multiplying the

constant shear force term along each wall of the cell by that wall's length. The terms for each wall of the cell were then summed together to get the total shear flow contribution.

This process was repeated for each of the two cells in the cross-section. The angle of twist equations for both cells were then expressed in regards to the $q_{0,1}$ and $q_{0,II}$ constant shear flow terms. The shared boundary from the quarter-chord spar allows the two shear flows to be coupled. Finally, the compatibility condition of a constant angle of twist was applied to the system to solve for the total shear flow. The system of equations consisting of the results of Eq. (35) and (38) was then solved for the total shear flow of the airfoil cross-section. These shear flow terms were then converted into shear stresses and used in failure analysis. The results of this shear flow calculation were plotted below in Fig. (23) while the total shear force at root and half-wing PHAA was plotted in Fig. (24) and (25) respectively. Similar plots for other critical points can be found in Appendix D.

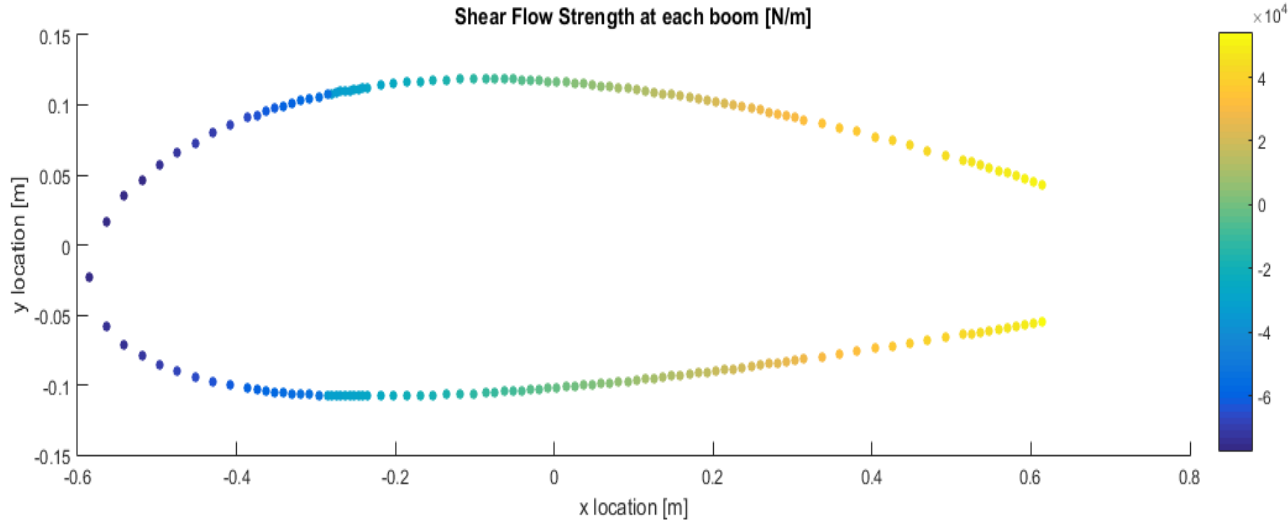


Figure 23: Total shear flow magnitude about airfoil surface at sea level PHAA

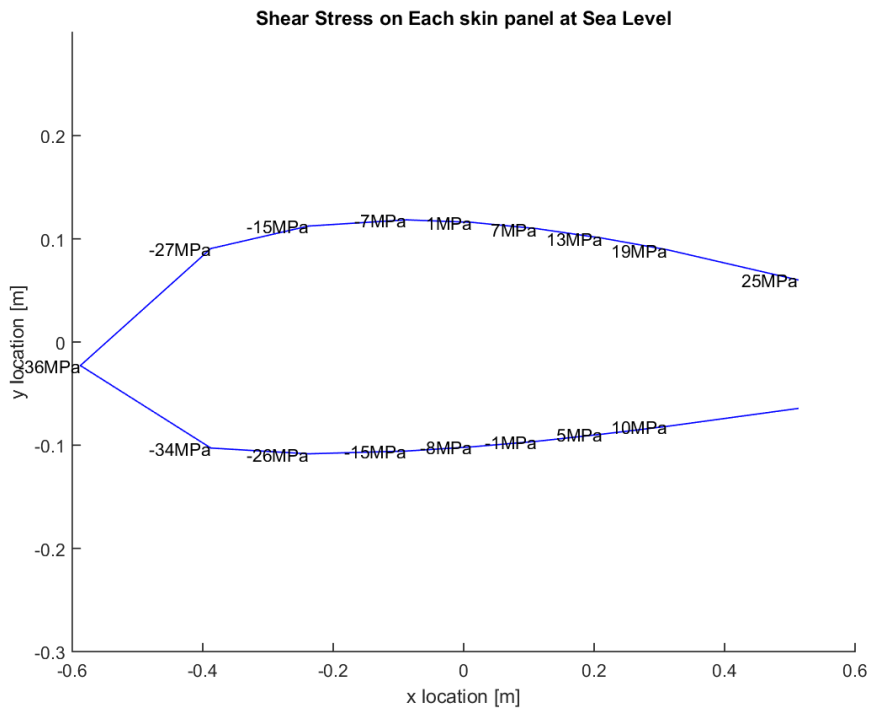


Figure 24: Shear stress distribution about skin panels on wing root airfoil surface at sea level PHAA

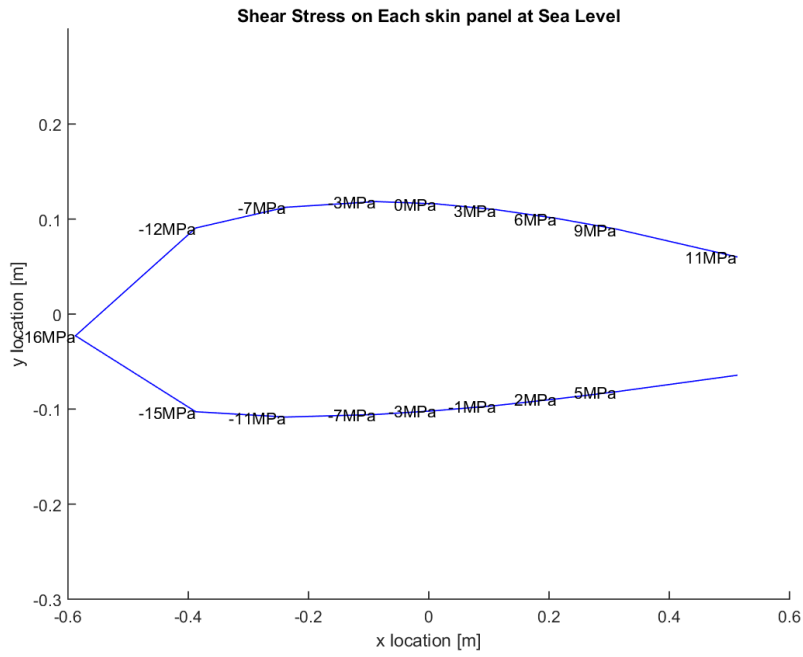


Figure 25: Shear stress distribution about skin panels on half-wing airfoil surface at sea level PHAA

Fig. (23) shows large shear flow concentrations at both the most forward and the most rearward portions of the cross-section. Fig. (24) and Fig. (25) also reflect this, as the shear stress values at the tips were three to four times higher than at the top and bottom skin sections. Therefore, it is at these locations where shear failure is most likely to occur. Additionally, the shear stress values also dropped dramatically between the root and half-wing. This further corroborated the assumption that the wing root would experience the harshest loading. This also allowed focus to be placed on only root conditions in future shear stress analyses. To determine the failure mechanisms of these sections of the airfoil, additional relations for buckling, yield, and fatigue needed consideration. Furthermore, several significant assumptions were made during the shear flow calculations. Additional verification was done in order to ensure the accuracy of these results.

Shear Flow Validation

The validation methods used to check for the accuracy of the shear flow code included: a boom direct stress balance, a shear force balance, and an open-cell shear flow check. The first check, the boom direct stress balance, simply required multiplying the direct stress at each boom location by each boom's area. Ideally, the sum of these forces would have been zero. The second shear force balance check required converting the total resultant shear flow into x and y shear forces. This was done by multiplying the shear flow at each skin section by the length of that skin section. These were then compared to the applied shear forces from the load estimates. Ideally, the results from shear flow and the applied loads would be equal. The final open-cell check simply required that the final open-cell shear flow term, q_b , be equal to or close to zero. This open cell shear flow was derived from the boom idealization method discussed previously in the report.

The first verification method produced results on the order of magnitude of 10^1 Newtons. That is, while the sum of the boom area axial forces was not zero, it remained under 100 N. The force terms at each boom were found to be on the order of magnitude of 10^3 and 10^4 Newtons. This indicates that the final error was on the order of magnitude of 0.1% to 1% of the total value of the system. This result was assumed to be close enough to zero, satisfying this check.

The second shear force check was not passed as cleanly, however. The applied forces at the root were determined from the loading data as -2.6907E3 Newtons for the x shear and 2.1589E4 Newtons for the y shear. The resulting x and y shear forces from shear flow were found to be -3.112E3 and 2.3506E4 Newtons respectively. The error here was approximately 20% for the x shear and 9% for the y shear forces. While these values were considered to be too high initially, consultation with Peng determined that the margins were acceptable for the purposes of the project.

The final check of the open cell shear flow results followed a similar pattern as the first test. The shear flow values were found to range from 10^3 to 10^5 N/m at all points along the open cross-section. The smallest of these values corresponded to the booms near the cut spars, indicating that the open cell shear flows here were the smallest. While these were supposed to be zero ideally, the trend of data still followed previous assumptions and decreased drastically at these end points. Since the end point values were approximately 1% of shear flows at other sections of the body, it was determined that this check was sufficiently satisfied as well. After these validation procedures were completed, additional failure testing was done to ensure that the structure would not buckle or yield under operation.

Since it was determined that the accuracy of the shear flow code was sufficient for the scope of this project, the results from this and previous stress analyses were used in several failure checks. These failure checks included column buckling for the spars, plate buckling for the skins, Von Mises yield, and fatigue analysis. The buckling analysis for the wing was split into column and plate buckling. Column

buckling dealt with potential failures in the supporting stringers of the wing, while the plate buckling analysis dealt with failures in the skin. The Von Mises yield criterion is an energy criterion that is used to determine the equivalent stress on a section, which can be compared to that section's material yield strength. This equivalent stress depends on all applied stresses on a section, which in turn are dependent on geometry. Finally, the fatigue behavior of a structure defines how many cycles of loading a structure can experience before micro-failures are amplified to cause full structural failure. In this case, crack propagation was determined to be the primary source of fatigue failure. Each of these failure scenarios was defined quantitatively and then checked to ensure that the wing structure would not fail.

Column Buckling

First, column buckling analysis was performed to determine the necessary rib spacing in the wing. The stringer buckling here was assumed to conform to Eulerian Buckling relations.

Beam buckling occurs when a critical compressive stress is applied, causing large deflections of the beam. After deflections, the buckled beam is generally no longer able to support substantial loads. Fig. (26) provides an example of buckling in a single beam.

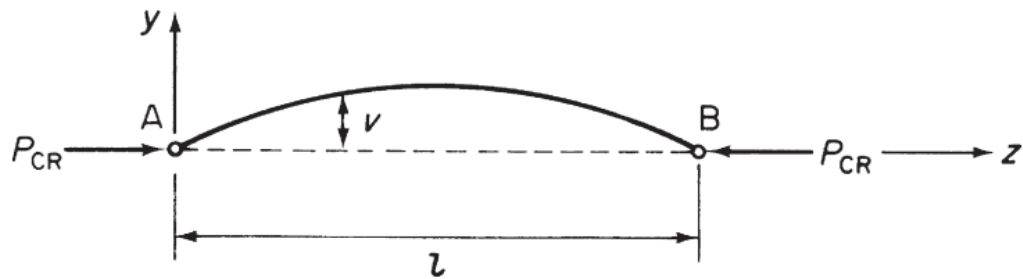


Figure 26: Example of Eulerian beam buckling

Here, the critical z loading P was seen to cause a large deflection along the beam. The stringers that were analyzed for the buckling analysis were assumed to be loaded in a similar manner. Furthermore,

the σ_{zz} beam stresses were assumed to be the primary cause of stringer buckling. The σ_{zz} stresses for each stringer were calculated using Eq. (26). These stresses were then multiplied by the stringer areas to determine the end loading forces on the stringers. An additional safety factor of 1.5 was then applied to this estimate to create a more conservative model. This process is can be simplified into Eq. (36) below.

$$P = 1.5\sigma_{zz}A_{str} \quad (36)$$

Here, P is the applied compression loads, 1.5 is the safety factor, A_{str} is the stringer cross-sectional area, and σ_{zz} is the bending stress calculated for each stringer. This value was then used with the critical buckling load equation to estimate the required rib spacing for the wing. This was possible because the ribs were considered to act as points of fixation along the wing, sectioning off parts of the stringers as different fixed rods. The relationship described here is defined in Eq. (37)

$$P_{crit} = \frac{n\pi^2EI}{l_e^2} \quad (37)$$

In Eq. (37), P_{crit} denotes the critical buckling load. E and I are constants and are the Young's modulus and the local x area moment of inertia of the stringers respectively. The Young's modulus for aluminum 2024 t3 was 73.1 GPa while the initial moment of inertia for each stringer was found to be 4.55E-10 m⁴. The l_e term represents the effective length of the beams. Since it was assumed that both ends of the stringer sections would be fixed by ribs, this effective length becomes 0.5*/l, or one half of the stringer section length. This l was also the stringer length that was solved for. Finally, the n term denotes the order of buckling the critical load is for. Since 1st order buckling occurs at the lowest loading, this was the only order of buckling tested. For this case, n was set to 1.

To prevent buckling, the resulting load from Eq. (36) needed to be lower than the critical load from Eq. (37). From this, the maximum allowable stringer length l was calculated. This maximum stringer length, and rib spacing, would prevent column buckling at all points along the wing. For the dimensions

given previously, the rib spacing was determined to be 0.3636 meters for sea level PHAA conditions. The skin buckling analysis followed a similar procedure.

Skin Buckling

The skin buckling relations also depended on calculating a critical buckling stress, which was compared directly to applied stresses. For skin buckling, the loading came from both shear direct stresses acting on the skin. The shear stresses along each skin panel were determined from shear flow, while the direct stresses were calculated in the same manner as column buckling. The same 1.5 safety factor was applied here as well. The shear flow and shear stress relation was defined by Eq. (38).

$$q = \tau t \quad (38)$$

where q represents shear flow while τ and t are shear stress and skin thickness respectively. This simple relation allowed for the conversion of shear flows to shear stresses. This resultant stress could be used to determine shear buckling behaviors. However, only direct stress buckling was accounted for in this project.

The critical buckling load for the skin panels was obtained through plate buckling models. The final model relates the critical buckling load to skin thickness, panel length, material, and support type. The full relation that was used was Eq. (39).

$$\sigma_{cr} = \frac{k\pi^2 E}{12(1-\nu^2)} \left(\frac{t}{b}\right)^2 \quad (39)$$

Here, σ_{cr} is the critical buckling load, E is the Young's modulus of the material (Aluminum 2024 T3), and ν is the Poisson's ratio of 0.33. The t and b terms are the thickness and length of the skin panels respectively. The initial thickness used for this was 1 mm, while the skin panel length b was the spar spacing for direct stress and rib spacing for shear stress checks. Finally, the k term was assumed to be approximately 8 due to the nature of the skin panel supports.

The convention used to define the b length in the direct stress and shear stress cases was taken from Fig. (27) below.

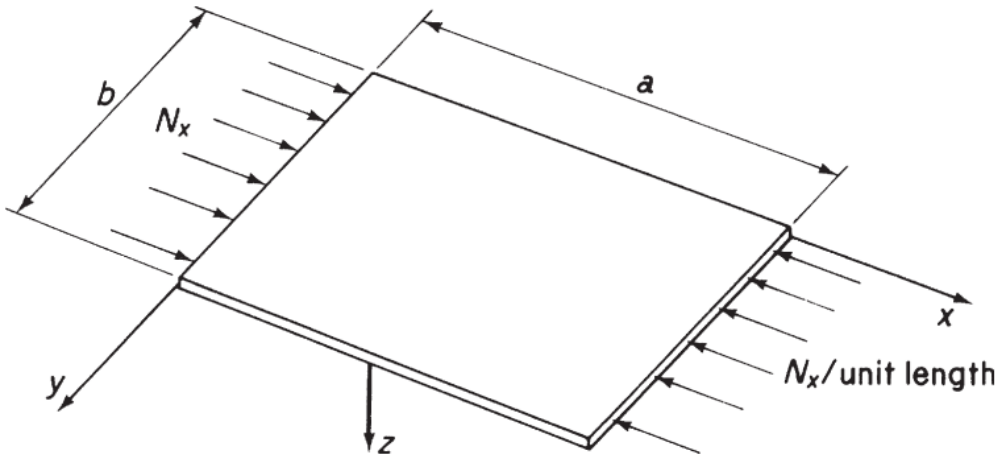


Figure 27: Visualization of thin plate buckling loads

In this case, the N_x force in each case was derived from either the direct stress. Following the orientation provided above, this required the use of the spar spacing or for the direct stress case. Additional dimensions identified in the equations above such as skin thickness and spar spacing would also be useful for preventing failure and optimizing weight.

Most of the analysis was focused on loading at the root of the wing. Previous calculations in the load estimate section determined that loads were greatest in this wing section. The skin panels failing through direct stresses at PHAA were plotted in Fig. (28). Similar plots are located in Appendix E.

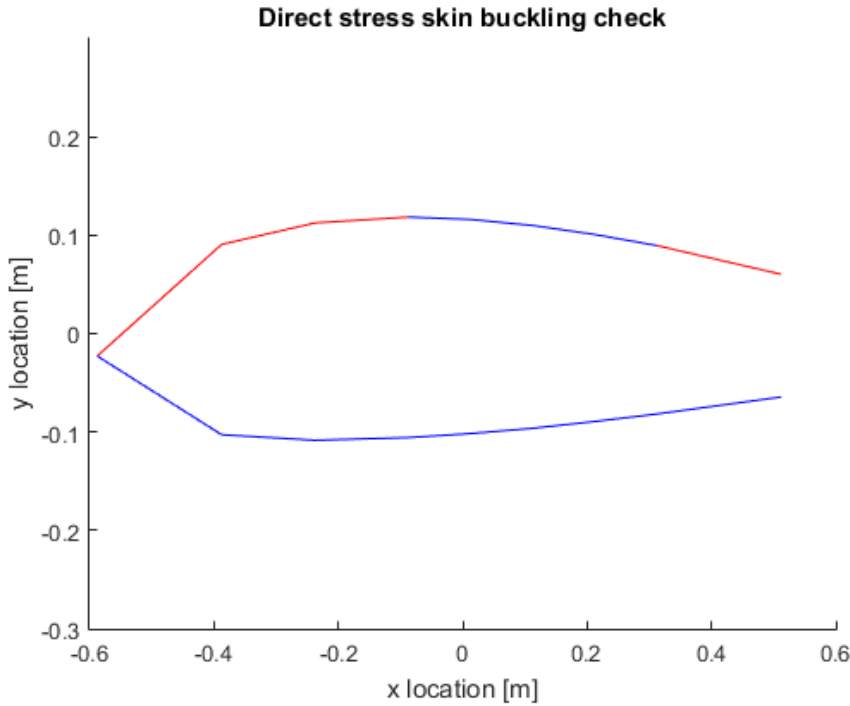


Figure 28: Skin buckling from direct stress at sea level PHAA. Red lines indicate failure

The critical loads used in the figures above were 16.6 MPa for the shear stress, and between 54 and 219 MPa for the direct stress. The critical buckling loads for the direct stress case varied since the stringers were not uniformly distributed at some points along the airfoil surface. For instance, additional stringers had been placed at the nose, since it was assumed stresses here would be strongest. Figs. (26) and (27) showed that this is the case, as the frontal sections were more prone to failure in direct stress cases.

Additionally, Eq. (39) was also used to solve for a critical stringer spacing in a similar manner to the rib spacing calculations done in the column buckling section. Here, the maximum compressive stress of 124.7 MPa was assumed to be the critical stress. Eq. (39) was then solved from the stringer spacing term, resulting in a maximum allowable stringer spacing of approximately 0.11 m. Failures occurred in Fig. (28) due to several stringers being spaced at 0.13 m or higher apart near points of the highest critical loads. Geometric manipulations were performed later to account for this by decreasing the applied stresses. The

direct and shear stresses discussed in this section were also used extensively for both the Von Mises and Fatigue behavior sections.

Von Mises Failure Criteria

The direct and shear stresses found in the buckling analyses were combined into an equivalent Von Mises stress, which was used to check against yield failures in the aircraft structure. The Von Mises yield criterion states that a ductile material will fail once its distortion energy density reaches a certain threshold [2]. In other words, this is an energy based and not a stress based failure criterion. However, several mathematical simplifications allow for the use of an equivalent failure stress to check against yield. This equivalent stress is a combination of all axial and shear stresses being applied to the body in question. This point is expanded on in Eq. (40).

$$\sigma_{eq} = \left[\frac{(\sigma_{11}-\sigma_{22})^2 + (\sigma_{22}-\sigma_{33})^2 + (\sigma_{33}-\sigma_{11})^2 + 6(\sigma_{12}^2 + \sigma_{23}^2 + \sigma_{31}^2)}{2} \right]^{1/2} \quad (40)$$

The above equation presents the full Von Mises equivalent stress equation. Here, σ_{11} , σ_{22} , and σ_{33} were the x, y, and z axial stresses respectively. Additionally, σ_{12} , σ_{23} , and σ_{31} were the xy, yz, and xz shear stresses. For the structural analyses used here, most of these terms were assumed to be zero. Specifically, the x and y axial stress and the xy and yz shear stresses. The simplified equation that was used is Eq. (41) below:

$$\sigma_{eq} = [\sigma_{zz}^2 + 3\sigma_{zs}^2]^{1/2} \quad (41)$$

where the equivalent stress σ_{eq} is related only to the bending stress σ_{zz} and the shear stress σ_{zs} . These are the same stress terms used in the column and skin buckling analysis discussed previously.

The equivalent stress resulting from this equation was then checked against the yield stress of the material in Eq. (42).

$$\sigma_y \geq 1.5\sigma_{eq} \quad (42)$$

Here, a 1.5 safety factor was again applied to the equivalent stress σ_{eq} . Additionally this yield stress is simply a material property. For Aluminum 2024 T3 this value was 345 MPa [3]. For PHAA the maximum equivalent stress was determined to be 193.2 MPa. With the safety factor applied, this maximum stress value was increased to 289.8 MPa. This corrected value was still 15% below the given yield stress, indicating that the material at PHAA loads was safe from yielding. The equivalent/yield stress percentage at each stringer was plotted for sea level PHAA in Fig. (29).

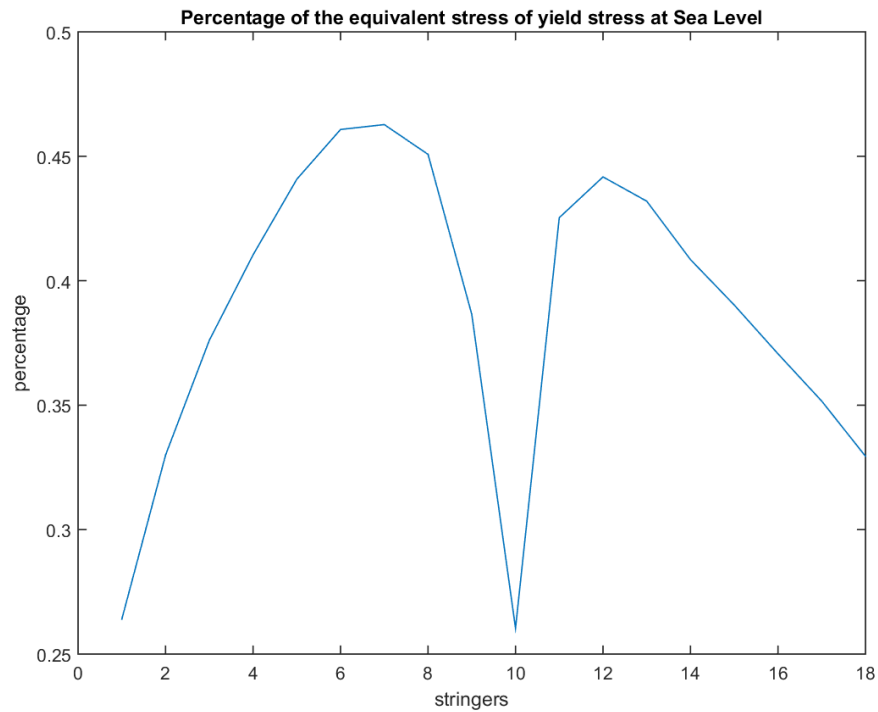


Figure 29: Percentage of equivalent/yield stress at sea level PHAA

From the Fig. (29), the peaks seem to occur at locations near the front of the wing. This coincides with loading predictions made previously, which predicted large forward and upward compression at PHAA. Similar plots at each critical point were placed in Appendix E.

Fatigue and Crack Analysis

The final failure analysis performed for the wing consisted of checking crack propagation and fatigue behavior in the wing. As crack and fatigue failures depend on localized conditions, a separate set of equations was needed to analyze these mechanisms. Additionally, the cracks being analyzed here were assumed to be near bolts on the wing surface and along the skin.

The standard crack propagation equation relates crack length, applied stress, and the fracture toughness of a material. The relation used here was Eq. (43).

$$K_I = f\sigma_{\infty}\sqrt{\pi a} \quad (43)$$

Here, K_I is the fracture loading of the material. The variable f is an empirical factor that is set to 1 for simplicity. Furthermore, σ_{∞} is the maximum applied stress to the wing, which is taken from direct stress. For PHAA the maximum direct stress was determined to be 124.7 MPa. Finally, the a term indicates the crack length. Using Aluminum 2024 T3's critical fracture toughness of 26 MPa*m^{1/2} the critical crack length a_{cr} was found. At PHAA, this value was 0.01635 m. This was the crack length that would cause additional crack propagation in the wing at the given loading.

This value was then used in Paris' Law to determine the cycles to failure for the material. Paris' Law, Eq. (44), related several empirical factors with the maximum direct stress and critical crack length from Eq. (43) in order to generate the cycles to failure.

$$N_f = \frac{1}{C[\Delta S\sqrt{\pi}]^n} \left[\frac{a^{1-n/2}}{1-\frac{n}{2}} \right]_{ai}^{af} \quad (44)$$

In this equation, N_f represents the cycles to failure. Additionally the C and n terms are constants given during lecture, being 1.6E-11 and 3.59 respectively. It was assumed that these constants were to be used with MPa and m units for ΔS and a respectively. On the same note, ΔS is the maximum loading for the aircraft, which was 114.7 MPa for PHAA. Additionally, the a term referred to the af and ai terms used in the evaluated integral form of Eq. (43). The af term was the critical crack length of 0.01635 m found previously, while the ai term was assumed to be 0.002 m. From this equation, the cycles to failure for sea level PHAA flight was calculated to be approximately 5290 cycles. This results were an order of magnitude lower than desired, indicating that design changes needed to be made. Additional cycle counts for operating conditions at all critical points are shown in Table 9.

Table 9: Cycles to Failure at Different Critical Points

Condition	Cycles to Failure
PHAA	5.29E3
PLAA	5.34E3
NHAA	2.52E5
NLAA	1.8E6
Gust Point 1	1.99E5
Gust Point 2	1.18E6

Again, it was seen that loading conditions at PHAA and PLAA caused the worst fatigue behavior, with PHAA having slightly fewer cycles to failure. Additionally, the PHAA and PLAA failures fell below 10E4 powers, which required additional tweaking to the structures to prevent failure.

Optimization and Failure Correction

Since the buckling and fatigue checks predicted undesirable failure performances, changes were made to the wing geometry to correct these failure cases. Furthermore, since it was seen previously that the highest loads and the worst failure cases occurred at sea level PHAA, all failure tests would be focused at this point. Additionally, the failure estimates for buckling would focus at the wing root since loads were determined to be highest there. The dimensions manipulated in this process included: stringer areas, cap areas, spar distribution, and skin thickness.

First, stringer areas were increased. The initial stringer areas were 5 mm^2 . This was increased to approximately 70 mm^2 in order to increase the moments of inertia of the cross section, which would in turn reduce the critical load for the direct stress case. Furthermore, the stringers were repositioned to focus towards the top, frontal portion of the cross section. This was to accommodate the higher compressive stress at that position. The reduced stresses from the increase in stringer area also a rib spacing increase from 0.36 to 0.48 m. This allowed for a reduction in the total number of ribs required for the wing, and thus the total structural weight of the wing. Spar cap areas were also increased to 60 mm^2 from their initial 40 mm^2 dimensions to further increase the area moment of inertia of the cross-section. This had a similar effect to the stringer area increases, and was done to conserve weight as well.

Another important parameter that was manipulated was the skin thickness, which was initially set at 2 mm. Higher skin thicknesses would improve buckling behavior in two ways. First, higher thicknesses would increase total area moments of inertia, thus decreasing the direct stress experienced

by the skin. The new moments of inertia are presented in Table 10. Additionally, the higher skin thicknesses would directly affect the critical load calculation in Eqn. (39) in the t term. However, the wing skin also provides for a large portion of the aircraft weight. Increasing the skin drastically would also negatively impact the total weight and performance of the aircraft. The manipulations of stringer and cap areas were performed to reduce necessary increases in skin thickness. With this in mind, the skin thickness only had to be increased to 2.2 mm to prevent buckling behavior at PHAA. These changes resulted in a maximum compressive stress of approximately 105 MPa, which was indeed lower than the initial value of 124.7 MPa. From Eq. (39) the maximum spar spacing was determined to be 0.1492 m for this new maximum stress. As the spar spacing were set to be approximately 0.13 m initially, this indicated that failures should have been rectified. Fig. (31) corroborated this assumption. The new shear stresses for the corrections were plotted in Fig. (30) while the final buckling behavior at PHAA was plotted in Fig. (31).

Table 10: New moments of inertia of the wing

I_{xx} (m^4)	6.6615e-05
I_{yy} (m^4)	0.0013e-04
I_{xy} (m^4)	7.4771e-06

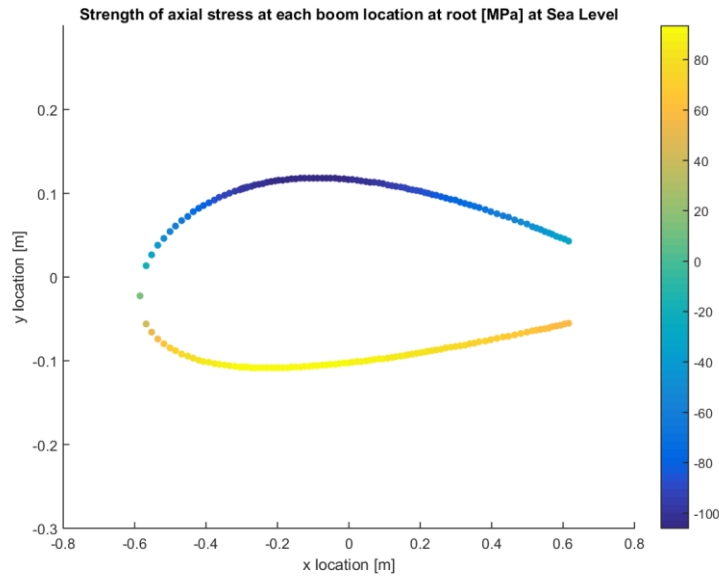


Figure 30: Direct stresses after failure corrections

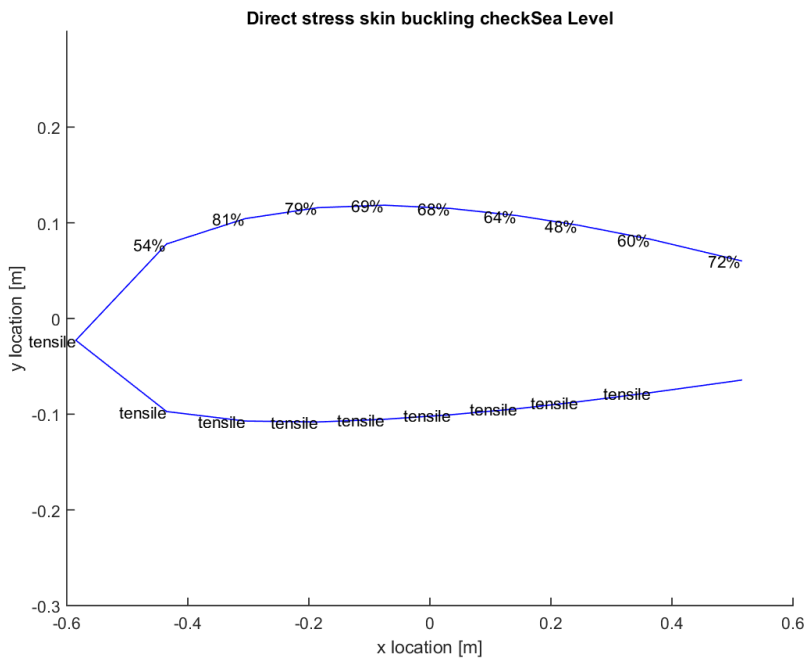


Figure 31: Direct stress skin buckling after failure corrections

The figure showed a significant failure margin remains at all points in the cross-section. This further indicated that excess structure was added to prevent buckling. The reason for this excess structure was to improve fatigue behavior at PHAA loads. Table 8 showed that only 5.29E3 cycles were required for failure here. To increase this to the 1E4 minimum specified in lecture, the maximum cycle load needed to be reduced. The processes defined above also contributed to this. The end result was that the cycles to failure at sea level PHAA increased to 1.22E4, matching initial requirements. Finally, the structural weight of the wing half span was determined to be 149 kg. This was calculated by taking the total cross-sectional area of the wing, found previously in the Airfoil Section portion of the report, and multiplying it by the density of the material and the half span of the wing. The density of aluminum 2024 T3 was 2780 kg/m³. Additional optimization of these parameters would also be possible to further refine these results and reduce the final wing weights.

Finite Element Analysis

In order to better understand how the wing would behave structurally at the predetermined critical points of its flight envelope, a finite element analysis (FEA) was performed using the commercially available simulation software COMSOL Multiphysics. Finite element analysis works by breaking down a geometry into a large number of finite elements, or mesh, and numerically solve for the behavior of each element. The sum of all these individual behaviors allow for the prediction of the actual behavior of the geometry of interest. While finite element analysis can help analyze many different kinds of physical effects like fluid flow and heat transfer, the primary focus of finite element analysis in this project is solid mechanics and modal analysis.

Computer-Aided Design

The first step to using COMSOL Multiphysics to conduct a finite element analysis involved the visualization of the wing structure using computer-aided design (CAD) software like SolidWorks. In order to simplify the model for mesh generation in COMSOL, the wing geometry was broken down into two major components: wing skin and its internal structures that consist of spars, ribs, and stringers. The locations of these internal components were determined by the shear flow and buckling analysis. Table 11 presents a summary of these parameters for the CAD model.

Table 11: Parameters used in the CAD model.

Parameter	Value
Skin Thickness	2.2 mm
Spar Thickness	6.8 mm
String Area	70 mm ²

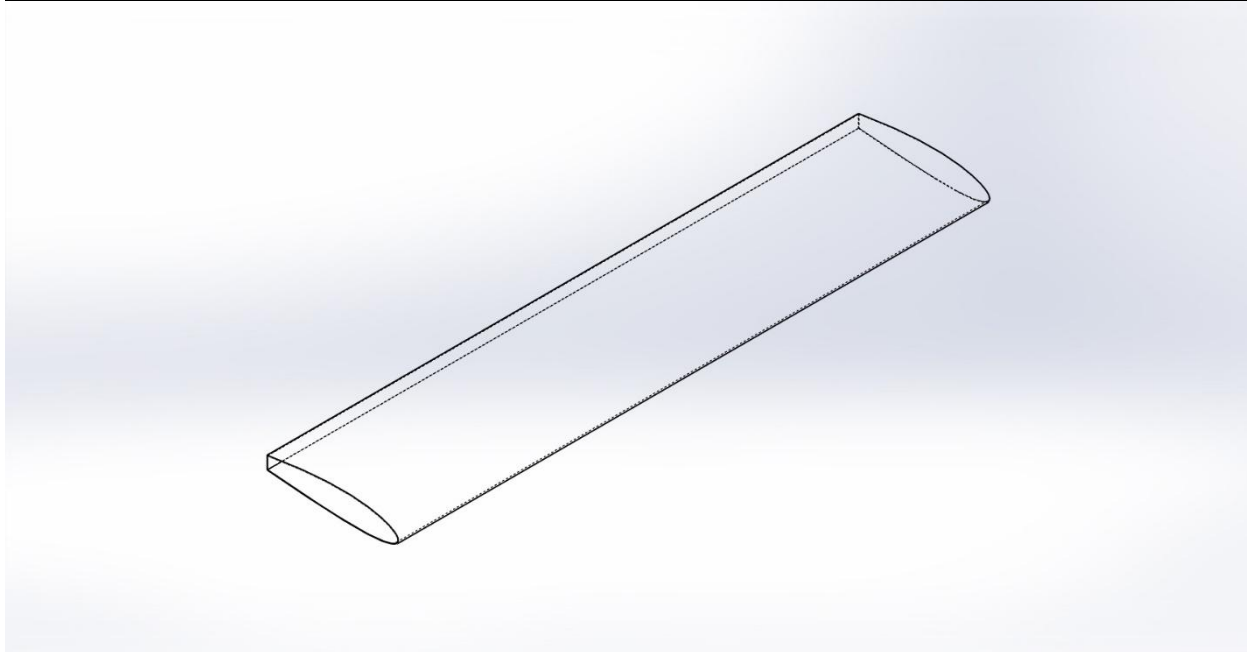


Figure 32: Wing skin CAD model

Fig. (32) illustrates the skin CAD model of the wing. The wing CAD model has a span of 5.41 m, reflecting the half span of the actual wing. The skin thickness was set to be 0.0022 m, reflecting the wing analyzed in this project. Additionally, as mentioned before, 20% of the airfoil section was to be cut off for control surfaces. This is reflected by the cut off near the trailing edge of the wing. Fig. (33) shows some of the internal structures of the wing, consisting only the spars and ribs. Spars run through the internals of the wing to support wing loading while ribs are spaced at a 0.4816 m interval to prevent skin buckling. However, it should be noted that these values are not finalized. The complete wing is shown in Fig. (34), which also depicts the stringers. Stringers used in analysis were located at $x = 0, 0.15, 0.28, 0.4, 0.51, 0.62, 0.73, 0.83, 0.95$, and 1.1 m from the leading edge of the airfoil section. They were placed on the upper inner surface as well as the lower inner surface and are symmetric about the horizontal axis of the airfoil. The placement of stringers was determined during the optimization process in which the group varied stringer locations, as well as area, to achieve minimum wing weight while maintaining desired failure characteristics and cycles, that is, not failing at the critical loads as well as having a fatigue cycle with an order of magnitude of at least 10^4 .

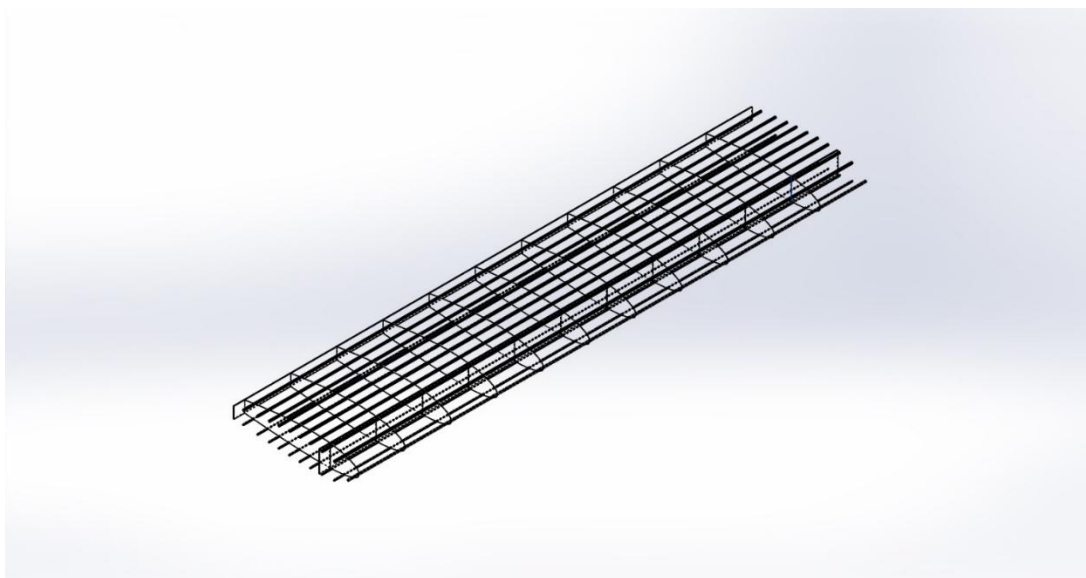


Figure 33: Wing internal structure CAD model, showing the stringers, ribs, and spars of the wing

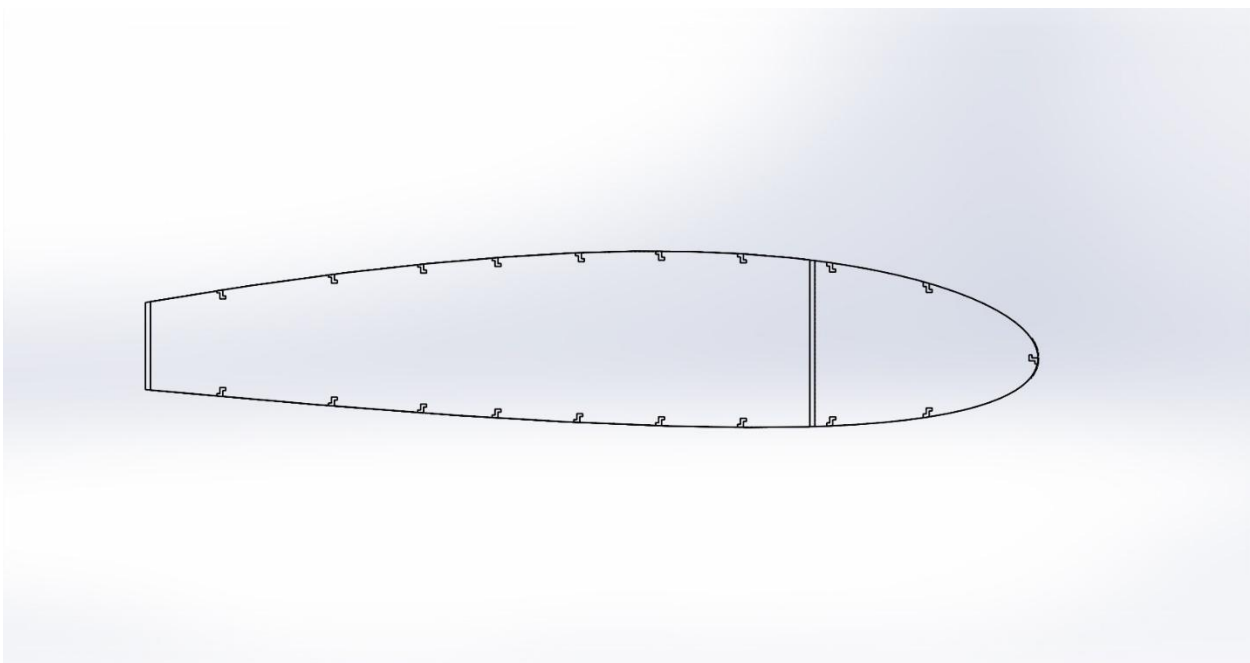


Figure 34: Cross-sectional view of the wing, showing spars, z-stringers, and skin

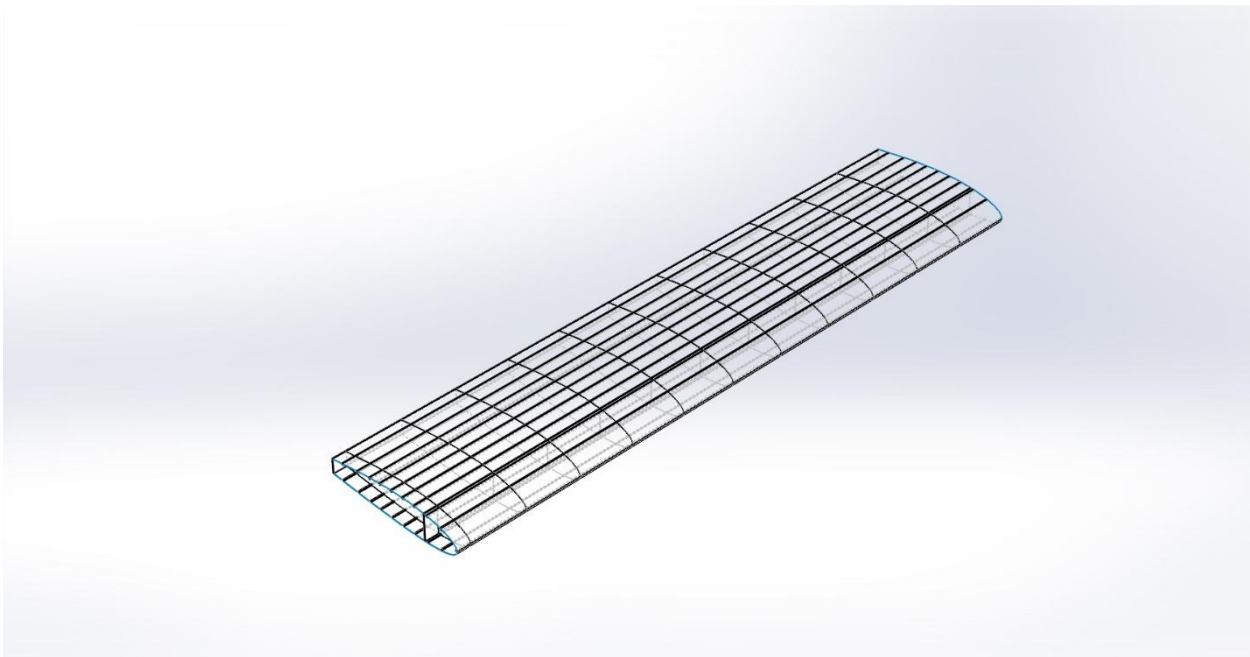


Figure 35: Wing CAD model, showing the stringers, ribs, and spars of the wing

Finite Element Analysis – Stress and Deflection

A finite element analysis was performed using COMSOL Multiphysics on the CAD model to simulate stresses the wing structure is expected to encounter at the critical points of the flight envelope. To simplify the model for finite element analysis, the CAD model imported into COMSOL Multiphysics was broken down into two parts: internal structures, which consist of only the spars and ribs, and the external skin with zero thickness. The stringers were omitted in the finite element analysis as they were creating memory issues in the simulation. Skin thickness was added in the COMSOL Multiphysics simulation rather than in the CAD model to avoid definition errors in COMSOL Multiphysics. Two meshes of fine fineness were generated in the simulation for the skin and the internal structures. These were coupled such that a cohesive analysis could be performed. The spars at one of the sides of the model were fixed and the other was free to deform depending on the applied load. Total forces at each critical points calculated in the previous sections were applied on to the structure for each finite element analysis simulation runs.

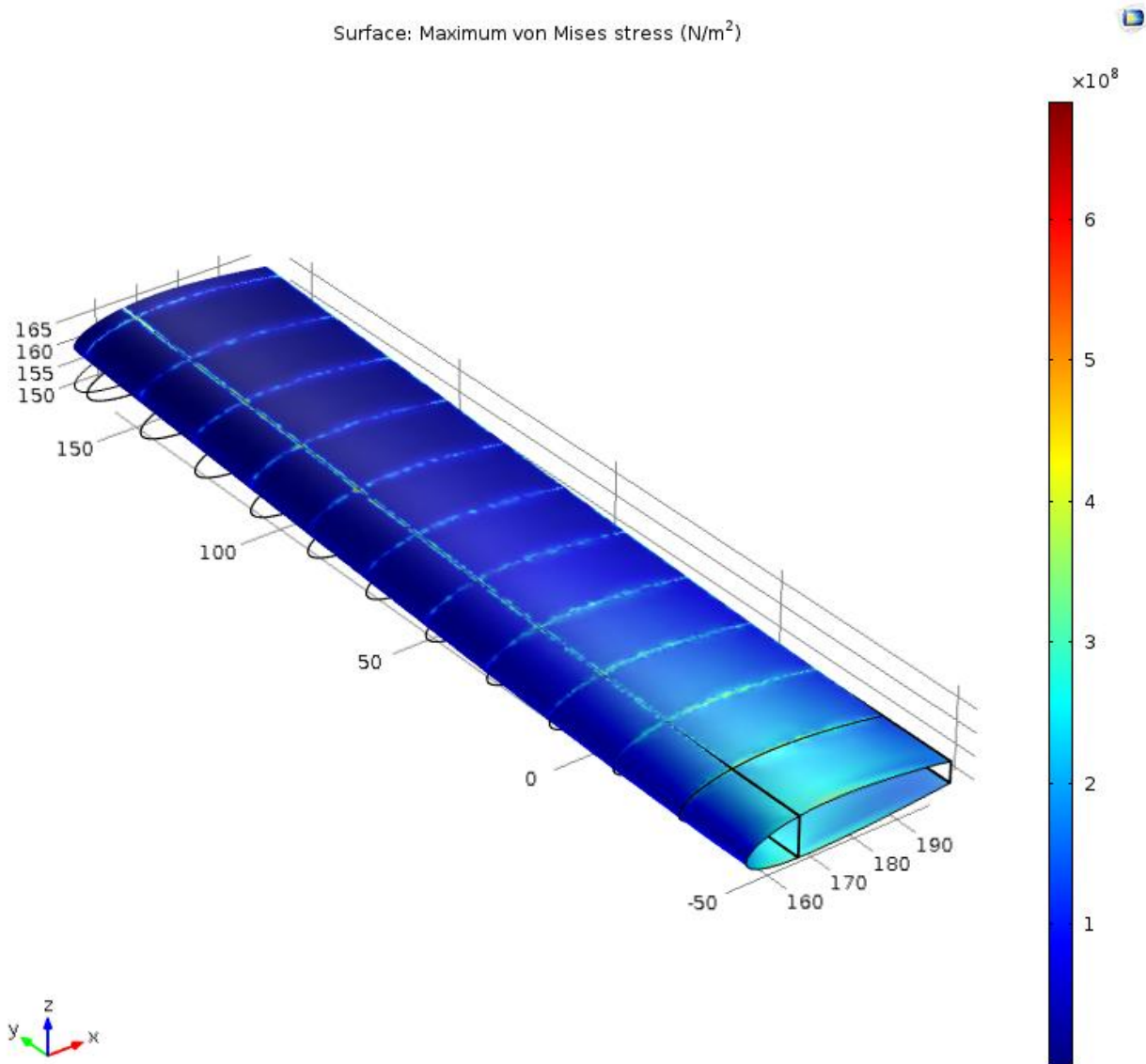


Figure 36: COMSOL Multiphysics finite element analysis for stress and deflection at PHAA

Fig. (36) depicts the result of the COMSOL Multiphysics finite element analysis for the critical load at PHAA, showing a high concentration of stress at the root of the wing at about 400 MPa. The stress per unit length decreases with span and reaches a minimum at the wing tip. Deflection of the wing under the predefined load was calculated to be about 0.10 m. Fig. (37) provides a more detailed look at the deflection of the wing under these flight conditions. These values of stress and deformation are of similar

order of magnitude with those of our analysis in Matlab. Note that the finite element analysis simulation excluded the influences of stringers, which were an integral part of the structural analysis in Matlab, and could be responsible for any major discrepancies in the values predicted by COMSOL Multiphysics and the Matlab code.

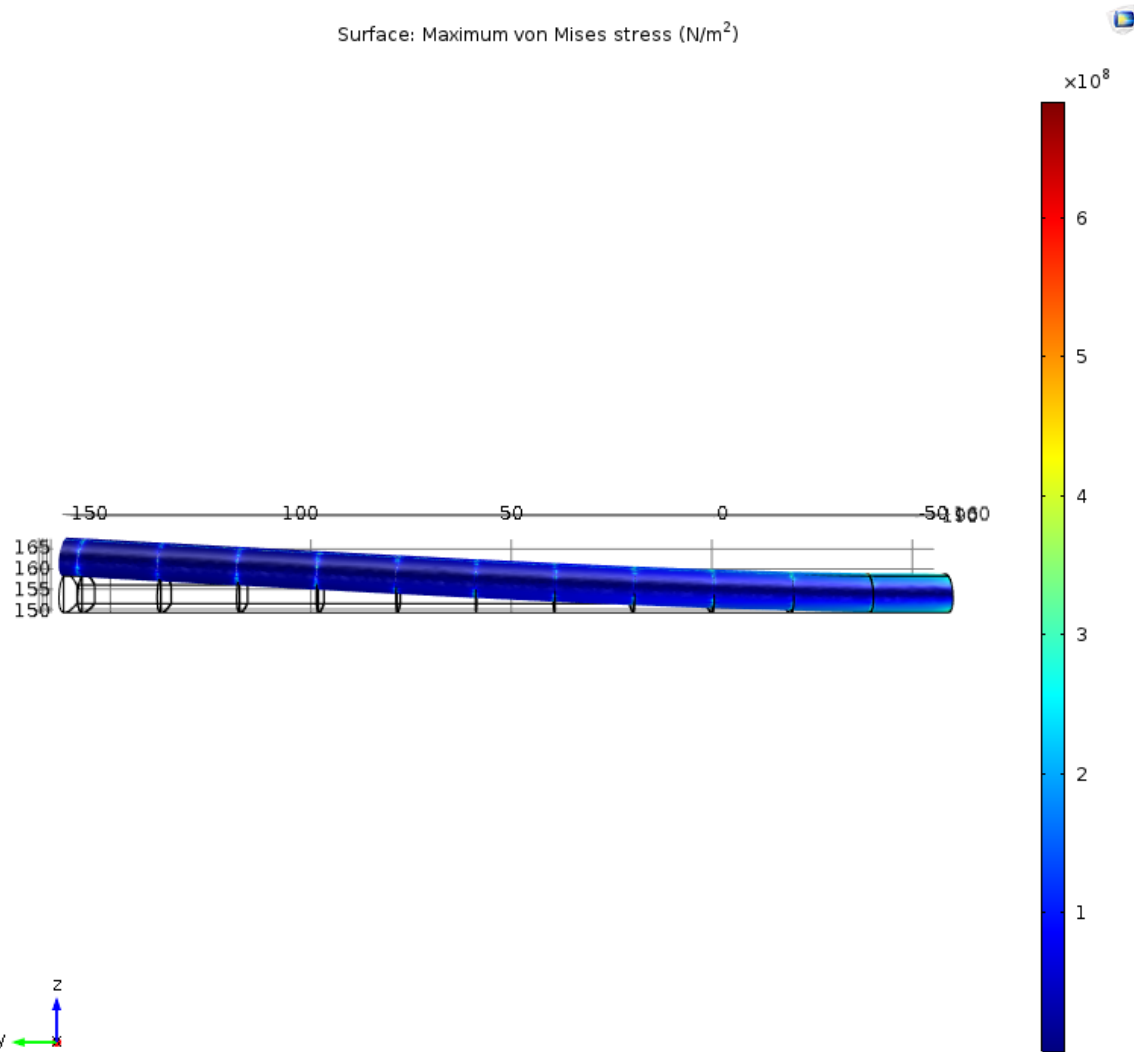


Figure 37: Wing Deflection at PHAA

This stress distribution is to be expected. As the wing is free to deform on the unfixed end, stress do not cumulate in these areas. On the other hand, compressive stress reaches a high point at the root where the wing is fixed. Since the critical point at PHAA is where the wing will experience the highest

amount of stress in its flight envelope, all design parameters were optimized based on this point. The deflection, as well as stress distribution of the internal structures are illustrated in Fig. (38). Again, stresses concentrate at the root of the wing as well as along the upper and lower edges of the spars. The finite element analysis for other critical points are presented in Appendix G.

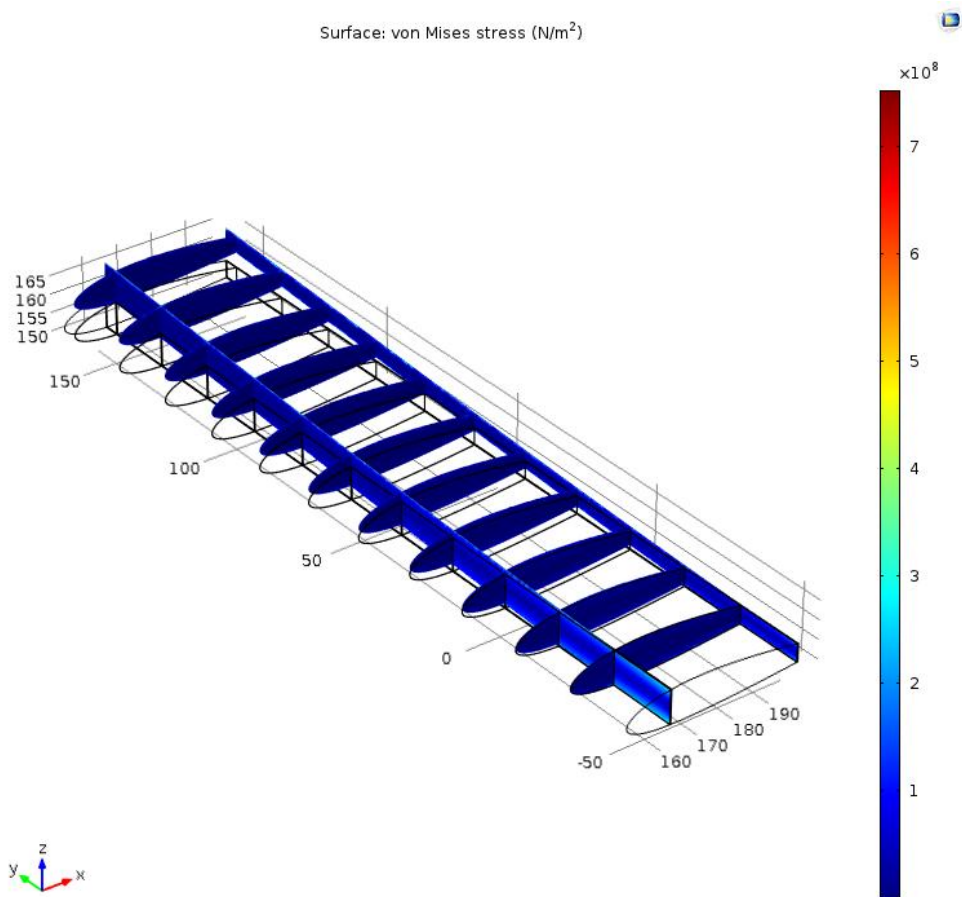


Figure 38: COMSOL Multiphysics finite element analysis for internal structures stress and deflection at PHAA

Modal Analysis

A modal analysis was also performed using COMSOL Multiphysics to study the dynamic properties of structures under vibrational excitation. The importance of such analysis lies in the fact that wing structures are not rigid and are subject to vibrational loads over the course of its operation. It is imperative to understand the structure's natural frequency in order to prevent catastrophic failure due to resonance. The computer simulation for modal analysis was done on the same model used in the simulation for stresses and deformation in the earlier section with one end fixed and the other was free to vibrate or deform. Four modes were analyzed using COMSOL Multiphysics and the results are depicted in Fig. (39) through Fig. (46). In the first mode at an eigenfrequency of 8.08 Hz, the wing deflects the most near the tip where it would deflect by 140 inches. A similar deflection happens in the second mode at an eigenfrequency of 32.58 Hz, with a maximum deflection of 140 inches at the tip. Deflection gradually decreases near the root. The wing, however, behaves differently at higher eigenfrequencies. In the third mode at an eigenfrequency of 44 Hz, the wing deflects the most in the middle, at a maximum deflection of 90 inches. The wing deforms somewhat like a string. In the fourth mode at an eigenfrequency of 54.76 Hz, the wing tip starts to twist about the y-axis. Maximum deflection occurs in the leading and trailing edges of the wing, at a maximum of plus or minus 60 inches. While the model analysis provides wing structural behavior at these frequencies, it does not predict failure. Because of the strength of resonance at these natural frequencies as well as the resultant deformation, the wing is likely to buckle under these dynamic loads. As such, these frequencies are to be avoided.

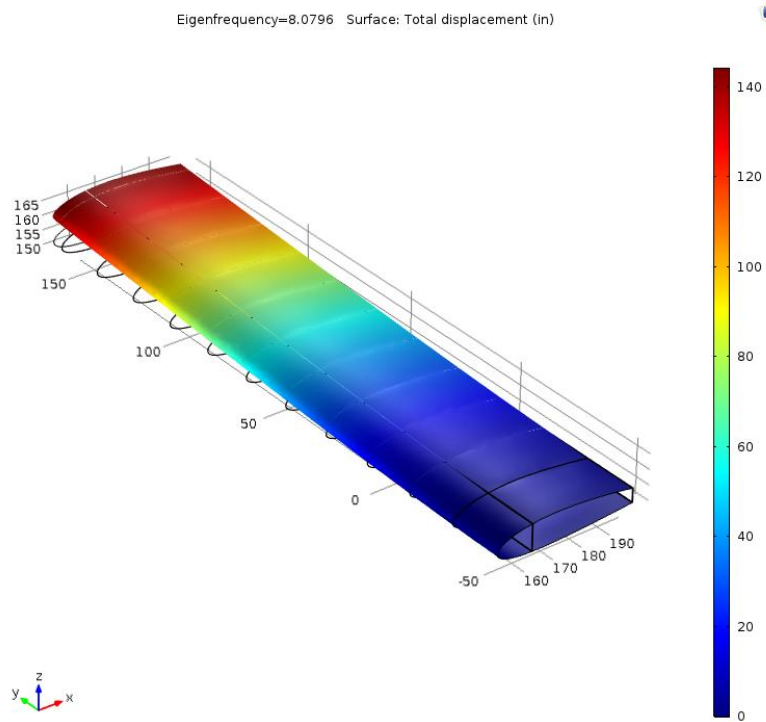


Figure 39: First mode at an Eigenfrequency of 8.08 Hz, showing the deflection of the wing

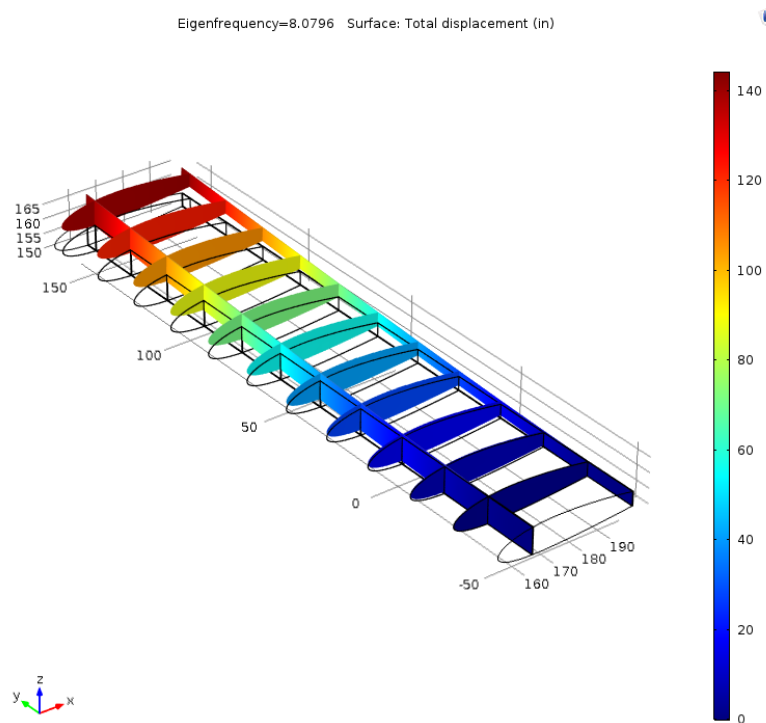


Figure 40: First mode at an Eigenfrequency of 8.08 Hz, showing the deflection of the internal structures

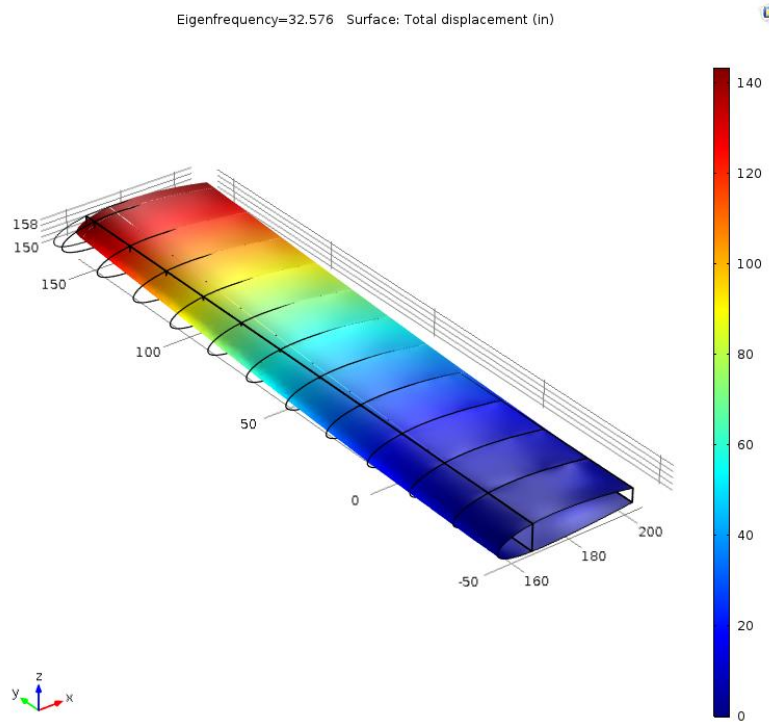


Figure 41: Second mode at an Eigenfrequency of 32.58 Hz, showing the deflection of the wing

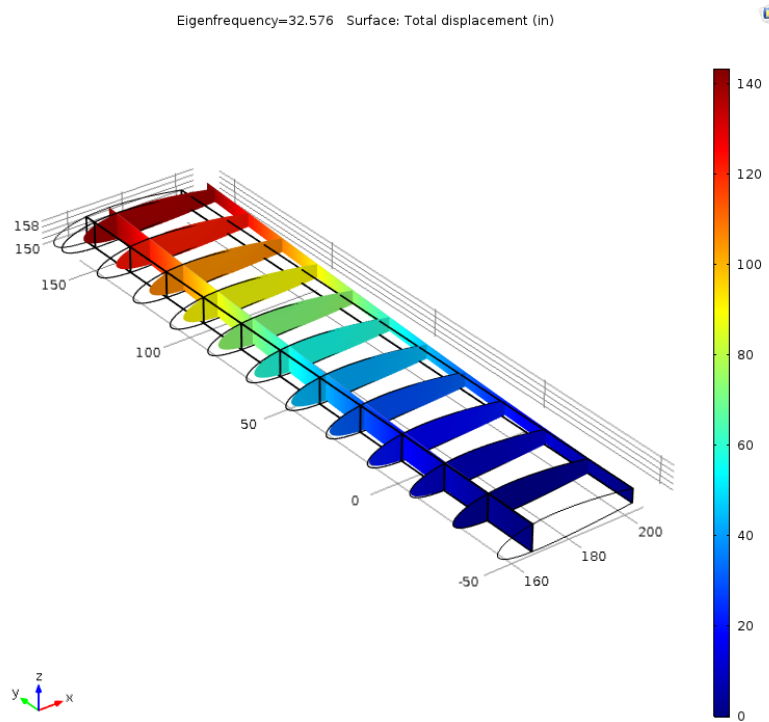


Figure 42: Second mode at an Eigenfrequency of 32.58 Hz, showing the deflection of the internal structures

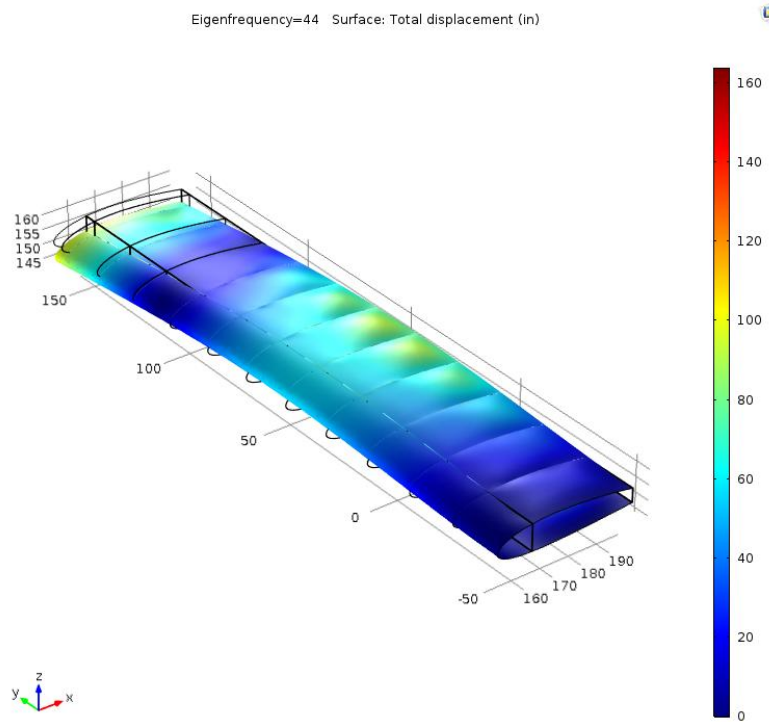


Figure 43: Third mode at an Eigenfrequency of 44.00 Hz, showing the deflection of the wing

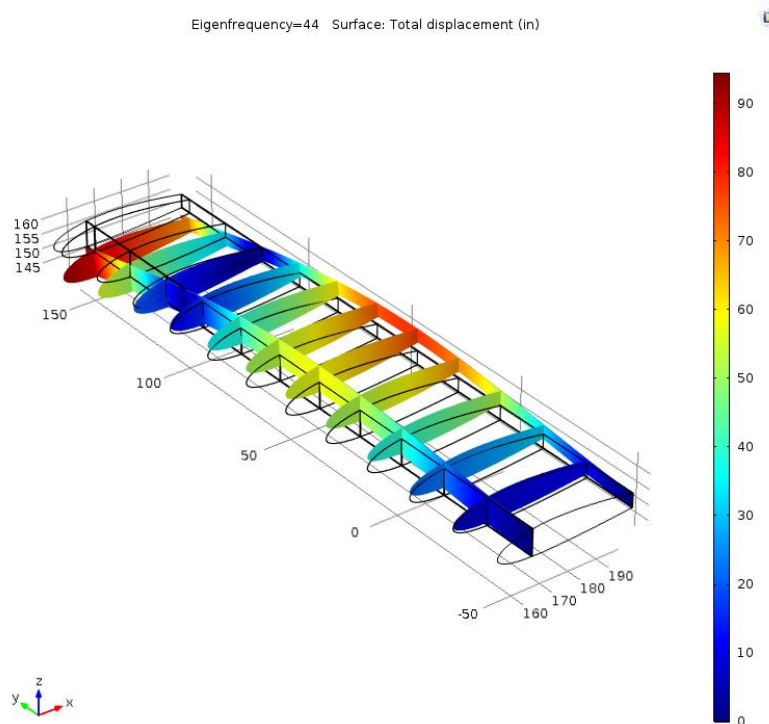


Figure 44: Third mode at an Eigenfrequency of 44.00 Hz, showing the deflection of the internal structures

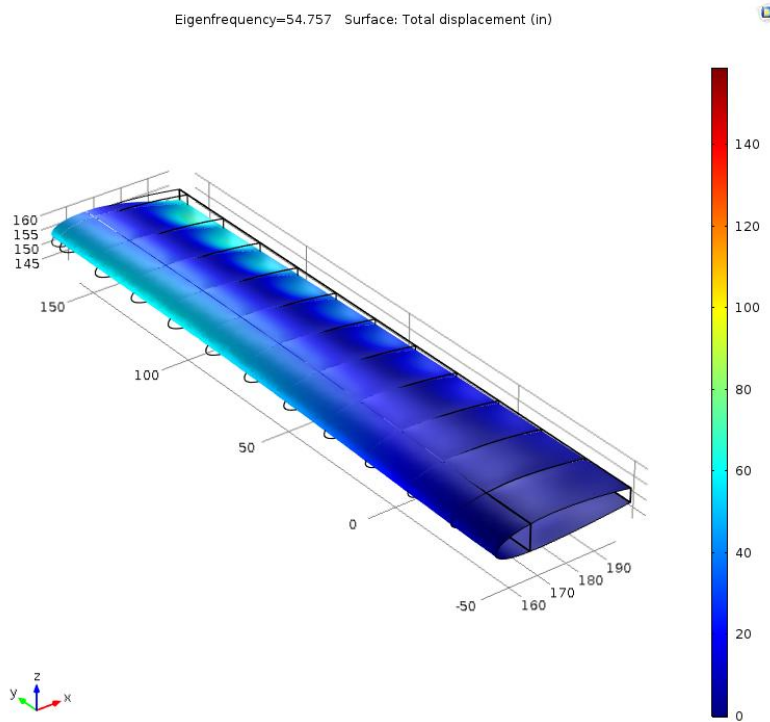


Figure 45: Fourth mode at an Eigenfrequency of 54.76 Hz, showing the deflection of the wing

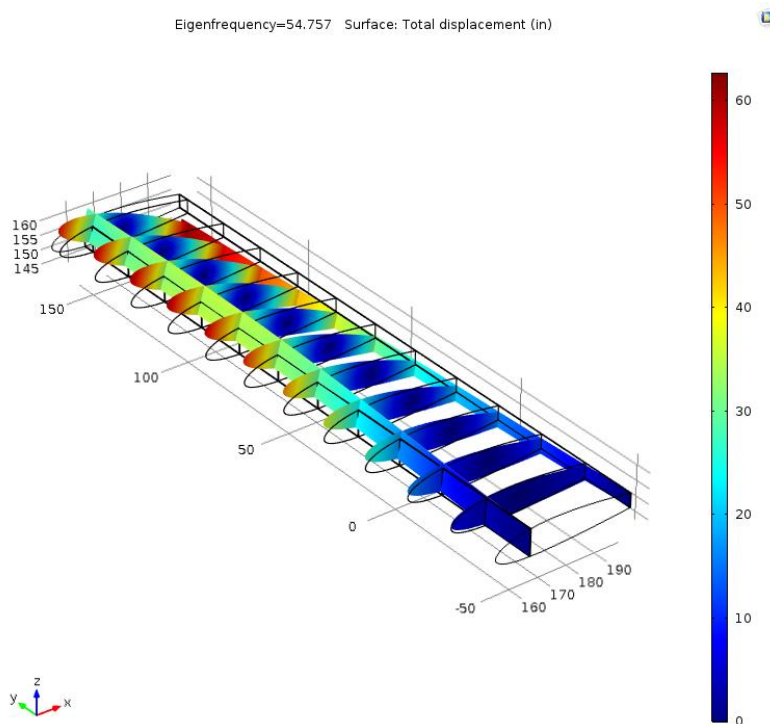


Figure 46: Fourth mode at an Eigenfrequency of 54.67 Hz, showing the deflection of the internal structures

Wing Divergence and Aileron Reversal Checks

A final check for wing divergence and aileron reversal was also performed on the wing. Wing divergence describes a phenomenon where increasing the lift on a wing, either with aileron deflection or higher angles of attack, causes warping that further increases the effective wing angle of attack. In turn, this also causes the lift the wing experiences to increase. This process continues until eventually the wings eventually fail. Aileron reversal occurs in a similar manner. In this case, the ailerons are deflected to increase the effective angle of attack on a wing. However, ailerons also provide additional forward pitching moment as well. At certain conditions, the forward pitching moment from aileron deflection may warp the wing and reduce the effective angle of attack. This would cause the wing to lose instead of gain lift, effectively reversing the outcome of the control input. Aileron reversals in essence decrease the controllability of an aircraft. The critical divergence and reversal velocities were both derived from a moment balance about the wing cross-section. Furthermore, the calculations were also simplified by assuming a two-dimensional case.

Divergence behavior was checked against by estimating the divergence velocity of the aircraft. This divergence velocity was then compared to the highest operational velocity of the aircraft. In the specifications, this dive velocity was defined as 1.5 times the cruise velocity of 63.9 m/s, or 95.8 m/s. As long as the divergence velocity was found to be above this value, the system would be assumed to have passed this test. The relation used to find this divergence velocity, shown in Eq. (45), was simplified from a moment balance about the flexural center of the wing cross-section. To get the divergence velocity, this relation was solved for the case where the angle of twist of the cross-section would approach infinity.

$$V_{div} = \sqrt{\frac{2K}{\rho Sec C_{l\alpha}}} \quad (45)$$

Here, the K term represents the torsional stiffness of the wing, which was assumed to be approximately 1E6 N*m². This value was estimated from the K derived in example 28.1 of [4]. Since the dimensions of the wing used in this report were smaller, the K value was scaled down to a similar degree as well. Additionally, the ρ and S terms describe the density and wing planform area which were discussed previously. The two dimensional lift curve slope C_{la} is also used in the equation above. Finally, the ec term represents the horizontal distance between the flexural and aerodynamic centers of the wing. These two points were assumed to be the centroid and quarter chord respectively. Furthermore, since the angles of attack on the wing were assumed to be relatively small, this ec term was assumed to be mostly constant at 0.225 m.

At both sea level and service ceiling conditions, this divergence velocity was calculated to be 260.4 m/s and 327.4 m/s respectively. With an additional 1.5 safety factor the sea level and ceiling divergence velocities reduce to 173.6 m/s and 218.3 m/s respectively. These values were still 80% to 120% larger than the given dive velocity. This indicated that divergence would not be an issue with the given parameters.

The aileron reversal speed was derived in a similar manner. A relation for the angle of twist was first isolated from the moment balance, which was then included into an equation for the change in lift from aileron deflection. The critical case here occurred when the change in lift from aileron deflection became zero, which resulted in Eq. (46).

$$V_{rev} = \sqrt{\frac{-KC_{l\varepsilon}}{0.5\rho Sc C_{M0,\varepsilon} C_{la}}} \quad (46)$$

Here, K, S, C_{la} , and ρ are the same torsional stiffness, wing planform area, lift/curve slope and density discussed for the divergence relation. Additionally, the c term here represents the total chord length of the wing, 1.5 m. The $C_{l\varepsilon}$ and $C_{M0,\varepsilon}$ terms are the two dimensional change in lift and change in pitching moment with respect to aileron deflection. The values used here were 0.8/rad and -0.25/rad. These values

were taken from example 28.3 in [4]. The reversal velocities for sea level and ceiling conditions were determined to be 180.4 m/s and 226.8 m/s respectively. With the 1.5 safety factor, the sea level and ceiling reversal velocities reduced to 120.3 m/s and 151.2 m/s respectively. Here the margins were 25% at sea level and 58% respectively. While the reversal margins are smaller than the divergence margins, the maximum dive velocity of the aircraft still falls under the critical reversal velocities. Thus, it can be seen that the derived wing structures will not experience divergence or reversal issues during standard operation.

Conclusion

The preliminary analysis of the aerodynamic generated loads on a wing that is similar to that of a Cessna 177 yielded not only the lift and drag distribution but also shear forces, moments, and wing deflection for each critical point. A direct stress calculation showed that highest stress occurs at PHAA loading at the wing root (at 124.7 MPa at the root and 28.2 MPa at mid-wing). As a result, the failure analysis was based on this critical point.

The wing was approximated as a two-cell structure with booms distributed throughout the skin contour and a shear flow analysis was conducted. High concentrations of shear flow were found at both the most forward and the most rearward portions of the root airfoil cross-section, maxing at 36 MPa at the front and 25 MPa at the rearward section. At the half-wing cross-section, the highest concentration of shear stress also occurred at the front and back sections, at 16 MPa and 11 MPa respectively.

Buckling analysis allowed for the determination of rib spacing that would prevent buckling. From a wing made of aluminum 2024-T3, the rib spacing was determined to be 0.3636 m with a safety factor of 1.5 for sea level PHAA conditions. Since the wing is under maximum loading at this critical point, such a rib spacing is expected to prevent buckling throughout the design flight envelope.

A preliminary skin buckling analysis showed that the initial skin panel dimensions would lead to skin buckling in the frontal area of the wing. Fatigue and crack analysis found a critical crack length of 0.01635 m at sea level PHAA. The cycle to failure was found to be about 5290 cycles. The results were an order of magnitude lower than the desired value, indicating the need for design changes.

Several steps were taken in the optimization process to rectify this failure. First, stringer areas were increased. The increase of stringer area to 70 mm² led to an increase in the moments of inertia of the cross-section, which in turn reduced the critical load for the direct stress. Additional stringers in the

top and frontal portion of the cross section was added to accommodate higher compressive stress. The reduced stresses from an increased stringer area led to an increase of rib spacing from 0.36 m to 0.48 m. An increase in skin thickness from 2 mm to 2.2 mm also helped increasing the total area moments of inertia thus decreasing the direct stress experienced by the skin and helped prevent buckling at PHAA. The increase of skin thickness led to an increase in total wing weight, yet changes made in stringer and cap areas helped reducing the need to increase skin thickness. These changes lowered the maximum compressive stress from 124.7 MPa to 105 MPa. The cycles to failure was also increased from 5290 cycles to 12200 cycles, satisfying the design requirements. Moreover, the mass of the wing half span was kept at 149kg.

Using the new design parameters, a CAD model was generated using SolidWorks and a finite element analysis was conducted using COMSOL Multiphysics to determine the stresses and deflection of the wing at the sea level critical point at PHAA. Because of mesh problems, the CAD model did not include the stringers, which were an integral part in the calculations of stresses and failure using Matlab. The finite element analysis showed maximum stresses concentrated at the root, at about 400 MPa and the maximum deflection was determined to be 0.10m. These values are of the same order of magnitude with the calculations done by Matlab. The lack of stringers could be responsible for the difference in stress values between the COMSOL Multiphysics finite element analysis and the analysis done by Matlab. Modal analysis allowed for the determination of wing behavior at various eigenfrequencies. Four modes were found by COMSOL Multiphysics at the eigenfrequencies of 8.08 Hz, 32.58 Hz, 44.00 Hz, and 54.76 Hz. Under low eigenfrequencies of 8.08 Hz and 32.58 Hz, the wing deflected at the tip at a maximum of 90 inches. At the third mode with an eigenfrequency of 44.00 Hz, the wing began to behave like a string, with maximum positive displacement occurring in the middle of the wing and maximum negative displacement occurring at the tip. In the fourth mode with an eigenfrequency of 54.76 Hz, the wing began to twist about

the y-axis. These deformations would mostly like lead to structural failure and as such, the frequencies at which these deformations occur are to be avoided.

Wing divergence and aileron reversal analysis were also performed. Using the several constant assumptions from Megson [4], the divergence velocity of the wing was calculated to be 260.4 m/s and 327.4 m/s at sea level and service ceiling conditions. Adjusting these values with a safety factor of 1.4, the divergence values were reduced to 173.6 m/s and 218.3 m/s at sea level and service ceiling respectively. These values are 80% to 120% larger than the given dive velocity thus divergence is not going to be an issue for the wing. Similarly, aileron reversal speeds were calculated to be 180 m/s and 226.8 m/s at sea level and service ceiling respectively. With a safety factor of 1.5, these values were reduced to 120.3 m/s and 151.2 m/s for sea level and service ceiling respectively. These indicated that maximum dive velocity of the aircraft falls under critical aileron reversal velocities and as such, the wing is not expected to experience either divergence or aileron reversal during normal operations.

Appendix A: Centroid and moments determination of a Simple Box beam

In the initial stages of the project, the wing of interested was approximated with a simplified cross section (Fig. A.1) with spars (green), brackets (black), and skin panels (blue). The component centroids were first calculated using Eq. (18a) and Eq. (18b), and finally, using the same equations, the overall centroid was obtained. The airfoil approximation dimensions and its centroid are provided in Table 12.

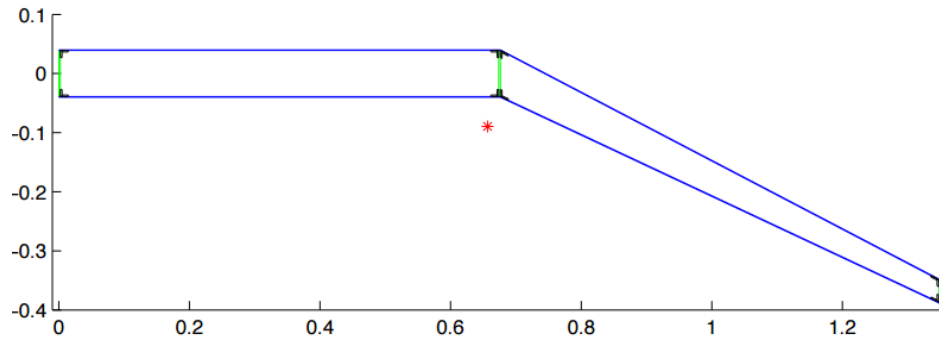


Figure A.1: Simplified cantilever beam model. Centroid location is marked by the red asterisk. Blue lines represent the skin while green lines are the spars and black components are the brackets in the simplified model.

In the cantilever beam approximation, the trailing edge is slanted at an angle. As a result, Eq. (21) do not apply. A new set of equations are used in determination of the moments of inertia at the trailing edge and are as follows

$$I_{xx} = \frac{a^3 t \sin^2 \beta}{12} + Ay^2 \quad (47)$$

$$I_{yy} = \frac{a^3 t \cos^2 \beta}{12} + Ax^2 \quad (48)$$

$$I_{xy} = \frac{a^3 t \sin^2 \beta}{12} + Axy \quad (49)$$

where a is the length over which the moment of inertia is calculated, t is the thickness of the component, and β is the angle at which the body is slanted with respect to the horizontal x axis. Since Eq. (47) through

Eq. (49) calculate the moment of inertia of each component with respect to a common centroid of the entire cantilever beam, the overall moment of inertia of the beam is simply the summation of all the moments of inertia of the components.

Table 12 through Table 14 show the calculation of moments of inertia of the individual components as well as total moments of inertia of the beam approximation in Table 15. With the total moments of inertia, shear forces, bending moments and wing deflections can be calculated as functions of distance along the span of the wing.

Table 12: Dimensions of the simplified cantilever beam model

Location of Spar					
x1	0	m			
x2	0.75	m			
x3	1.5	m			
Chord Length	1.5	m			
Component Thickness			Component Height		
t_spar	0.0025	m	h_section	0.08	m
t_bracket	0.0025	m	h_spar	0.077968	m
t_skin	0.001016	m	h_bracket	0.012	m
Theta	30	deg			
Alpha	10	deg			
Area			Skin Lengths		
A_spar	0.0002	m ²	L1	0.5	m
A_skin1	0.000762	m ²	L2	0.8660254038	m
A_skin2	0.0008799	m ²			
A_bracket	0.00003	m ²			

Table 13: Centroid calculations for the simplified cantilever beam model. X and y coordinates of the beam model are highlighted.

Centroid Calculations					
Cx_spar1	0	m	Cy_spar1	0	m
Cx_spar2	0.75	m	Cy_spar2	0	m
Cx_spar3	1.5	m	Cy_spar3	-0.4330127019	m
Cx_skin1top	0.375	m	Cy_skin1top	0.04	m
Cx_skin1bot	0.375	m	Cy_skin1bot	-0.04	m
Cx_skin2top	1.125	m	Cy_skin2top	-0.1765063509	m
Cx_skin2bot	1.125	m	Cy_skin2bot	-0.2565063509	m
Cx_b1top	0.00125	m	Cy_b1top	0.04	m
Cx_b1bot	0.00125	m	Cy_b1bot	-0.04	m
Cx_b2top	0.74875	m	Cy_b2top	0.04	m
Cx_b2bot	0.74875	m	Cy_b2bot	-0.04	m
Cx_b3top	0.75125	m	Cy_b3top	0.04	m
Cx_b3bot	0.75125	m	Cy_b3bot	-0.04	m
Cx_b4top	1.49875	m	Cy_b4top	-0.3930127019	m
Cx_b4bot	1.49875	m	Cy_b4bot	-0.4730127019	m
Cx	0.7714394824	m			
Cy	-0.1196924334	m			

Table 14: Moment of inertia calculations for spars

Spars		
lxx_spar1	0.000002971922389	m ⁴
lyy_spar1	0.0001190238792	m ⁴
lxy_spar1	-0.00001846709377	m ⁴
lxx_spar2	0.000002971922389	m ⁴
lyy_spar2	0.00000009203444803	m ⁴
lxy_spar2	-0.0000005132287645	m ⁴
lxx_spar3	0.0000197405848	m ⁴
lyy_spar3	0.0001061601897	m ⁴
lxy_spar3	-0.0000456545554	m ⁴

Table 15: Moment of Inertia calculations for brackets.

Brackets					
lxx_b1top	0.0000007650501985	m^4	lxx_b1bot	0.0000001905265182	m^4
lyy_b1top	0.00001779575517	m^4	lyy_b1bot	0.00001779575517	m^4
lxy_b1top	-0.000003689802979	m^4	lxy_b1bot	-0.000001841348221	m^4
lxx_b2top	0.0000007650501985	m^4	lxx_b2bot	0.0000001905265182	m^4
lyy_b2top	0.00000001544437839	m^4	lyy_b2bot	0.00000001544437839	m^4
lxy_b2top	-0.0000001087001598	m^4	lxy_b2bot	-0.00000005424540202	m^4
lxx_b3top	0.0000007650501985	m^4	lxx_b3bot	0.0000001905265182	m^4
lyy_b3top	0.00000001222845602	m^4	lyy_b3bot	0.00000001222845602	m^4
lxy_b3top	-0.00000009672322734	m^4	lxy_b3bot	-0.00000004826846951	m^4
lxx_b4top	0.000002241119075	m^4	lxx_b4bot	0.000003745056364	m^4
lyy_b4top	0.00001586941767	m^4	lyy_b4bot	0.00001586941767	m^4
lxy_b4top	-0.000005963661178	m^4	lxy_b4bot	-0.00000770920642	m^4

Table 16: Moment of inertia calculations for skins. Total moments of inertia of the cantilever beam model are highlighted.

Skins					
lxx_skin1top	0.00001943234059	m4	lxx_skin1bot	0.000004839439111	m4
lyy_skin1top	0.0001554779186	m4	lyy_skin1bot	0.0001554779186	m4
lxy_skin1top	-0.00004824098986	m4	lxy_skin1bot	-0.00002407403901	m4
lxx_skin2top	0.00001658825447	m4	lxx_skin2bot	0.00003021782327	m4
lyy_skin2top	0.0001512341204	m4	lyy_skin2bot	0.0001512341204	m4
lxy_skin2top	-0.00004148682503	m4	lxy_skin2bot	-0.00006637414248	m4
lxx	0.0001056151926	m4			
lyy	0.0009060858726	m4			
lxy	-0.0002643228304	m4			

Appendix B: Shear forces, Moments, and Deflections

This section presents the moment distribution, shear distribution, and deflection for operation at each critical points. Like those depicted in the Shear, Moment, and Deflection section, these distributions are calculated through the use of Eq. (27), Eq. (28), and Eq. (29) using different input parameters from various critical points.

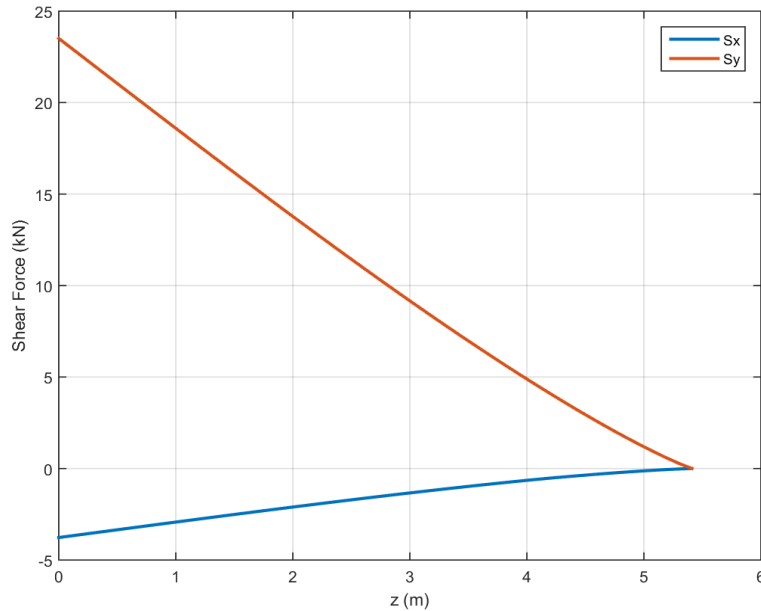


Figure B.1: Shear distribution of the wing at sea level (PHAA).

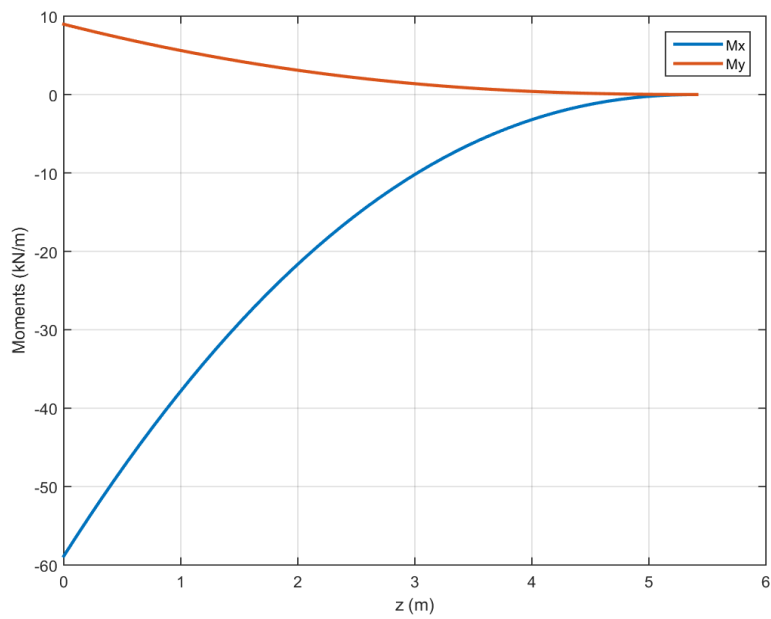


Figure B.2: Moment distribution of the wing at sea level (PHAA).

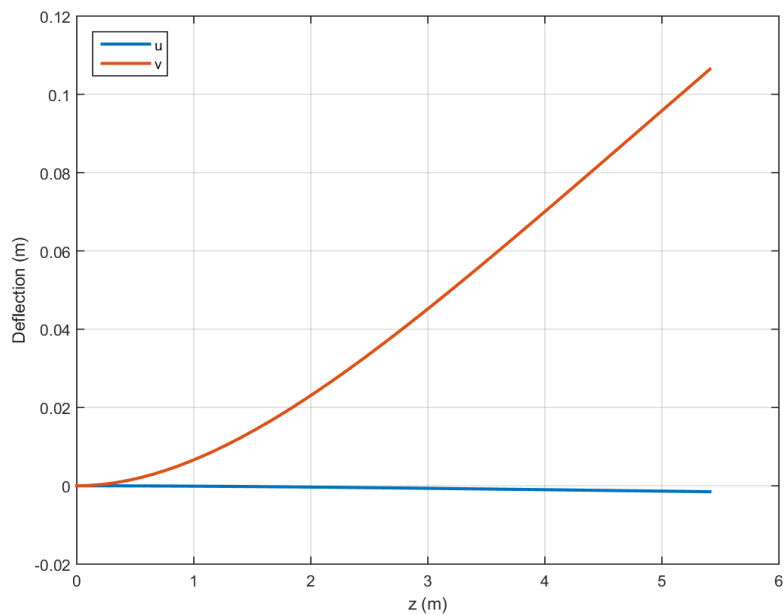


Figure B.3: Wing deflection at sea level (PHAA).

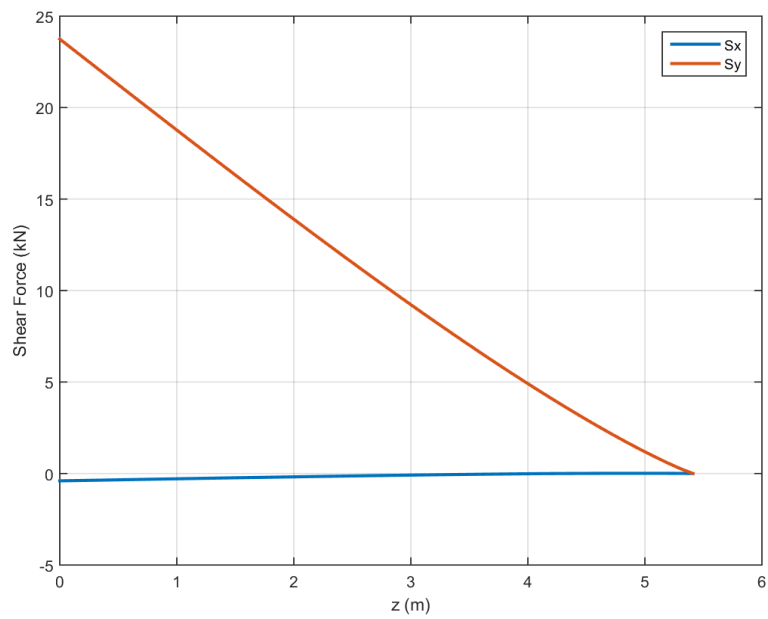


Figure B.4: Shear distribution of the wing at sea level (PLAA).

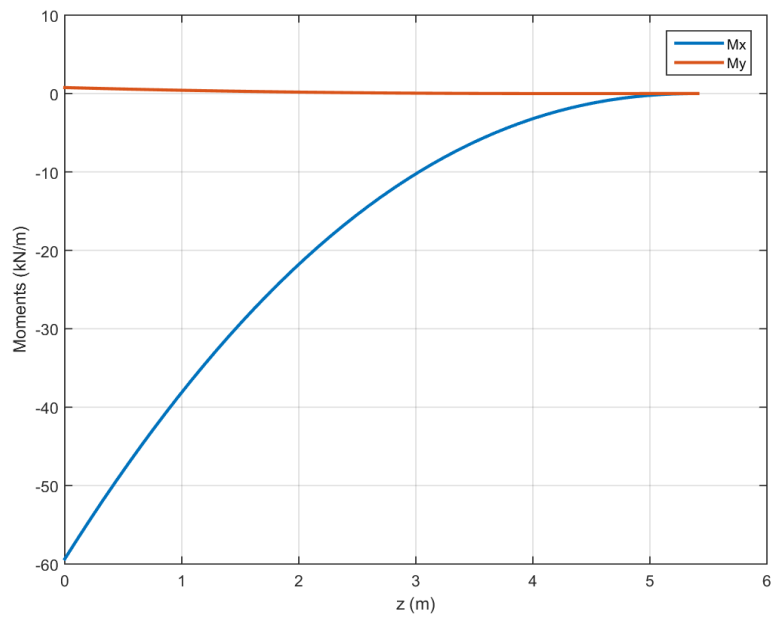


Figure B.5: Moment distribution of the wing at sea level (PLAA).

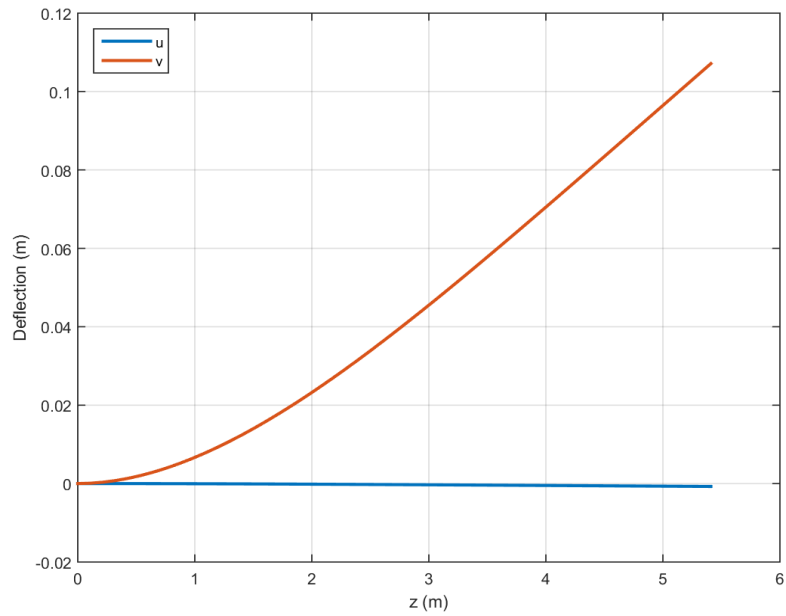


Figure B.6: Wing deflection at sea level (PLAA).

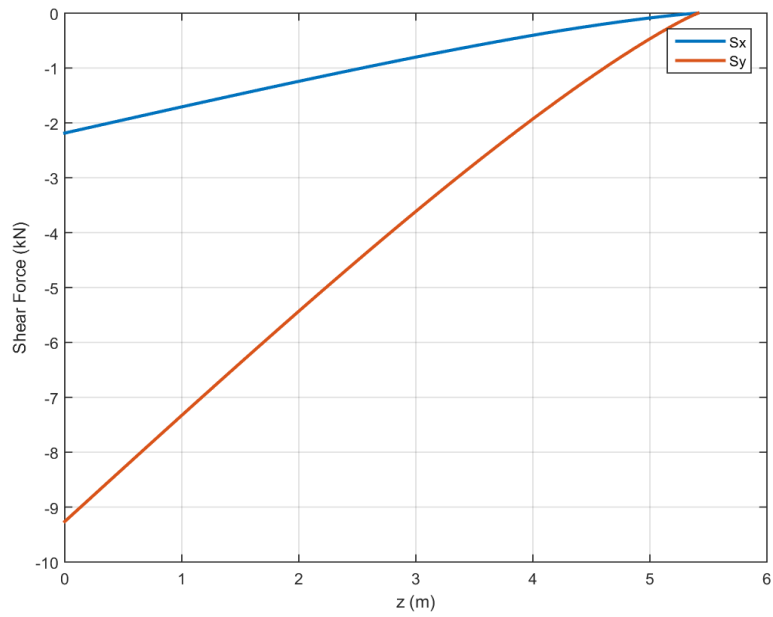


Figure B.7: Shear distribution of the wing at sea level (NHAA).

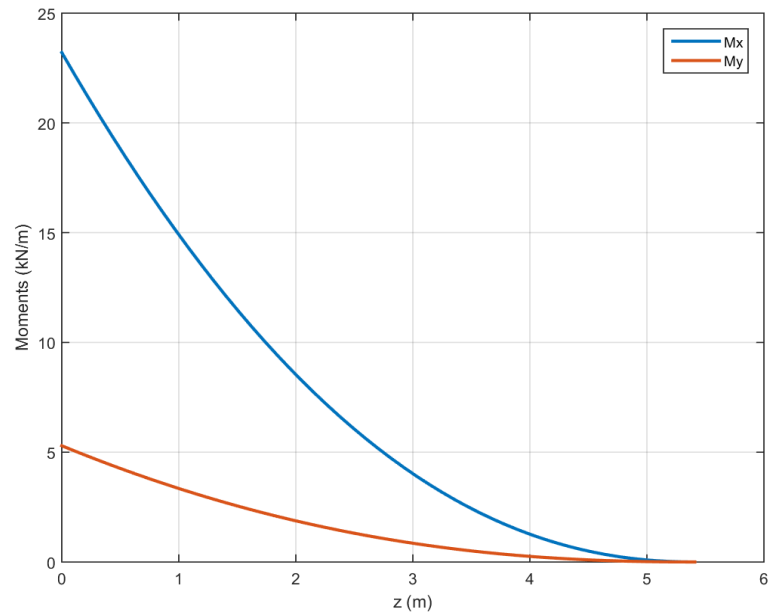


Figure B.8: Moment distribution of the wing at sea level (NHAA).

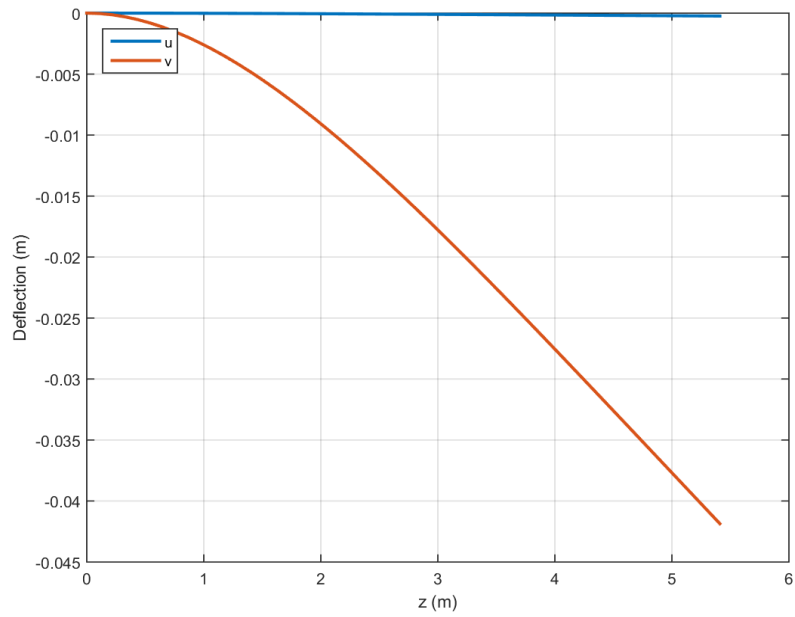


Figure B.9: Wing deflection at sea level (NHAA).

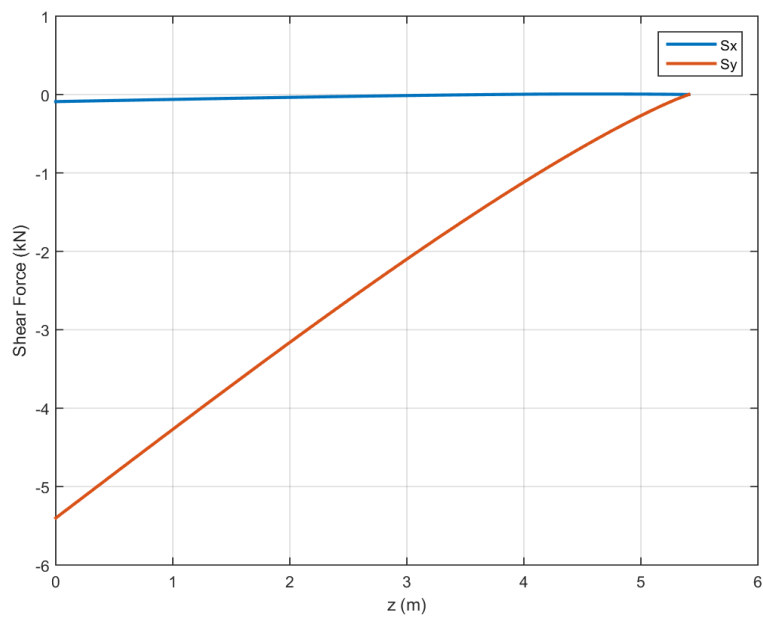


Figure B.10: Shear distribution of the wing at sea level (NLAA).

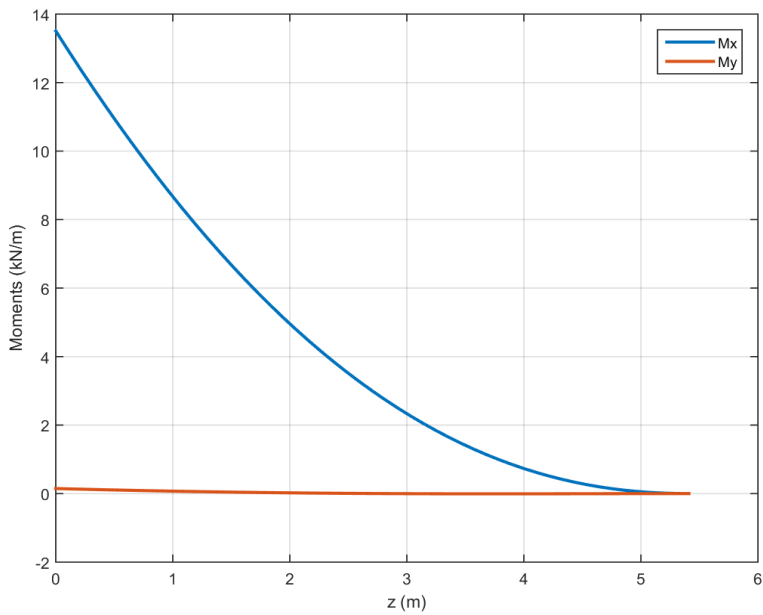


Figure B.11: Moment distribution of the wing at sea level (NLAA).

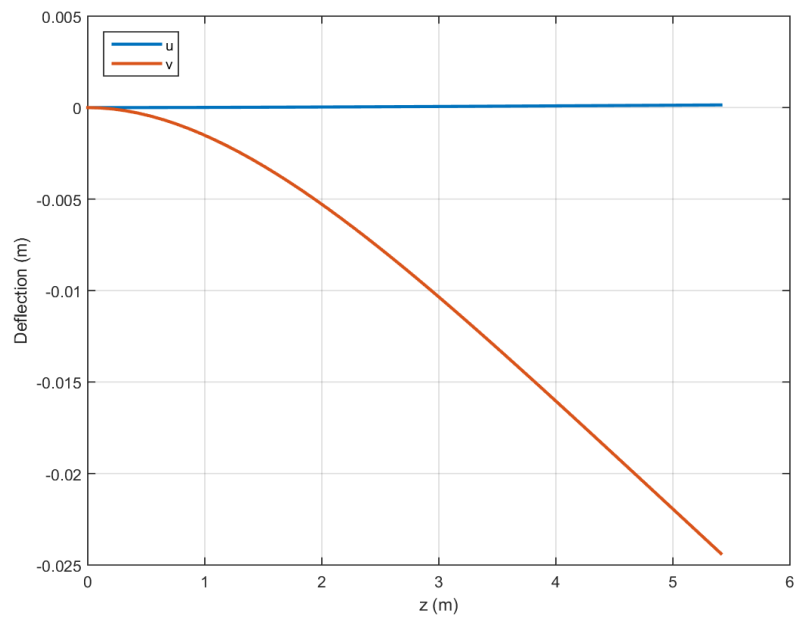


Figure B.12: Wing deflection at sea level (NLAA).

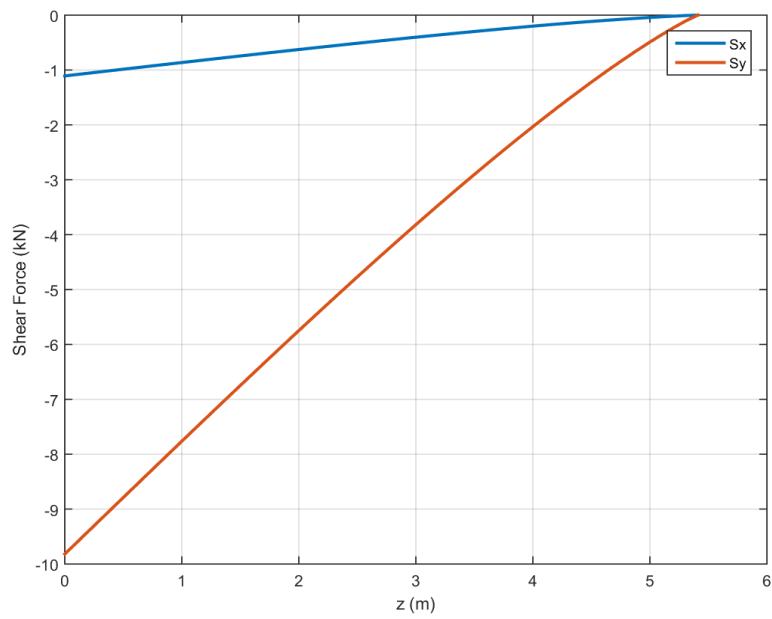


Figure B.13: Shear distribution of the wing at sea level (gust point 1).

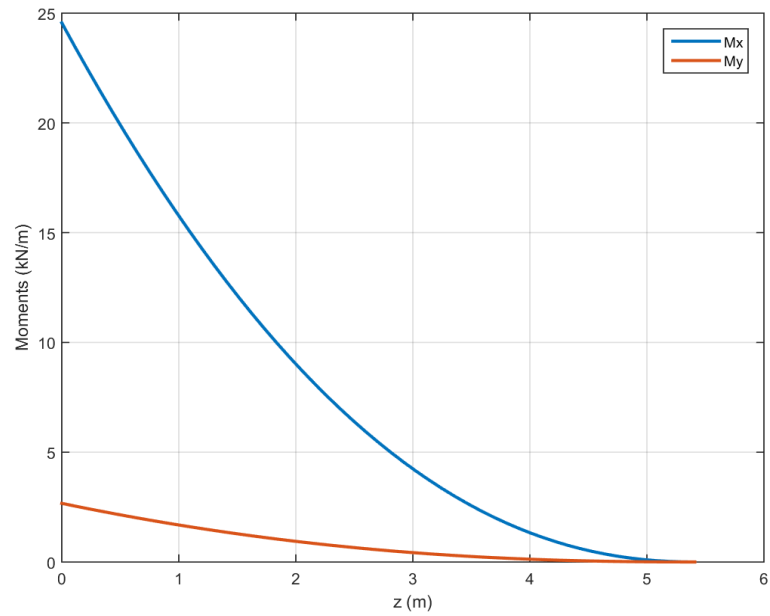


Figure B.14: Moment distribution of the wing at sea level (gust point 1).

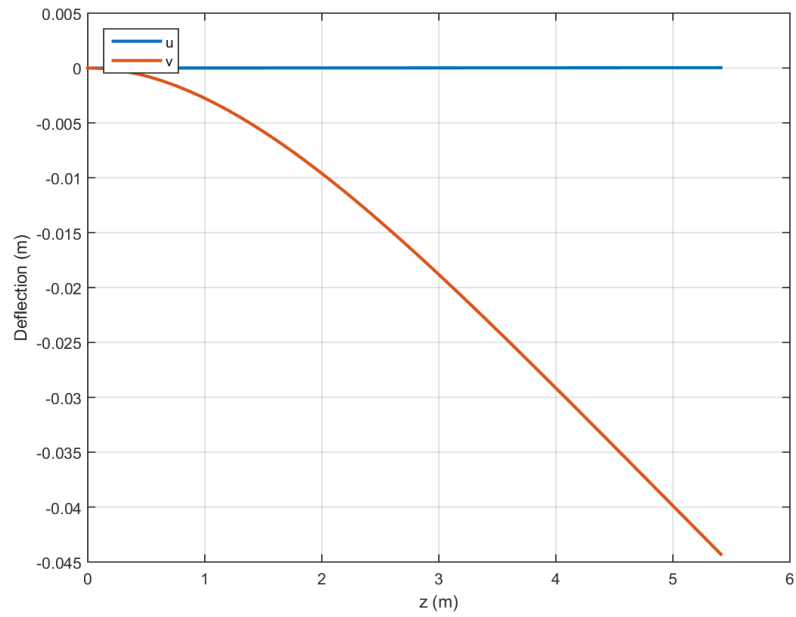


Figure B.15: Wing deflection at sea level (gust point 1).

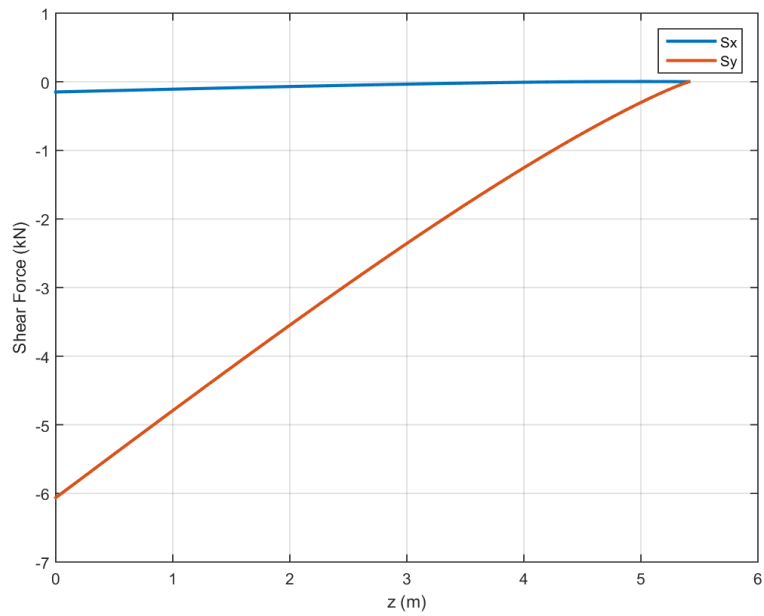


Figure B.16: Shear distribution of the wing at sea level (gust point 2).

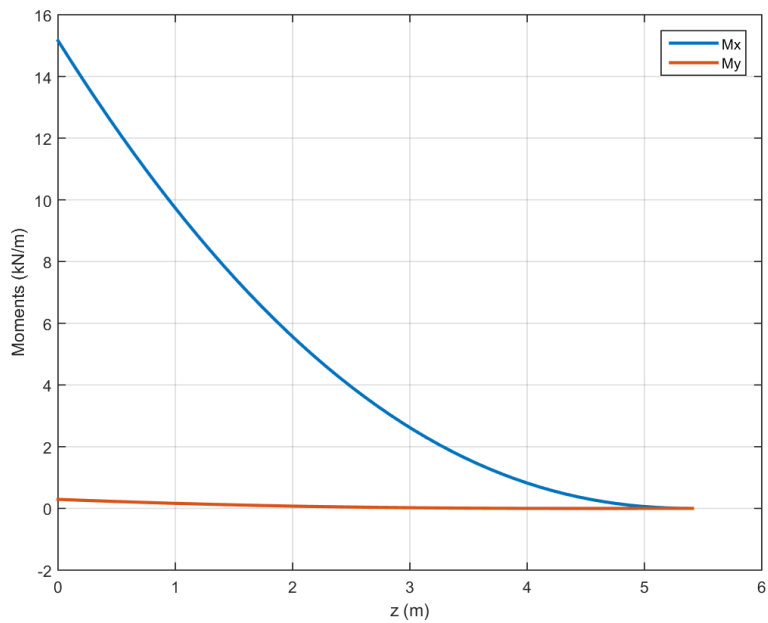


Figure B.17: Moment distribution of the wing at sea level (gust point 2).

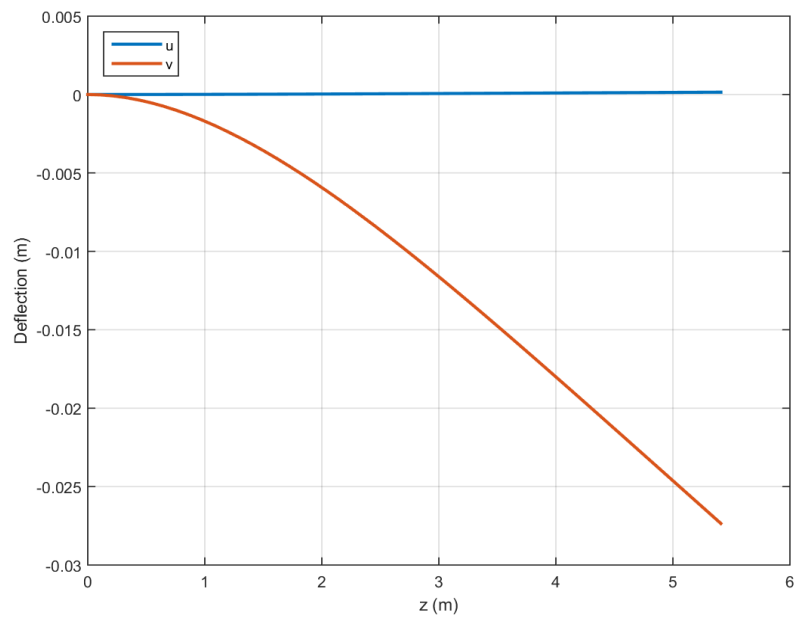


Figure B.18: Wing deflection at sea level (gust point 2).

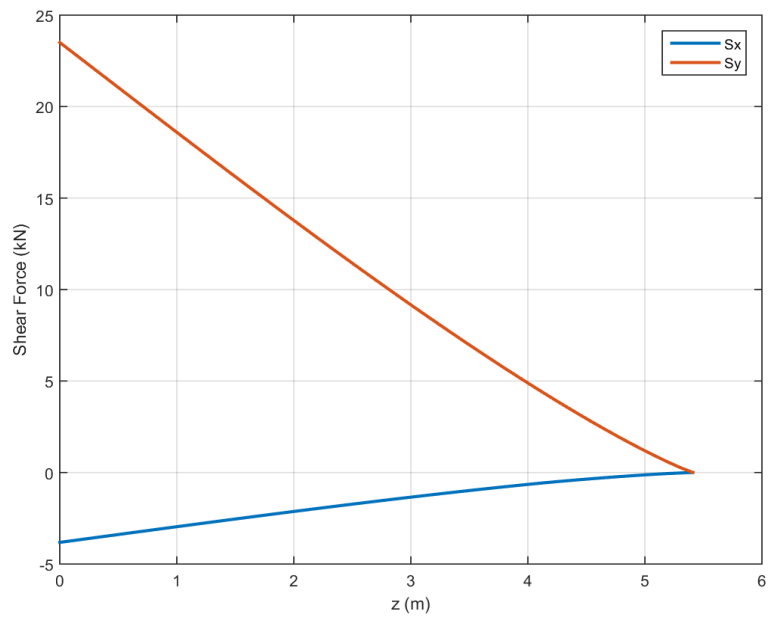


Figure B.19: Shear distribution of the wing at ceiling (PHAA).

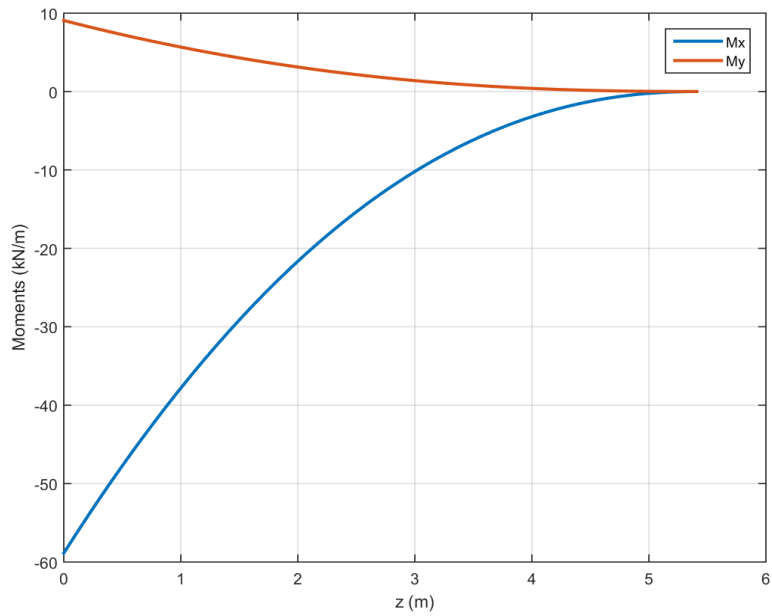


Figure B.20: Moment distribution of the wing at ceiling (PHAA).

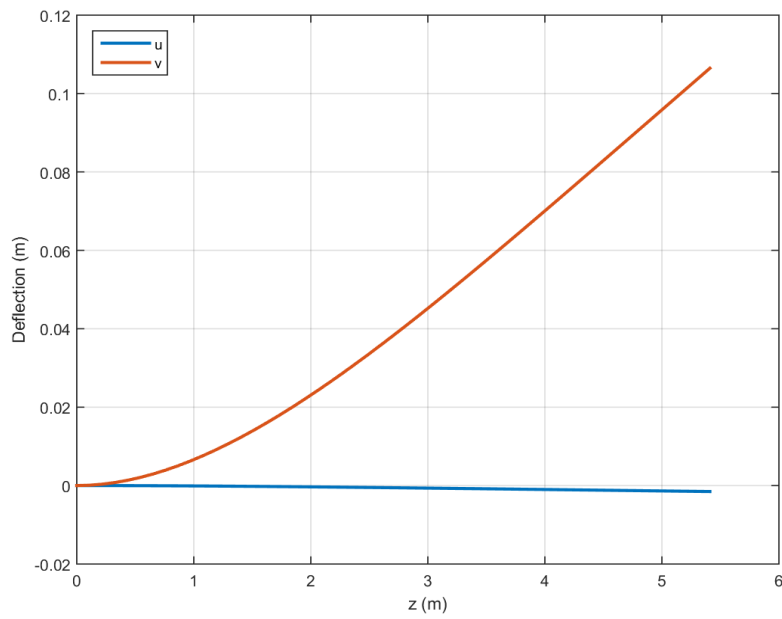


Figure B.21: Wing deflection at ceiling (PHAA).

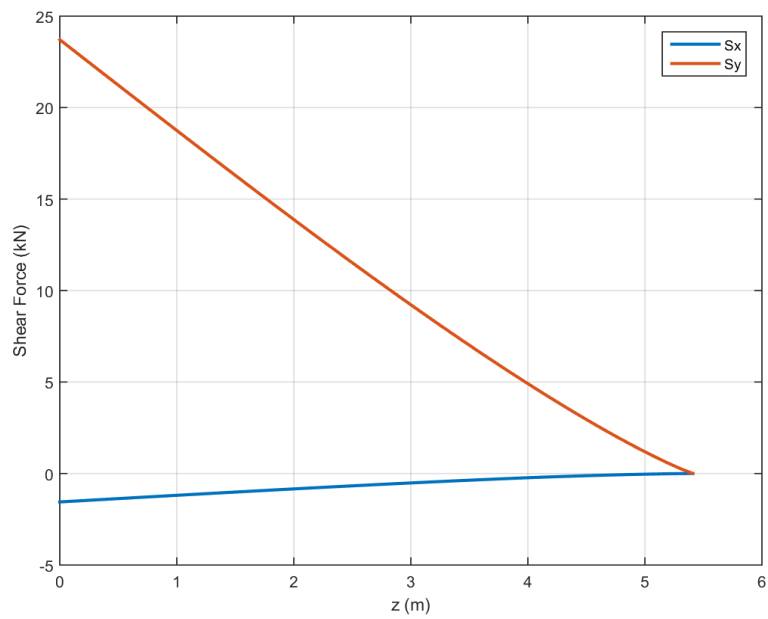


Figure B.22: Shear distribution of the wing at ceiling (PLAA).

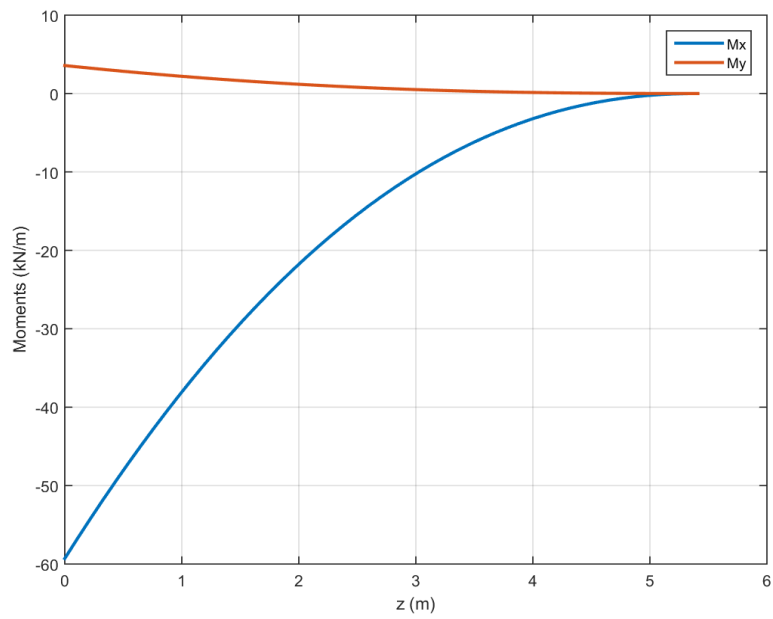


Figure B.23: Moment distribution of the wing at ceiling (PLAA).

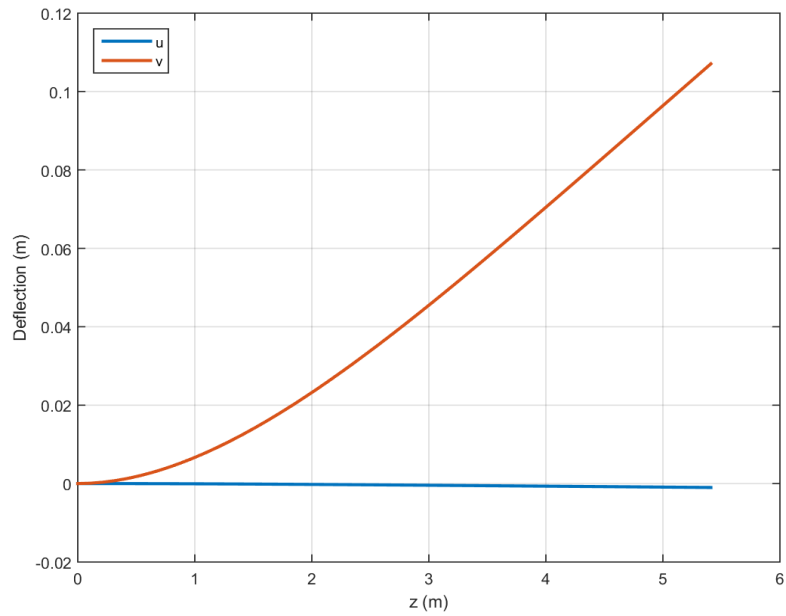


Figure B.24: Wing deflection at ceiling (PLAA).

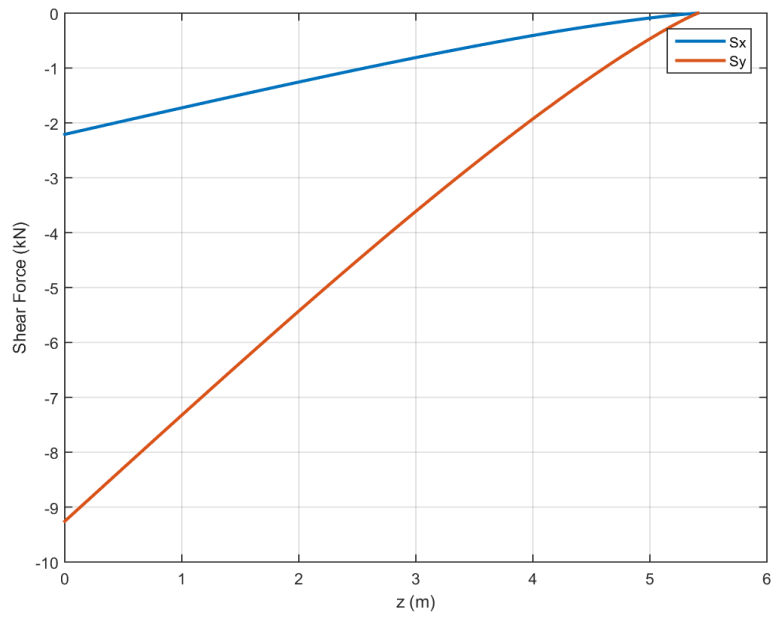


Figure B.25: Shear distribution of the wing at ceiling (NHAA).

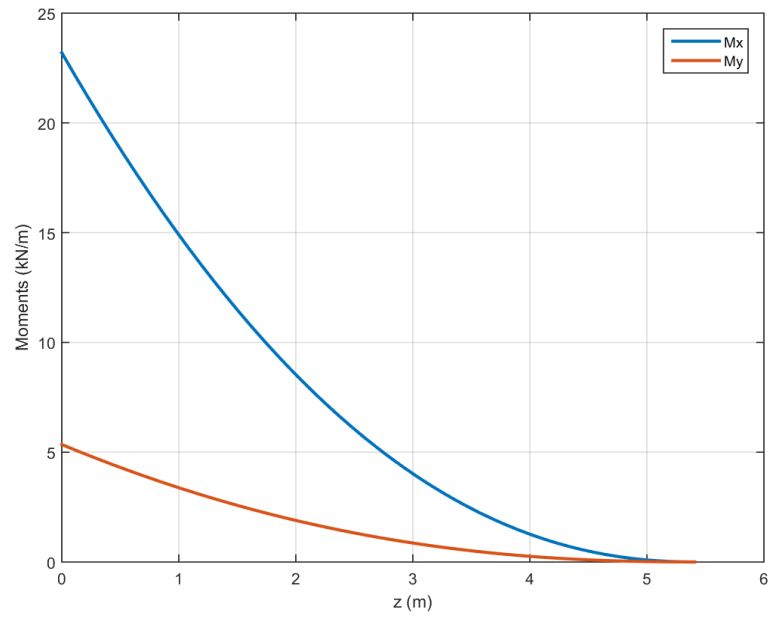


Figure B.26: Moment distribution of the wing at ceiling (NHAA).

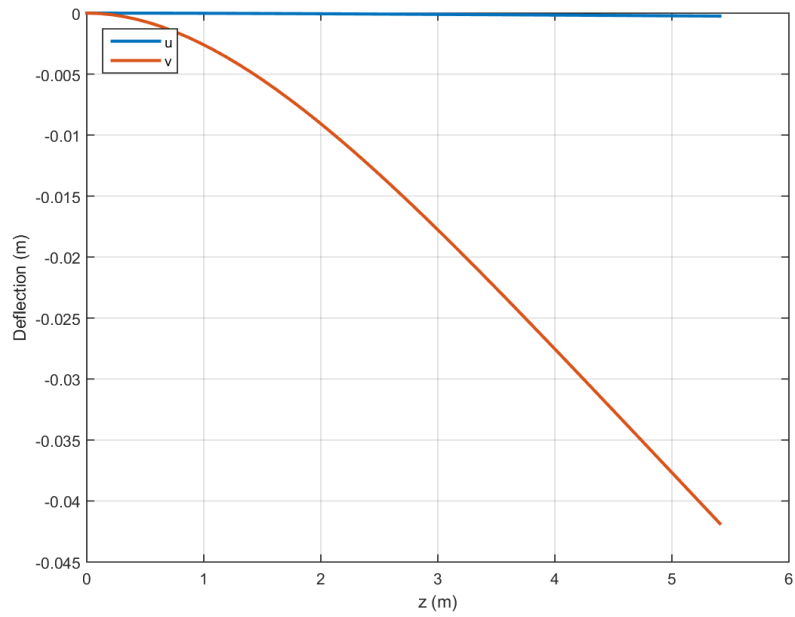


Figure B.27: Wing deflection at ceiling (NHAA).

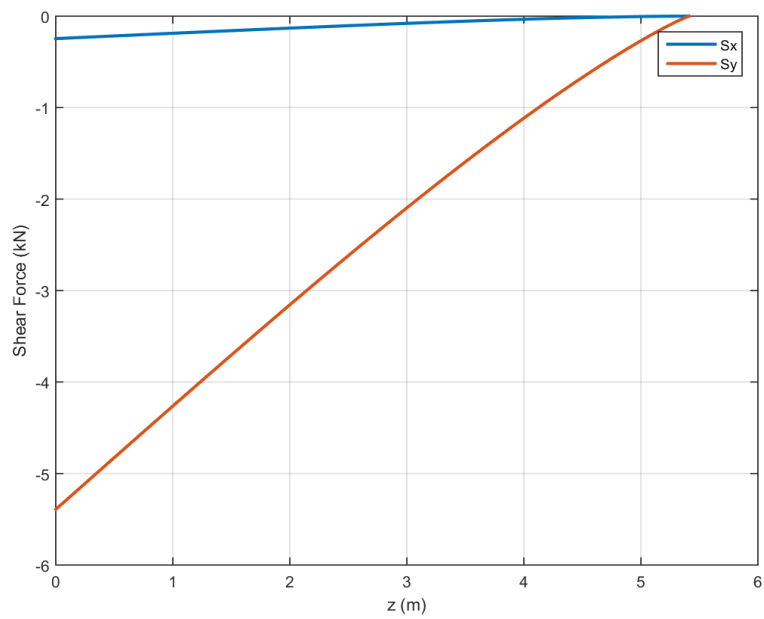


Figure B.28: Shear distribution of the wing at ceiling (NLAA).

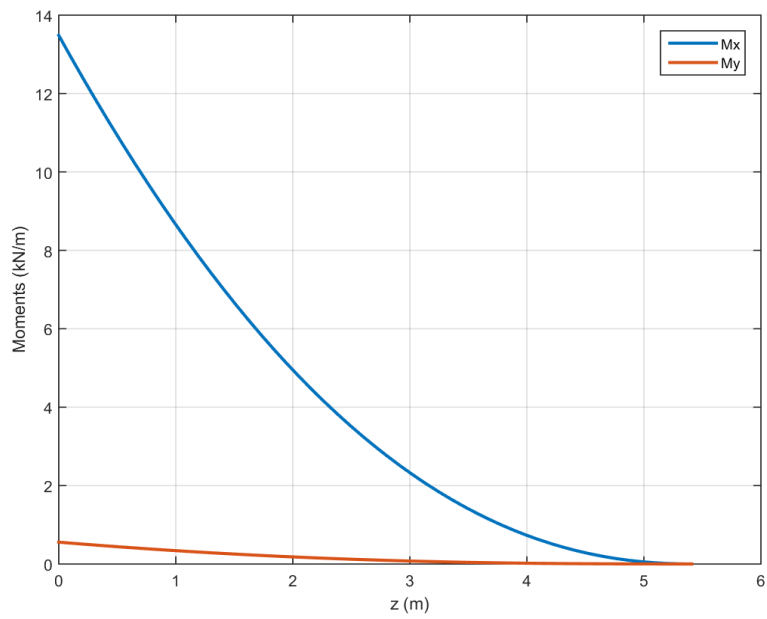


Figure B.29: Moment distribution of the wing at ceiling (NLAA).

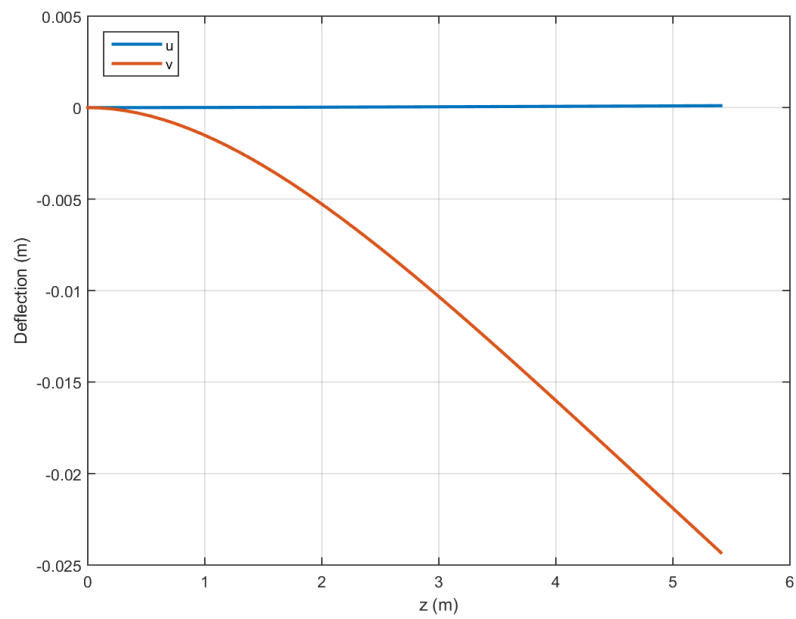


Figure B.30: Wing deflection at ceiling (NLAA).

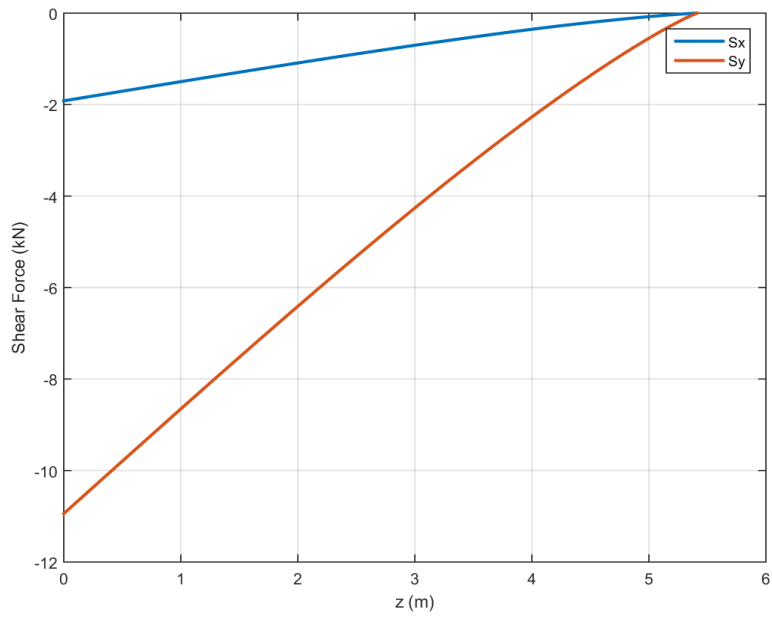


Figure B.31: Shear distribution of the wing at ceiling (gust point 1).

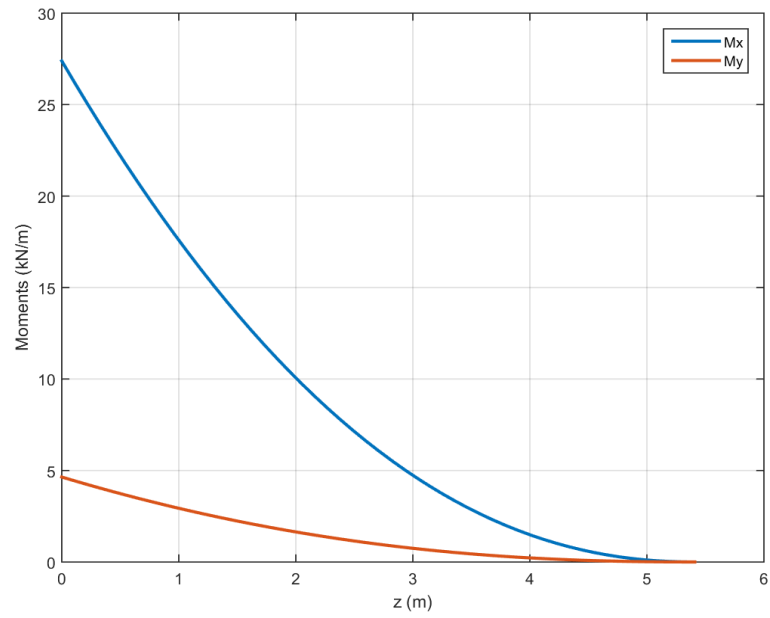


Figure B.32: Moment distribution of the wing at ceiling (gust point 1).

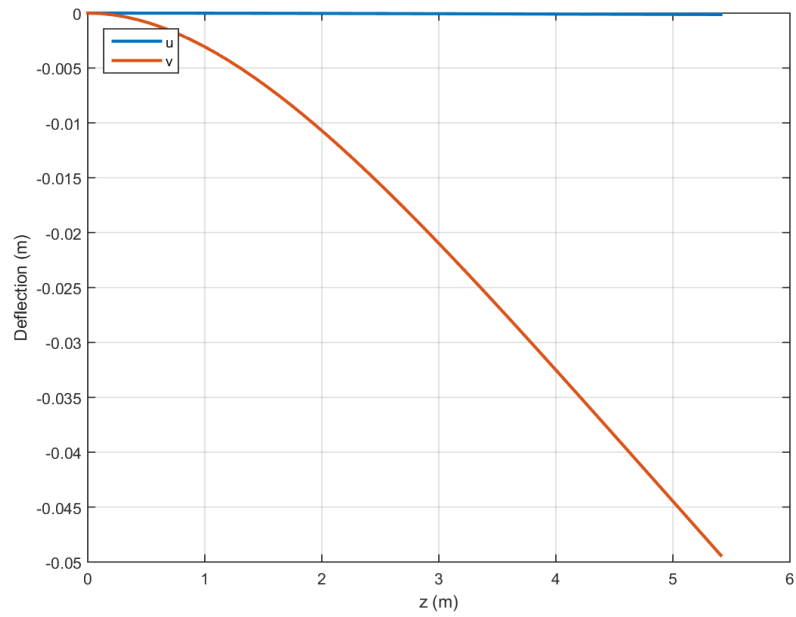


Figure B.33: Wing deflection at ceiling (gust point 1).

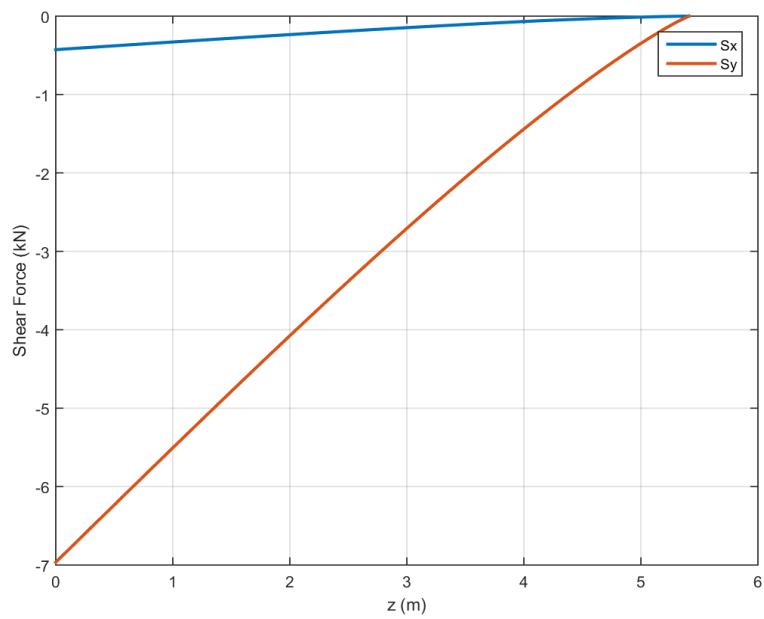


Figure B.34: Shear distribution of the wing at ceiling (gust point 2).

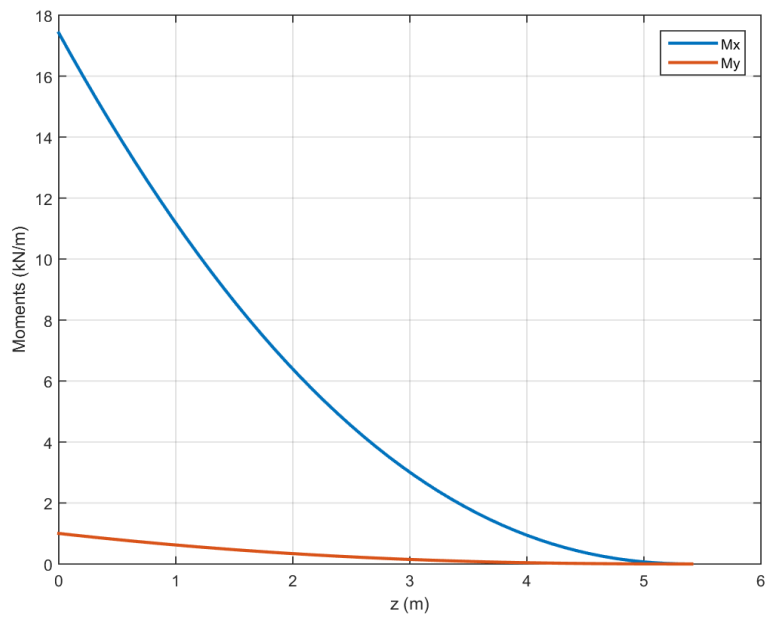


Figure B.35: Moment distribution of the wing at ceiling (gust point 2).

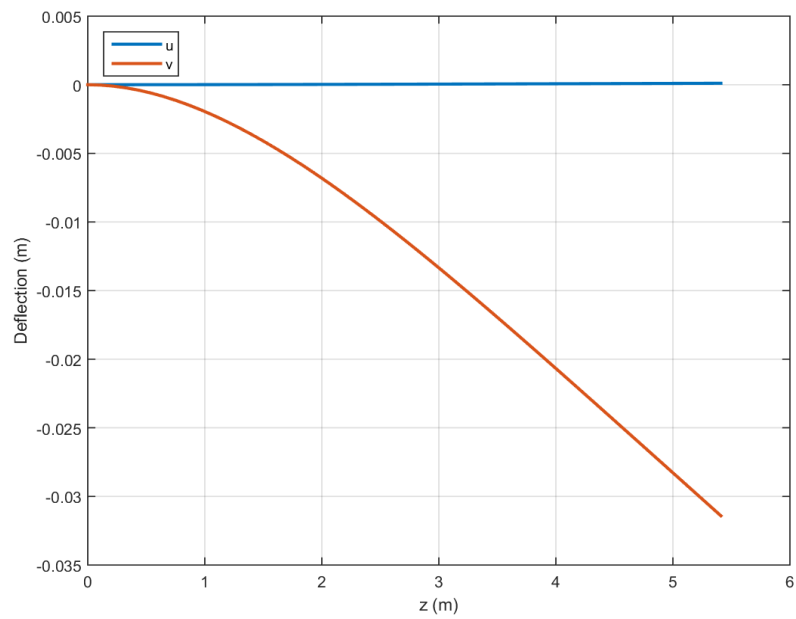


Figure B.36: Wing deflection at ceiling (gust point 2).

Appendix C: Direct Stresses

This section presents the direct stresses calculated using Eq. (25) for operation at each critical point. These direct stresses provided values used for buckling, Von Mises, and fatigue analysis. The direct stresses were separated into root and mid-wing plots in order to show how they changed along the wing span. As expected, these stresses decreased along the wing span, with the root experiencing the highest levels of direct stress.

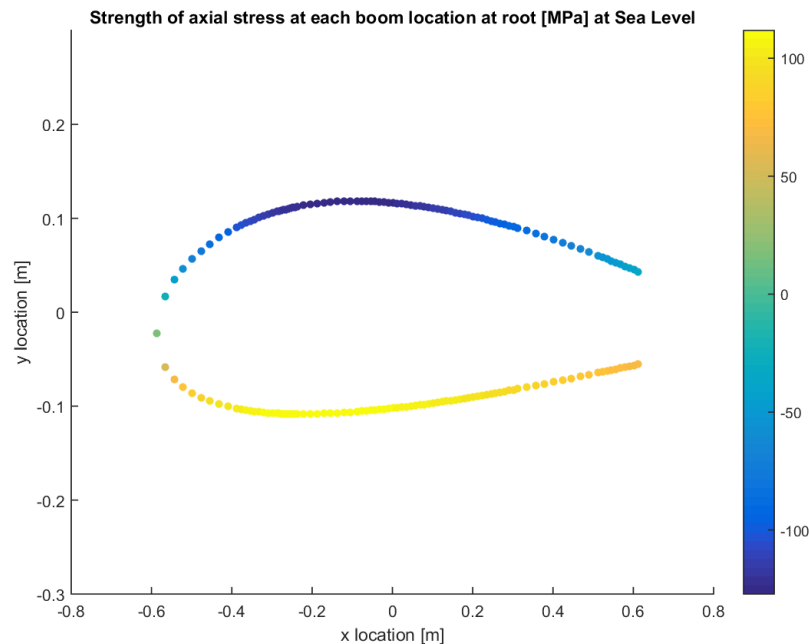


Figure C.1: Direct stress at root for sea level PHAA.

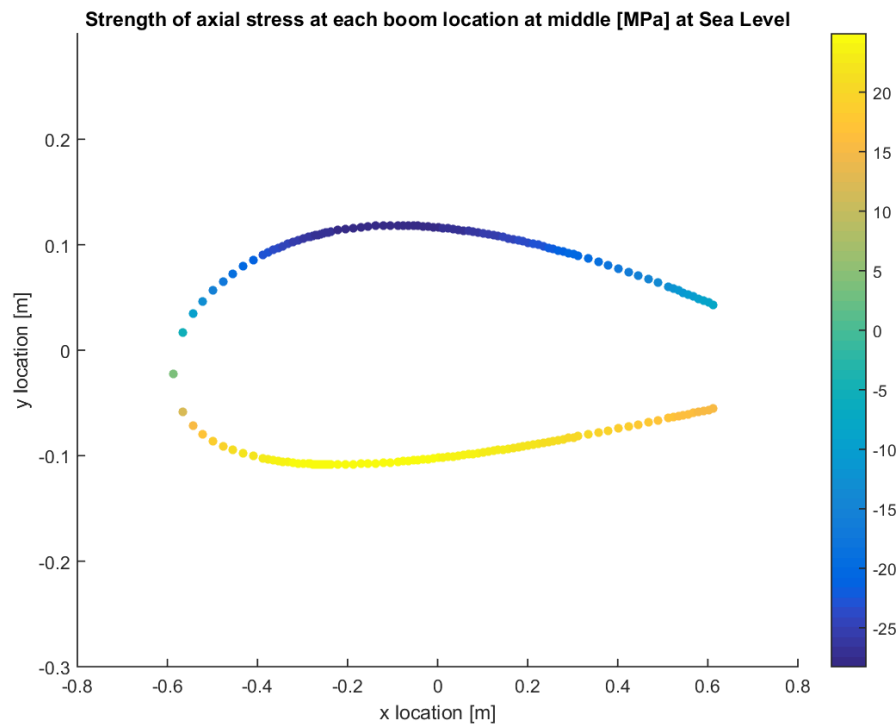


Figure C.2: Direct stress at half of semi-span (0.25b) for sea level PHAA.

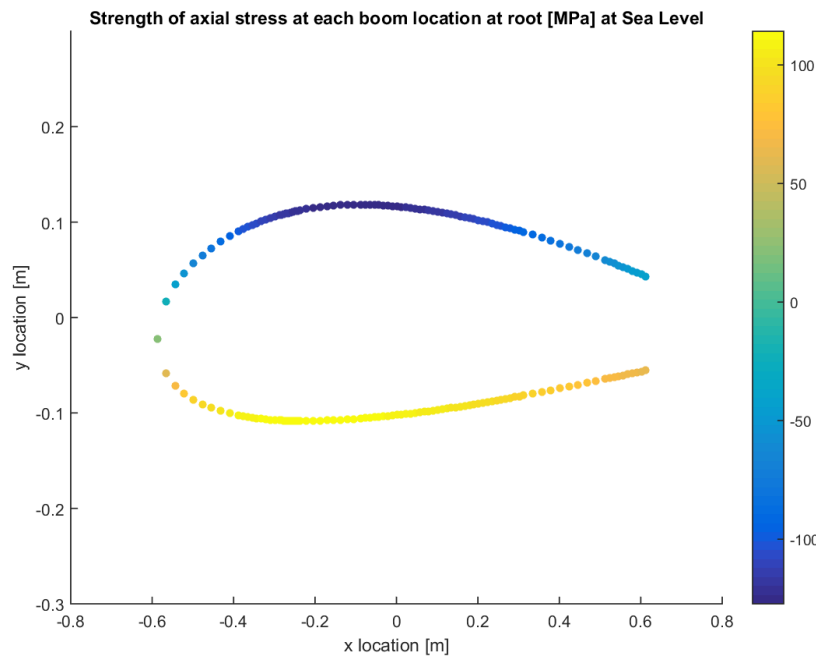


Figure C.3: Direct stress at root for sea level PLAA.

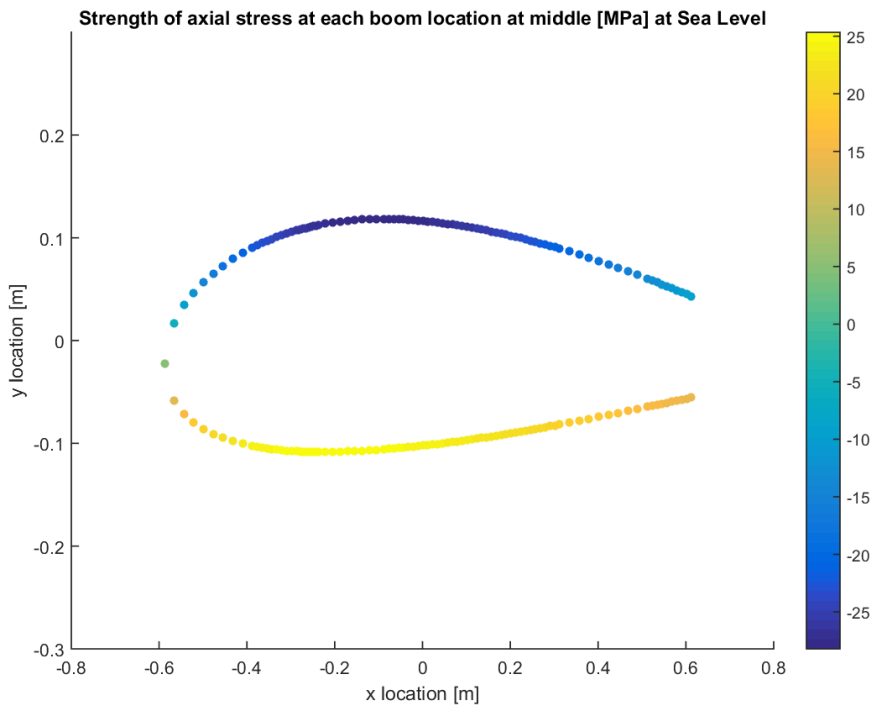


Figure C.4: Direct stress at half of semi-span (0.25b) for sea level PLAA.

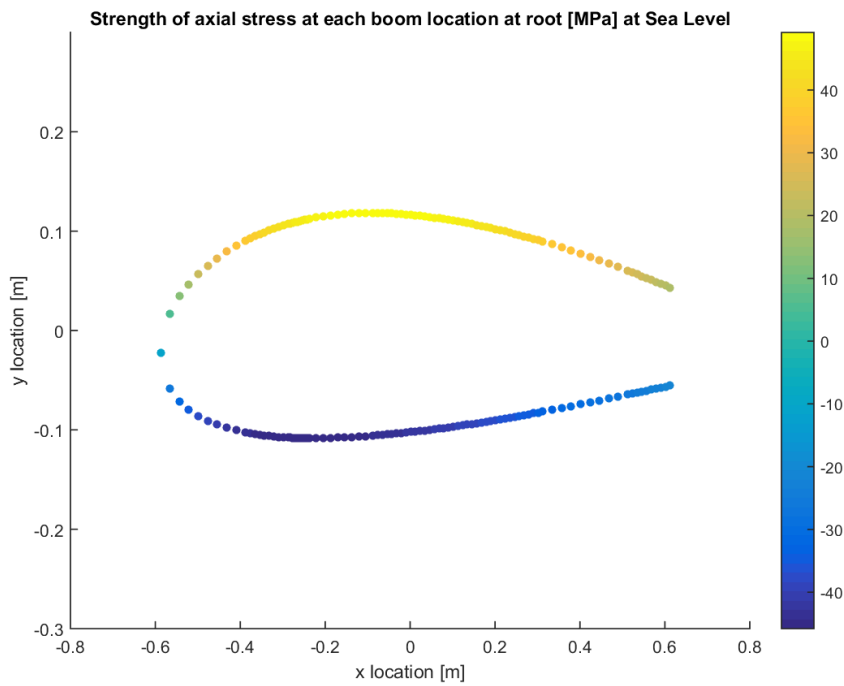


Figure C.5: Direct stress at root for sea level NHAA.

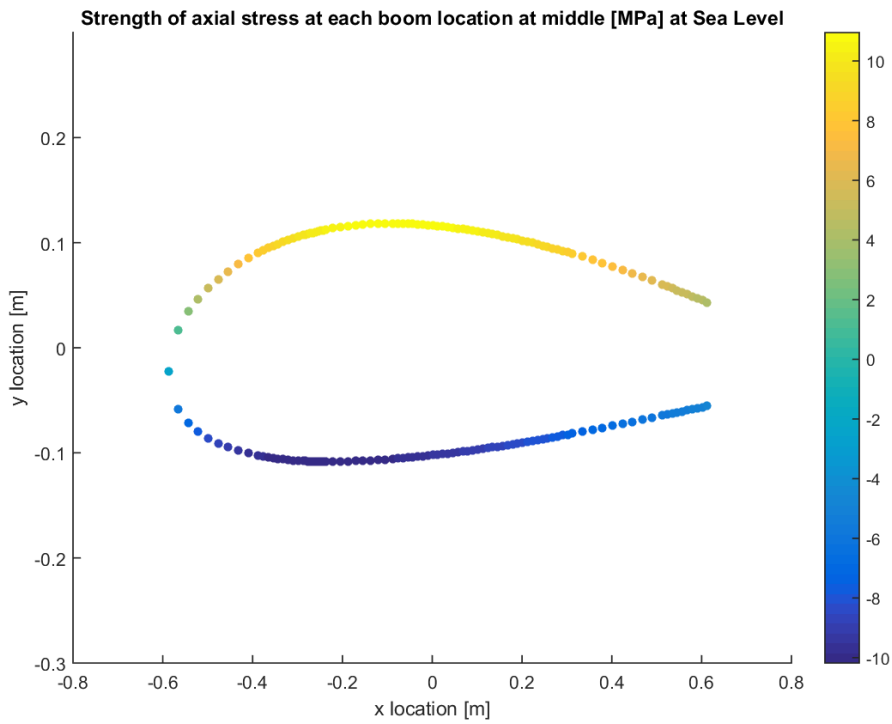


Figure C.6: Direct stress at half of semi-span (0.25b) for sea level NHAA.

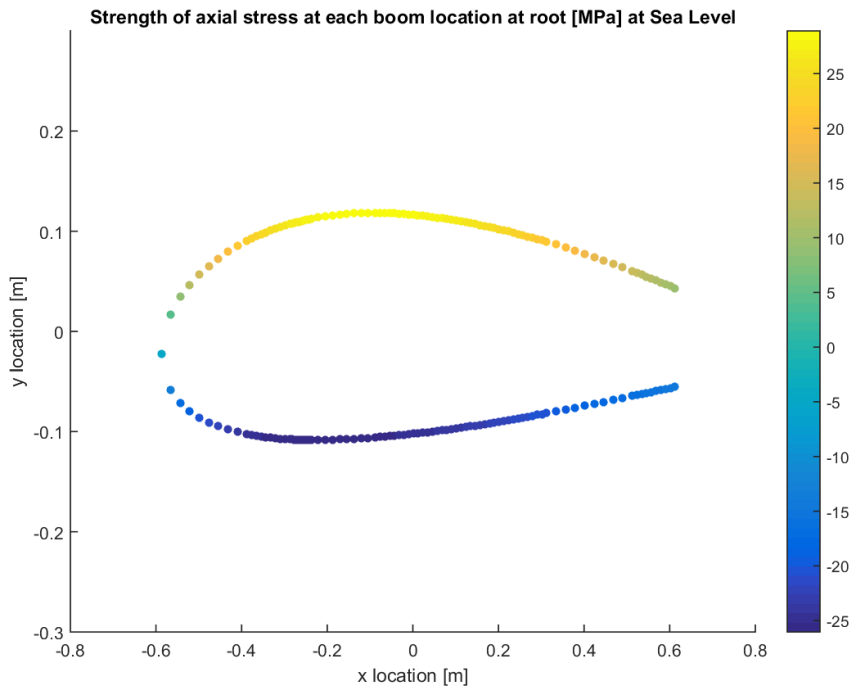


Figure C.7: Direct stress at root for sea level NLAA.

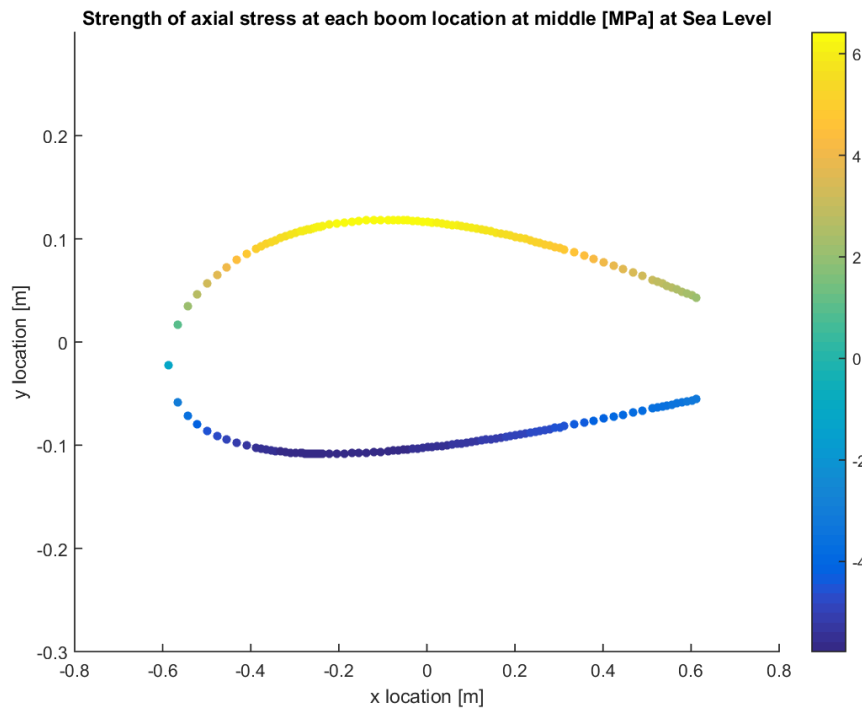


Figure C.8: Direct stress at half of semi-span (0.25b) for sea level NLAA.

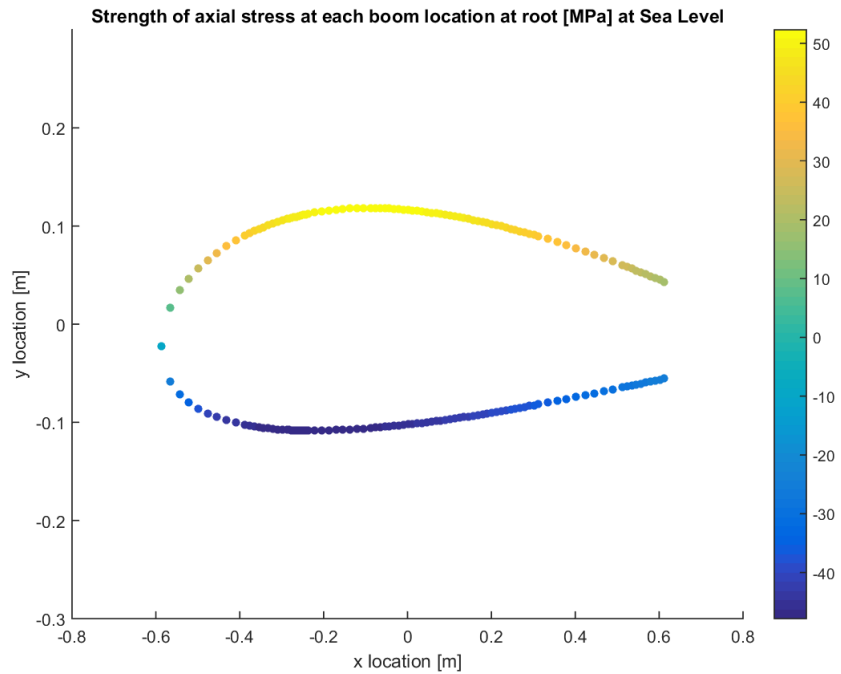


Figure C.9: Direct stress at root for sea level gust point 1.

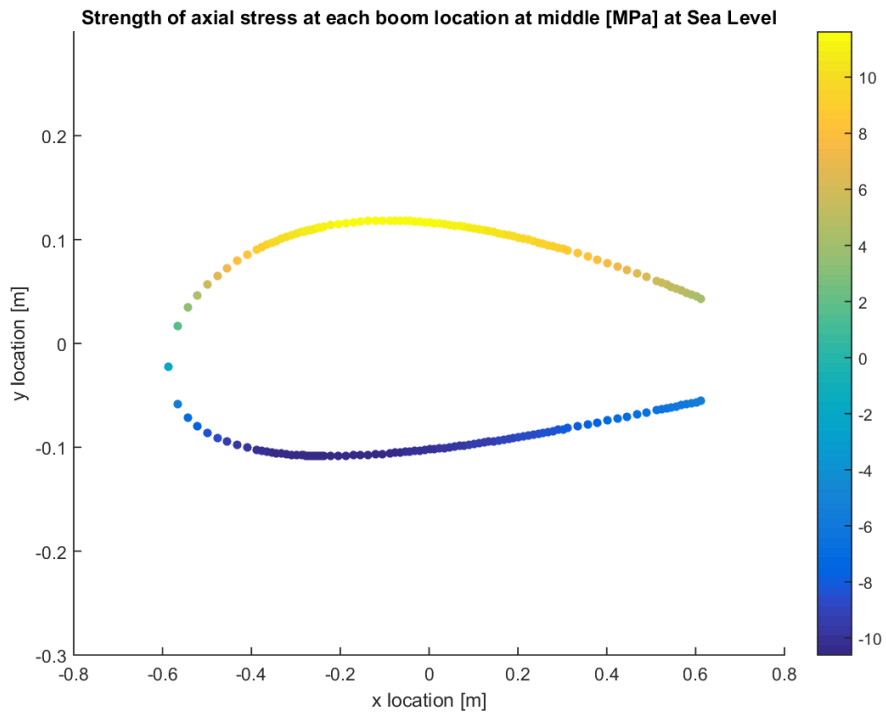


Figure C.10: Direct stress at half of semi-span (0.25b) for sea level gust point 1.

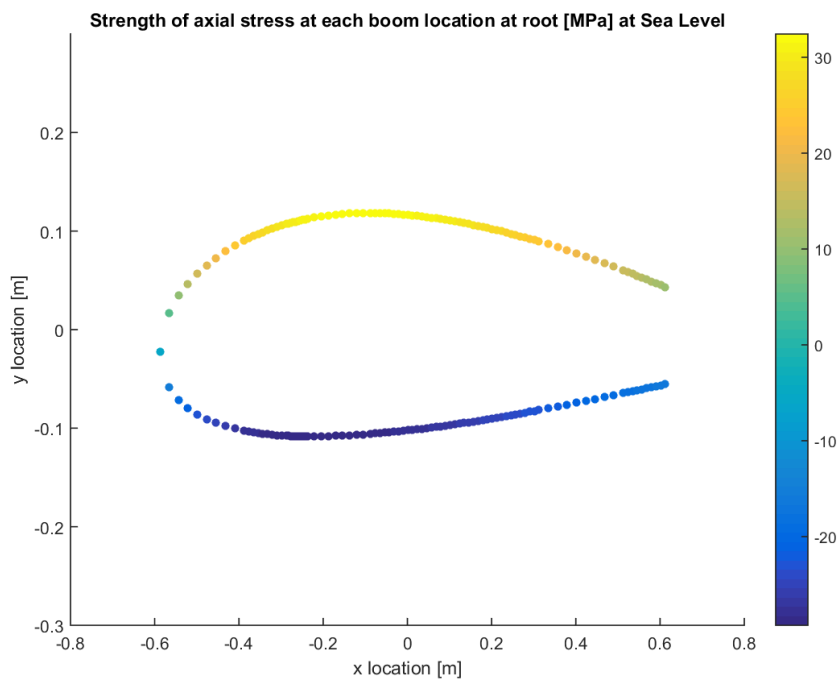


Figure C.11: Direct stress at root for sea level gust point 2.

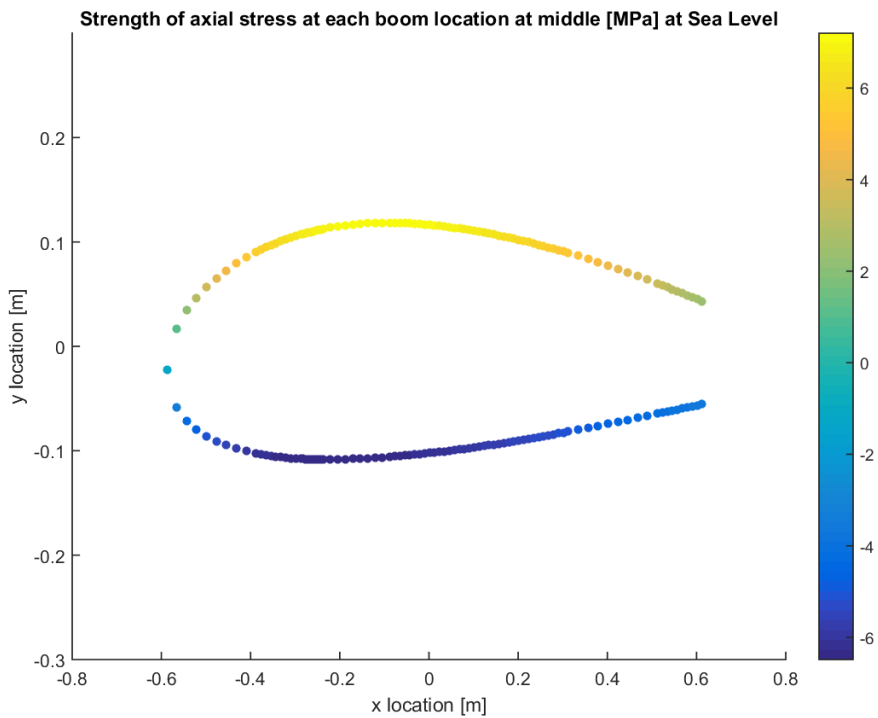


Figure C.12: Direct stress at half of semi-span (0.25b) for sea level gust point 2.

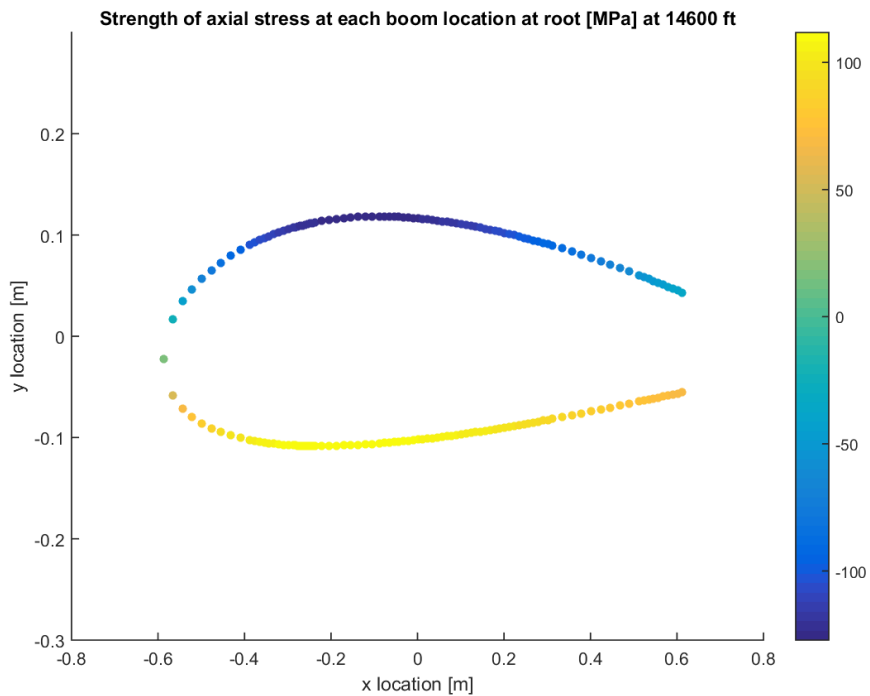


Figure C.13: Direct stress at root for ceiling PHAA.

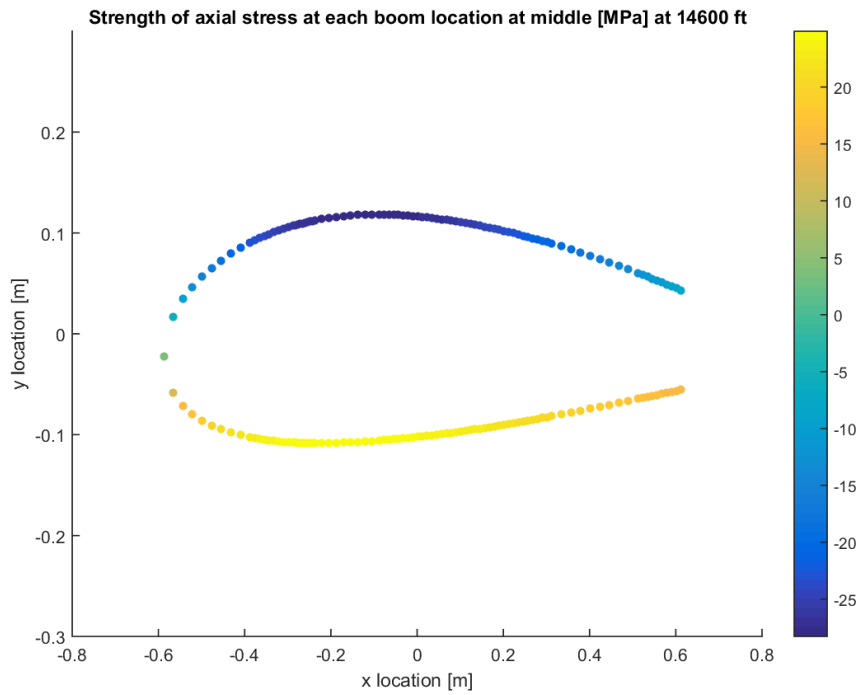


Figure C.14: Direct stress at half of semi-span ($0.25b$) for ceiling PHAA.

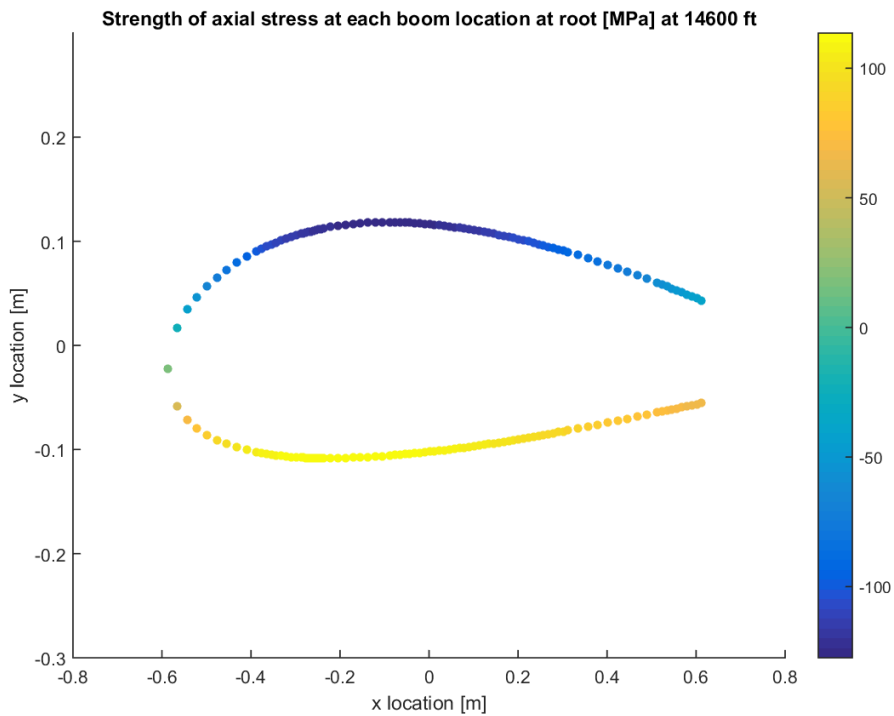


Figure C.15: Direct stress at root for ceiling PLAA.

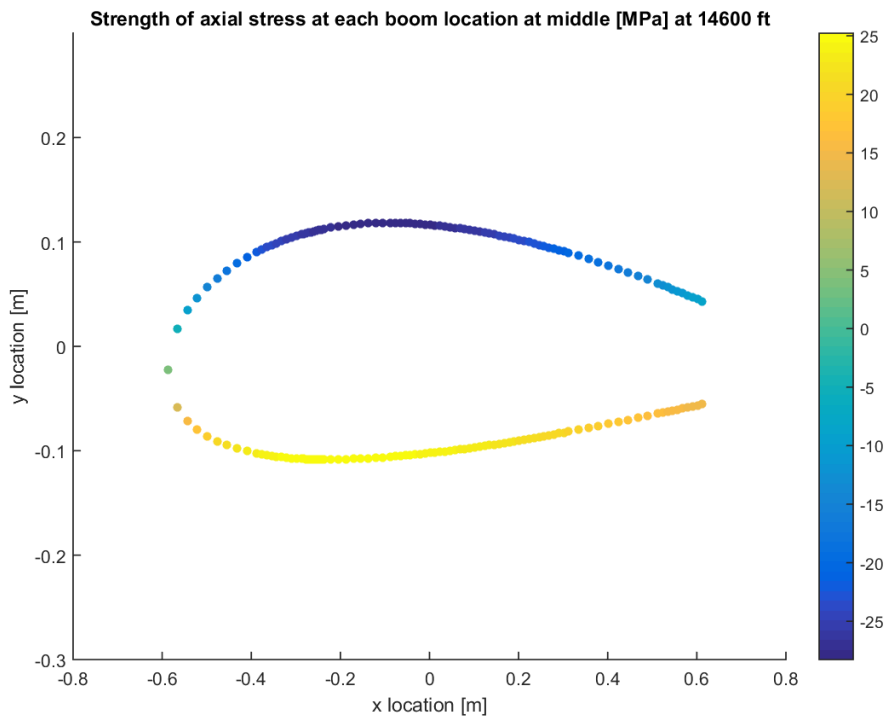


Figure C.16: Direct stress at half of semi-span (0.25b) for ceiling PLAA.

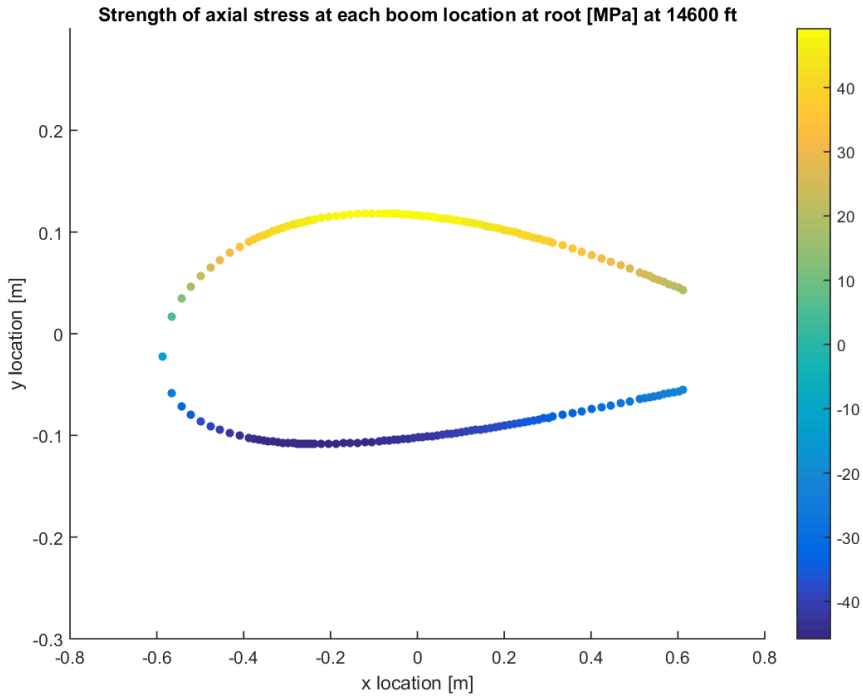


Figure C.17: Direct stress at root for ceiling NHAA.

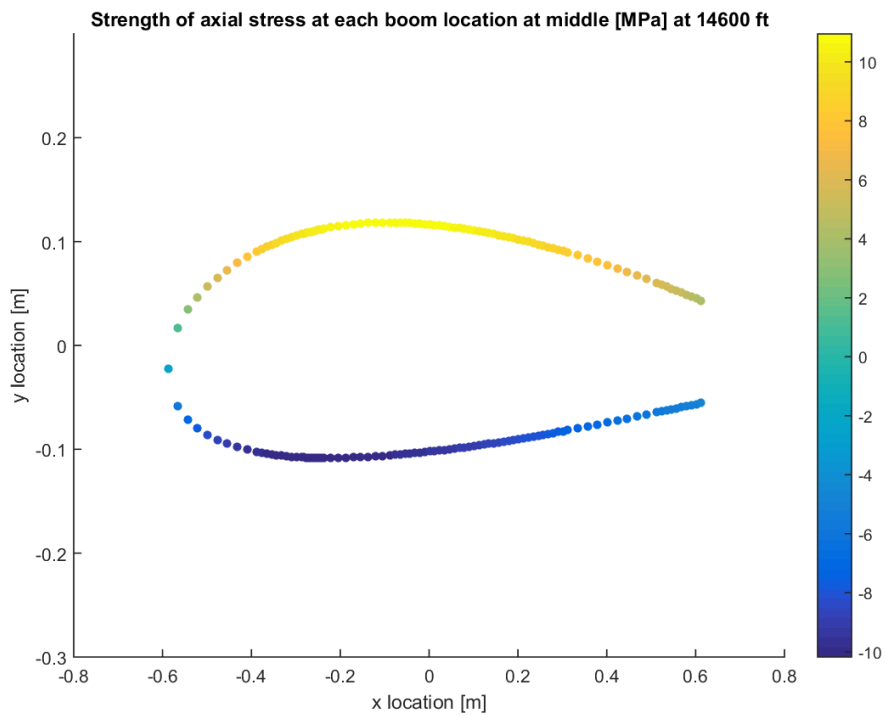


Figure C.18: Direct stress at half of semi-span (0.25b) for ceiling NHAA.

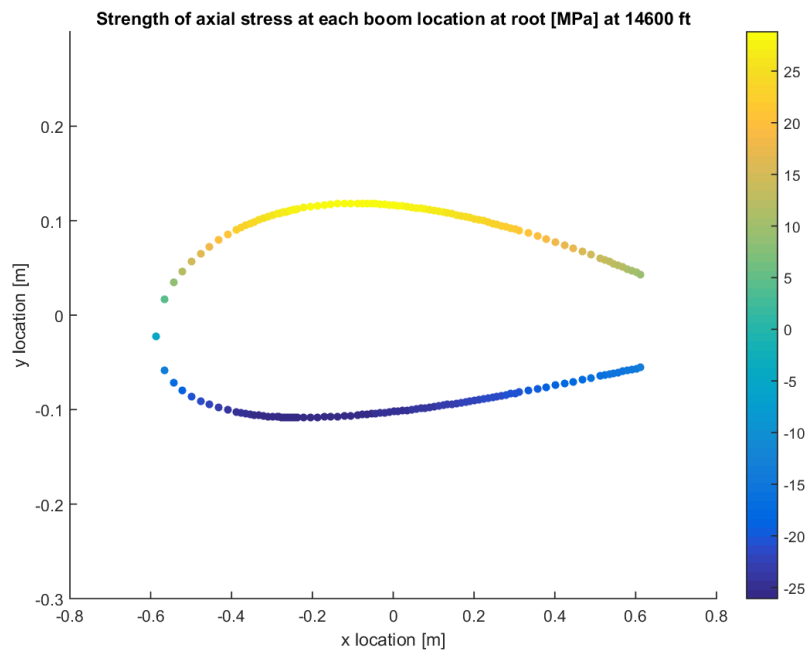


Figure C.19: Direct stress at root for ceiling NLAA.

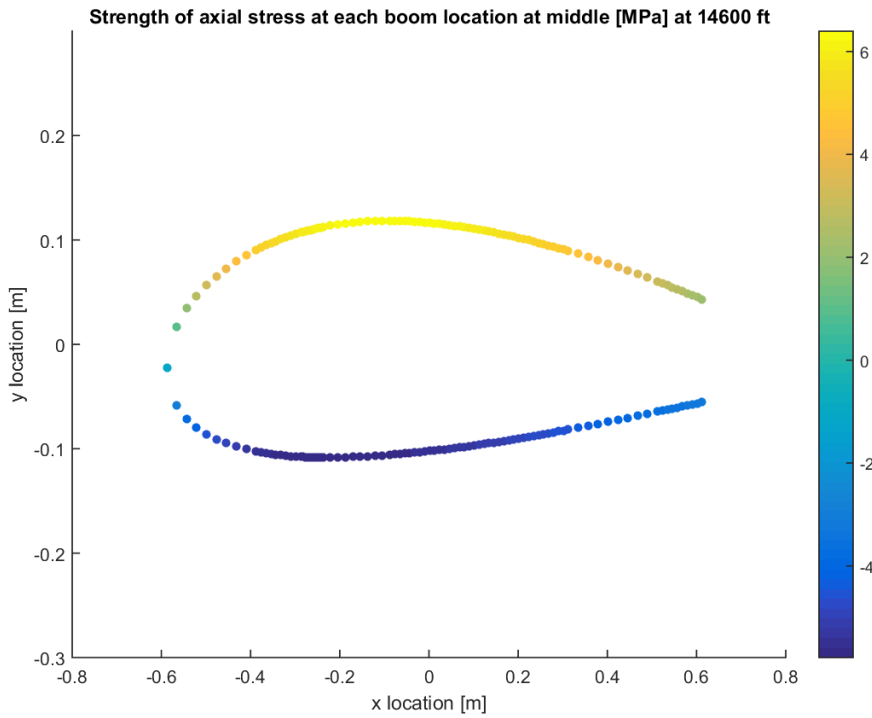


Figure C.20: Direct stress at half of semi-span (0.25b) for ceiling NLAA.

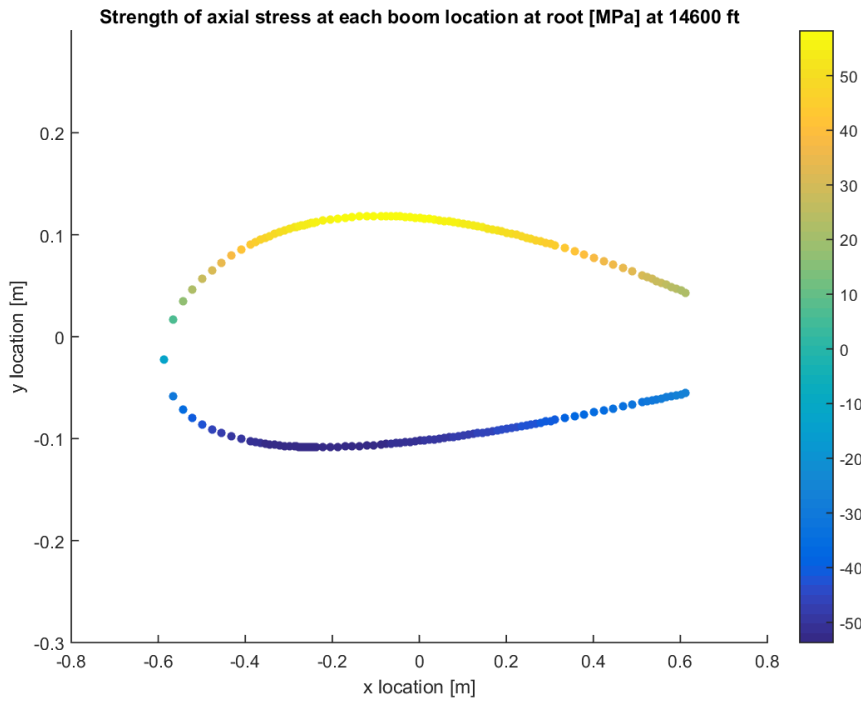


Figure C.21: Direct stress at root for ceiling gust point 1.

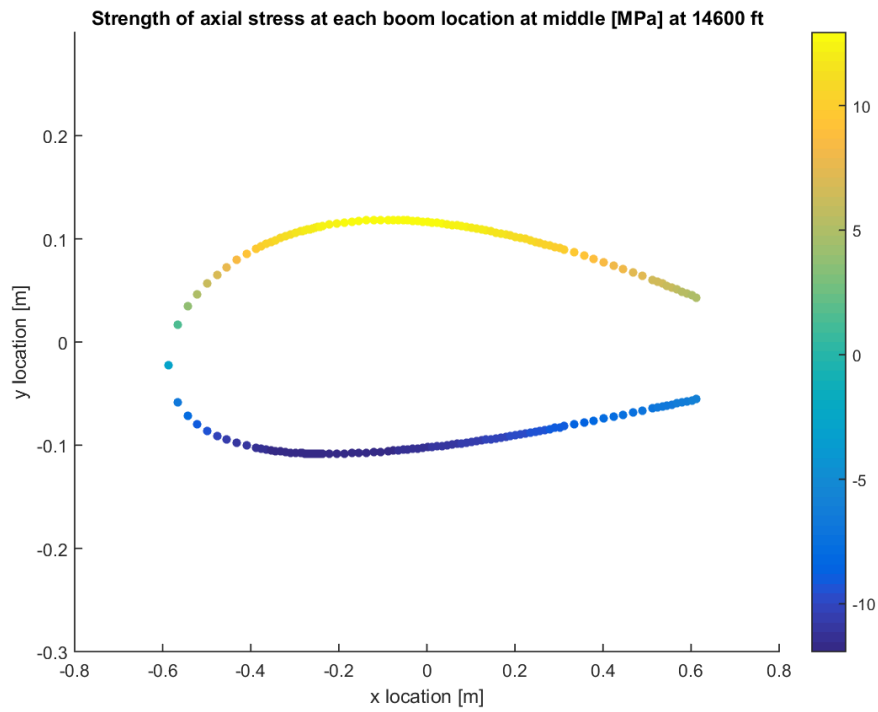


Figure C.22: Direct stress at half of semi-span (0.25b) for ceiling gust point 1.

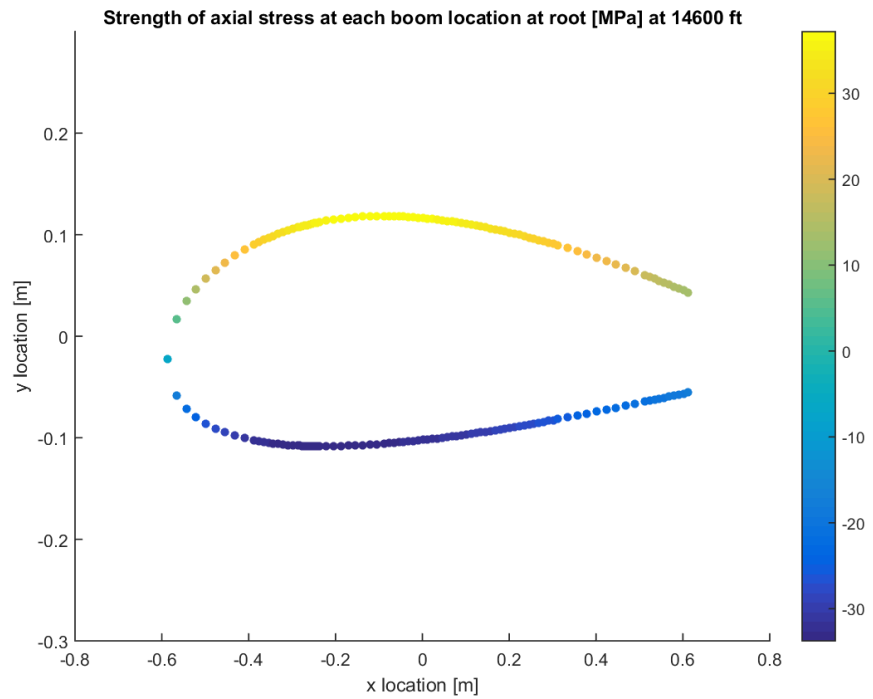


Figure C.23: Direct stress at root for ceiling gust point 2.

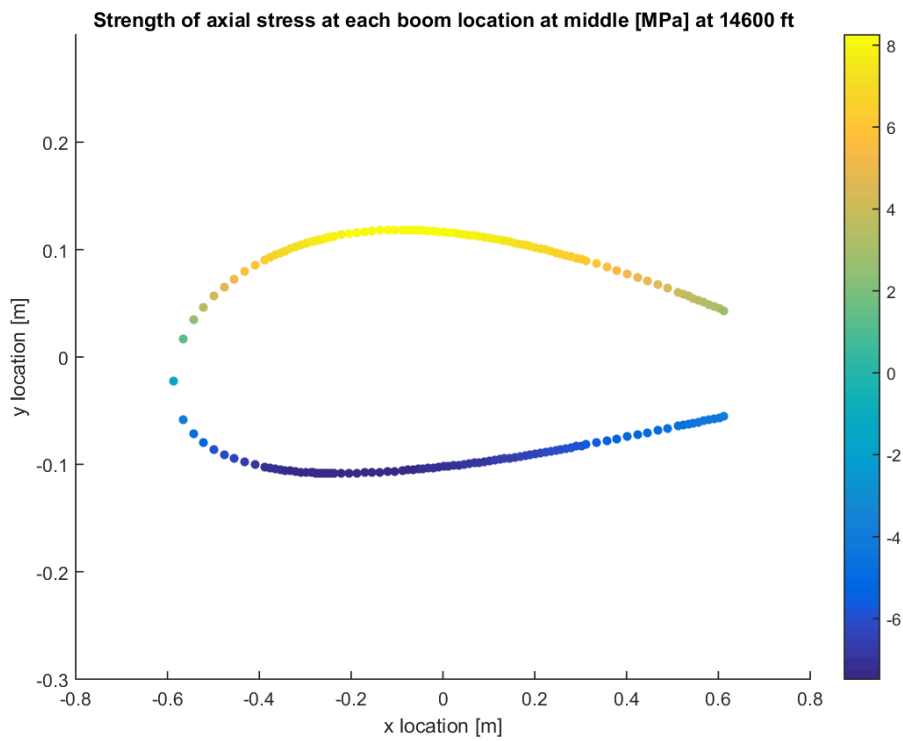


Figure C.24: Direct stress at half of semi-span (0.25b) for ceiling gust point 2.

Appendix D: Shear Flows and Shear Stresses

Section D.1: Shear Flow

These shear flow plots were generated in the same manner as Fig. (23). They all show the total calculated shear flows along the cross-section at each critical point and altitude. Specifically, these shear flows were found at the root of the wing. This location was where loading was estimated to be highest.

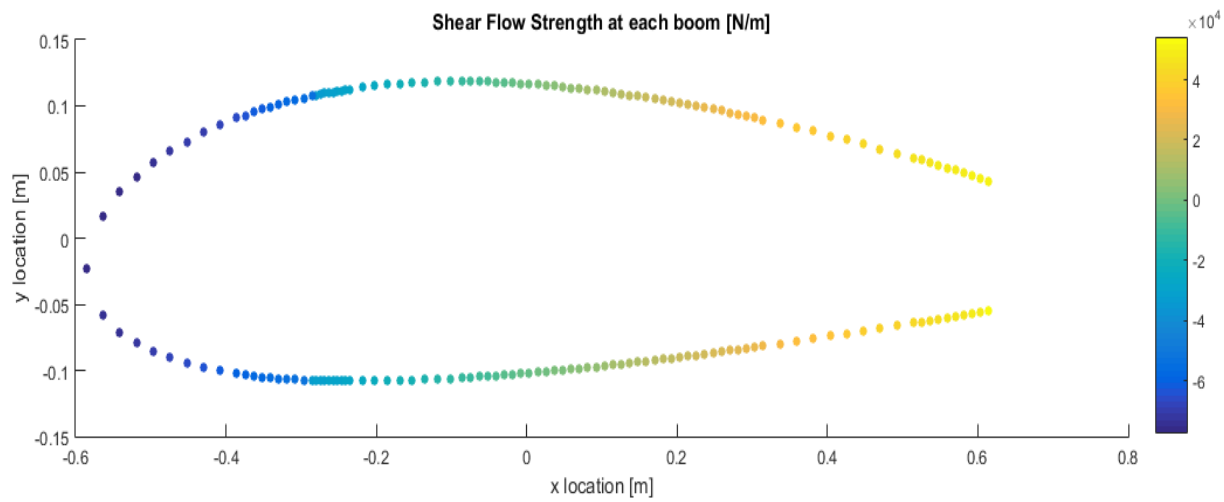


Figure D.1.1: Shear flow at wing root for sea level PHAA.

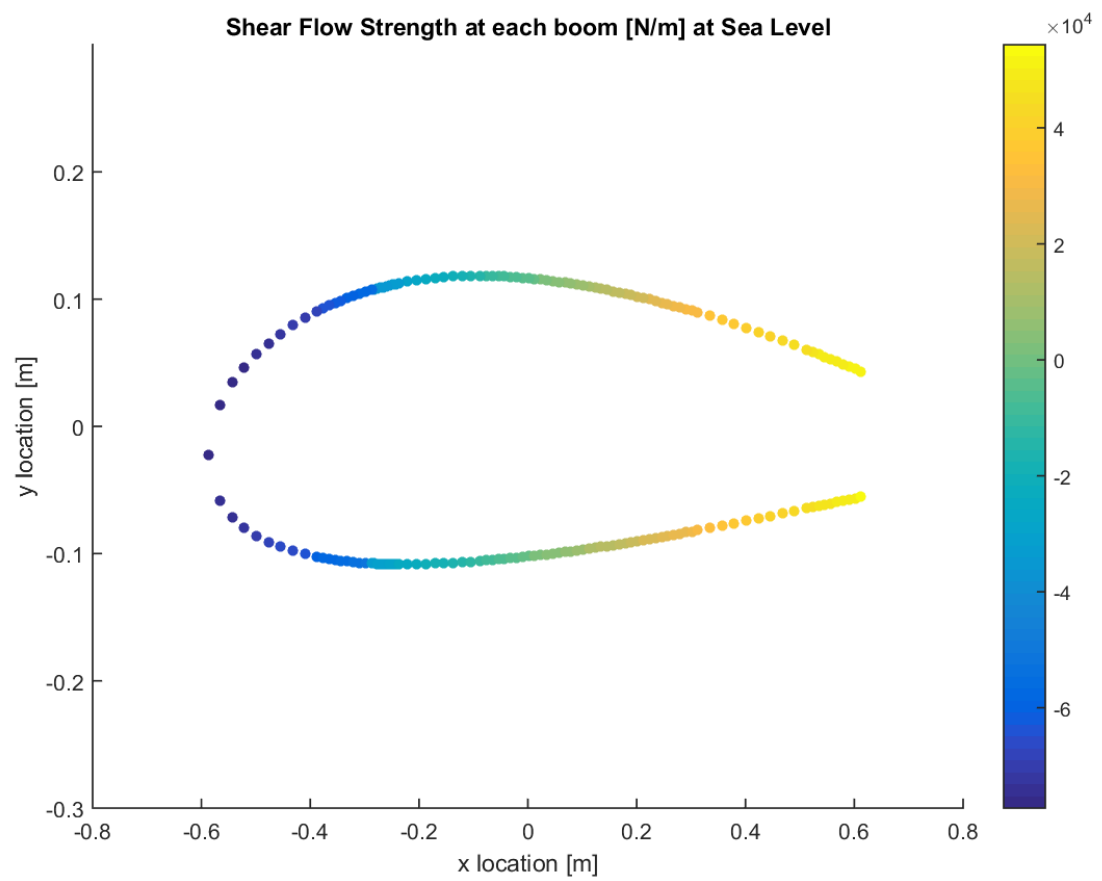


Figure D.1.2: Shear flow at wing root for sea level PLAA.

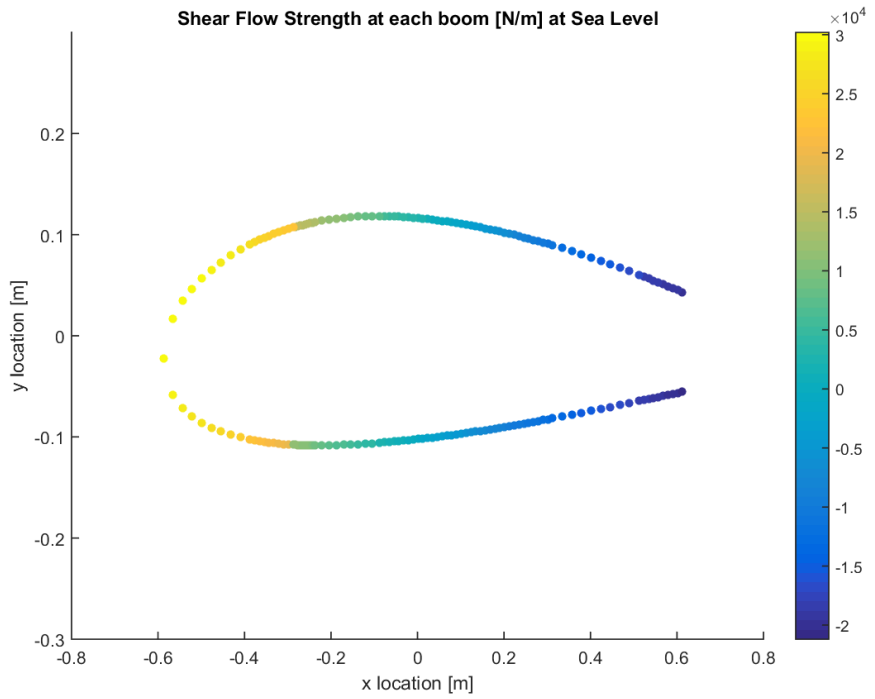


Figure D.1.3: Shear flow at wing root for sea level NHAA.

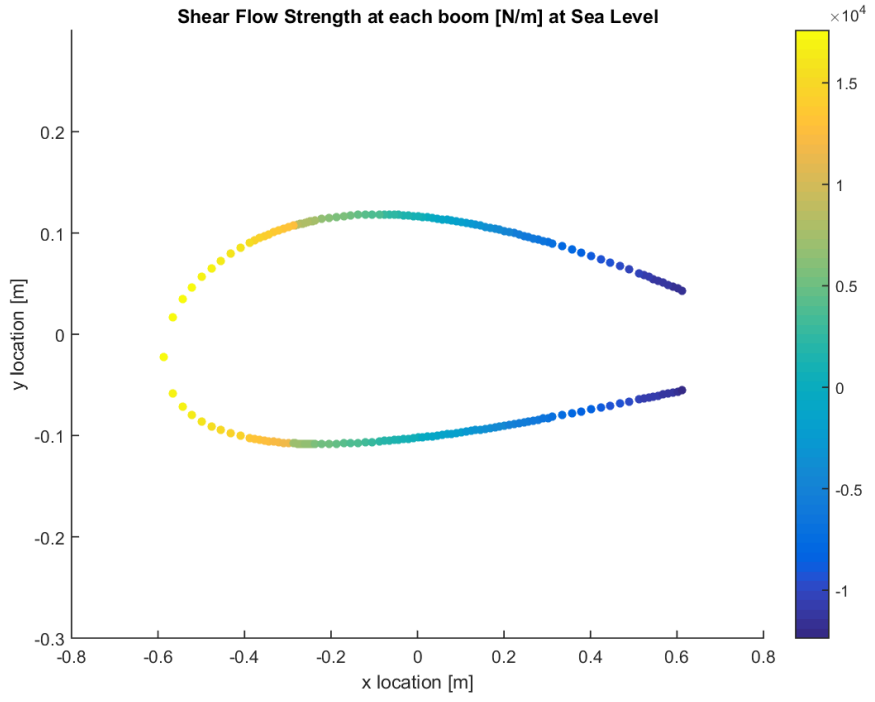


Figure D.1.4: Shear flow at wing root for sea level NLAA.

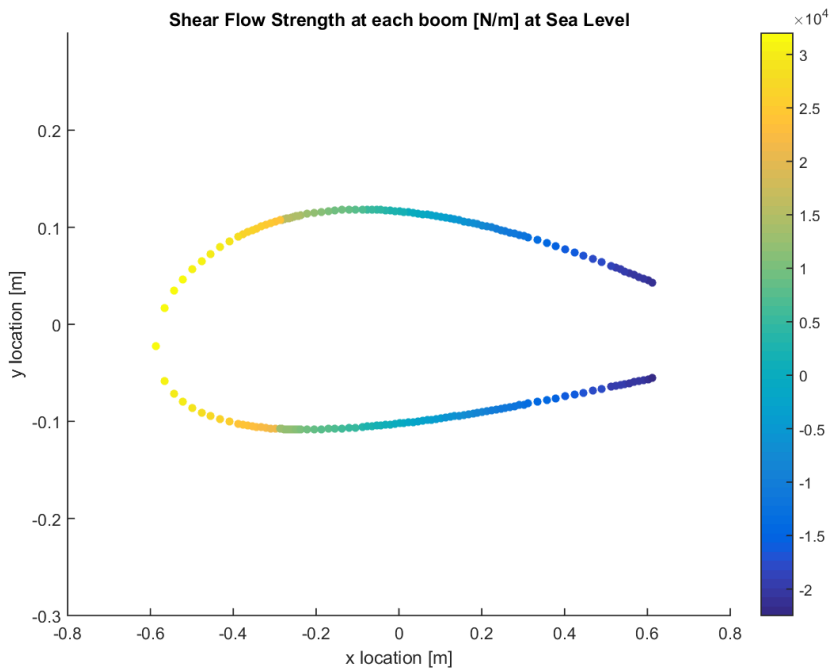


Figure D.1.5: Shear flow at wing root for sea level gust point 1.

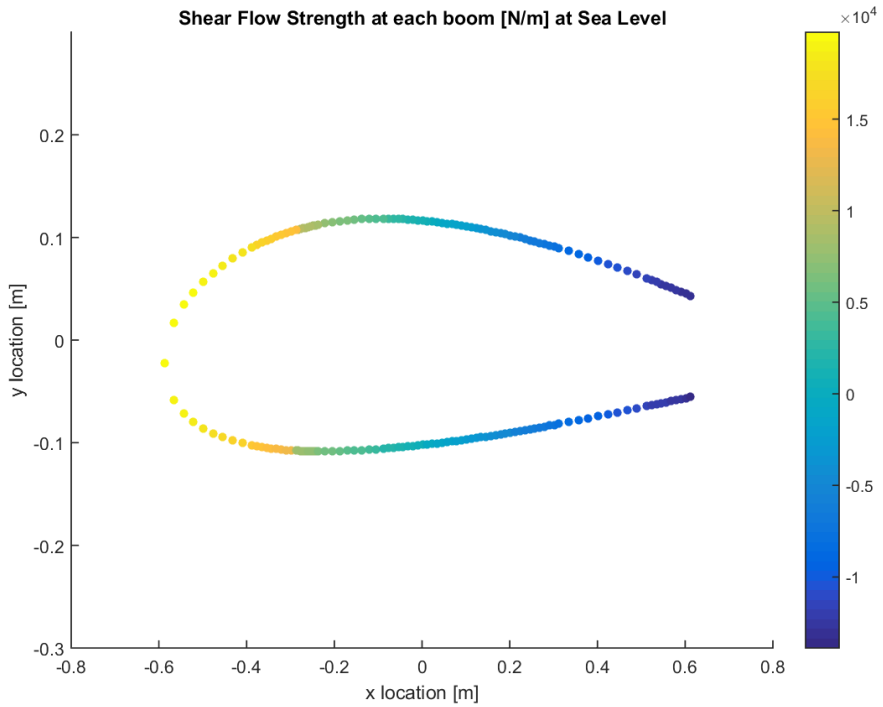


Figure D.1.6: Shear flow at wing root for sea level gust point 2.

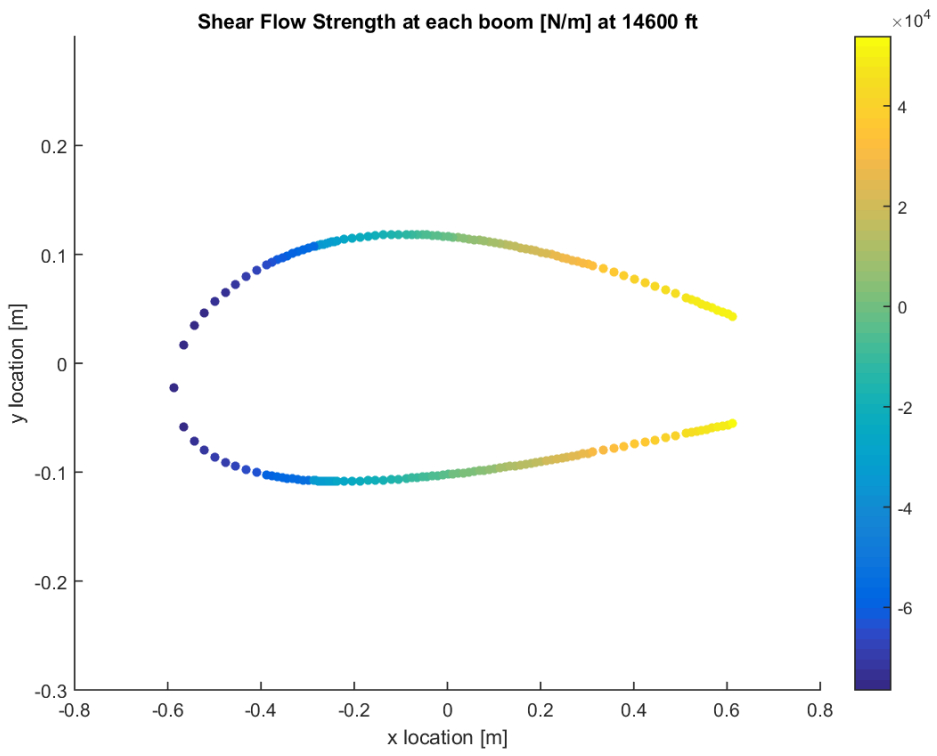


Figure D.1.7: Shear flow at wing root for ceiling PHAA.

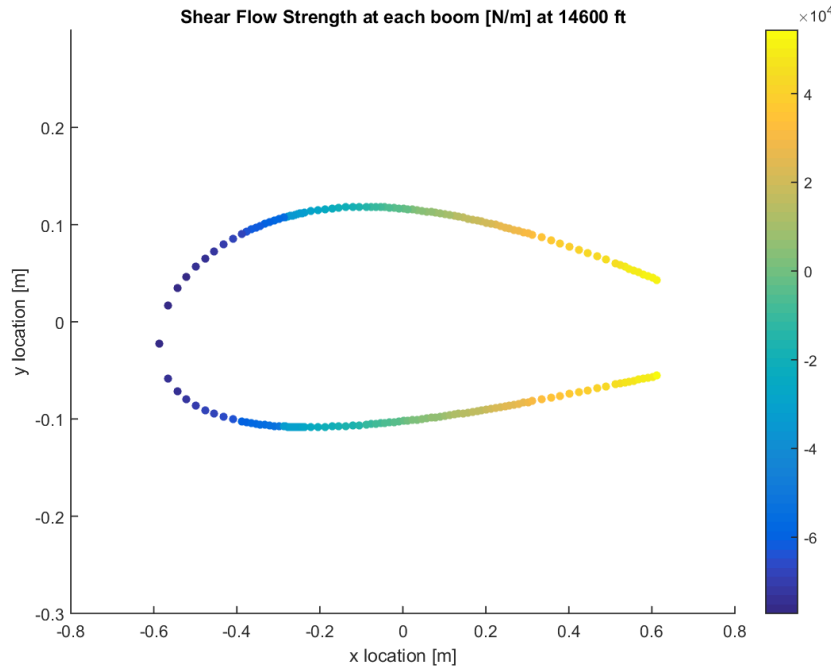


Figure D.1.8: Shear flow at wing root for ceiling PLAA.

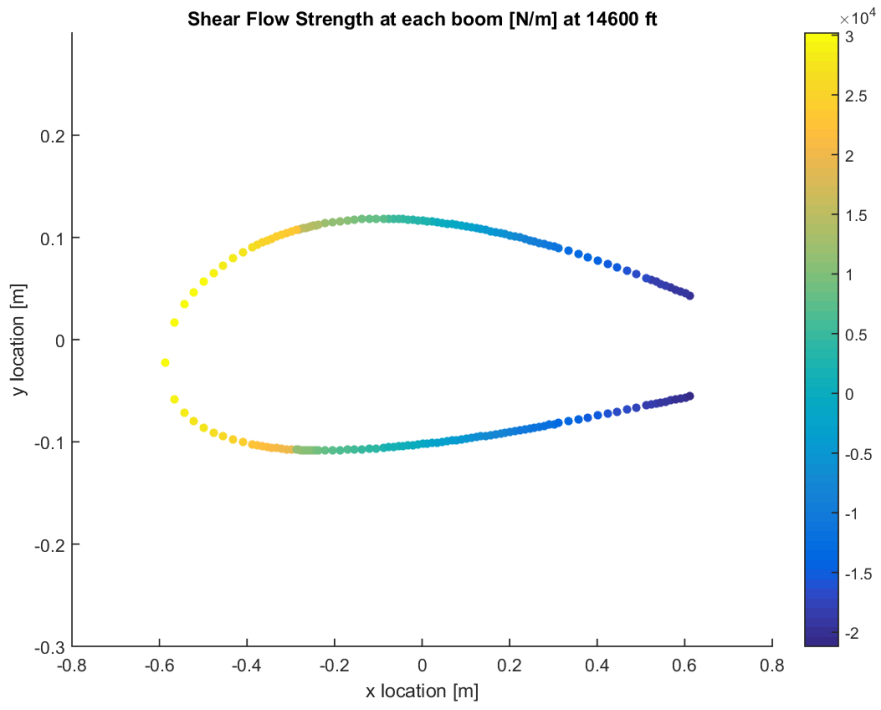


Figure D.1.9: Shear flow at wing root for ceiling NHAA.

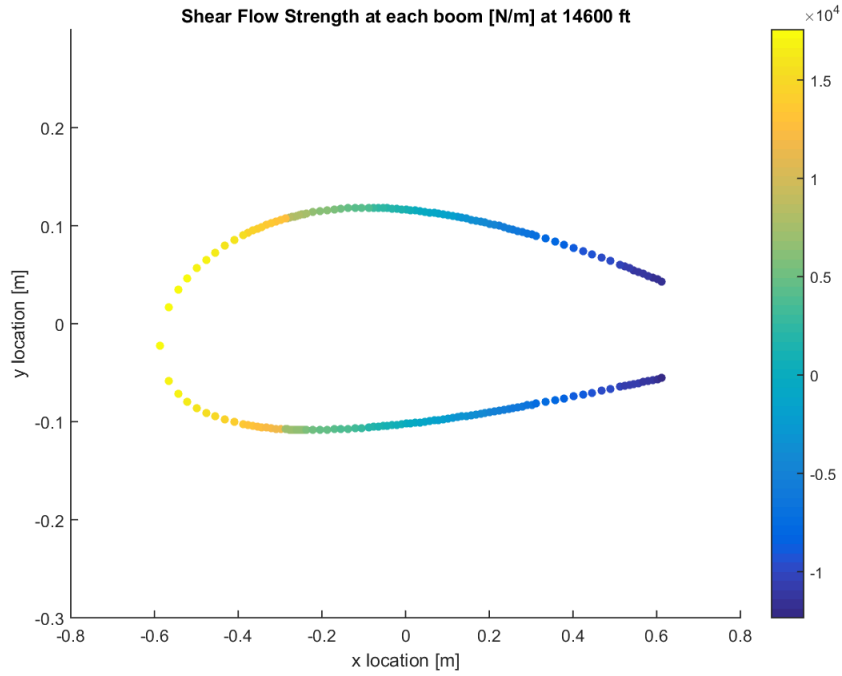


Figure D.1.10: Shear flow at wing root for ceiling NLAA.

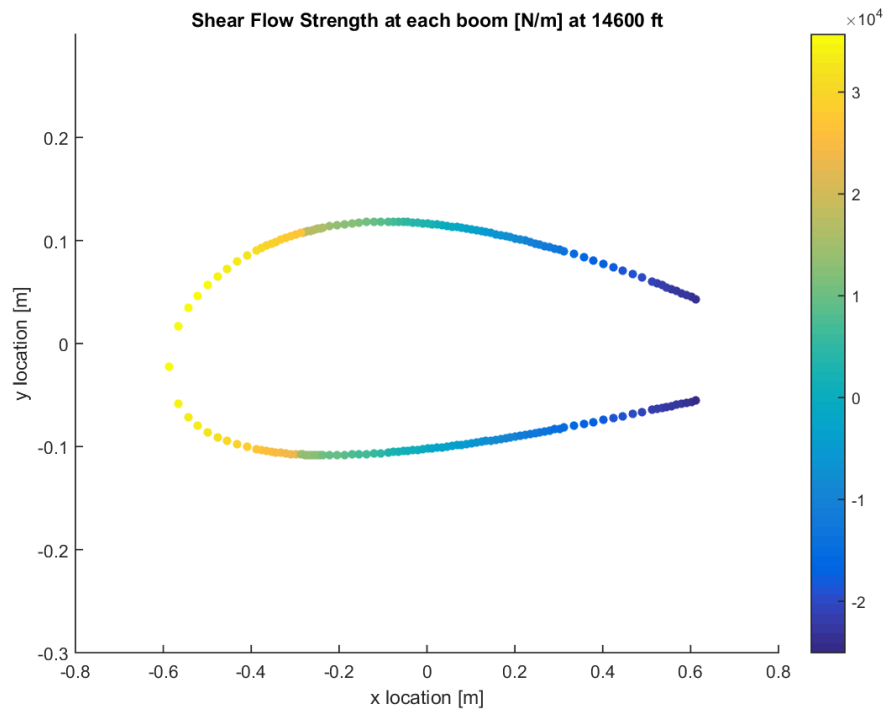


Figure D.1.11: Shear flow at wing root for ceiling gust point 1.

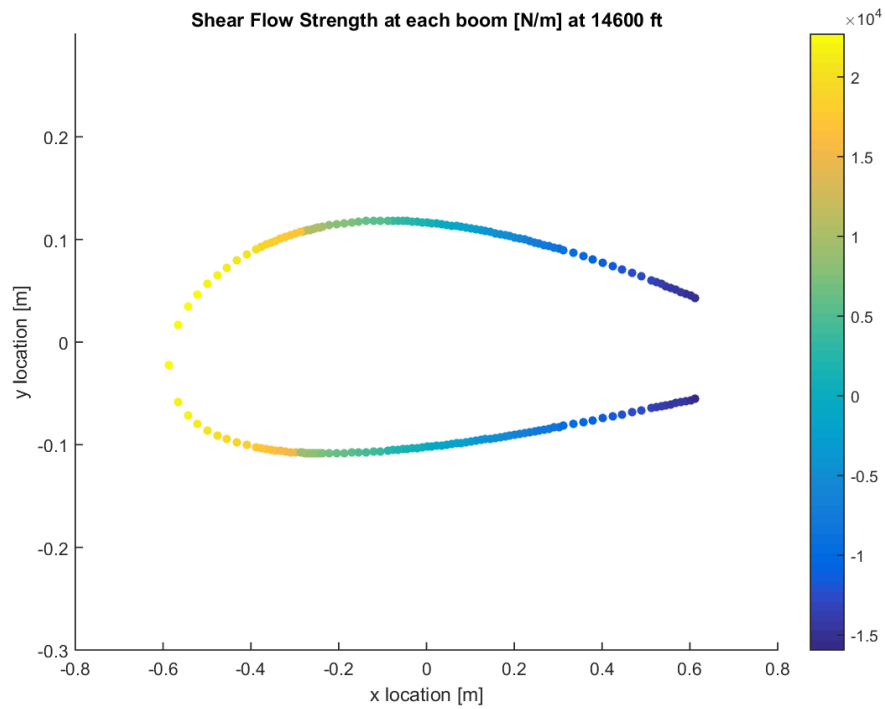


Figure D.1.12: Shear flow at wing root for ceiling gust point 2.

Section D.2: Shear Stress

The shear stresses plotted here were derived from the shear flows shown in section C.1. The conversion was made using Eq. (40). The shear stresses were also plotted at both the root and the mid-wing at each critical point. These shear stresses followed a similar pattern as the direct stresses, as the shear stress increased at the root compared to the mid-wing.

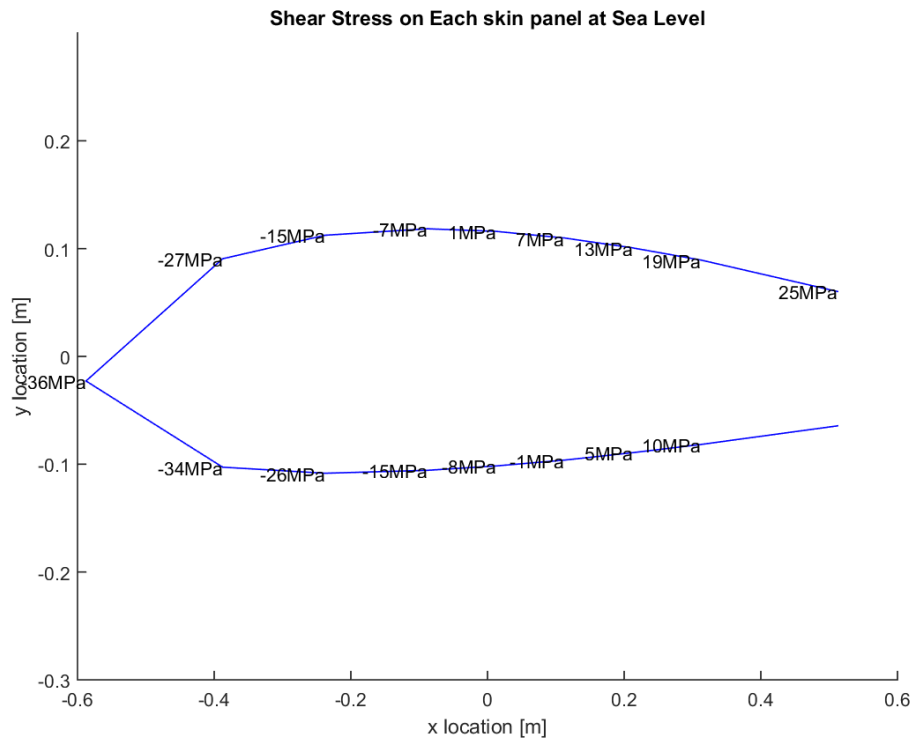


Figure D.2.1: Shear stress at root for sea level PHAA.

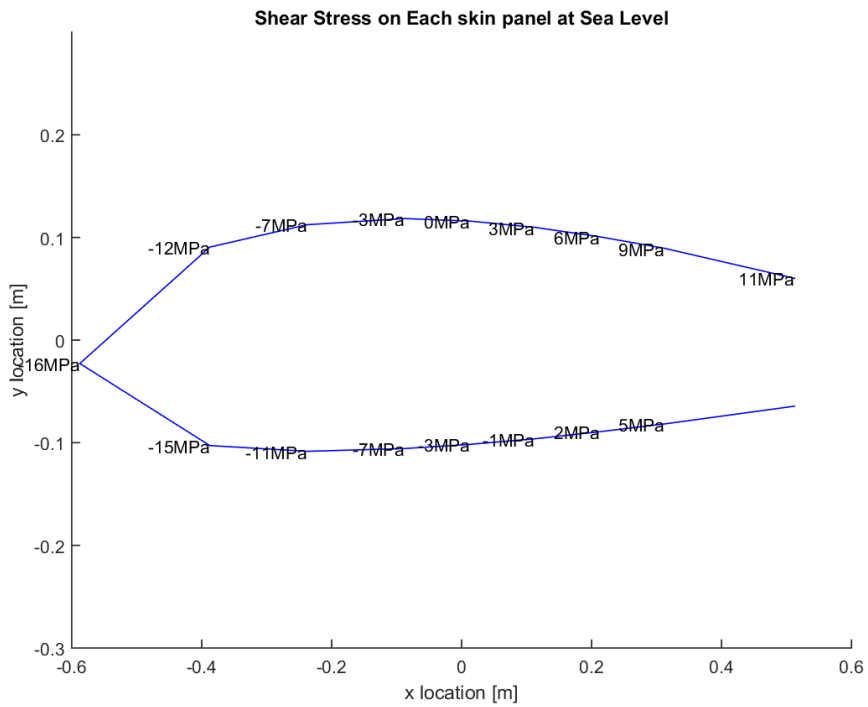


Figure D.2.2: Shear stress at half of semi-span (0.25b) for sea level PHAA.

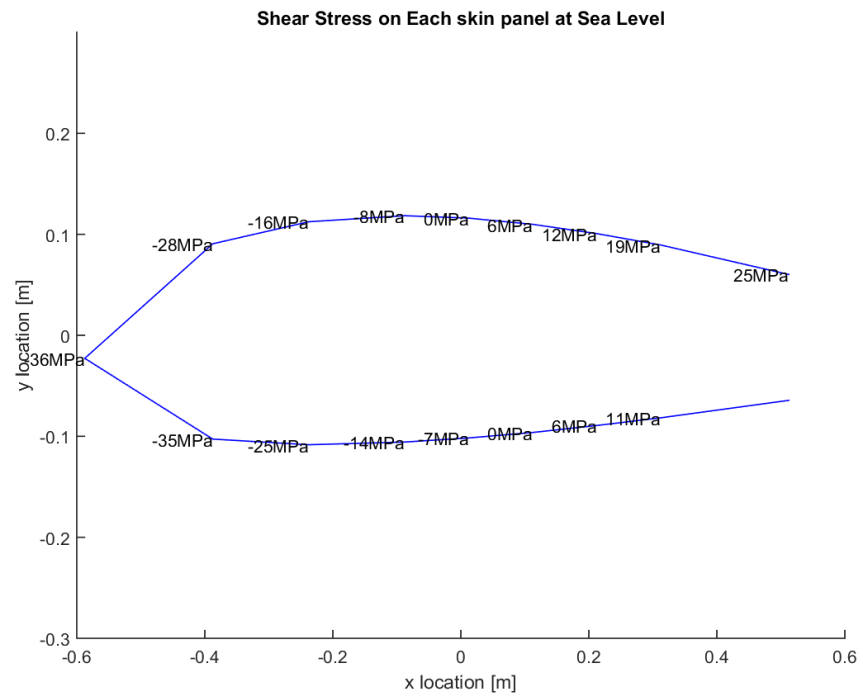


Figure D.2.3: Shear stress at root for sea level PLAA.

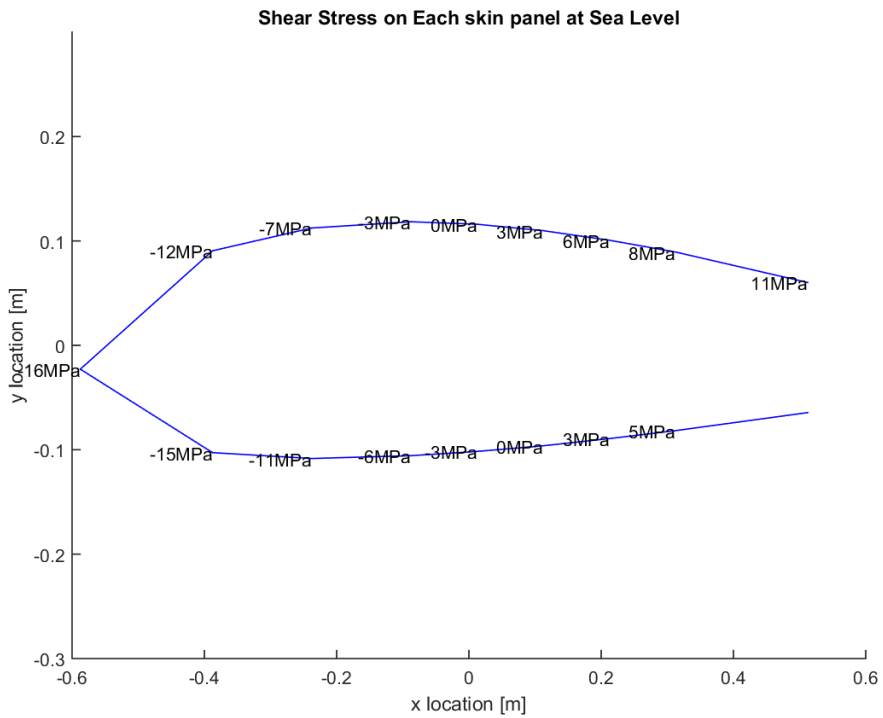


Figure D.2.4: Shear stress at half of semi-span (0.25b) for sea level PLAA.

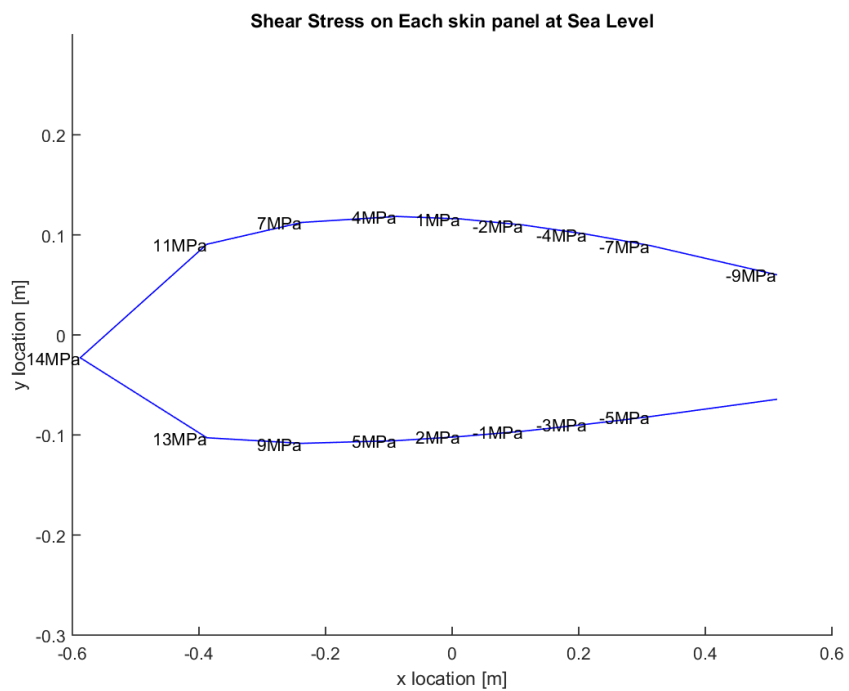


Figure D.2.5: Shear stress at root for sea level NHA.

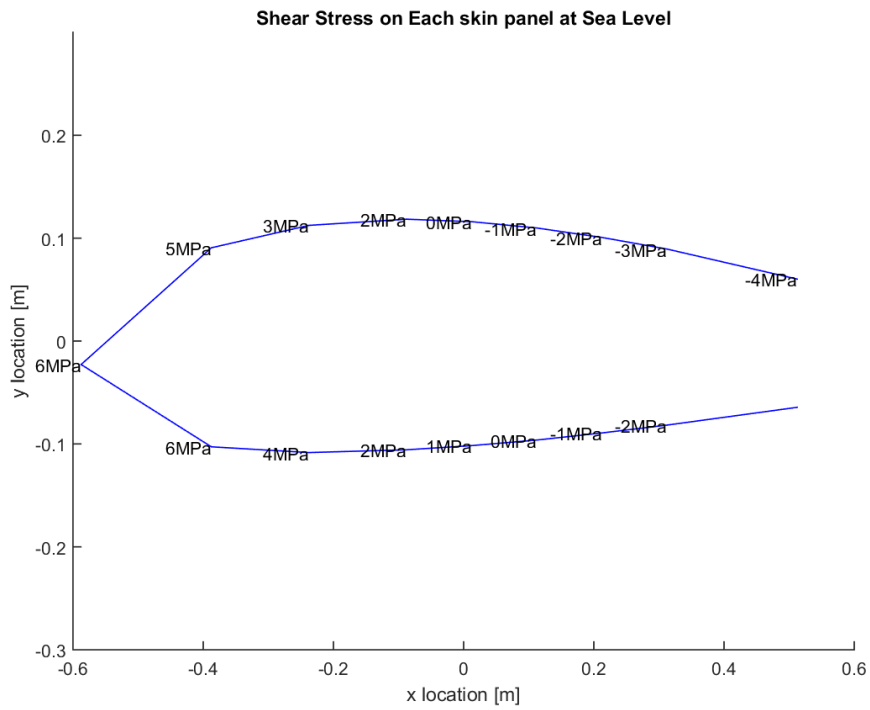


Figure D.2.6: Shear stress at half of semi-span (0.25b) for sea level NHAA.

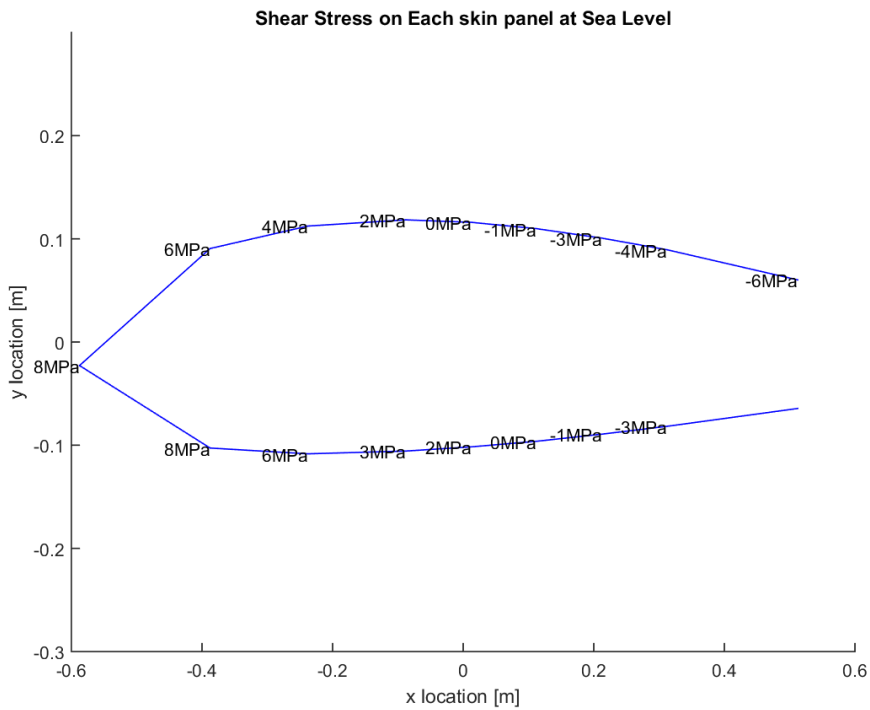


Figure D.2.7: Shear stress at root for sea level NLAA.

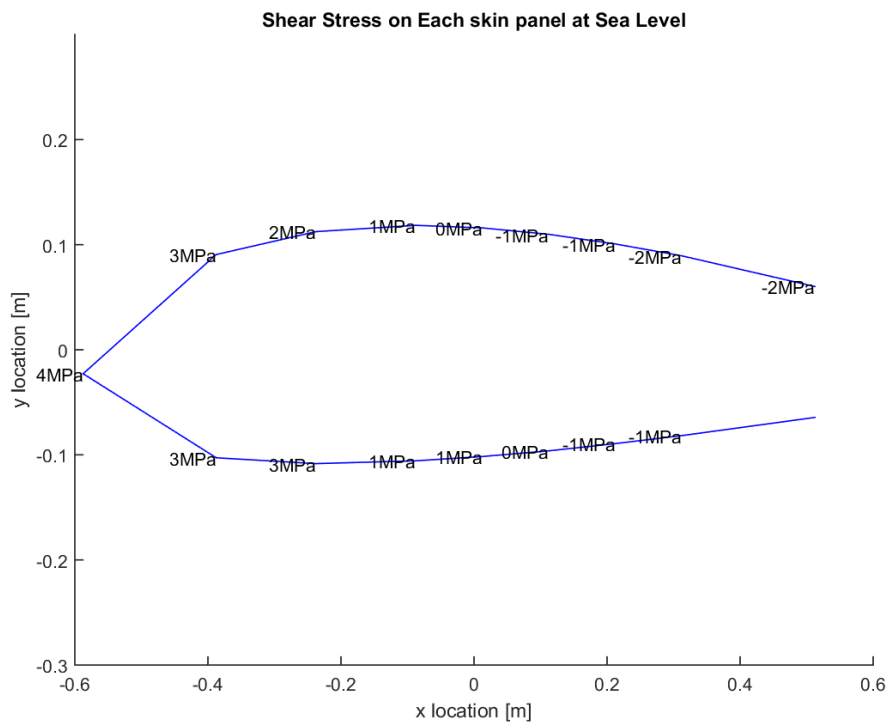


Figure D.2.8: Shear stress at half of semi-span (0.25b) for sea level NLAA.

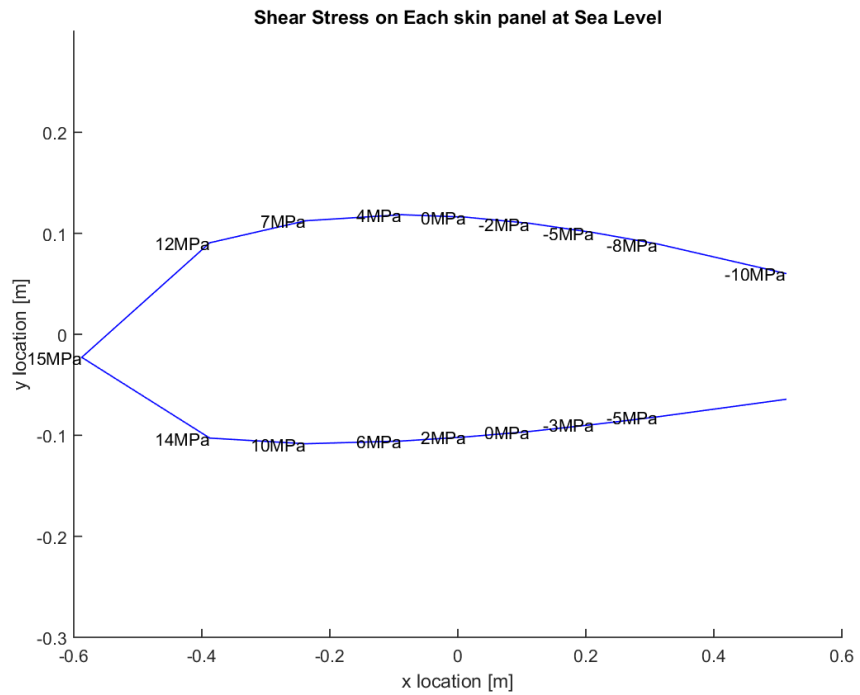


Figure D.2.9: Shear stress at root for sea level gust point 1.

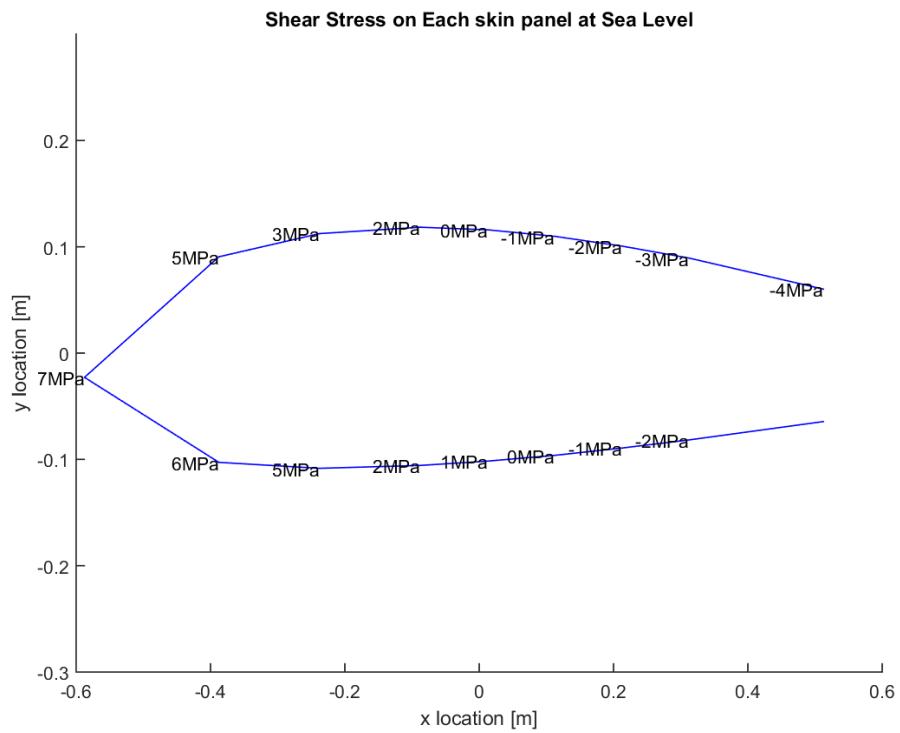


Figure D.2.10: Shear stress at half of semi-span (0.25b) for sea level gust point 1.

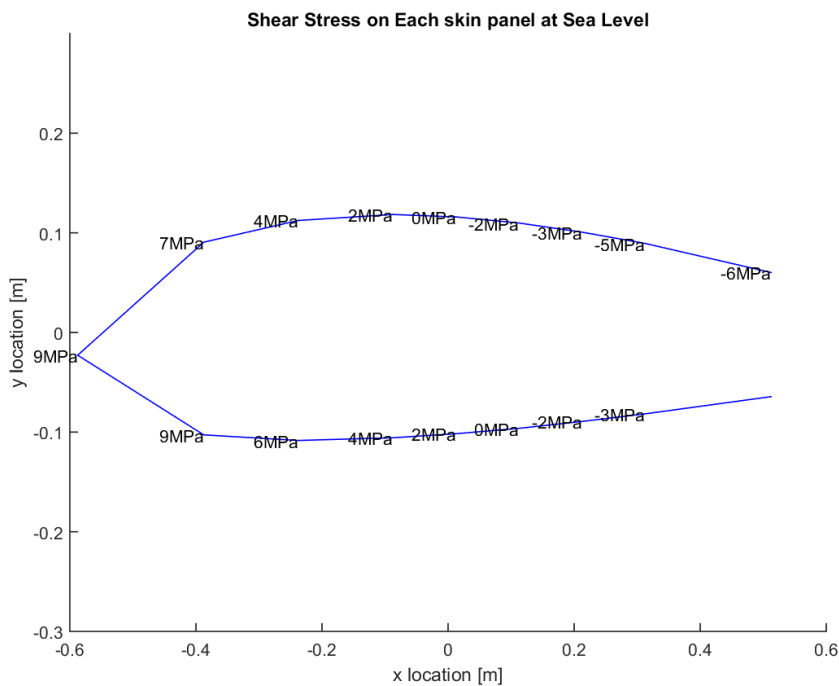


Figure D.2.11: Shear stress at root for sea level gust point 2.

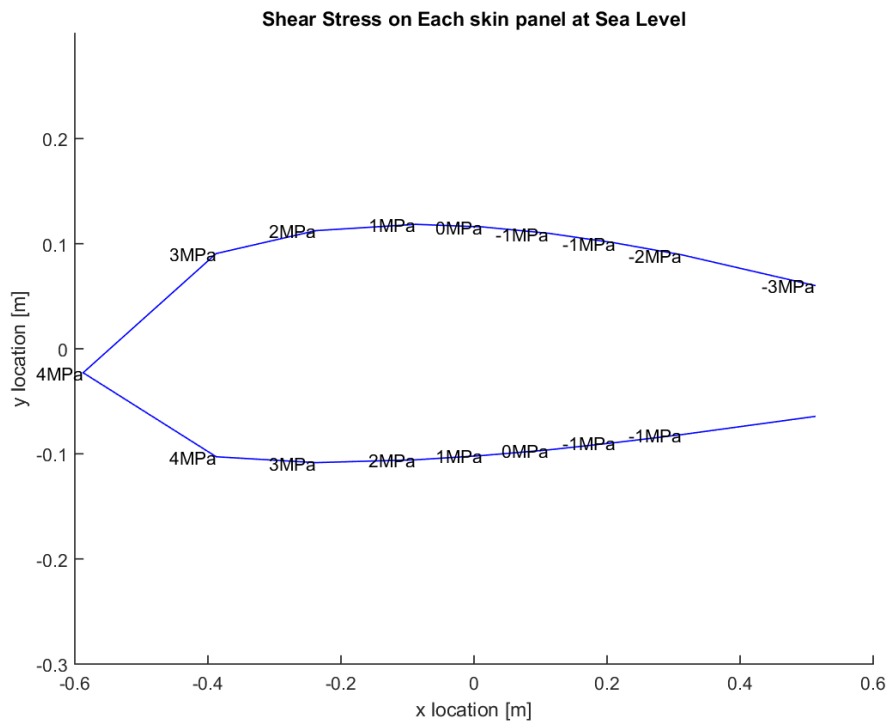


Figure D.2.12: Shear stress at half of semi-span (0.25b) for sea level gust point 2.

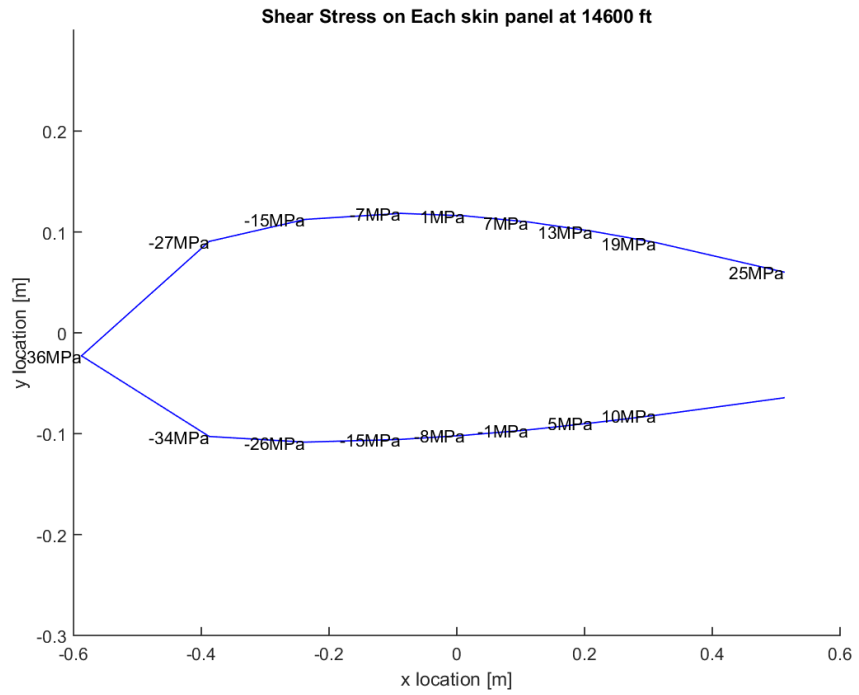


Figure D.2.13: Shear stress at root for ceiling PHAA.

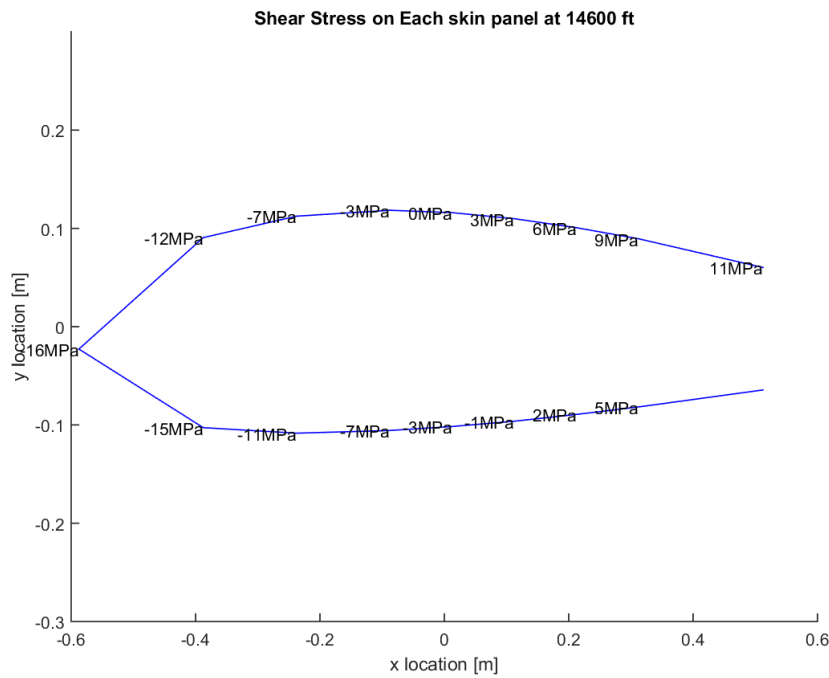


Figure D.2.14: Shear stress at half of semi-span (0.25b) for ceiling PHAA.

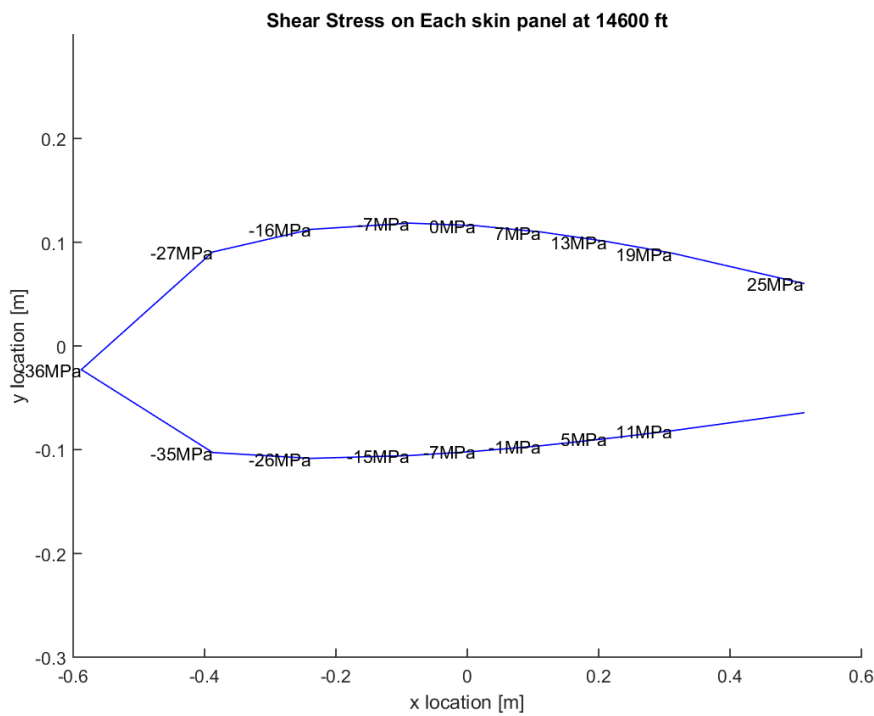


Figure D.2.15: Shear stress at root for ceiling PLAA.

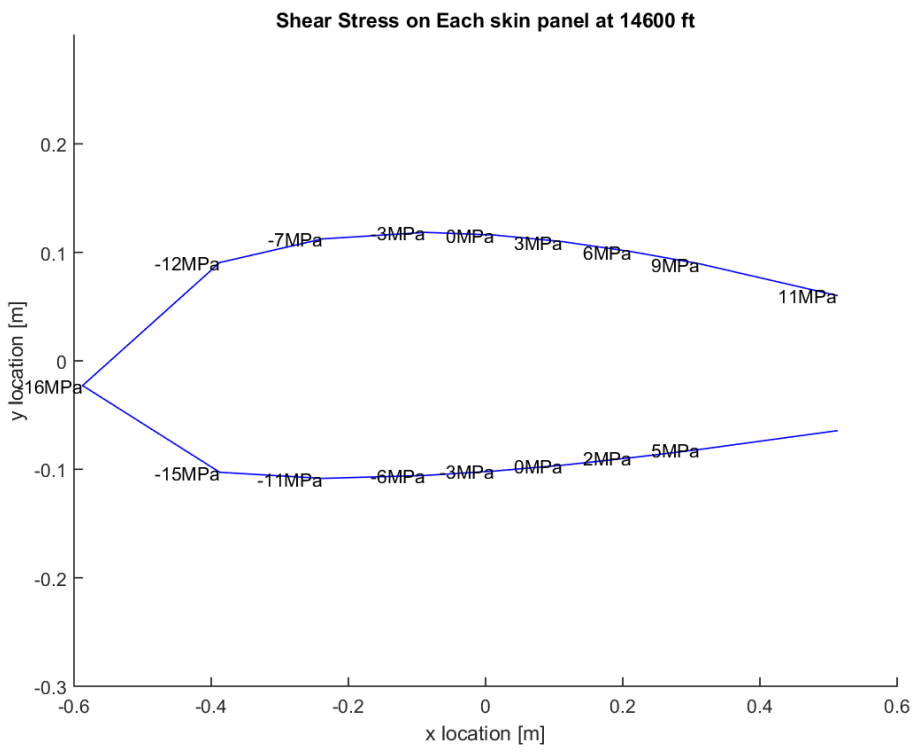


Figure D.2.16: Shear stress at half of semi-span (0.25b) for ceiling PLAA.

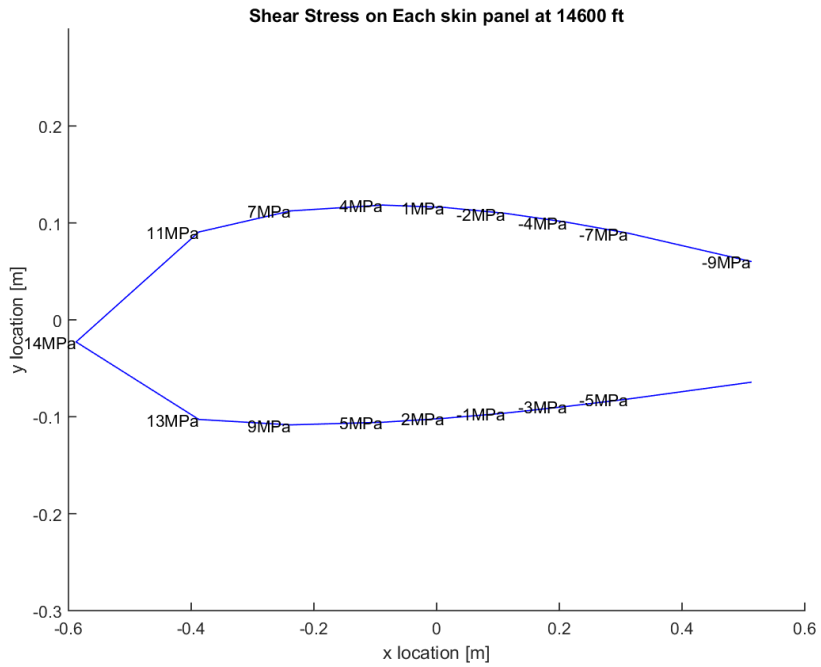


Figure D.2.17: Shear stress at root for ceiling NHAA.

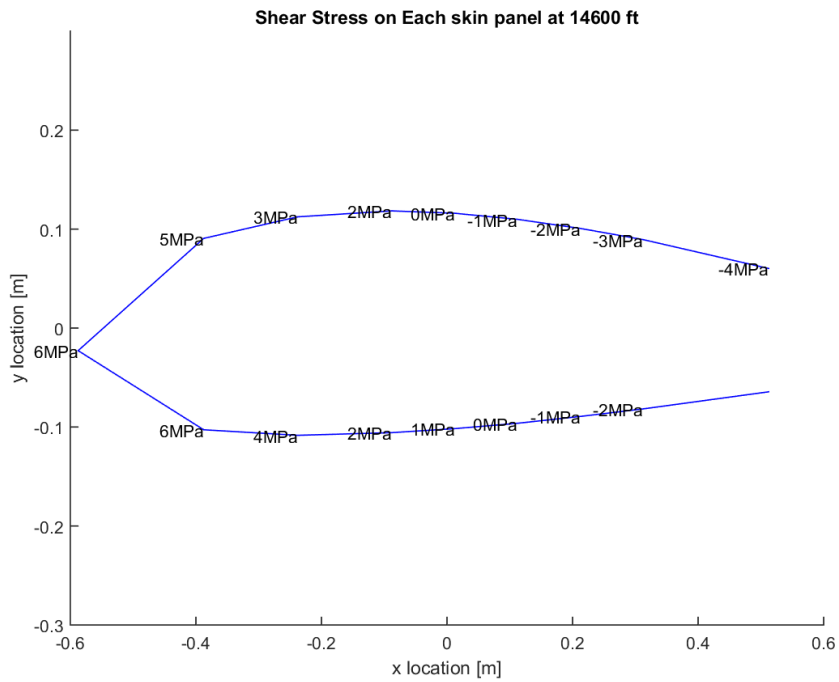


Figure D.2.18: Shear stress at half of semi-span (0.25b) for ceiling NHAA.

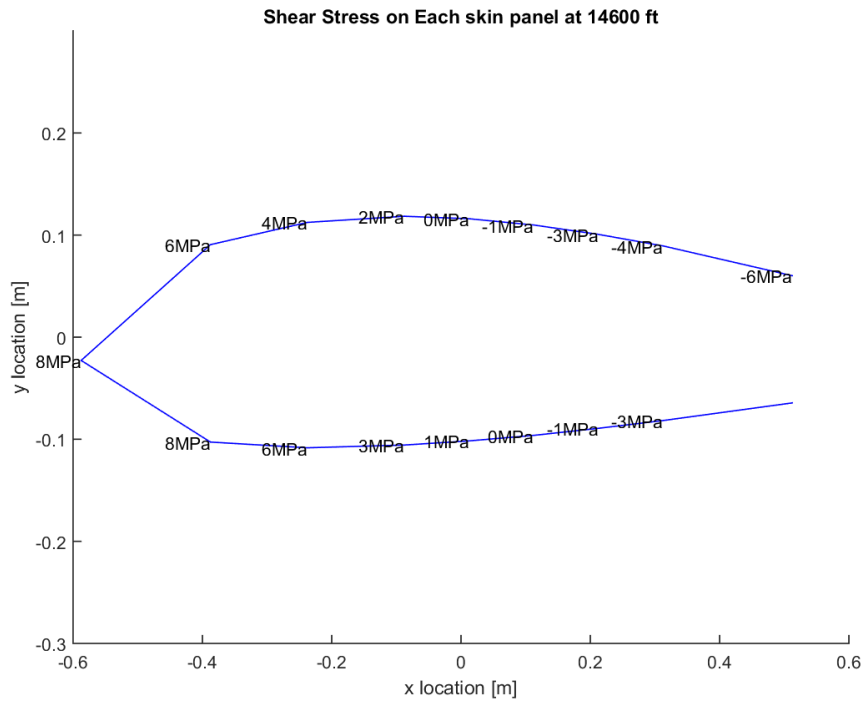


Figure D.2.19: Shear stress at root for ceiling NLAA.

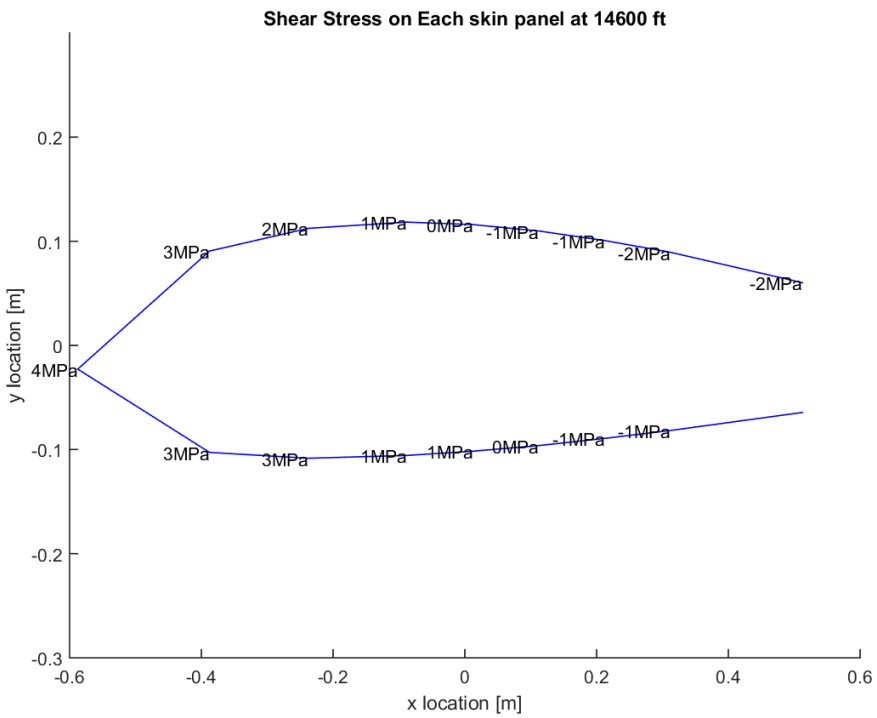


Figure D.2.20: Shear stress at half of semi-span (0.25b) for ceiling NLAA.

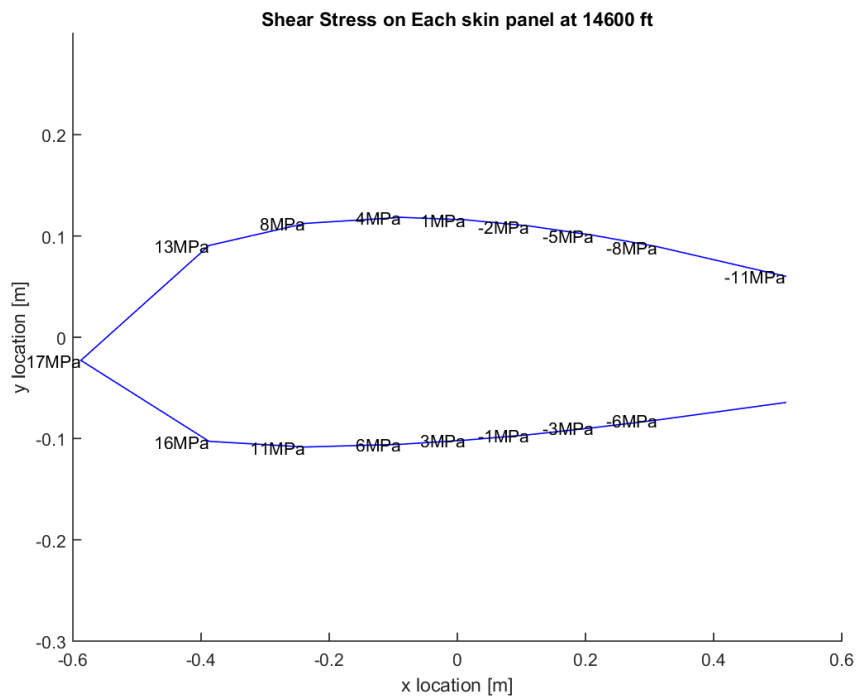


Figure D.2.21: Shear stress at root for ceiling gust point 1.

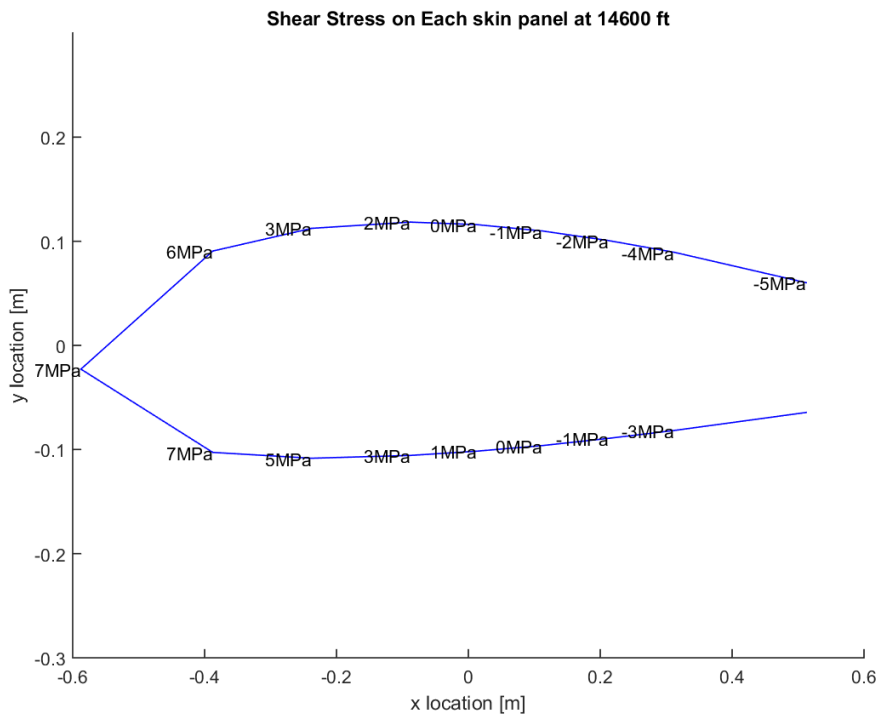


Figure D.2.22: Shear stress at half of semi-span (0.25b) for ceiling gust point 1.

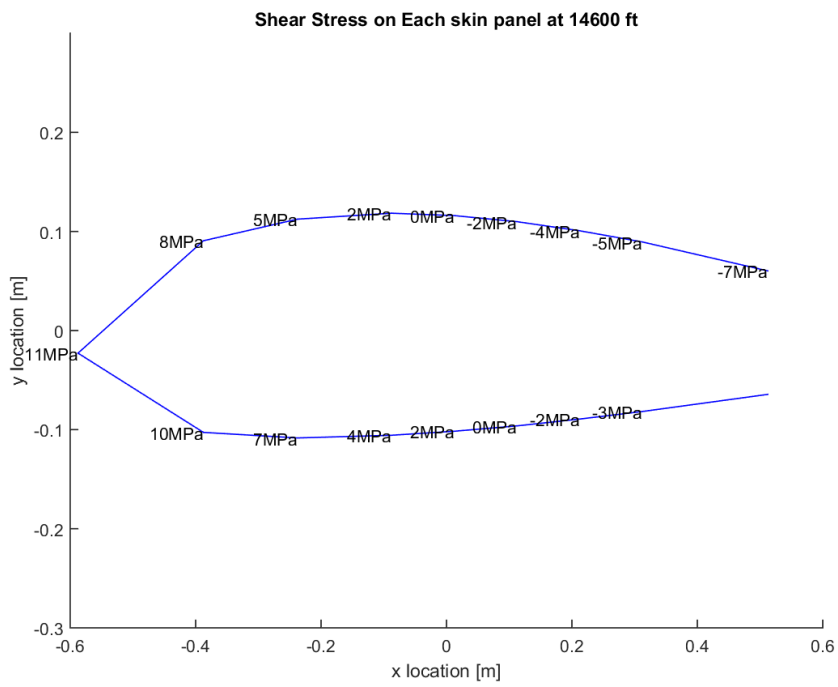


Figure D.2.23: Shear stress at root for ceiling gust point 2.

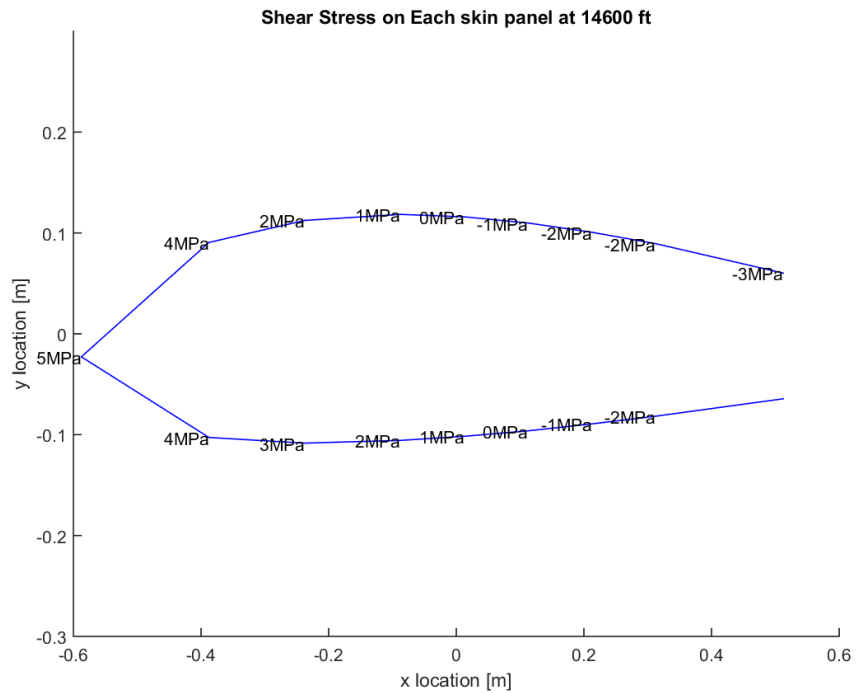


Figure D.2.24: Shear stress at half of semi-span (0.25b) for ceiling gust point 2.

Appendix E: Additional Failure Plots

Section E.1: Von Mises

The Von Mises failure plots listed below were generated in the same manners as Fig. (30). Additionally, they provide the failure margin for the wing at each critical point, either at sea level or ceiling altitudes. The plots show that the equivalent stresses would not cause yield in any case. Additionally, the equivalent stress seems to peak at positions near the front of the cross-section in all cases. This indicated large stress concentrations in these areas. Design considerations in the optimization and failure correction section considered this trend.

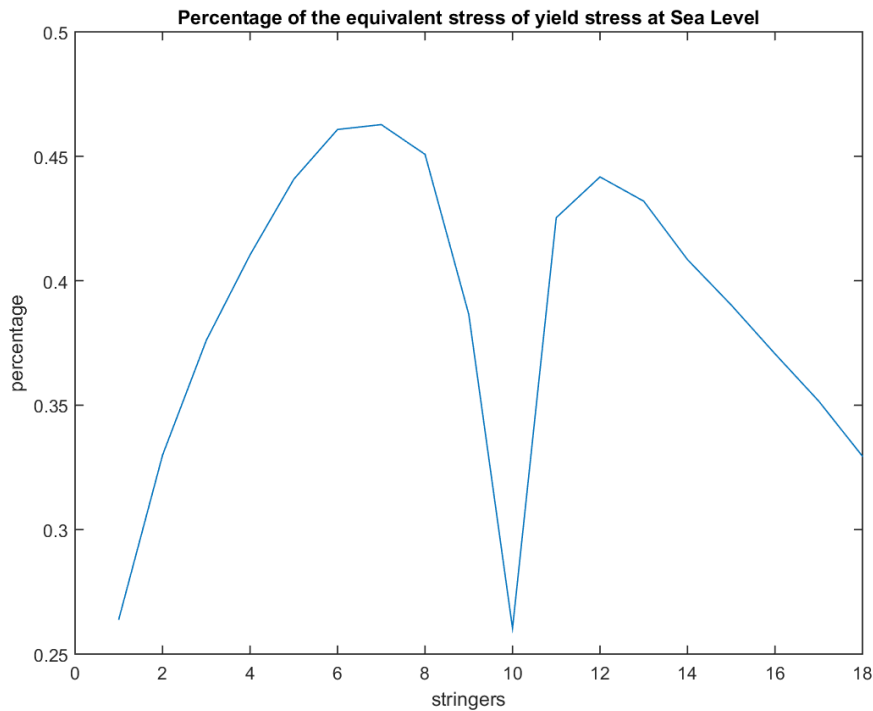


Figure E.1.1: Von Mises Equivalent/Yield percentage plot at sea level PHAA.

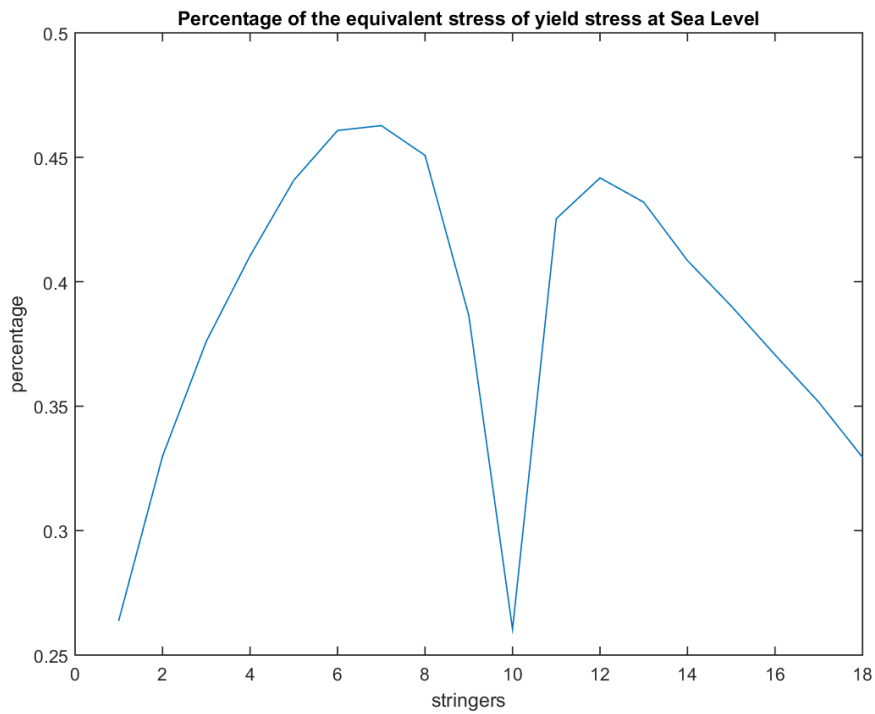


Figure E.1.2: Von Mises Equivalent/Yield percentage plot at sea level PLAA.

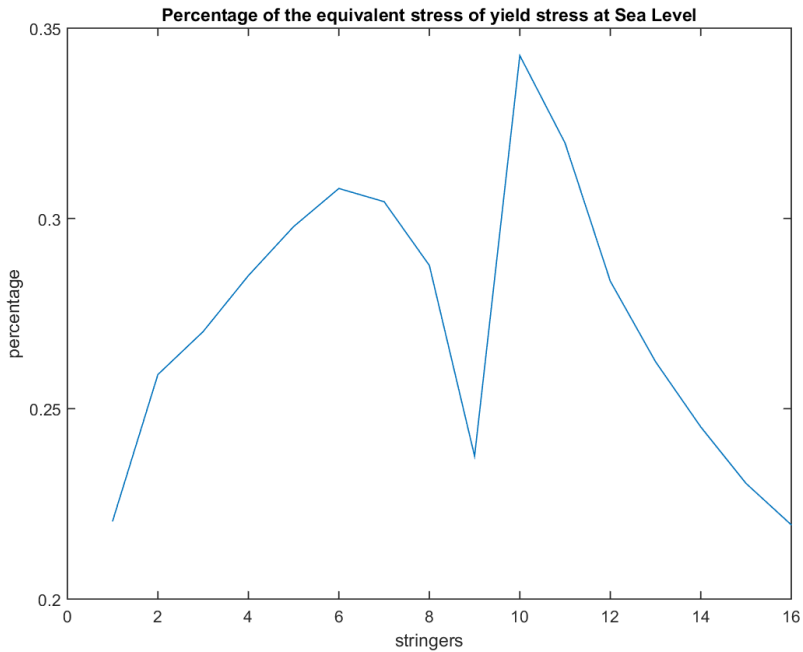


Figure E.1.3: Von Mises Equivalent/Yield percentage plot at sea level NHAA.

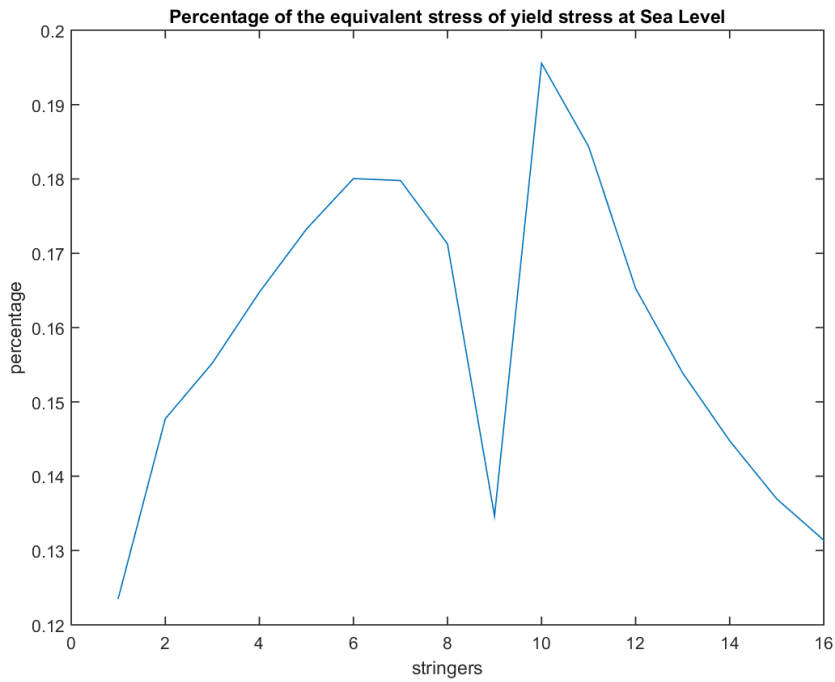


Figure E.1.4: Von Mises Equivalent/Yield percentage plot at sea level NLAA.

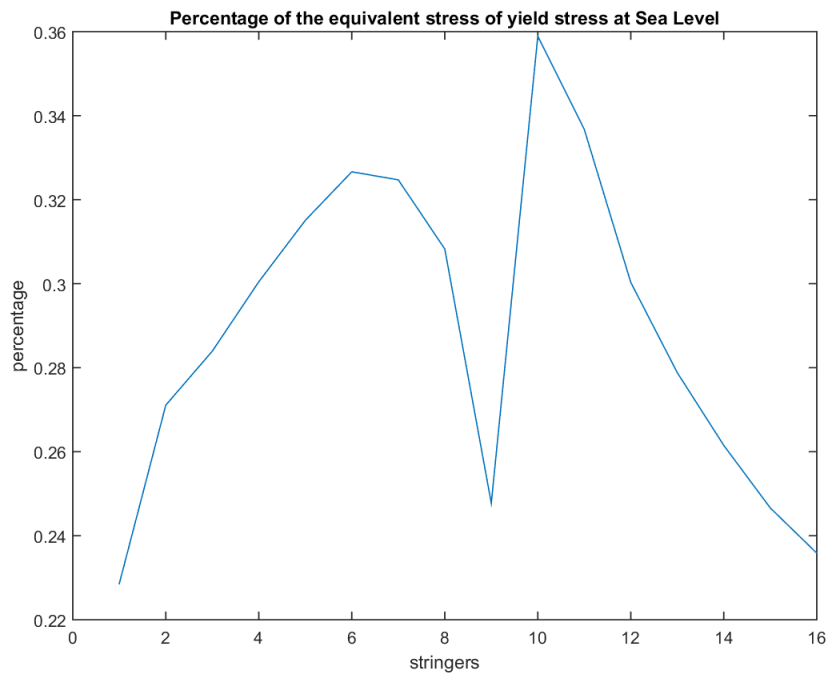


Figure E.1.5: Von Mises Equivalent/Yield percentage plot at sea level gust point 1.

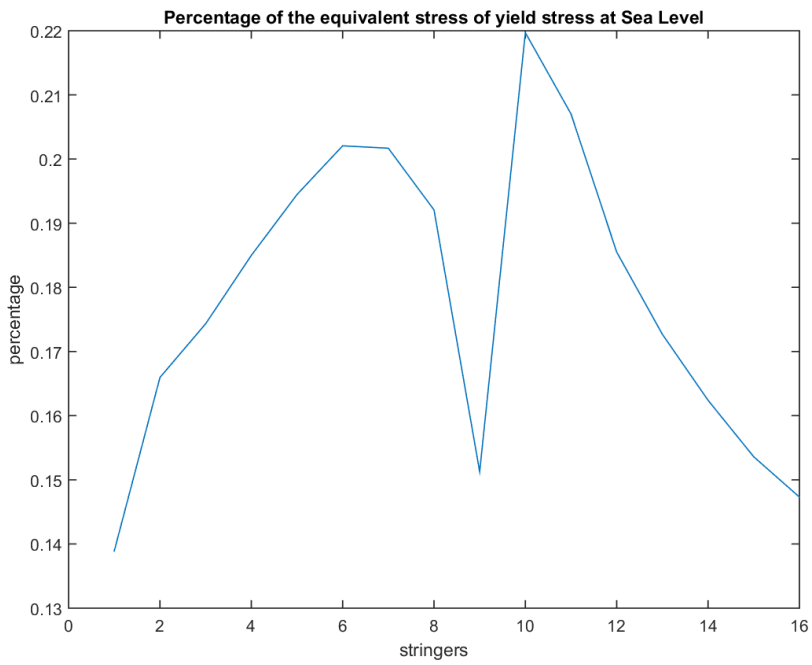


Figure E.1.6: Von Mises Equivalent/Yield percentage plot at sea level gust point 2.

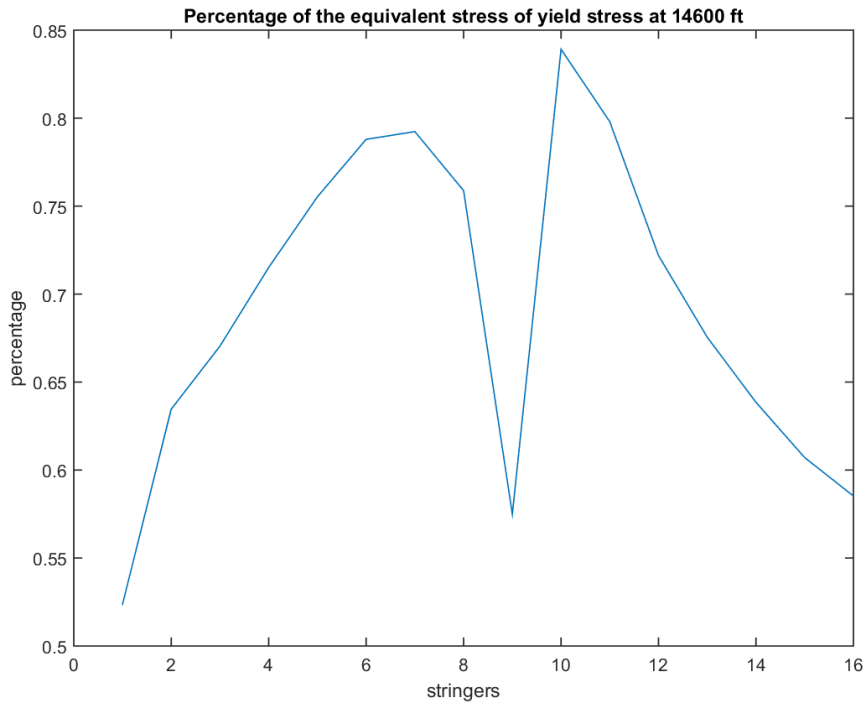


Figure E.1.7: Von Mises Equivalent/Yield percentage plot at ceiling PHAA.

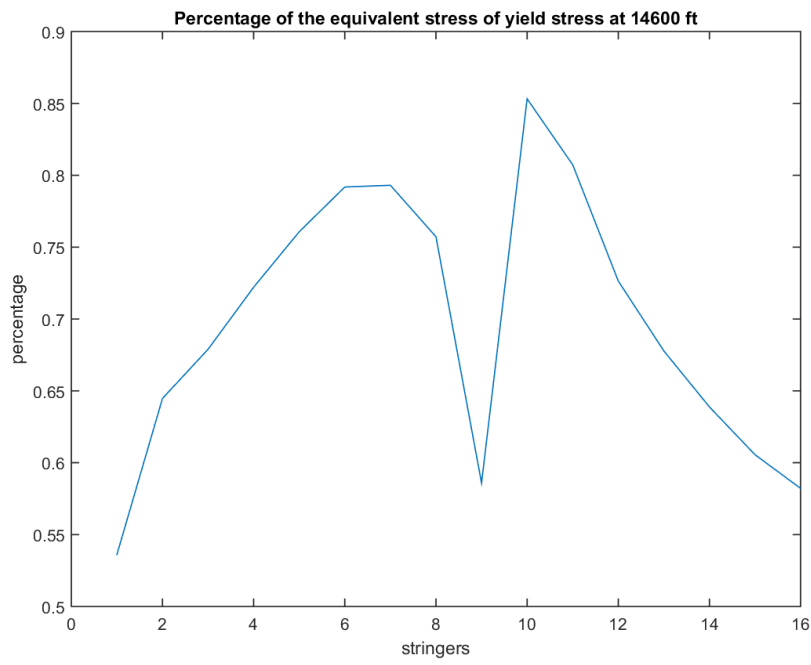


Figure E.1.8: Von Mises Equivalent/Yield percentage plot at ceiling PLAA.

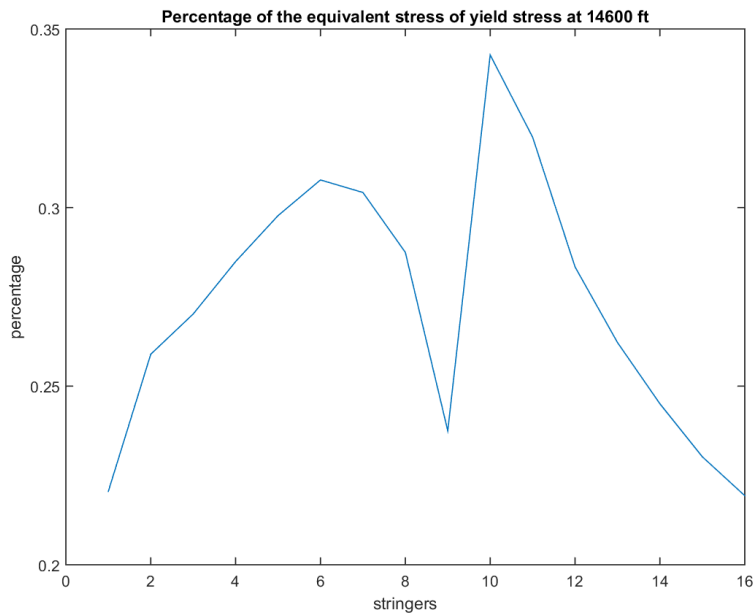


Figure E.1.9: Von Mises Equivalent/Yield percentage plot at ceiling NHAA.

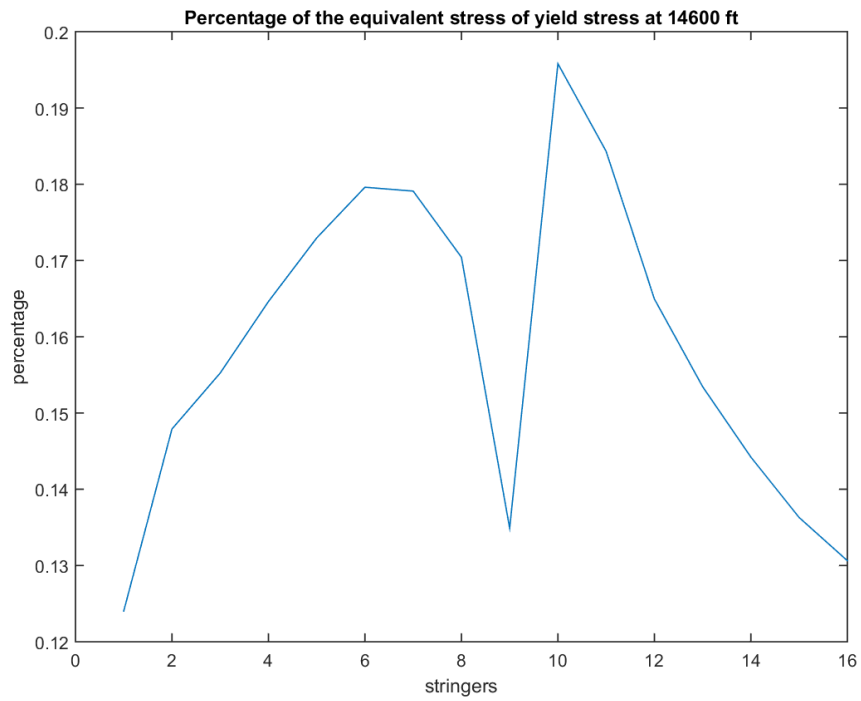


Figure E.1.10: Von Mises Equivalent/Yield percentage plot at ceiling NLAA.

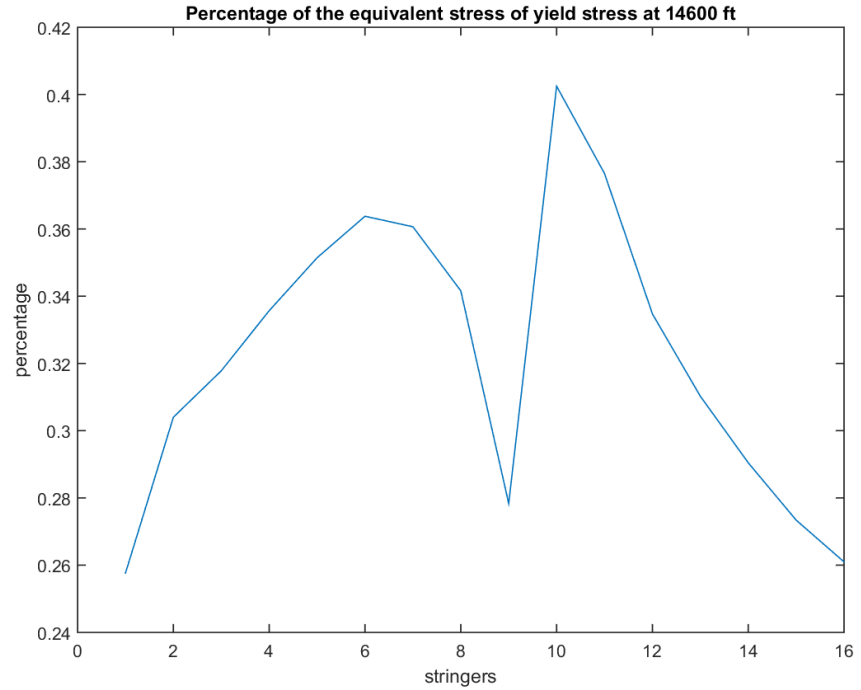


Figure E.1.11: Von Mises Equivalent/Yield percentage plot at ceiling gust point 1.

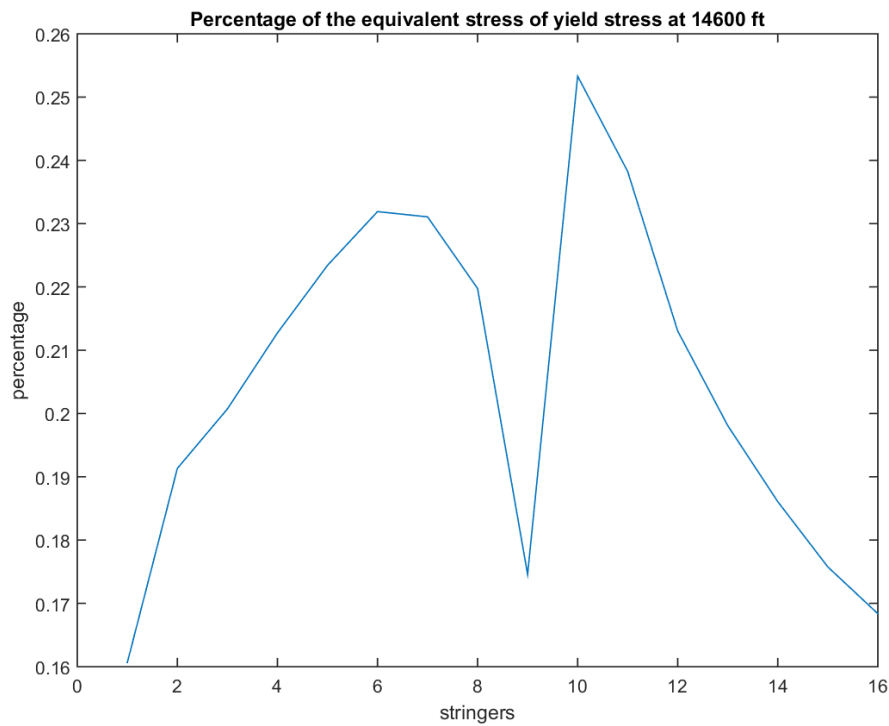


Figure E.1.12: Von Mises Equivalent/Yield percentage plot at ceiling gust point 2.

Section E.2: Direct Stress Skin Buckling

The figures presented below show the skin buckling behavior of the cross section under direct stresses. The given plots cover all critical points at both sea level and service ceiling conditions. The red lines indicated failure, while the blue lines indicated a passing skin section. For total stress values, see appendix C. The buckling test was applied only at the wing roots since it was determined previously that this point experienced the highest loading. The plots also show the percentage of the buckling load achieved at each skin panel.

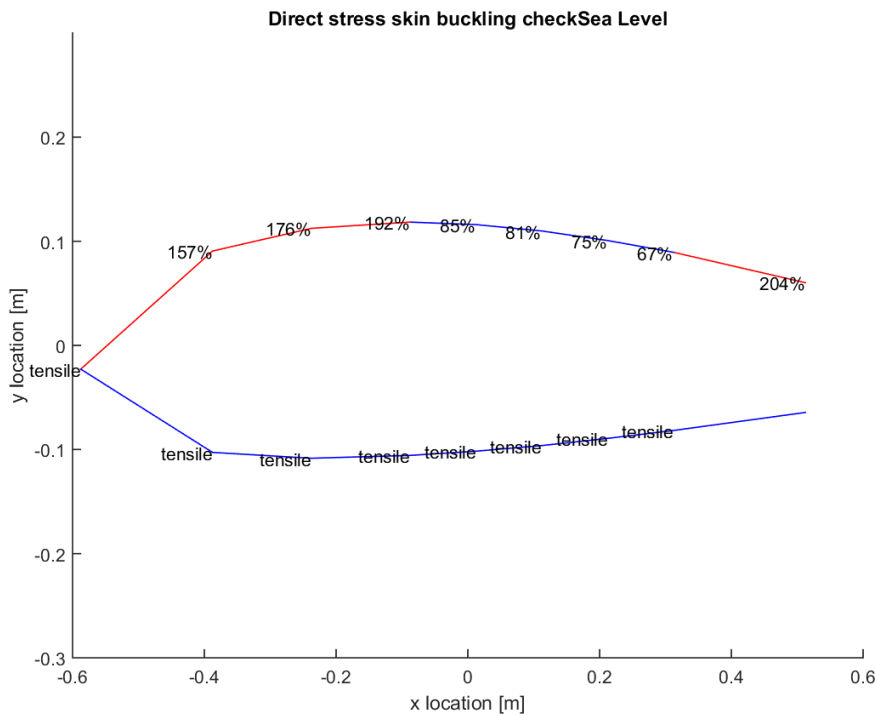


Figure E.2.1: Direct stress skin buckling plot at sea level PHAA.

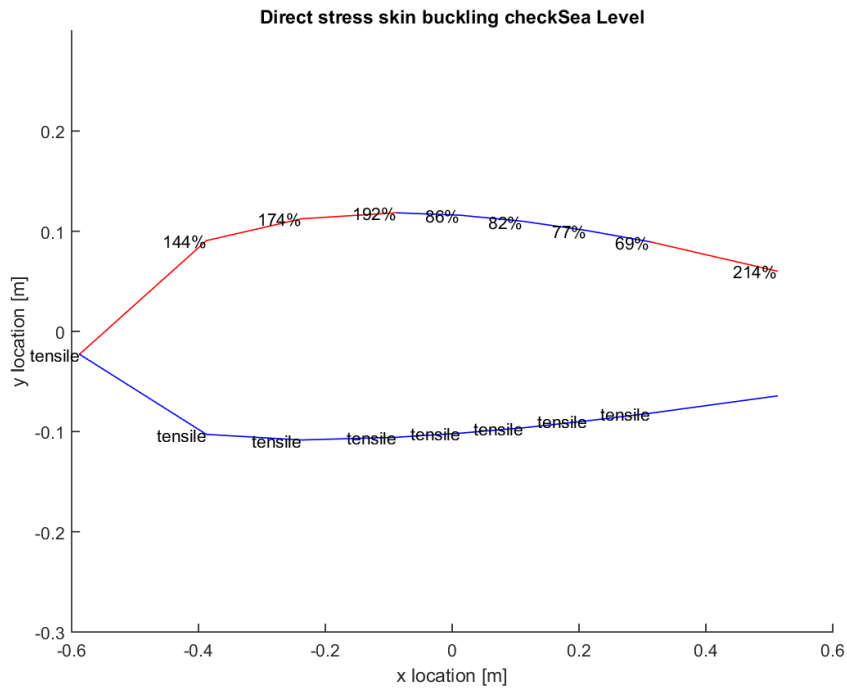


Figure E.2.2: Direct stress skin buckling plot at sea level PLAA.

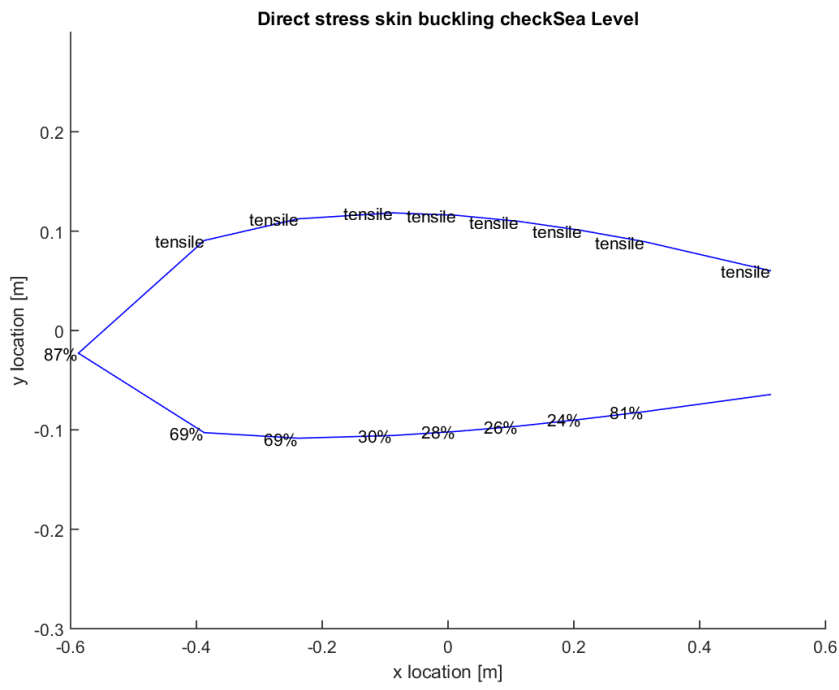


Figure E.2.3: Direct stress skin buckling plot at sea level NHAA.

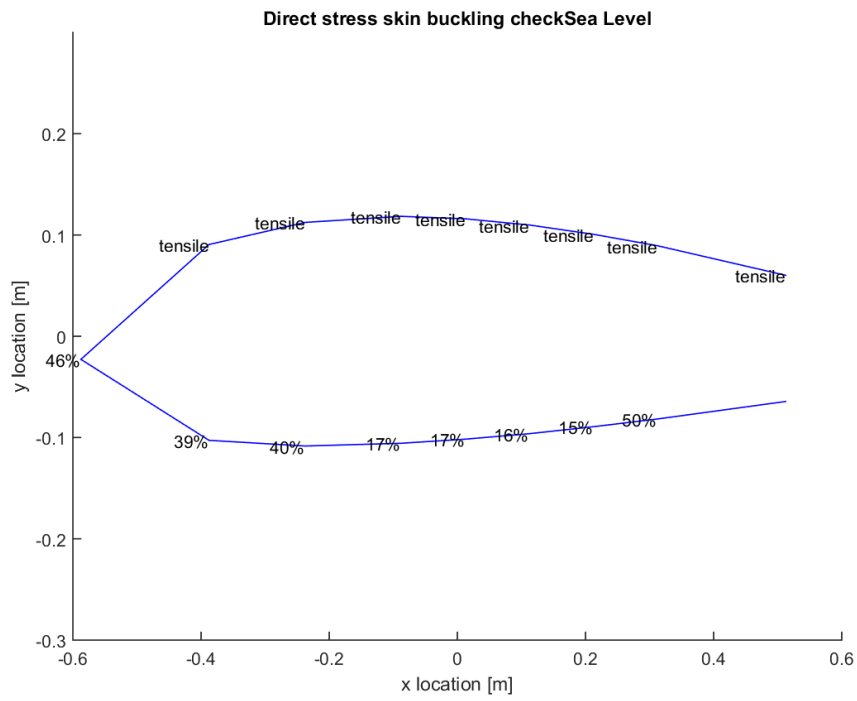


Figure E.2.4: Direct stress skin buckling plot at sea level NLAA.

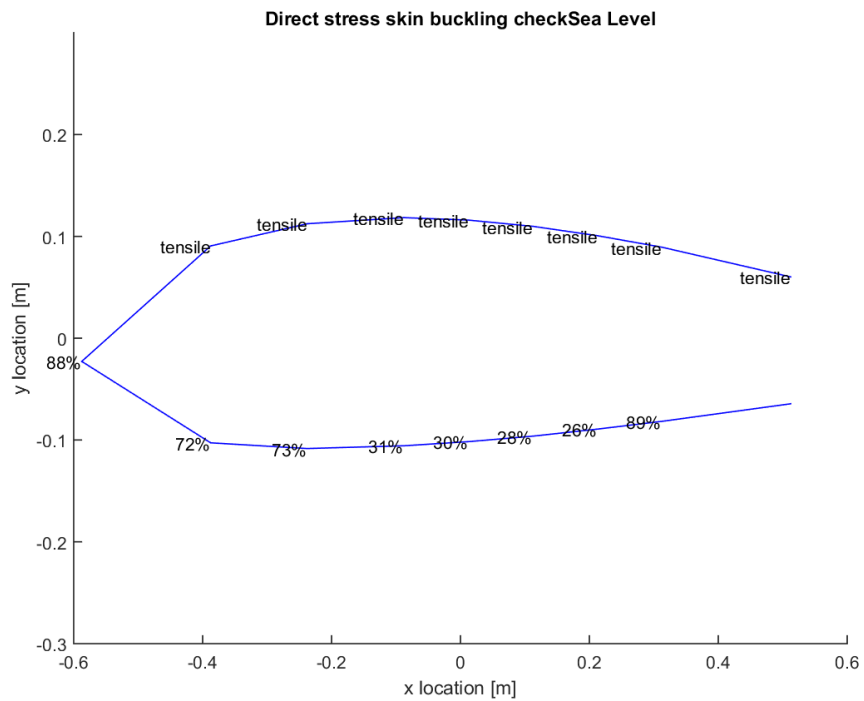


Figure E.2.5: Direct stress skin buckling plot at sea level gust point 1.

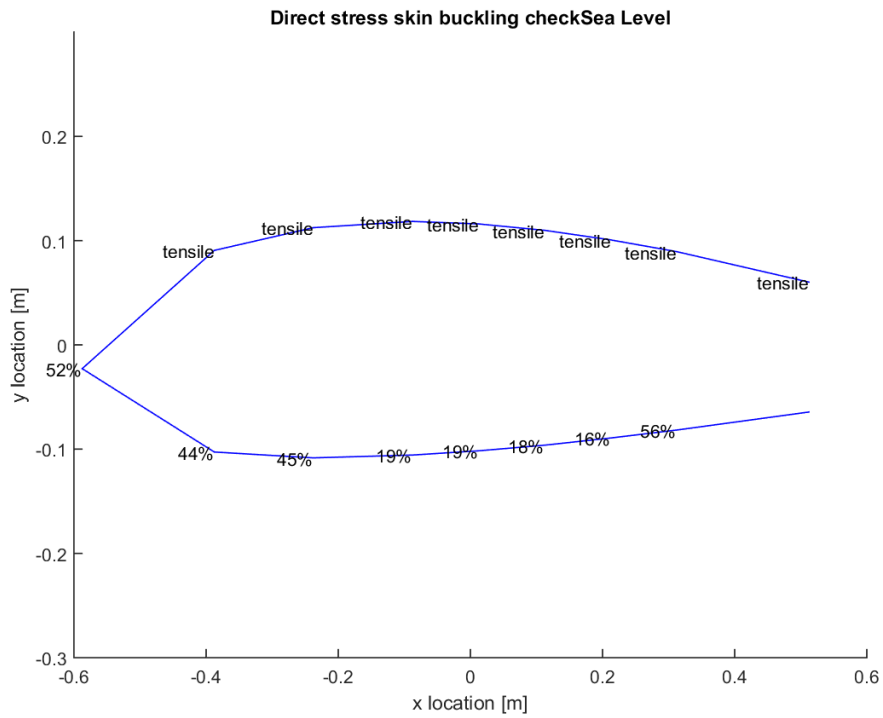


Figure E.2.6 Direct stress skin buckling plot at sea level gust point 2.

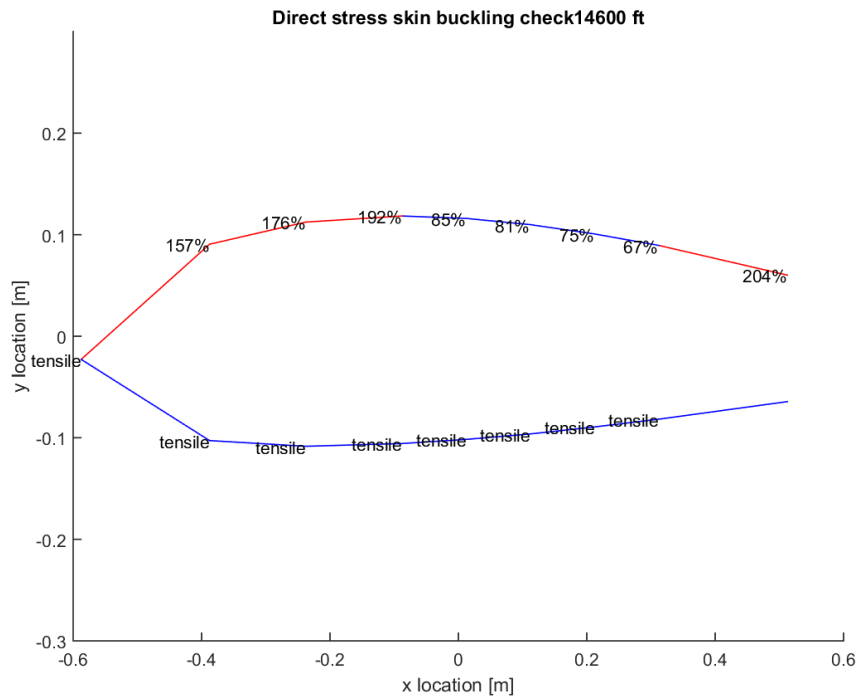


Figure E.2.7: Direct stress skin buckling plot plots at ceiling PHAA.

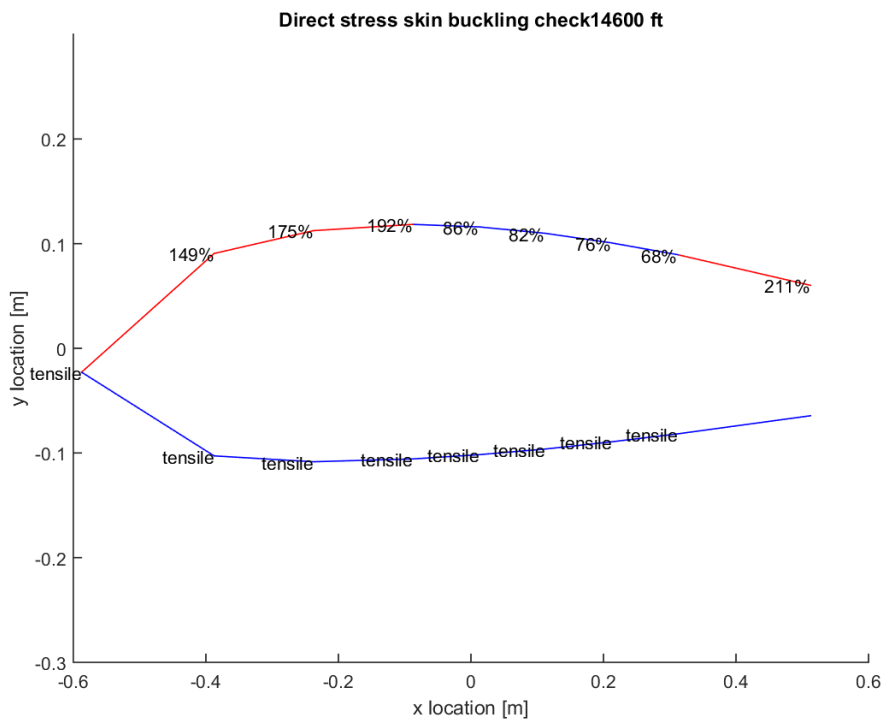


Figure E.2.8: Direct stress skin buckling plot plots at ceiling PLAA.

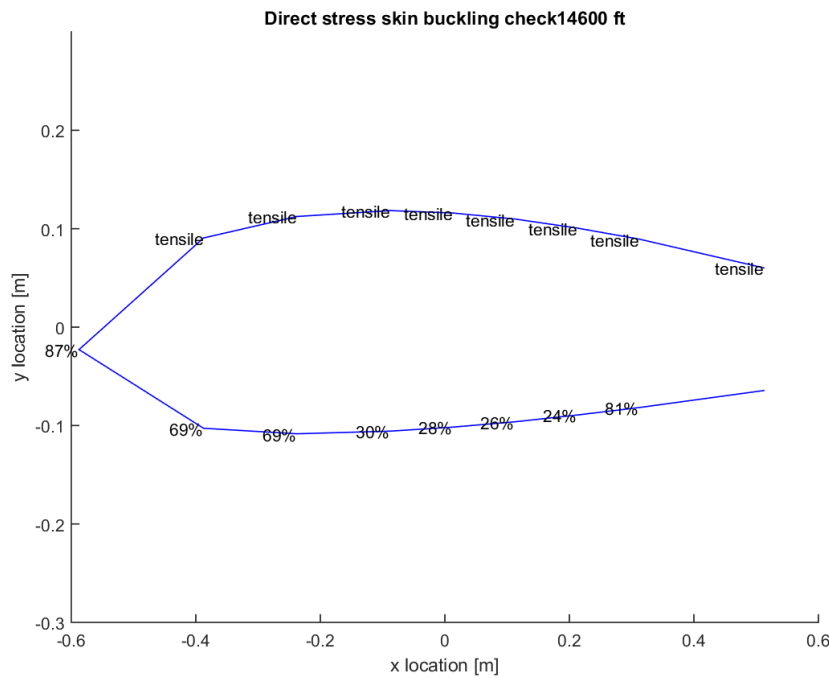


Figure E.2.9: Direct stress skin buckling plot at ceiling NHAA.

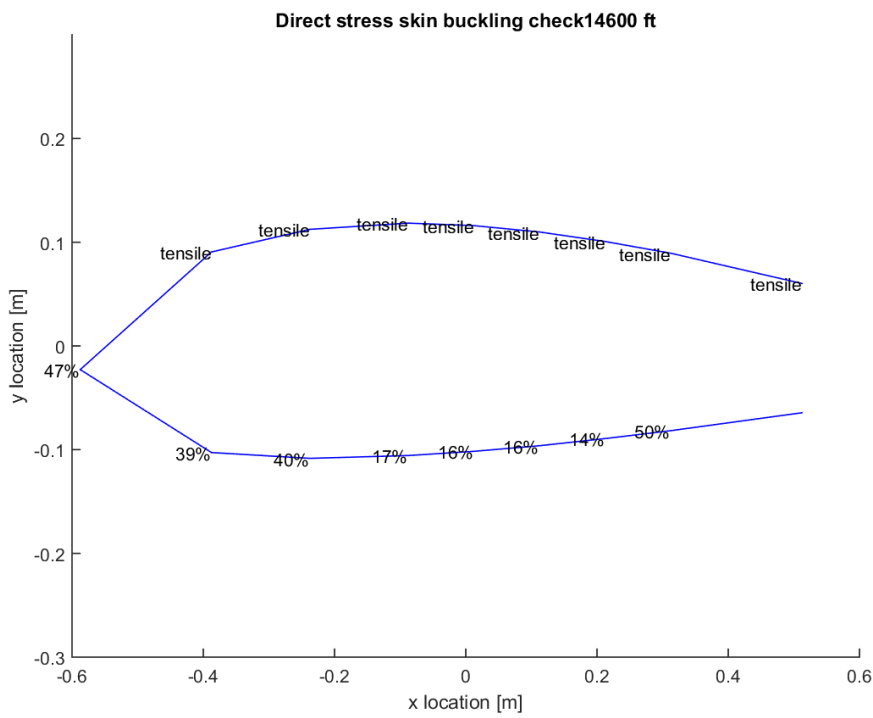


Figure E.2.10: Direct stress skin buckling plot at ceiling NLAA.

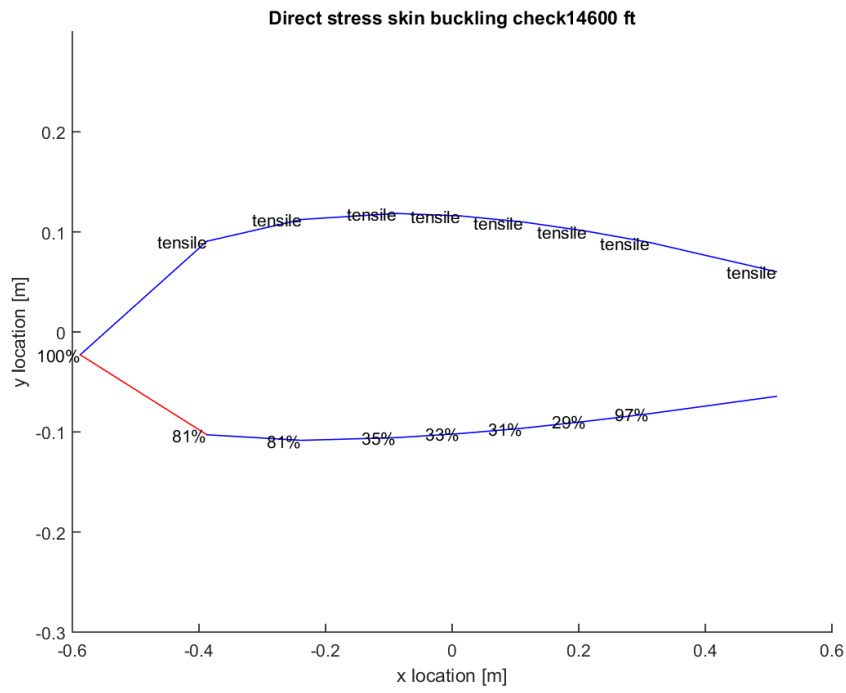


Figure E.2.11: Direct stress skin buckling plot at ceiling gust point 1.

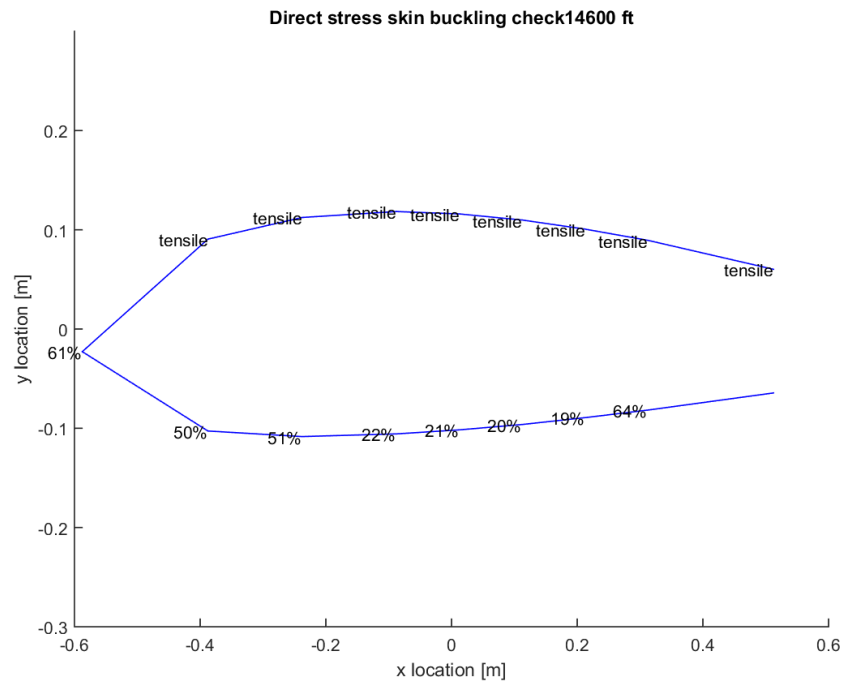


Figure E.2.12: Direct stress skin buckling plot at ceiling gust point 2.

Appendix F: Maneuvering

The aircraft loading requirements listed in the specifications defined the maximum load factors that were designed for. These load factors would occur during various maneuvers, including climbing, diving, banking, and intermediate pull out maneuvers. Climbing and diving simply refer to increases and decreases in flight altitude respectively. Climbing results in a positive load factor to facilitate the positive lift necessary to accelerate the plane upwards, while diving generates a negative load factor for similar reasons. A banking maneuver refers to a constant elevation turn. In this case, the aircraft is accelerated into turning by pitching the aircraft. This creates an imbalanced lift force, a portion of which acts centripetally to provide the turning acceleration. While this additional acceleration does provide increased load factors, in general, these load factors are smaller than those for climbing and diving maneuvers are. Another point of high loading occurs in pull-out. Pull-out occurs during the end of a dive when flight becomes steadied, necessitating additional acceleration to change from dive to steady forward movement. This maneuver once again makes use of centripetal lift forces to reorient the aircraft. Additionally, in both banking and the pull-out maneuvers, sharper turns (i.e. lower turn radii) result in dramatically higher load factors. The maneuvering limits discussed previously were assumed to be the highest load factors that would be encountered by the aircraft. Additionally, each of the critical points defined along the V-n diagrams corresponded to the climbing, diving, and pull-out maneuvers discussed here. Fig. F.1 and F.2 depict the pull-out and banking maneuvers. Fig. F.3 and F.4 depict climbing and descent.

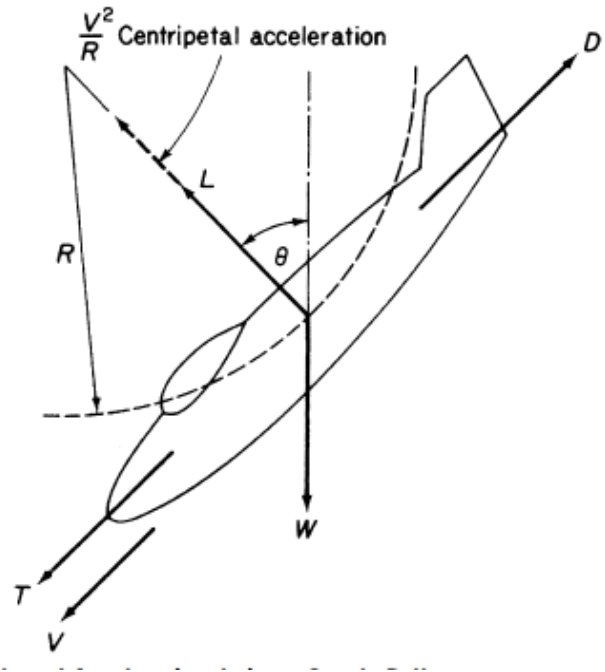


Figure F.1: Pull-out maneuvering at end of dive [4].

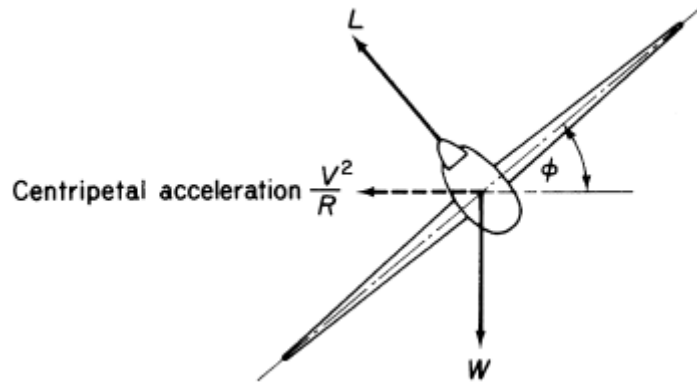


Figure F.2: Banking maneuvering to provide in plane turning [4].

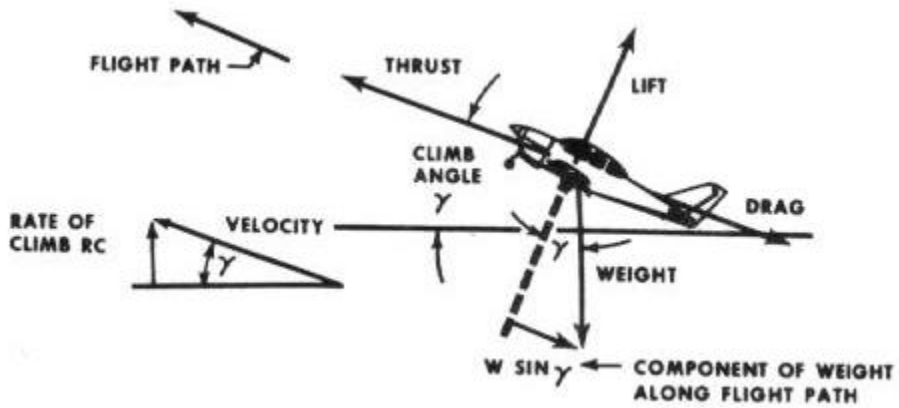


Figure F.3: Aircraft climb, acceleration leads to additional positive load factor [5].

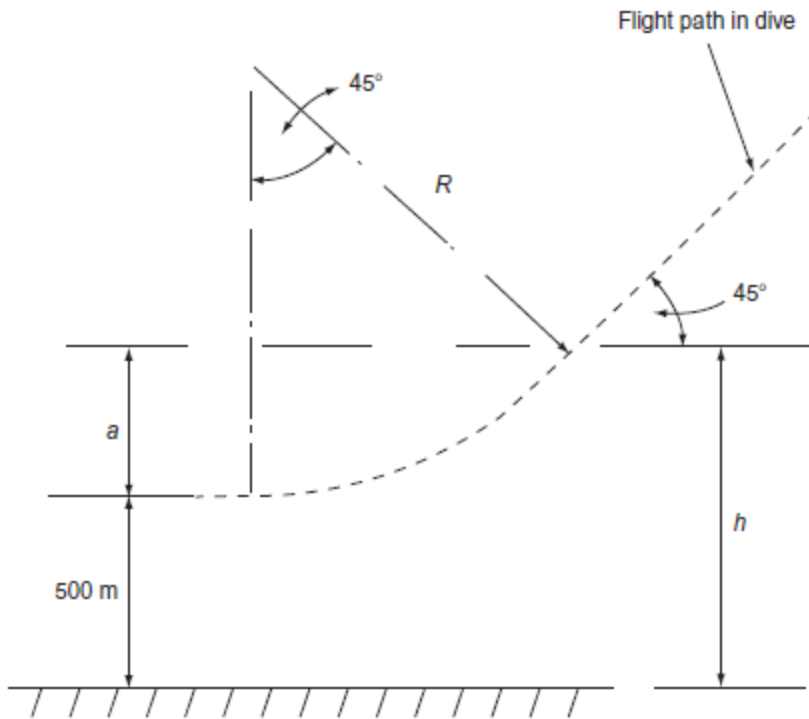


Figure F.4: Aircraft descent and steady pull-out.

The maneuver depicted in Fig. F.4 specifically shows both a dive and a steady pull-out done to reposition the aircraft at a lower altitude. The dive itself provides a negative load factor on the aircraft due to the direction of its acceleration. The pull-out turn, however, generates a positive load factor on

the airplane. At this point, the lift vector accelerates the aircraft centripetally, which counteracts the previous downward acceleration from gravity.

Appendix G: COMSOL Multiphysics Results

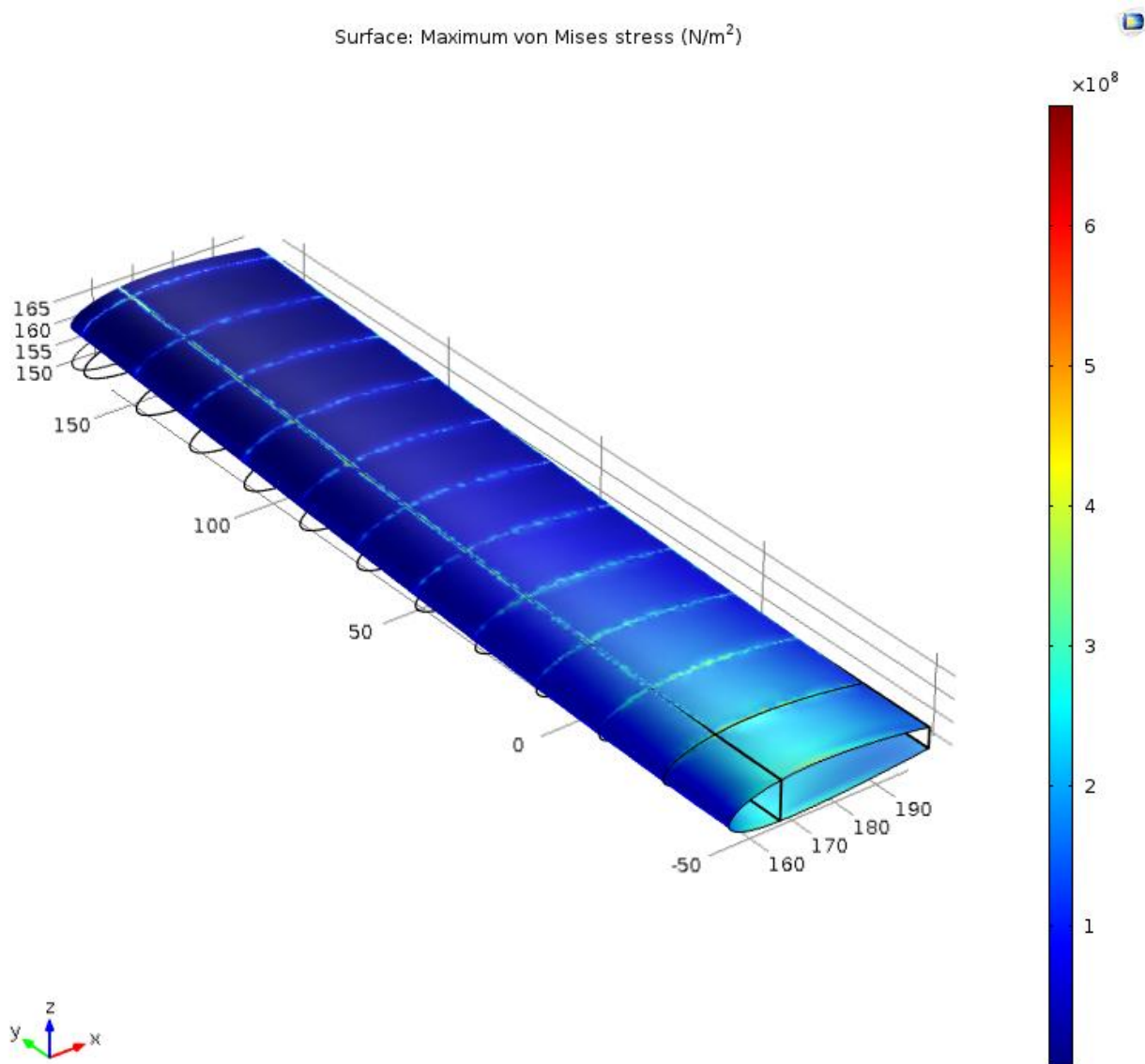


Figure G.1: COMSOL Multiphysics finite element analysis for stress and deflection at PLAA

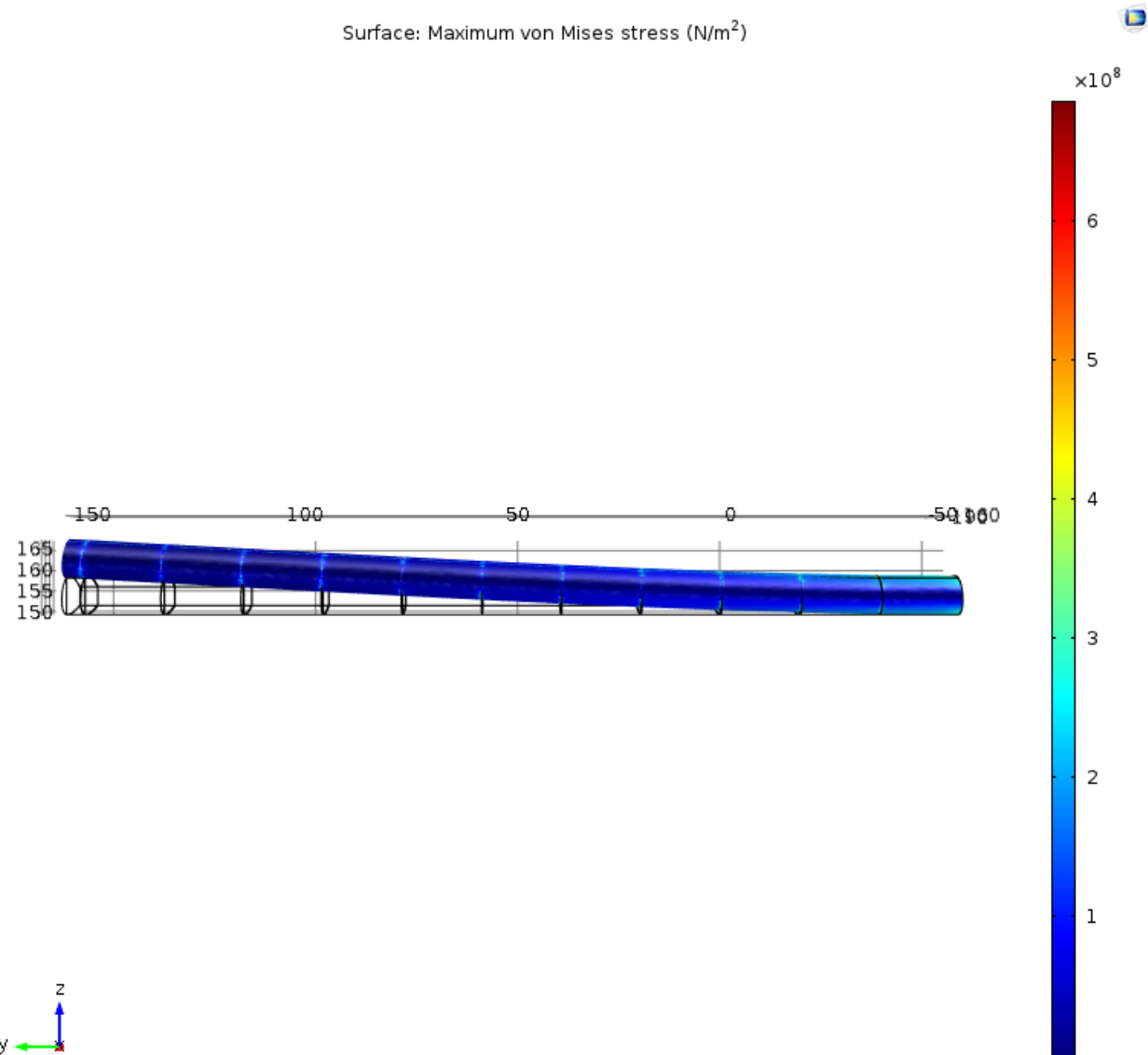


Figure G.2: Deflection at PLAA

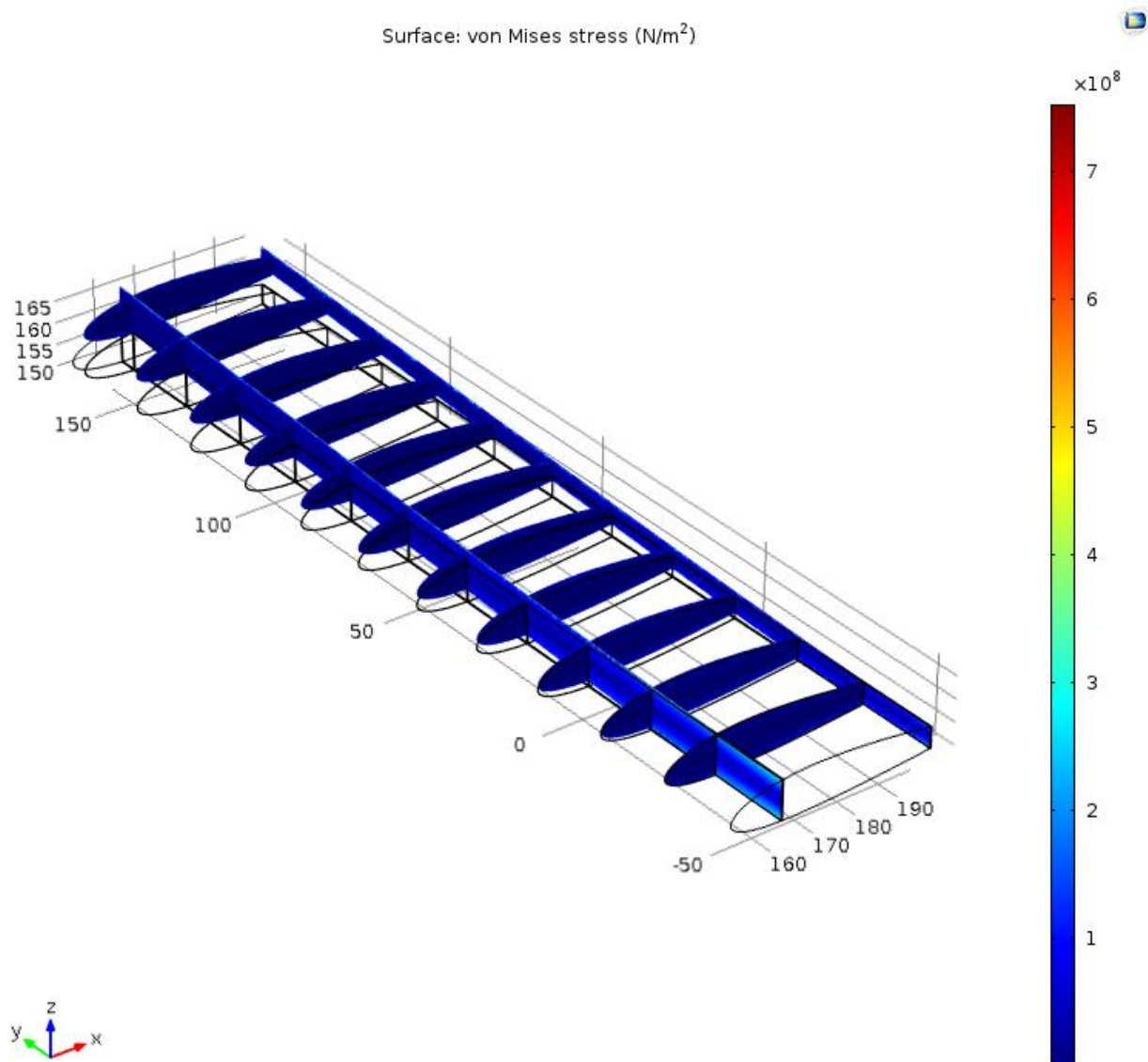


Figure G.3: Internal stress distribution at PLAA

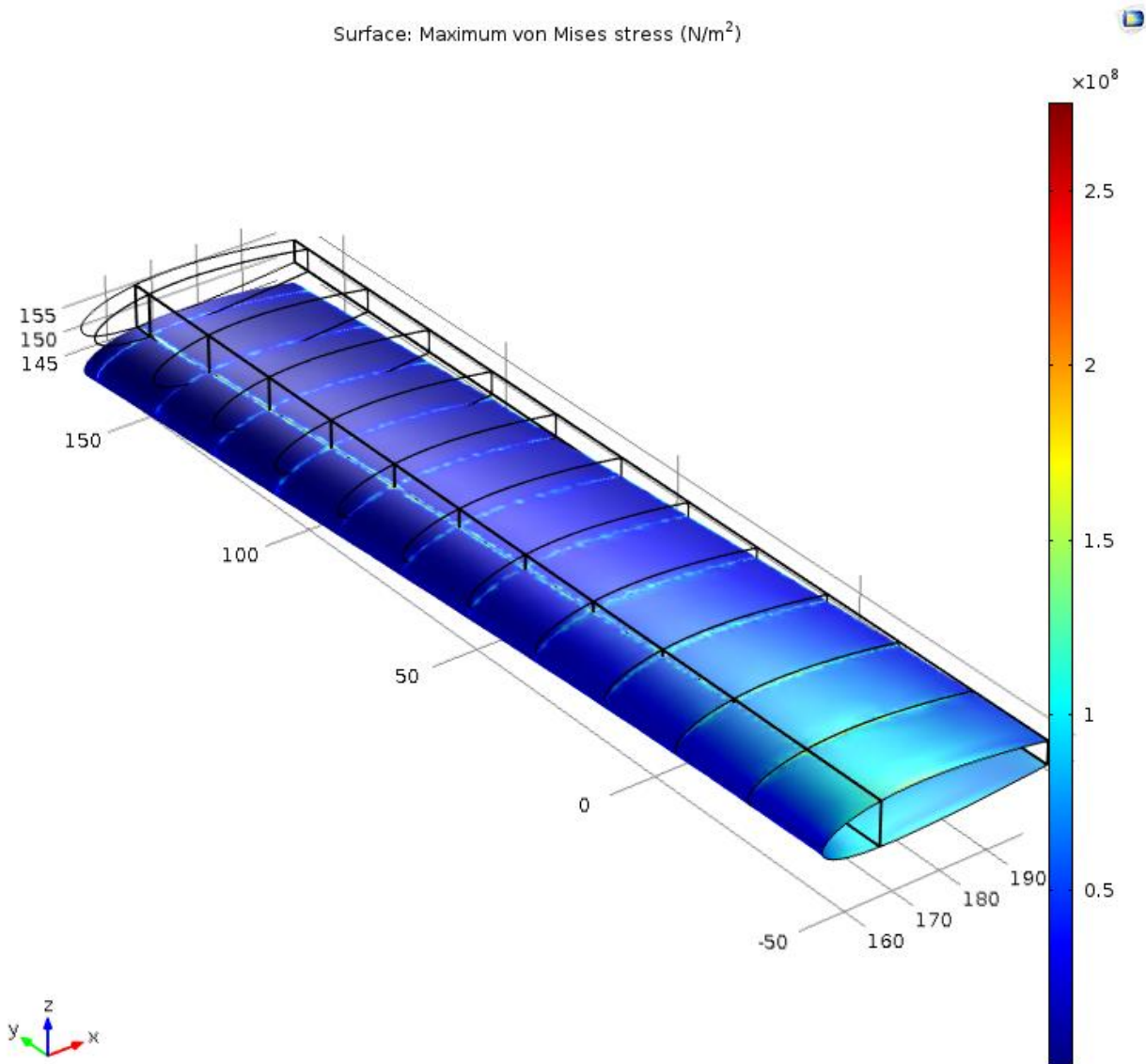


Figure G.4: COMSOL Multiphysics finite element analysis for stress and deflection at NHAA

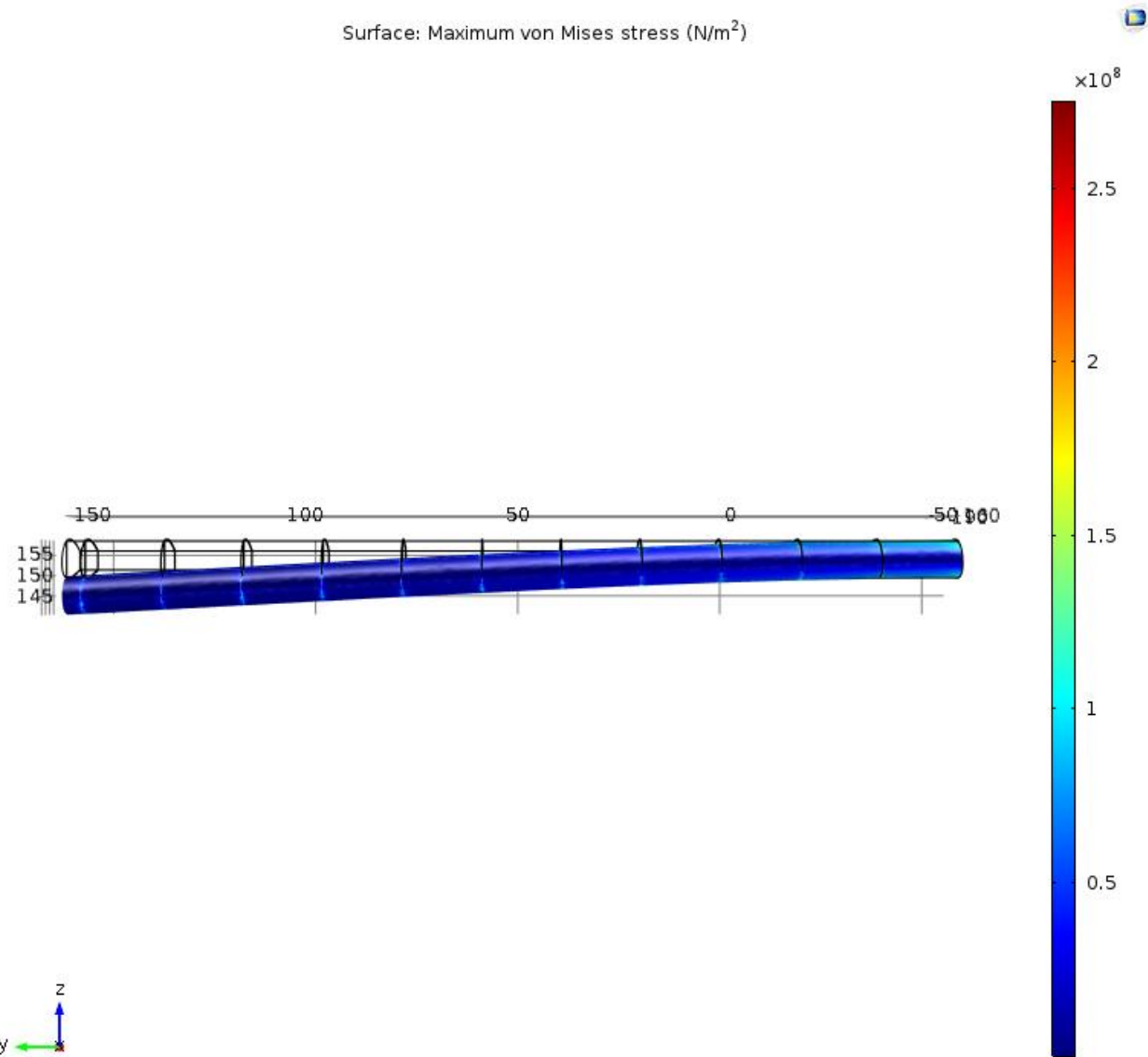


Figure G.5: Deflection at NHAA

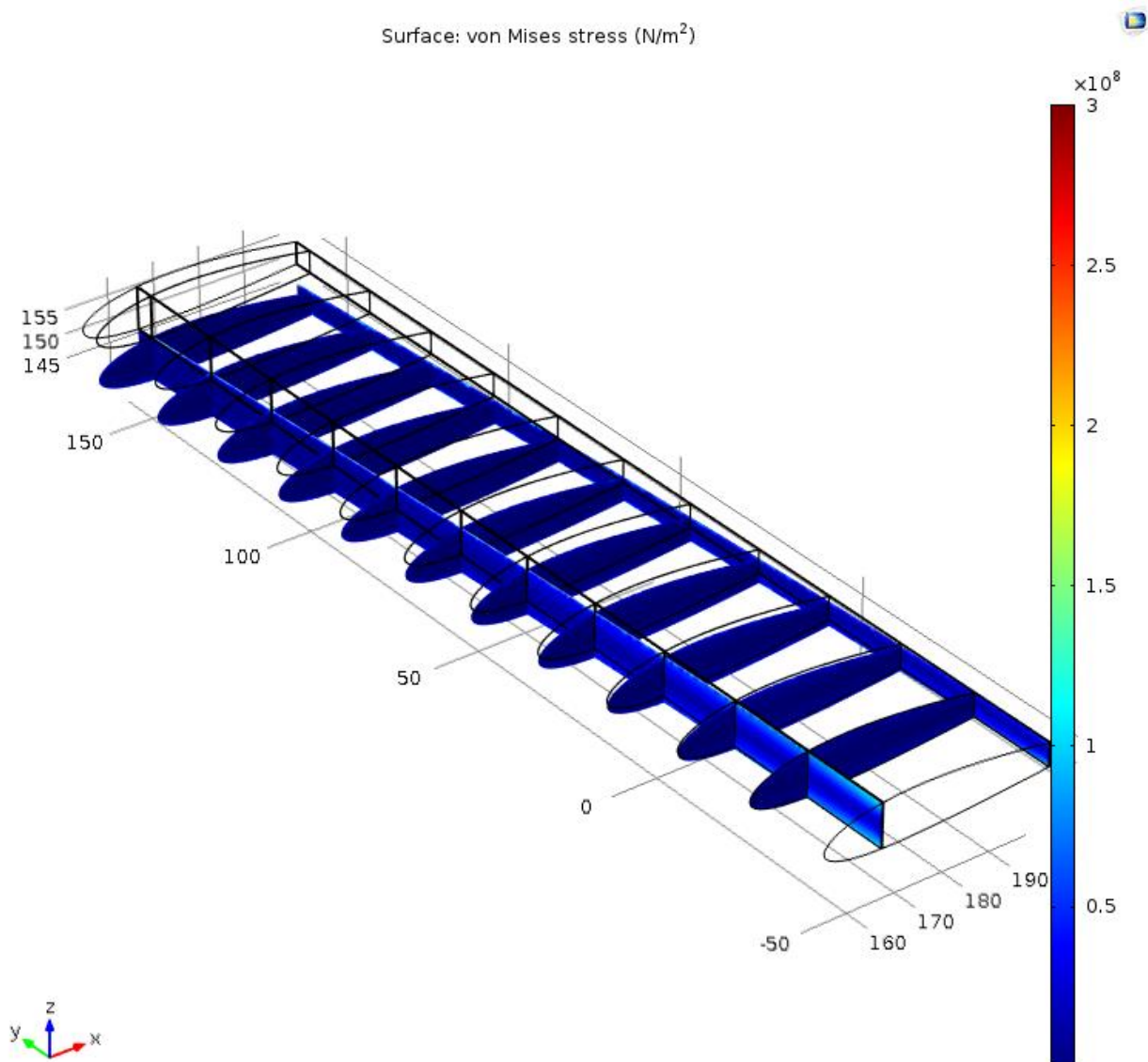


Figure G.6: Internal stress distribution at NHAA

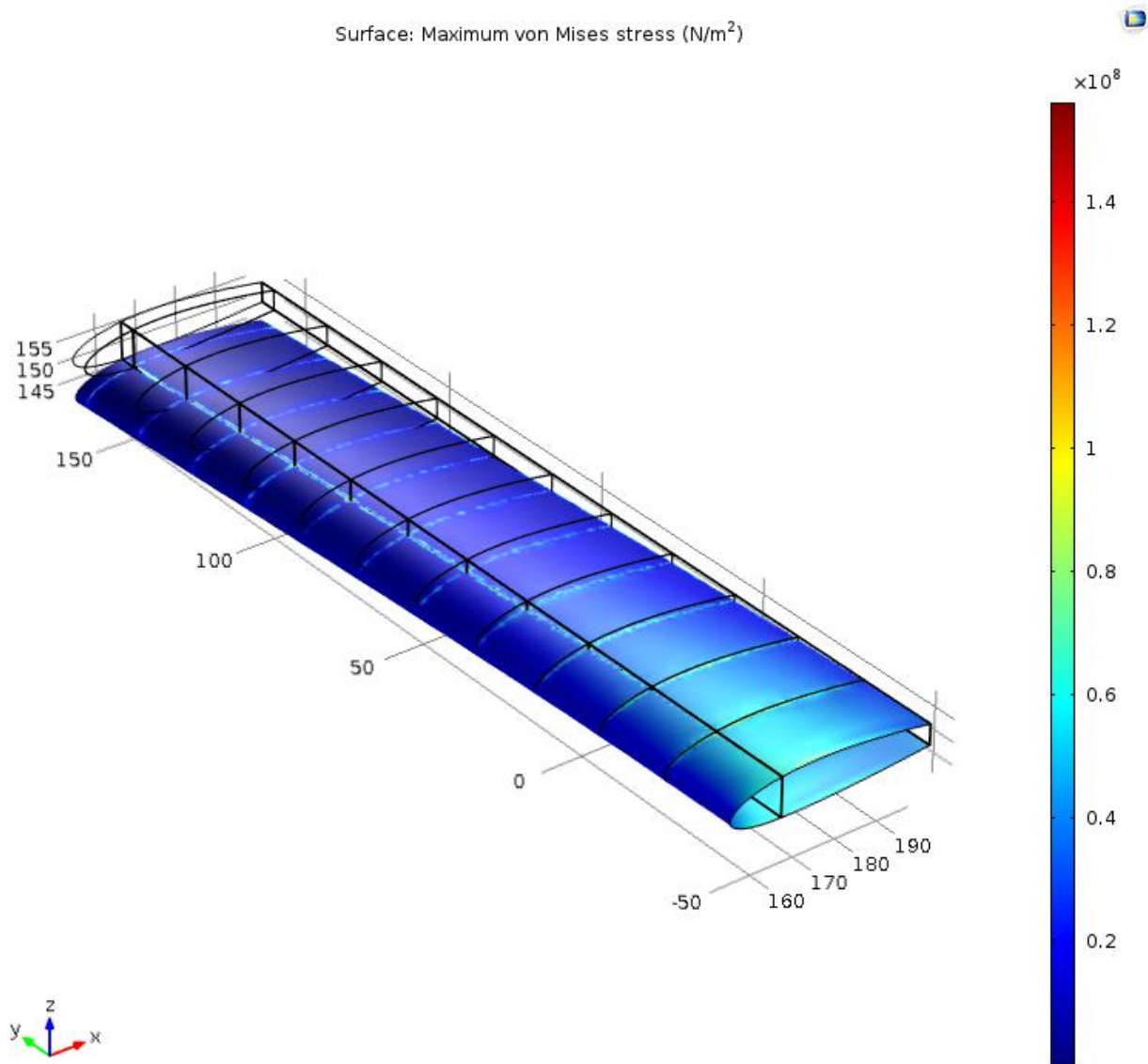


Figure G.7: COMSOL Multiphysics finite element analysis for stress and deflection at NLAA

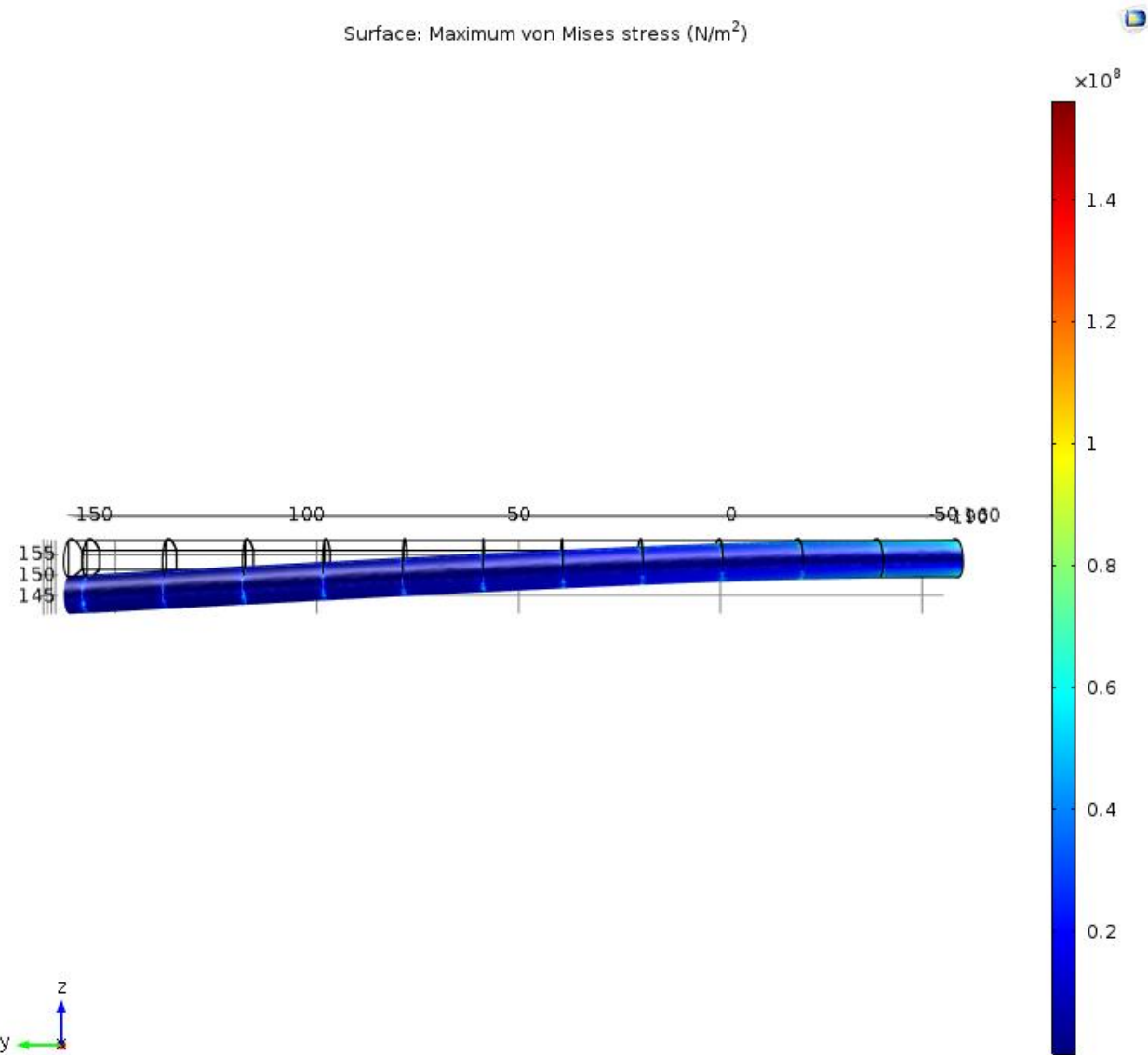


Figure G.8: Deflection at NLAA

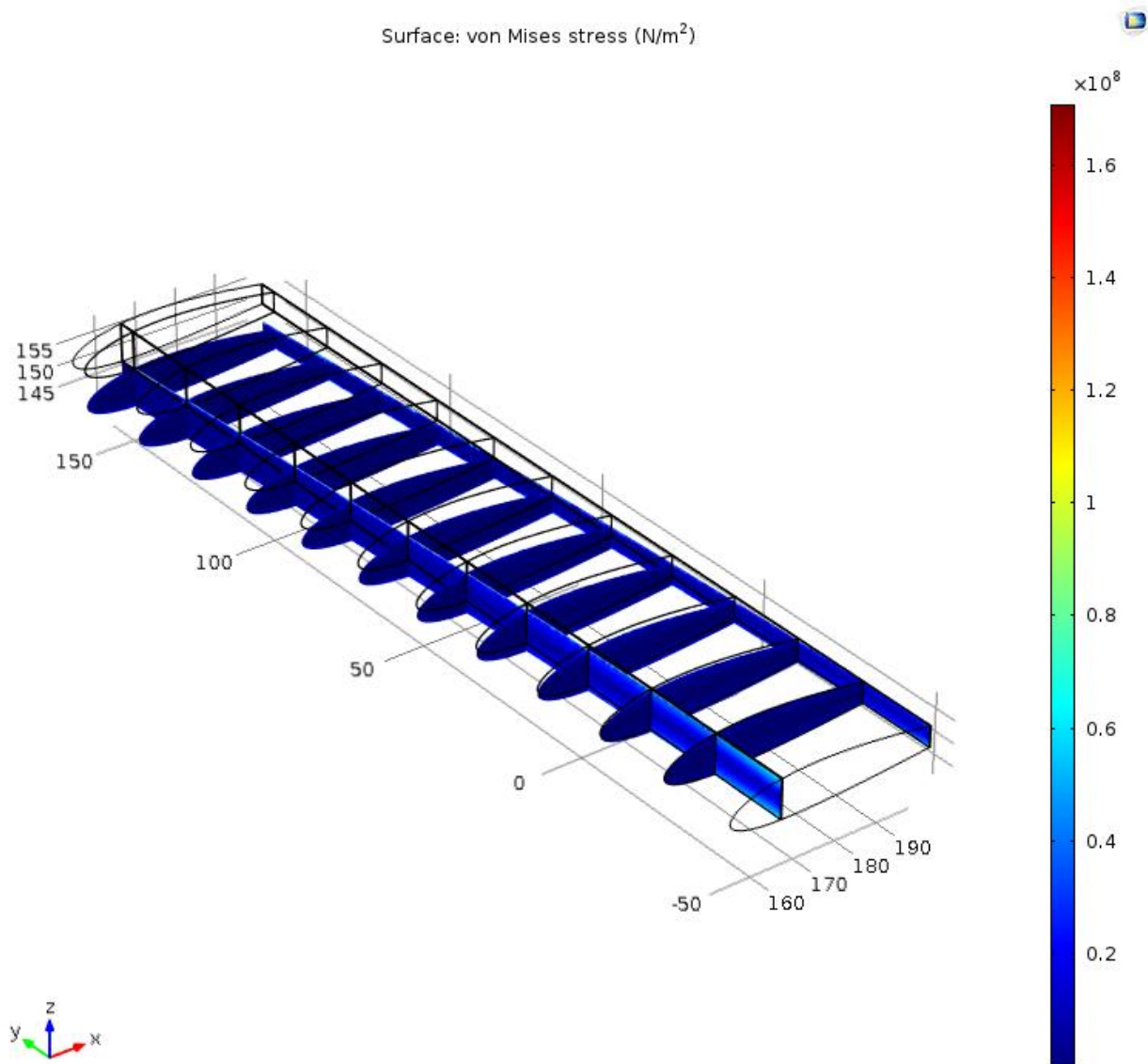


Figure G.9: Internal stress distribution at NLAA

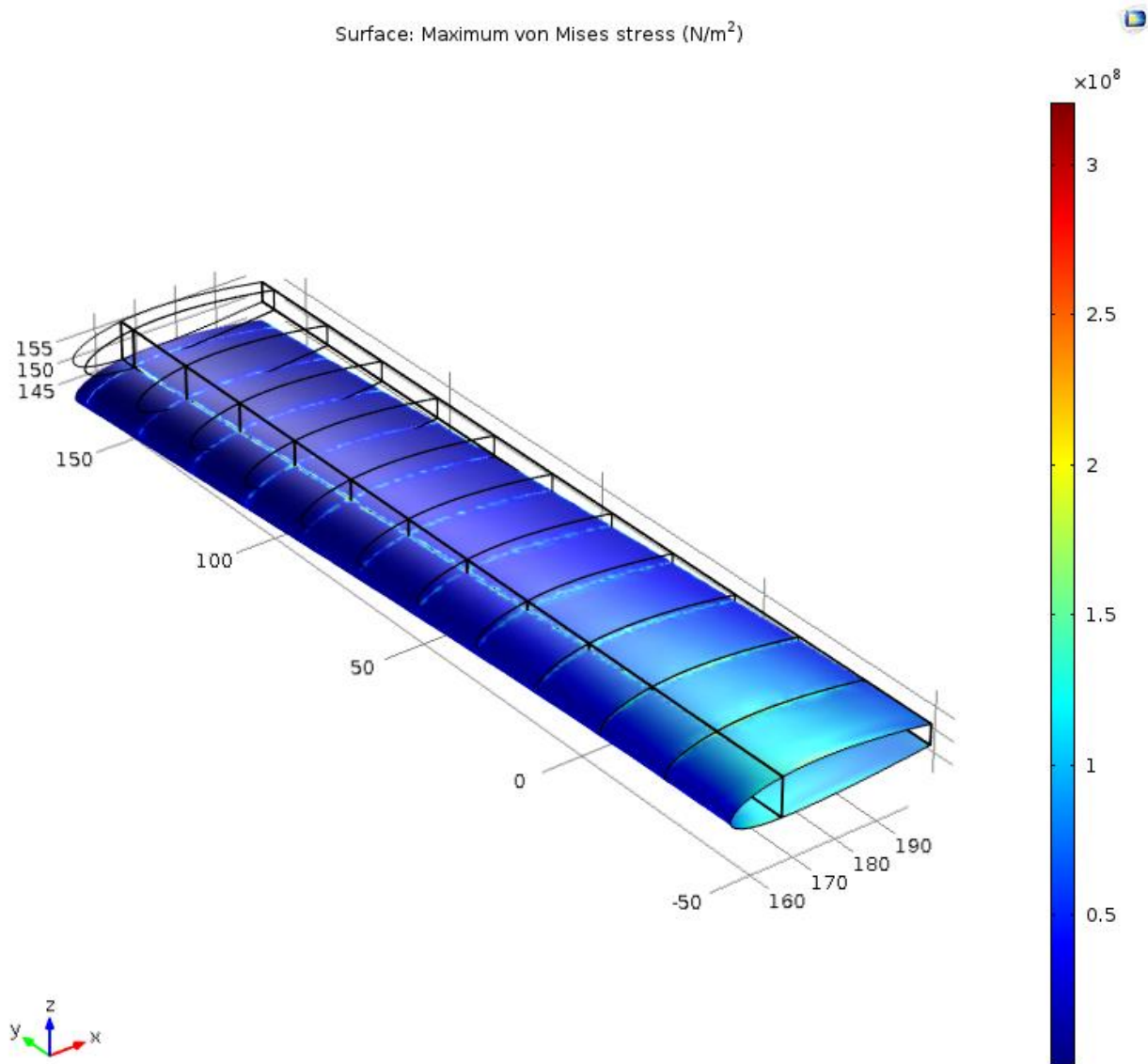


Figure G.10: COMSOL Multiphysics finite element analysis for stress and deflection at gust point 1

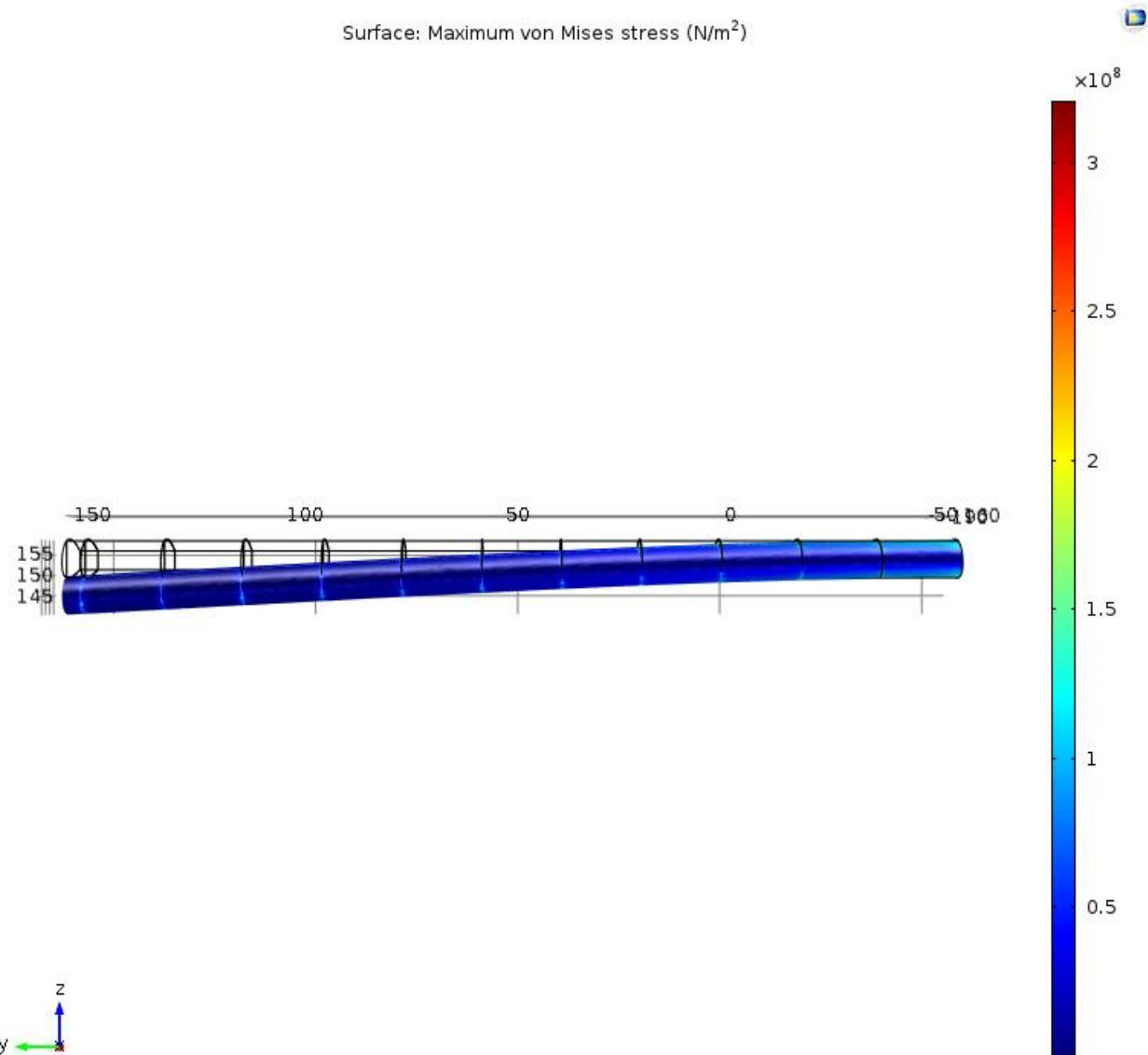


Figure G.11: Deflection at gust point 1

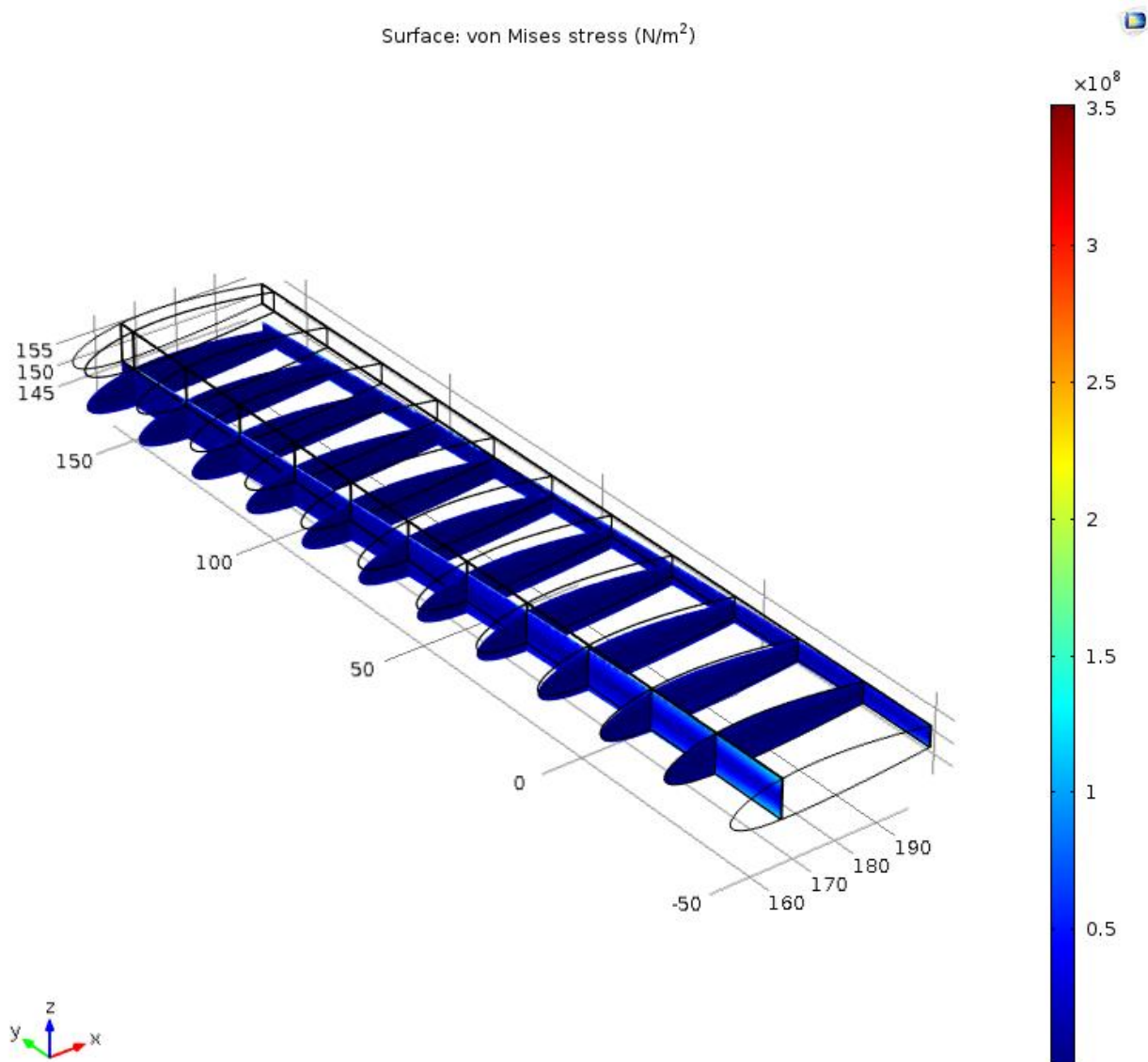


Figure G.12: Internal stress distribution at gust point 1

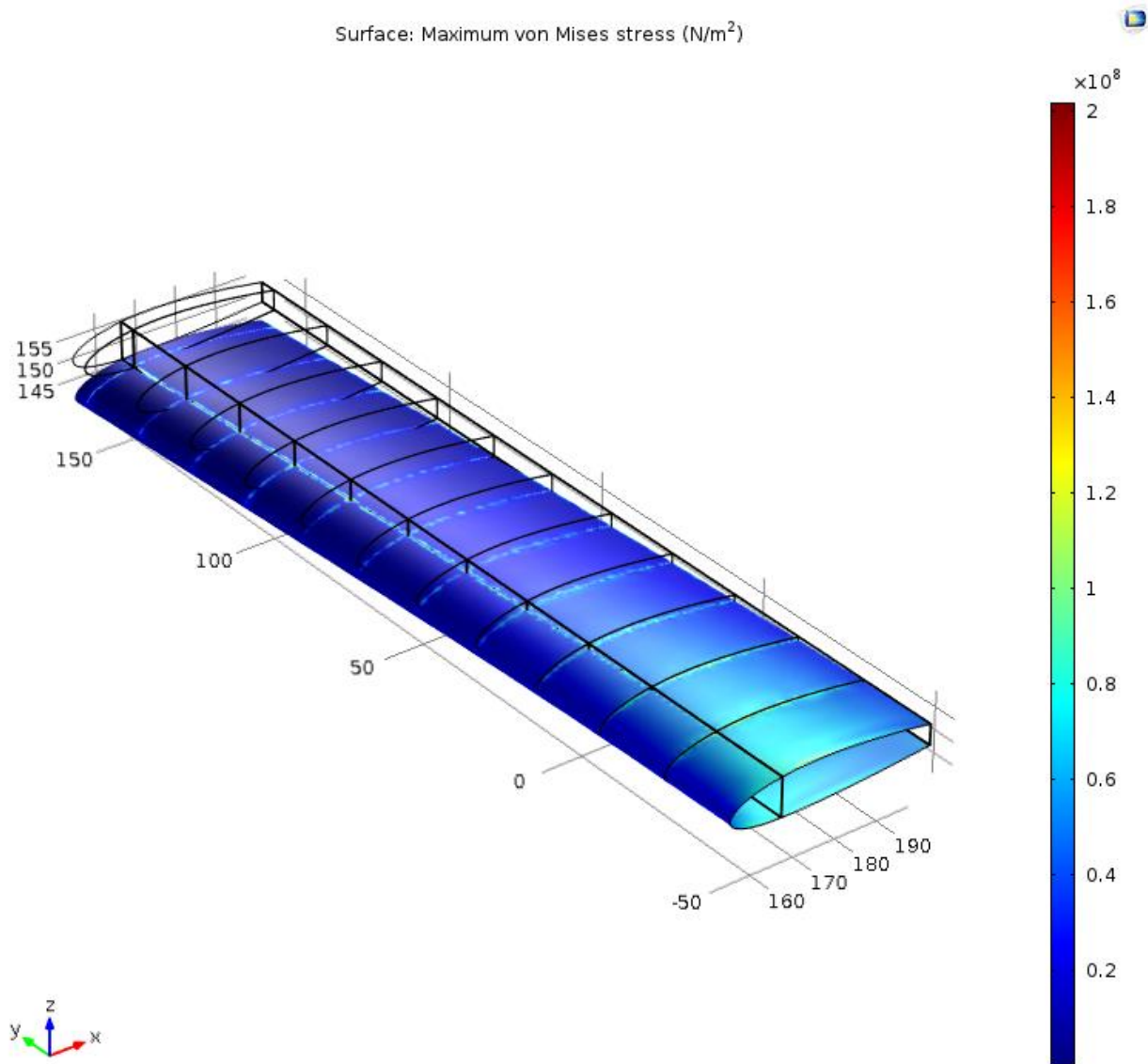


Figure G.13: COMSOL Multiphysics finite element analysis for stress and deflection at gust point 2

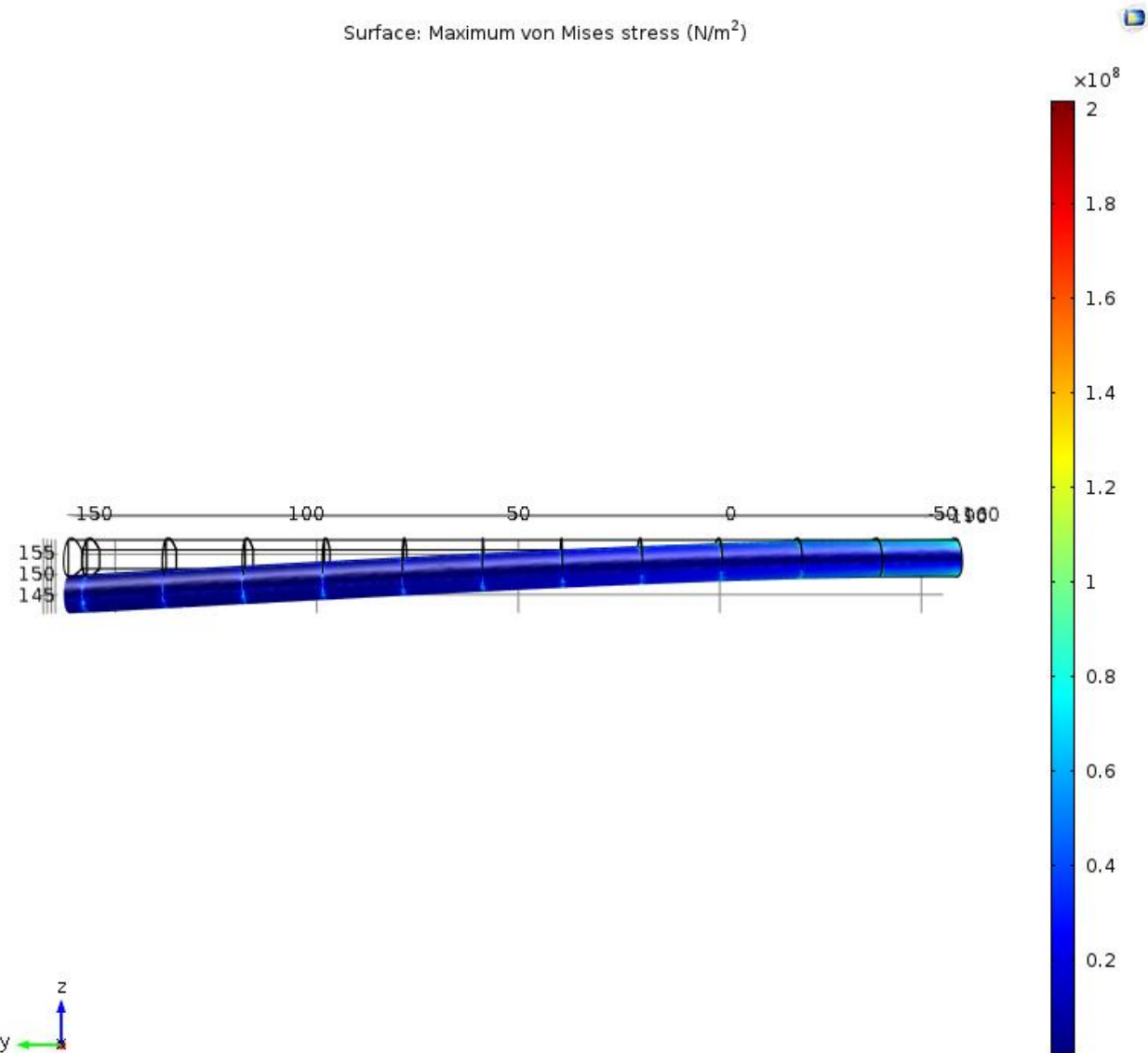


Figure G.14: Deflection at gust point 2

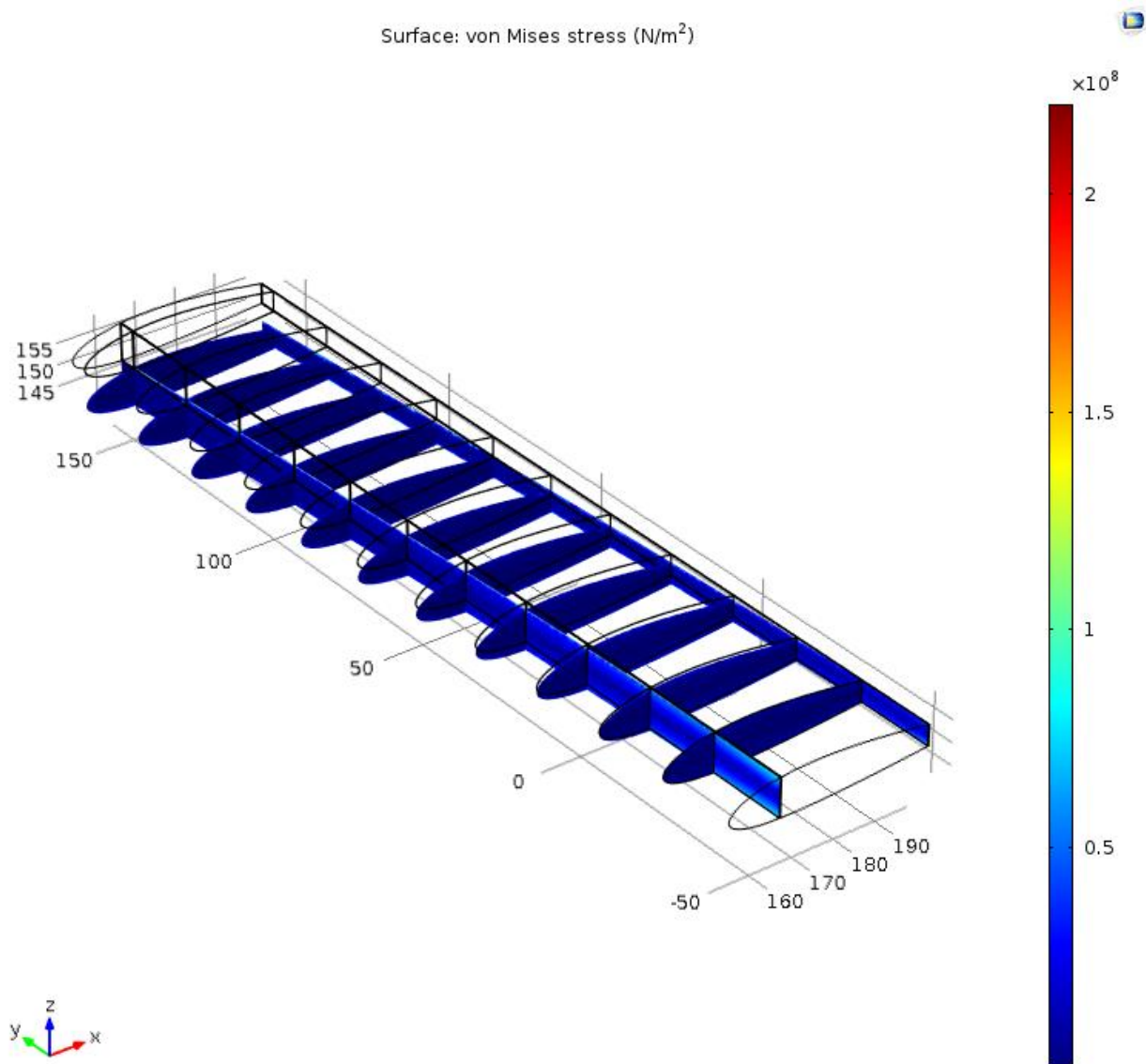


Figure G.15: Internal stress distribution at gust point 2

Reference

- [1] "U.S. Standard Atmosphere." *U.S. Standard Atmosphere*. The Engineering Toolbox, n.d. Web. 10 Apr. 2016.
- [2] Kim, Nam-Ho. "Von Mises Criterion." University of Florida, Web. 15 May 2016.
- [3] "Aluminum 2024 T3." ASM Material Data Sheet. Aerospace Specification Metals Inc., n.d. Web. 15 May 2016.
- [4] Megson, T. H. G. Aircraft Structures for Engineering Students. 5th ed. Oxford: Elsevier/Butterworth-Heinemann, 2013. PDF.
- [5] "Climb Performance." Avstop.com. Aviation Online Magazine, n.d. Web. 29 May 2016.